Institut für Wasserbau · Universität Stuttgart

Mitteilungen

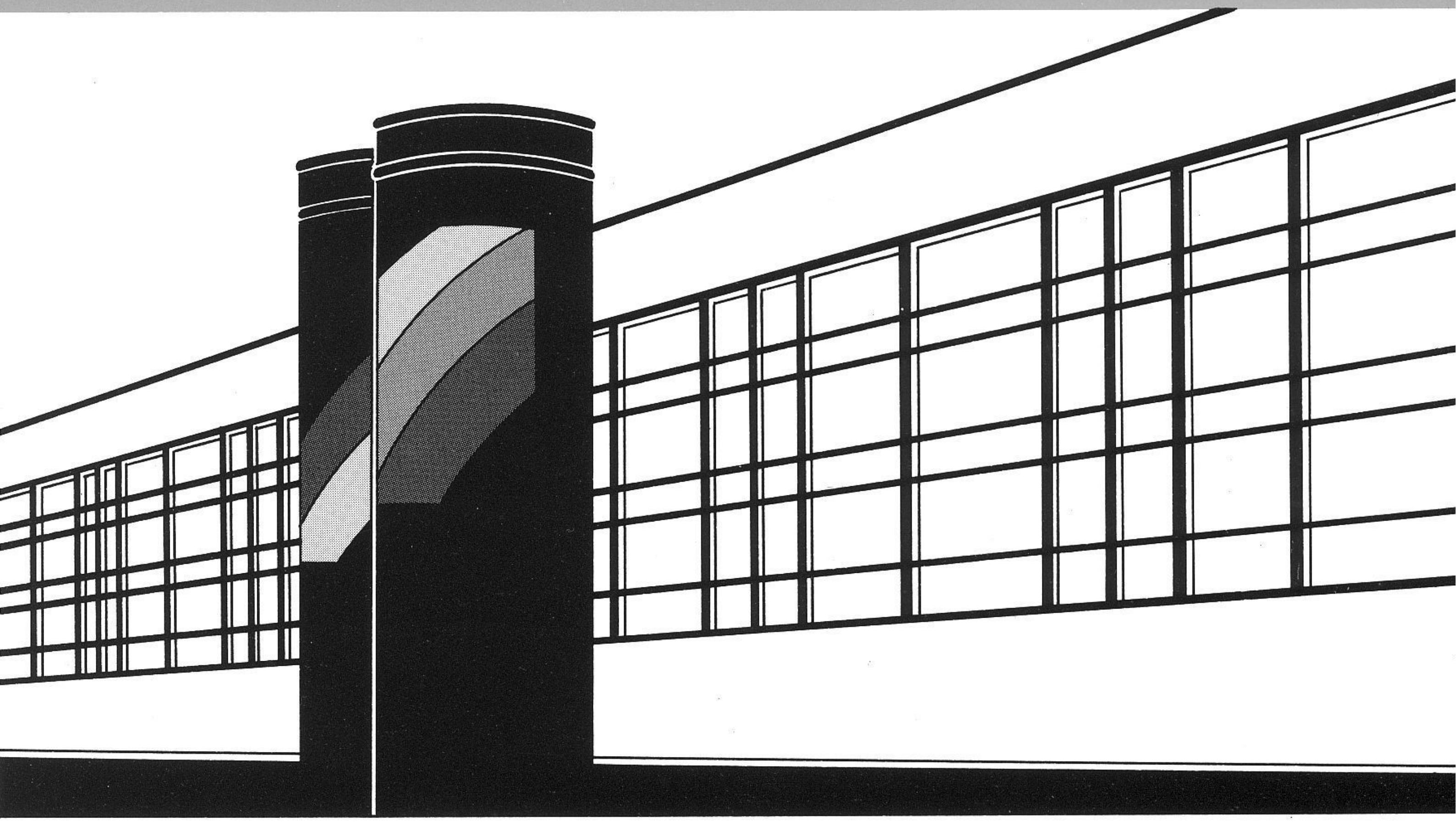

Heft 121 Uwe Ehret

Rainfall and Flood Nowcasting in Small Catchments using Weather Radar

Rainfall and Flood Nowcasting in Small Catchments using Weather Radar

Von der Fakultät Bau- und Umweltingenieurwissenschaften der
Universität Stuttgart zur Erlangung der Würde eines
Doktor-Ingenieurs (Dr.-Ing.) genehmigte Abhandlung

Vorgelegt von
Uwe Ehret
aus Stuttgart

Hauptberichter: Prof. Dr.-Ing. habil. Dr. rer. nat. András Bárdossy
Mitberichter: Prof. Geoffrey G.S. Pegram, Pr Eng, PhD (Lancaster)

Tag der mündlichen Prüfung: 8. Oktober 2002

Institut für Wasserbau der Universität Stuttgart
2003

Heft 121 Rainfall and Flood Nowcasting in Small Catchments using Weather Radar

von
Dr.-Ing.
Uwe Ehret

Eigenverlag des Instituts für Wasserbau der Universität Stuttgart

D93 Rainfall and Flood Nowcasting in Small Catchments using Weather Radar

Titelaufnahme der Deutschen Bibliothek

Ehret, UweVorname:
Rainfall and Flood Nowcasting in Small Catchments using Weather Radar / von Vorname Name. Institut für Wasserbau, Universität Stuttgart. - Stuttgart: Inst. für Wasserbau, 2003

(Mitteilungen / Institut für Wasserbau, Universität Stuttgart: H. 121)
Zugl.: Stuttgart, Univ., Diss., 2008)
ISBN 3-933761-24-7
NE: Institut für Wasserbau <Stuttgart>: Mitteilungen

Herausgegeben 2003 vom Eigenverlag des Instituts für Wasserbau
Druck: Sprint-Druck, Stuttgart

Preface

This work is the result of a research project 'Short term flood-forecasting for the Goldersbach catchment' sponsored by the city of Tübingen. The goal of the project was to develop a short time flood warning model for the Goldersbach (catchment size 75 km^2).

Operational flood forecasting for small catchments is an extremely difficult task. In these cases a forecast based on observed discharge is useless due to the very short lead time. Forecasts based on observed discharge combined with a rainfall runoff model using observed precipitation have a slightly increased lead time. Unfortunately, due the short concentration times even this is not sufficient to take any preventive actions. The only possibility of improvement is the use of precipitation forecasts. Meteorological models provide regular forecasts, however they are not appropriate for this problem. There are several reasons for this: the spatial resolution of the models is not fine enough; the forecasts are inaccurate on small space scales; they are not continuously available but are regularly updated every 6 hours. Short time forecasts of a few hours (nowcasts) can be based on radar data using statistical methods. Due to the uncertainties and errors associated with radar rainfall measurements, reasonable forecasts can only be achieved if radar precipitation is combined with surface observations of rainfall. These combined rainfall rates with their high spatial and temporal resolution can be used to develop a reasonable rainfall forecast. These can then be used as input for rainfall runoff models, and provide a discharge forecast.

Several important steps of the radar based discharge forecasting are addressed in this work. A new method for the calibration of radar measurements was developed. A Markov-chain based spatial rainfall forecasting method is suggested and tested and the forecasts are used in combination with a rainfall runoff model to obtain a set of probable future discharge series.

We gratefully acknowledge the support of the city of Tübingen without which the completion of this work would not have been possible.

Stuttgart 29.05.2003

András Bárdossy

For Dagmar, Christel and Charly

Acknowledgements

First of all, I want to thank my advisors, Professor András Bárdossy and Professor Geoffrey Pegram. Professor Bárdossy for the time I could spend at the Institute for Hydraulic Engineering, the trust he put in me by letting me find my own way, but also the guidance he gave when this way seemed at times to be a dead-end street. Professor Pegram for the introduction to his work and many inspiring discussions wherever we met.

I am also indebted to Professor Hans-Joachim Caspary. During my studies at the HfT Stuttgart, he supported and encouraged me to continue my way at the University of Stuttgart and has since then shown great interest in my whereabouts.

Special thanks go to Dr. Erwin Zehe. During many discussions, he gave me a better insight into the fascinating world of physics. He read and commented critically on each chapter of this work and has been a constant source of motivation through all stages of its completion.

Without my colleague Fridjof Schmidt, the Geographical Information System expert, many of the images in this work would not exist. Also, without his constant chocolate supply, I probably would have starved.

Rolf Becker's experience and support in the more technical, especially database-related parts of my work has been invaluable. Even more so as he was more than busy with other projects and still found time to help me.

I am also grateful for the very constructive co-operation with Dr. Ludwig consulting engineers and the flood-forecasting centre (Hvz) in Karlsruhe, namely Dr. Kai Gerlinger and Dr. Manfred Bremicker. Both have sacrificed a considerable amount of time to answer my questions about the Fgmod/Larsim model. The same applies to Dr. Hermann Gysi from Radar-Info, who introduced me to the possibilities and limitations of radar meteorology.

All colleagues at the Institute for Hydraulic Engineering, I want to thank for atmosphere of support and friendliness, it was a pleasure to work with them.

This work is the result of many people's contributions. Even if they are not mentioned here personally, I am grateful for the support they granted me along the way.

Abstract

The work presented here is based on the project 'Short-term flood-forecasting for the Goldersbach river', initiated by the town of Tübingen. The goal was to develop an operational flood-forecasting system for the Goldersbach catchment. Due to its small size of only 75 km^2, the anticipated lead time of 3.5 hours could not be achieved by gauge observations only. The principal approach was then to develop a weather radar-based, short-term rainfall forecasting system, valid for roughly 2 hours lead time, and to use its forecasts in combination with real-time observations in a rainfall-runoff model to gain the desired lead time.

Firstly, a gauge system in the Goldersbach catchment was established, along with a data transmittal and data storage system to retrieve and store data from rain-gauges, river-gauges and a Doppler weather radar. Then, a radar-based, fuzzy-rule rainfall type classification technique was developed to consider the unique properties of different rainfall types in interpolation and forecasting.

As especially for short-term rainfall forecasting, knowledge of the current rain-field advection is crucial, two estimation techniques were investigated: one based on the Doppler effect, the other on covariance maximization. Based on the advection estimates, a short-term, auto-regressive forecast model was developed.

Then, in order to make optimum use of all available sources of rainfall observation, namely radar and rain-gauges, several combination methods were investigated, and a new method termed 'Merging' was developed. It preserves both the mean rainfall field estimated by the rain-gauges and the spatial variability of the radar image.

For short-term rainfall forecasting, a new model named 'SCM model', short for 'Spectrum-Corrected Markov chain' was developed. Based on radar data, it follows a two-step hierarchical approach. A bi-variate, auto-regressive process is used to forecast the large-scale development of rainfall in a radar image. The individual development of each grid-cell in the image is forecasted by a Markov chain approach. The model can produce forecast scenarios, which makes it suitable for the assessment of upper and lower bounds of future rainfall developments.

Finally, two rainfall-runoff models were tested with respect to their suitability for short-term flood forecasting. The first, FGMOD/LARSIM, is an event-based model, the second, HBV-IWS, is a continuous time model. Using rainfall forecast ensembles generated by the SCM model, upper and lower bounds for the development of discharge could be calculated.

In conclusion, both rainfall-runoff models, in combination with the rainfall forecast, allowed reasonable discharge estimates for up to 3 hours.

Zusammenfassung

Kein anderes Naturphänomen tritt weltweit so häufig auf und verursacht in der Summe so hohe Schäden wie die verschiedenen Arten von Hochwasser (Münchener Rück, 2000). Während man dabei meist an die Überschwemmungen großer Flüsse denkt, wird die Gefahr durch lokal begrenzte Hochwasser oder Sturzfluten, aufgrund ihrer kürzeren Dauer, geringerer Abflussvolumen und einer kleineren Zahl direkt Betroffener, häufig unterschätzt. Durch ihr äußerst schnelles Auftreten bilden jedoch auch sie eine erhebliche Gefahr und führen in der Summe zu großen Schäden.

Dies mussten die Anwohner von Tübingen-Lustnau schon häufig erfahren, zuletzt im Juli 1987. Obwohl das Einzugsgebiet des Goldersbaches mit nur 75 km^2 relativ klein und zudem fast vollständig bewaldet ist, überflutete die Hochwasserwelle innerhalb von nur drei Stunden das Goldersbachtal und erhebliche Teile von Lustnau; Schäden in Millionenhöhe entstanden.

In den folgenden Jahren wurden mehrere, 'konventionelle' Abhilfemaßnahmen untersucht, mussten aber verworfen werden: Die Ausweisung von Überflutungsflächen war aus Platzgründen nicht möglich, ein Entlastungskanal um Lustnau herum war zu kostspielig, ein System kleiner, über das Einzugsgebiet verteilter Rückhaltebecken erreichte nicht das erforderliche Speichervolumen, ein Damm vor dem Ortseingang, mit einer Kronenhöhe von vierzehn Metern groß genug, um ein hundertjährliches Hochwasser aufzunehmen, wurde aus Gründen der Ökologie und des Landschaftsschutzes nicht realisiert.

Schließlich wurde ein neuer Ansatz, bestehend aus drei Bausteinen, entwickelt: Auf Basis einer präzisen Kurzzeit-Niederschlags- und Abflussvorhersage wird ein kleineres Rückhaltebecken, bemessen für ein Hochwasser mit einer Wiederkehrzeit von ungefähr 25 Jahren gesteuert. Darüber hinaus soll durch einen Alarmplan und Objektschutzmaßnahmen an bedrohten Gebäuden das Gefahren- und Schadenspotential in Lustnau minimiert werden.

Dieser Ansatz stellt einen gewissen Paradigmenwechsel dar, da er von der Zielvorgabe hundertjährigen Hochwasserschutzes abrückt und sich in Richtung Risikomanagement entwickelt. Der Vorteil besteht dabei darin, dass sich sowohl Behörden als auch die Öffentlichkeit mit der stets präsenten Hochwassergefahr auseinandersetzen müssen und dadurch im Ernstfall besser reagieren können. Ein weiterer Vorteil ist die Vermeidung großer Eingriffe in den natürlichen Wasserhaushalt.

Das Institut für Wasserbau der Universität Stuttgart (IWS) wurde daher im Juli 1999 mit der Entwicklung und Realisierung eines Niederschlags- und Abflussvorhersagesystems für den Goldersbach beauftragt, aus der die vorliegende Arbeit hervorging. Von Seiten der Stadt lag der gewünschte Vorhersagehorizont bei sechs Stunden. Nach ersten Analysen wurde offensichtlich,

dass diese Zeitspanne nur durch eine Kombination von Niederschlags- und Abflussvorhersage sowie der teilweisen Speicherung der Flutwelle in einem Rückhaltebecken erreicht werden kann. Die maximale Dauer der Niederschlagsvorhersage kann, je nach Niederschlagstyp variierend, mit ungefähr zwei Stunden angesetzt werden, der Zeitgewinn durch Niederschlags-Abfluss Modellierung mit 1,5 Stunden, die Befüllung der Rückhalteräume erreicht weitere 2,5 Stunden.

Die Aufgabenstellung an das IWS konnte daher in folgende Teilaufgaben untergliedert werden:

- Einrichtung eines in Echtzeit abrufbaren Niederschlags- und Abflussmesssystems im Goldersbachgebiet und der notwendigen Kommunikationsstrukturen für die Datenübertragung.
- Entwicklung eines Datenbanksystems für effiziente Datenhaltung und schnellen Datenzugriff.
- Entwicklung von Methoden zur Schätzung der aktuellen Windverhältnisse in einem Radarbild. Diese Information ist vor allem bei schnell ziehenden Niederschlagsfeldern wichtig für die Vorhersage.
- Identifikation unterschiedlicher Niederschlagstypen anhand von Radarbildern. Da diese teilweise sehr unterschiedliche Eigenarten bezüglich Lebenszyklus und Niederschlagsintensitäten aufweisen, ist diese Information sowohl bei der räumlichen Niederschlagsschätzung als auch bei der Vorhersage relevant.
- Bewertung bestehender und Entwicklung neuer Methoden zur kombinierten Schätzung des räumlichen Niederschlages aus Wetterradar und Bodenstationsdaten.
- Entwicklung einer räumlich und zeitlich hochauflösenden Niederschlagsvorhersagetechnik mit Hilfe von Wetterradardaten. Um der nur bis zu einem gewissen Grad vorhersagbaren Natur des Niederschlagsgeschehen zu entsprechen, wurde die Vorhersage als Ensemble möglicher Entwicklungen entwickelt.
- Anpassung und Vergleich zweier Niederschlags-Abfluss Modelle an das Goldersbachgebiet. Dies ist zum einen das FGMOD/LARSIM Modell (Homagk und Ludwig, 1998), das auch bei der Hochwasservorhersagezentrale in Karlsruhe (HVZ) in operationellem Betrieb ist, als auch das am IWS im Einsatz befindliche HBV-IWS Modell. Mit den Szenarien vorhergesagter Niederschlagsentwicklungen als Input, konnten die Abflussvorhersagen ebenfalls als Ensemble gerechnet und obere und untere Grenzen der weiteren Entwicklung angegeben werden.

Messnetz und Datenbanksystem

Im Goldersbachgebiet wurde ein zunächst ein Netz aus Niederschlagsstationen und Pegeln aufgebaut. Alle Stationen können im Zehnminutentakt über das Mobiltelefonnetz abgerufen werden. Weiter wurden für die Gewinnung flächendeckender Niederschlagsinformationen und für die Niederschlagsprognose Daten des Doppler-Wetterradars am Forschungszentrums Karlsruhe genutzt.

Alle Messdaten werden in Datenbanken abgelegt, um mit einem Minimum an Speicherplatz ein Maximum an Zugriffsgeschwindigkeit zu erreichen.

Windverhältnisse

Unter Ausnutzung des Doppler-Effekts verfügte man durch den Wetterradar über Messwerte der aktuellen Zugrichtung und –geschwindigkeit von Niederschlagsfeldern. Da diese Information jedoch nicht immer errechnet werden konnte, aber insbesondere für die Vorhersage schnell ziehender Niederschlagsfelder wichtig ist, wurde aus Gründen der Redundanz eine weitere Methode entwickelt. Bei dieser wird die zwischen zwei Radarbildern stattgefundene Verschiebung der Niederschlagsfelder durch Maximierung der Kovarianz zwischen den Bildern bestimmt. Um eine möglichst rasche Konvergenz der Windschätzung zu erreichen, wurde der iterative 'Simulated Annealing' Optimierungsalgorithmus verwendet.

In Abbildung I sind die über einen Tag aufsummierten Verschiebungsvektoren beider Verfahren dargestellt. Beide Verfahren liefern ähnliche Ergebnisse. Einzig in den Fällen, wenn ein größeres Niederschlagsgebiet den Bereich der Radarbilder betritt oder verlässt, es also nicht auf zwei zeitlich benachbarten Bildern zu sehen ist, irrt das Kovarianzverfahren. Im Bild ist dies zweimal als unrealistischer Sprung der summierten Verschiebungsvektoren zu sehen. Sobald das Niederschlagsfeld jedoch dauerhaft im Radarbild zu sehen ist, stabilisiert sich die Windschätzung wieder.

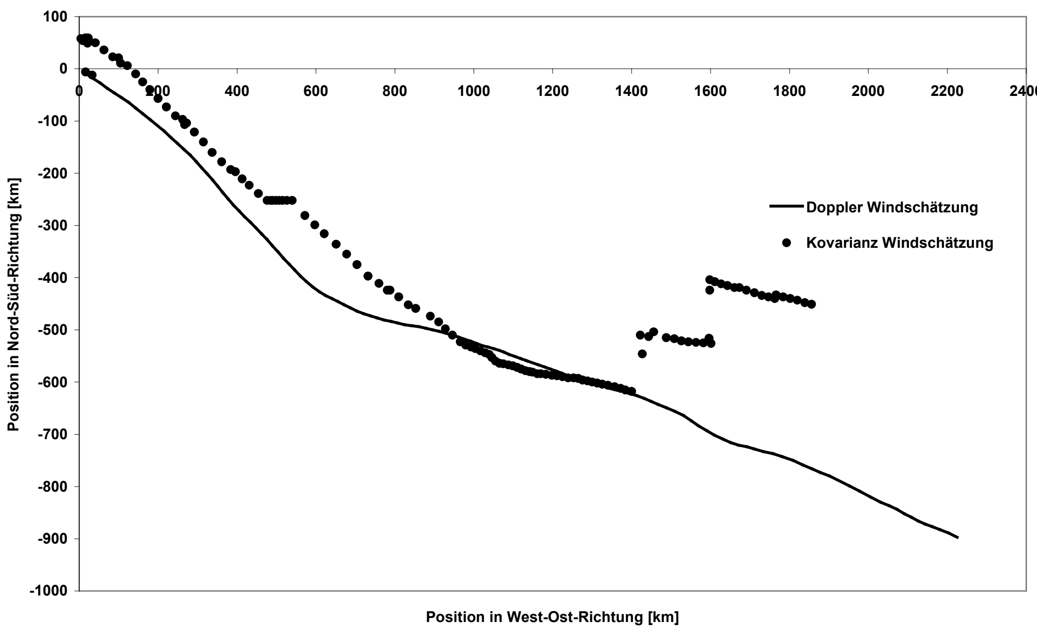

Abbildung I: Windschätzung durch das Dopplerverfahren und Kovarianz-Maximierung

Niederschlagstypen

Niederschlag kann, hauptsächlich aufgrund seiner Genese, in Typen unterteilt werden. Diese können sich, was ihre Lebensdauer, räumliche Erstreckung und typische Intensitäten angeht, deutlich voneinander unterscheiden. In Abbildung II ist exemplarisch die Niederschlagsüberdeckung (der Prozentsatz eines Radarbildes der Niederschlag aufweist) verschiedener Typen gezeigt. Während konvektive Zellen, die oft mit Gewittern einhergehen, nur selten mehr als zehn Prozent des Bildes überdecken, können Warmfrontniederschläge durchaus das gesamte Bild ausfüllen.

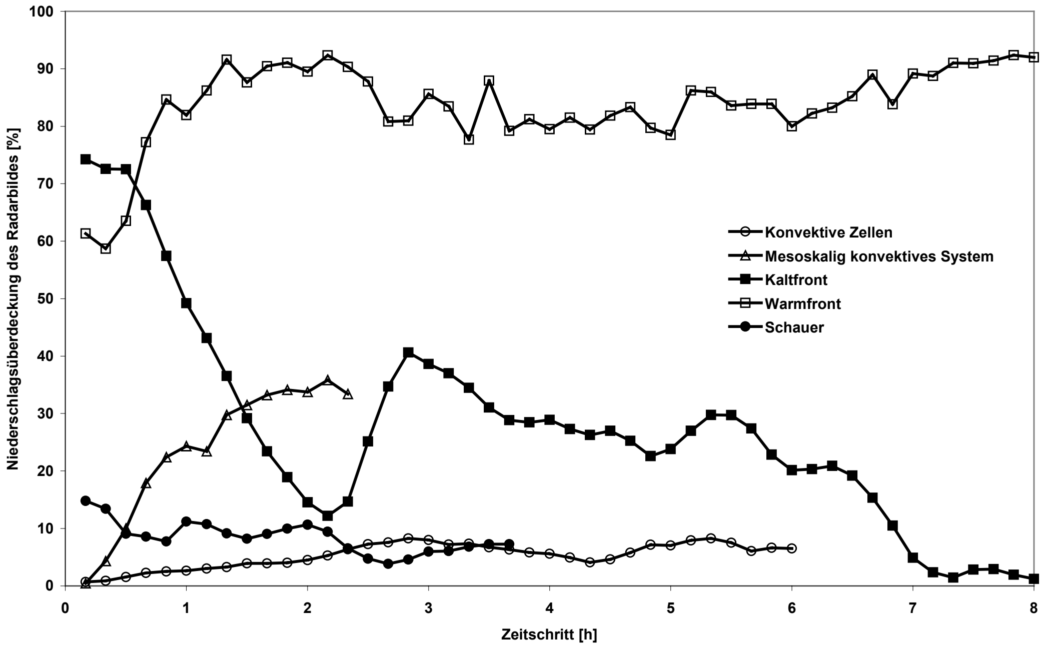

Abbildung II: Typische Zeitreihen der Niederschlagsüberdeckung eines Radarbildes für verschiedene Niederschlagstypen

Für die Niederschlagsvorhersage ist die Kenntnis typischer, weiterer Entwicklungen von Niederschlagsfeldern sehr hilfreich, daher wurde anhand der aus Radarbildern extrahierten Parameter Überdeckungsgrad, mittlerer Niederschlagsintensität und Anteil hoher Niederschlagsintensitäten eine Klassifizierungstechnik auf Basis eines Fuzzy-Regelsystems entwickelt. In Testläufen wurde mit damit eine Trefferquote von 63 Prozent erreicht, wobei Fehlklassifikationen vor allem zwischen Kaltfront- und Schauerniederschlägen auftraten.

Räumliche Niederschlagsschätzung

Niederschlag ist ein zeitlich und räumlich höchst variabler Prozess. Das ist eine Binsenweisheit, vor dem Einsatz von Wetterradar mit seiner hohen räumlichen Auflösung jedoch, als die einzige Informationsquelle die Aufzeichnungen von Niederschlagsstationen waren, konnte man ihr nur unzureichend gerecht werden. Obwohl die Kenntnis von Niederschlagsprozessen mit dem Wetterradar einen Quantensprung erlebte, ist dieser aufgrund seines indirekten Messprinzips bisweilen mit Messfehlern in der Größenordnung von hundert Prozent behaftet.

Es liegt daher nahe, die Vorteile der beiden Meßmethoden, die Genauigkeit der Stationsmessungen und die räumliche Information der Radardaten, zu kombinieren. Während schon seit einigen Jahren multiplikative und andere Kombinationsverfahren existieren, wurde für das Goldersbach Projekt ein neues Verfahren entwickelt, das im Folgenden und in Abbildung III a) – d) erläutert wird.

a) Im Original-Radarbild ist ein Starkniederschlagsfeld über dem Goldersbachgebiet zu sehen, dessen Struktur zwar gut zu erkennen ist, in seinen Absolutwerten jedoch die Stationsmessungen unterschätzt.
b) Um aus den Stationsniederschlägen eine räumliche Information zu gewinnen, werden sie mit dem geostatistischen Verfahren 'Kriging' interpoliert. An den Stationen und im räumlichen Mittel ist das interpolierte Feld zwar korrekt, weist aber eine unrealistisch 'glatte' Struktur auf.
c) Mit den Beobachtungen des Radars direkt an den Stationskoordinaten wird ebenfalls ein Niederschlagsfeld interpoliert. Die Felder aus b) und c) ähneln sich in der Struktur, weisen jedoch unterschiedliche Absolutwerte auf.
d) Zuletzt zieht man vom ursprünglichen Radarbild das interpolierte ab und prägt auf das entstandene Bild die Interpolation aus den Stationsmessungen auf. Damit hat man an den Koordinaten der Stationen die Bodenmesswerte, im Mittelwert das interpolierte Stationsfeld, aber in der räumlichen Struktur das Radarbild weitgehend erhalten. Im Bild ist wieder die Form des Niederschlagsfeldes zu erkennen, die Werte sind allerdings auf das Niveau der Bodenmessungen angehoben worden.

a) Radarbild

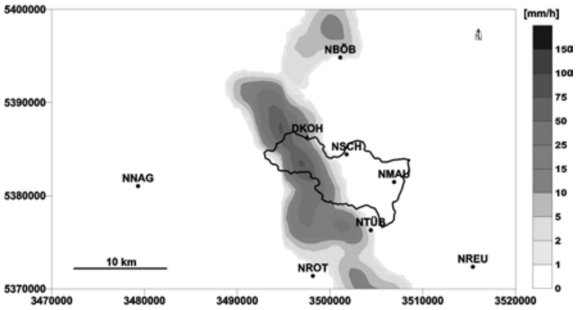

b) Interpolation aus Stationsdaten

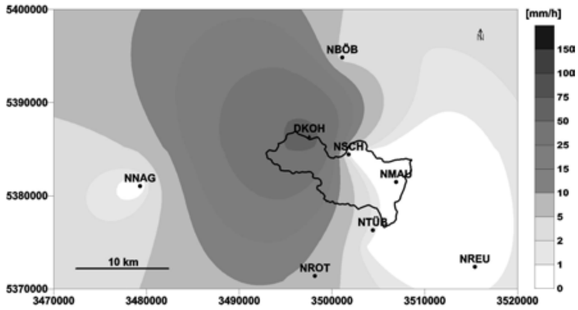

c) Interpoliertes Radarbild

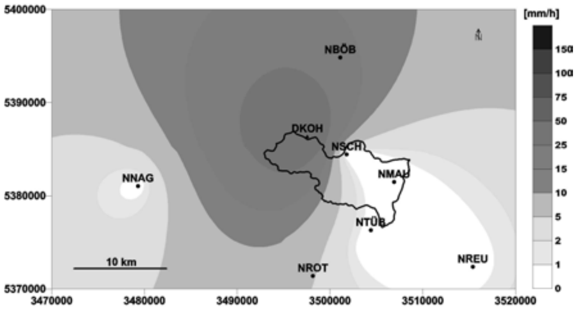

d) Kombination aus Radar und Stationsdaten

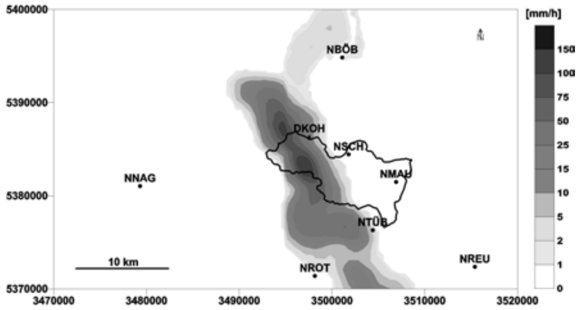

Abbildung III: Kombination von interpolierten Stationsdaten und Radardaten zu einem räumlichen Niederschlagsbild

Niederschlagsvorhersage

Die Unmöglichkeit, das Niederschlagsgeschehen im Radarbild selbst für die Dauer weniger Stunden exakt vorherzusagen, legte einen stochastischen Vorhersageansatz nahe. Damit ist man in der Lage, Ensembles zu rechnen und somit Anhaltspunkte über die Bandbreite möglicher Entwicklungen zu gewinnen.

Für das Goldersbach Projekt wurde das hierarchische 'SCM' Modell, angelehnt an das 'String of Beads' Modell (Pegram und Clothier, 2001) entwickelt: Zuerst wird für das gesamte Radarbild die Überdeckung und mittlere Niederschlagsintensität vorhergesagt, dann die Intensitätsentwicklung jeder einzelnen Rasterzelle im Bild. Die Rastervorhersage wird an die Bildvorhersage angepasst und schließlich das vorhergesagte Radarbild mit dem aktuellen Windvektor verschoben.

Auf der Bildskale wird die Entwicklung durch einen bivariaten, autoregressiven Prozess beschrieben, auf Skale der Rasterzellen durch eine modifizierte Markov-Kette. Dabei werden die möglichen Systemzustände einer Rasterzelle durch ihre Niederschlagsintensität, den aktuellen Niederschlagstyp und die Niederschlagsentwicklung der letzten dreißig Minuten definiert. Mit Hilfe eines Zufallszahlengenerators können nun, verkettet durch die Übergangsmatrix der Systemzustände, beliebig lange Vorhersagesequenzen erzeugt werden.

Da es wahrscheinlich ist, dass sich benachbarte Rasterzellen ähnlich entwickeln, wird die Vorhersage nicht für jede Zelle völlig unabhängig durchgeführt, sondern durch nachträgliches Aufprägen einer räumlichen Struktur eine gewisse Einheitlichkeit der Entwicklung erreicht. Die zu erhaltende räumliche Struktur für jeden Zeitpunkt wird aus dem mittleren Fourierspektrum von Radarbildern der davor liegenden dreißig Minuten gewonnen.

Wie man an dem Vergleich in Abbildung IV erkennen kann, wird die Entwicklung gemessener Niederschlagsfelder durch die Vorhersage zufriedenstellend reproduziert. Der Niederschlagsvorhersage sind in ihrer Dauer jedoch durch die Windverschiebung Grenzen gesetzt. Zieht ein Niederschlagsfeld, wie im gezeigten Beispiel, nach Osten, so entsteht am westlichen Bildrand mit jedem Vorhersagezeitschritt ein größerer Bereich, in dem keine Vorhersage erstellt werden kann, da zum Vorhersagezeitpunkt keine Messdaten zur Verfügung stehen. Ein größeres Radarbild könnte dem Abhilfe schaffen.

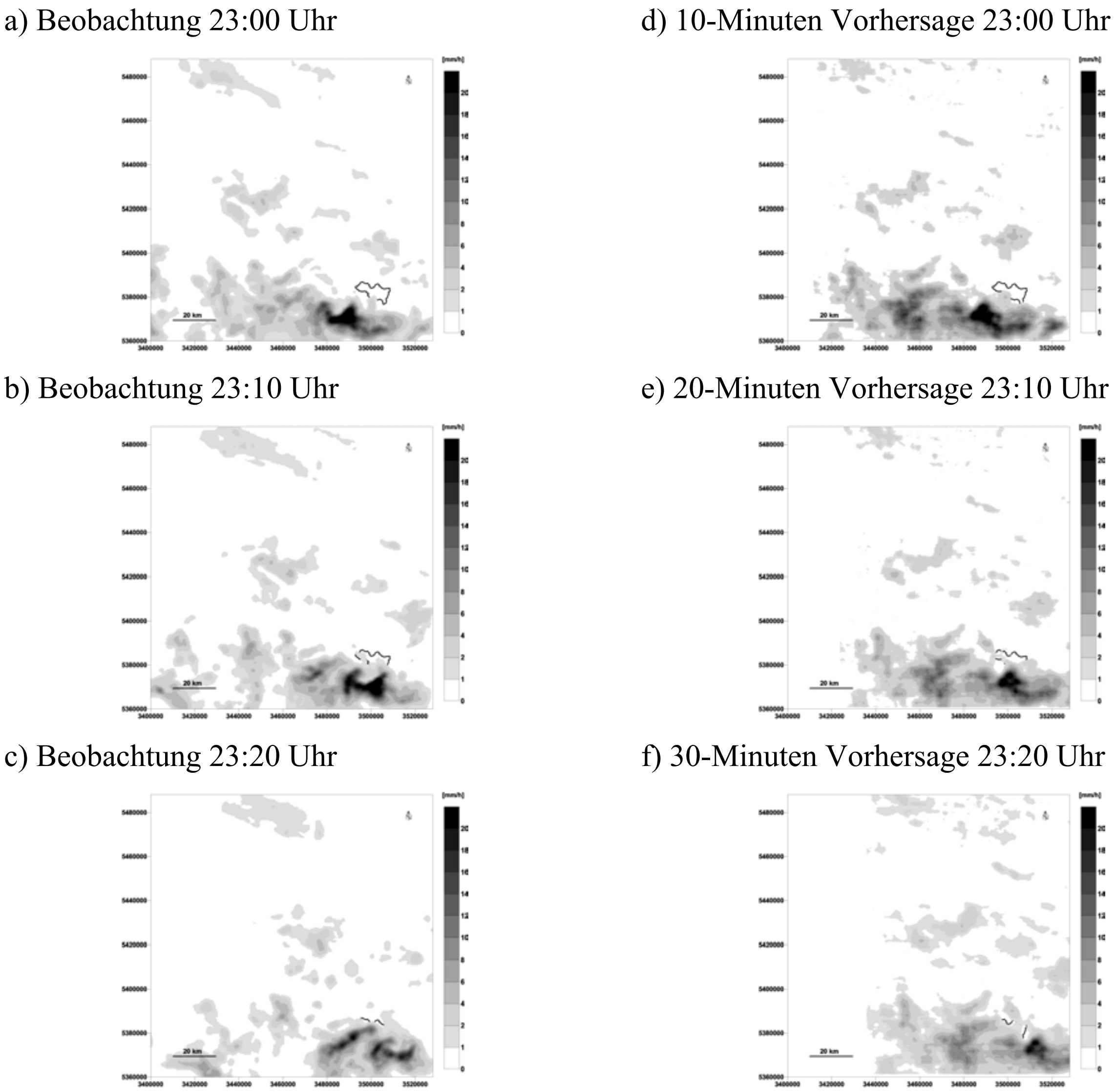

Abbildung IV: Beobachteter und vorhergesagter Niederschlag über Südwest Baden-Württemberg, 20.03.01 23:00 – 23:20 Uhr

Abflussvorhersage

Mit den gemessenen und vorhergesagten Niederschlägen als Input ist die Modellierung und Vorhersage des Niederschlags-Abfluss Prozesses im Einzugsgebiet möglich. Die dazu verwendeten Modelle, FGMOD/LARSIM und HBV-IWS sind sogenannte Blockmodelle, das heißt die abflusswirksamen, physikalischen Prozesse werden nur näherungsweise und in größeren räumlichen Einheiten berücksichtigt.

Während FGMOD/LARSIM ein ereignisbasiertes Modell ist, also eine (automatische) Parameteroptimierung für jedes Niederschlag-Abfluss Ereignis durchgeführt wird, ist HBV-IWS ein Wasserhaushaltsmodell. Dabei werden alle Wasserhaushaltskomponenten wie Abfluss, Bodenfeuchte, Verdunstung usw. kontinuierlich modelliert, eine ereignisabhängige Anpassung ist nicht notwendig.

Gefördert durch das Land Baden-Württemberg, wurde das bei der HVZ im Einsatz befindliche FGMOD/LARSIM an das Goldersbachgebiet angepasst, zu Vergleichszwecken auch HBV-IWS. Wie sich zeigte, waren beide ähnlich gut für die Hochwasservorhersage im Goldersbachgebiet geeignet. In Abbildung V ist eine mit HBV-IWS gerechnete Hochwasservorhersage zu sehen.

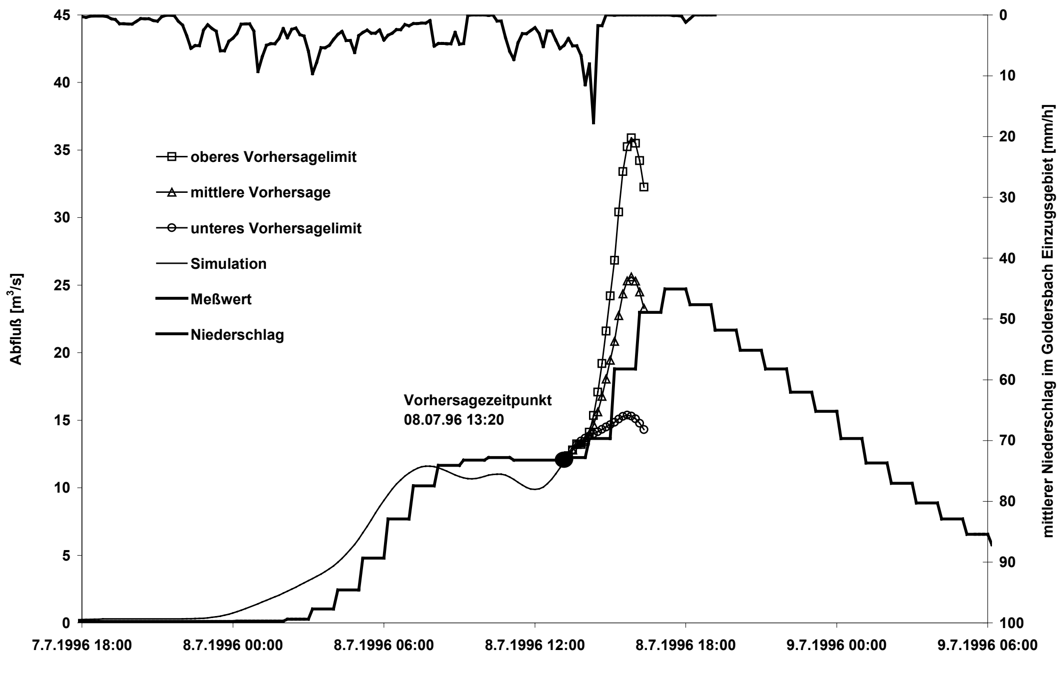

Abbildung V: Abflussbeobachtung, Simulation und Vorhersage, 08.07.96 am Pegel Bebenhausen/Goldersbach. Die Vorhersage ist als oberes und unteres Limit der Vorhersageszenarien sowie als Mittelwert aller Szenarien zu sehen

Bis zum Vorhersagezeitpunkt konnten gemessene, eindeutige Niederschlagsdaten verwendet werden, daher ist bis zu diesem Zeitpunkt auch die Abflusssimulation eindeutig. Jenseits des Vorhersagezeitpunktes werden die Niederschlagsszenarien genutzt (im Bild nicht gezeigt), die Abflussvorhersage spaltet sich daher auf. Während die maximale und die minimale Abflussprognose durch die maximale bzw. minimale Niederschlagsprognose entsteht und die Bandbreite möglicher, weiterer Entwicklungen anzeigt, stimmt das aus allen Vorhersagen gemittelte Szenario mit dem tatsächlich gemessenen Verlauf relativ gut überein.

Damit kann die Einsatzleitung in Tübingen, nur unter Zuhilfenahme des Vorhersagesystems, mit einem zeitlichen Vorlauf von ungefähr 3,5 Stunden Entscheidungen über einzuleitende Maßnahmen für den Hochwasserschutz von Lustnau treffen. Rechnet man den zusätzlichen Zeitgewinn durch die Bewirtschaftung des Rückhaltebeckens hinzu, erreicht man die geforderten sechs Stunden Vorwarnzeit.

Mit dem Tübinger 3-Säulen-Modell aus Hochwasservorhersage, teilweisem Hochwasserrückhalt und Objektschutzmaßnahmen wurden im Hochwasserschutz kleiner Einzugsgebiete neue Wege beschritten. Während das geplante Rückhaltebecken momentan noch in der Genehmigungsphase ist, wird das Mess- und Vorhersagesystem im Herbst 2002 in Betrieb gehen und den Tübinger Bürgern und Behörden das Leben mit der Hochwassergefahr hoffentlich berechenbarer machen.

Table of contents

Figures

Tables

Appendices

Symbols

In case of multiple use, the meaning of a symbol is evident from the context. If the units of a quantity represented by a symbol is not unique, the unit is indicated as [variable] .

Symbol	Unit	Explanation
a	[variable]	bisector
$(a_1,a_2,a_3)_T$	[-]	triangular fuzzy number
A	[-]	empirical constant in the rainfall-reflectivity relation
A	[mm/h]	threshold for sub-division of effective precipitation in FGMOD
A	[variable]	fuzzy set
A	[variable]	parameter matrix
A_k	[-]	amplitude of harmonic k
A_{sc}	[m^2]	sub-catchment area in HBV-IS
AIC_C	[variable]	corrected Akaike Information Criterion
b	[-]	slope
B	[-]	empirical constant in the rainfall-reflectivity relation
B	[variable]	fuzzy set
B	[variable]	parameter matrix
B_k	[-]	amplitude of harmonic k
BAF	[-]	calibration parameter in FGMOD
c_d	[mm/h]	difference of radar rainfall and interpolated radar rainfall
c_{ln}	[-]	logarithmic quotient of radar rainfall and interpolated radar rainfall
c_q	[-]	quotient of radar rainfall and interpolated radar rainfall
C	[$W \cdot m^5/mm^6$]	radar coefficient
C	[1/°C]	empirical evapotranspiration parameter in HBV-IWS
C	[variable]	parameter matrix
C_k	[-]	amplitude of harmonic k
C_1'	[-]	Muskingum parameter in HBV-IWS
C_2'	[-]	Muskingum parameter in HBV-IWS
C_3'	[-]	Muskingum parameter in HBV-IWS
CAF	[-]	calibration parameter in FGMOD
COV	[variable]	covariance
d_λ	[-]	λ-statistic
D_i	[mm]	initial soil-moisture deficit

Symbol	Unit	Explanation
DD	[mm/(°C·day]	degree-day factor in HBV-IWS
DX	[500 m]	shift of a field in x-direction
DY	[500 m]	shift of a field in y-direction
E	[variable]	error (difference)
E_a	[mm]	evapotranspiration in HBV-IWS
E(x)	[variable]	energy of a system X in state x
EKL	[$m^{1/3}$/s]	roughness coefficient of the left embankment in FGMOD
EKM	[$m^{1/3}$/s]	roughness coefficient of the main channel in FGMOD
EKR	[$m^{1/3}$/s]	roughness coefficient of the right embankment in FGMOD
EQD	[-]	retention constant of the fast interflow reservoir in FGMOD
EQI	[-]	retention constant of the slow interflow reservoir in FGMOD
FC	[m]	maximum soil storage capacity in HBV-IWS
FT	[km^2]	sub-catchment area in FGMOD
g_1	[variable]	skewness
g_2	[variable]	curtosis
h	[variable]	distance
H_k	[-]	complex Fourier coefficient of harmonic k
$H_{j,k}$	[-]	complex Fourier coefficient of harmonic j,k
$\hat{H}_{j,k}$	[-]	complex conjugate of $H_{j,k}$
$\tilde{H}_{j,k}$	[-]	adjusted complex Fourier coefficient of harmonic j,k
$\lvert H_{j,k}\rvert^2$	[-]	complex Fourier spectrum
HQ_2	[m^3/s]	2-year recurrence flood
HYDCON	[mm/h]	soil infiltration capacity in HBV-IWS
i	[-]	unit imaginary number
IMF	[mm/h]	mean rainfall intensity in a radar image
IMF_t	[-]	IMF, transformed to a standard normal distribution
k	[-]	hydrometeor reflection factor
k	[-]	order of an auto-regressive process
K	[h]	Muskingum retention constant in HBV-IWS
K_0	[h]	fast interflow storage constant in HBV-IWS
K_1	[h]	interflow storage constant in HBV-IWS
K_2	[h]	baseflow storage constant in HBV-IWS
K_{perc}	[h]	percolation storage constant in HBV-IWS
L	[mm]	threshold waterlevel for fast interflow in HBV-IWS

Symbol	Unit	Explanation
m	[-]	order of a Markov chain
m	[variable]	mean
M	[variable]	spatial field
$\bar{\mathbf{M}}$	[variable]	mean of spatial field **M**
$\mathbf{M_0}$	[variable]	lag-0 covariance matrix
$\mathbf{M_1}$	[variable]	lag-1 covariance matrix
$\mathbf{M_2}$	[-]	lag-2 covariance matrix
MAXBAS	[h]	length of Unit Hydrograph in HBV-IWS
MELT	[mm]	snowmelt in HBV-IWS
n	[-]	state of a Markov chain
n	[-]	number of values
N	[variable]	spatial field
$\bar{\mathbf{N}}$	[variable]	mean of spatial field **N**
$p_{1,2}$	[-]	transition probability from a system state 1 to 2
P	[mm]	precipitation
P	[-]	transition probability matrix
P_B	[W]	back-scattered radiation
$\mathbf{P_{cumulative}}$	[-]	cumulative transition probability matrix
P_{eff}	[mm]	effective precipitation in HBV-IWS
PE_a	[mm]	potential evapotranspiration in HBV-IWS
PE_m	[mm]	mean monthly potential evapotranspiration in HBV-IWS
PWP	[mm]	lower soil-moisture limit in HBV-IWS
Q	[m^3/s]	discharge in HBV-IWS
Q_0	[m^3/s]	fast interflow in HBV-IWS
Q_1	[m^3/s]	interflow in HBV-IWS
Q_2	[m^3/s]	baseflow in HBV-IWS
Q_d	[m^3/s]	direct runoff
$Q_{in}(t_i)$	[m^3/s]	discharge at time-step t_i in HBV-IWS
$Q_{in}(t_{i-1})$	[m^3/s]	discharge at time-step t_{i-1} in HBV-IWS
$Q_{out}(t_i)$	[m^3/s]	discharge at time-step t_i in HBV-IWS
$Q_{out}(t_{i-1})$	[m^3/s]	discharge at time-step t_{i-1} in HBV-IWS
Q_{perc}	[m^3/s]	percolation in HBV-IWS
QI	[10^3 m^3]	slow interflow discharge in FGMOD
r	[m]	distance from radar to target

Symbol	Unit	Explanation
r_k	[-]	lag-k auto-correlation
R	[mm/h]	rainfall intensity
R^*	[mm/h]	rainfall estimate
$R_{radar,kriged}$	[mm/h]	interpolated radar rainfall
$R_{radar,obs}$	[mm/h]	observed radar rainfall
$R_{rg,kriged}$	[mm/h]	interpolated rain-gauge rainfall
$R_{rg,obs}$	[mm/h]	rain-gauge rainfall observation
S_b	[mm]	baseflow reservoir waterlevel in HBV-IWS
S_i	[mm]	interflow reservoir waterlevel in HBV-IWS
SE	[variable]	sum of squared errors
SM	[mm]	soil-moisture in HBV-IWS
t	[variable]	time
t_n	[-]	Annealing temperature of a system at step n
T	[°C]	daily mean temperature in HBV-IWS
T	[variable]	length of a time-series
T_{crit}	[°C]	threshold temperature in HBV-IWS
T_H	[m]	main channel depth in FGMOD
T_m	[°C]	mean monthly temperature in HBV-IWS
TA	[h]	calculation time-step in FGMOD
u	[variable]	coordinate vector
U	[-]	size of a field in u-direction
V	[-]	size of a field in v-direction
VAR	[variable]	variance
W_H	[m]	main channel width at bankful flow in FGMOD
WAR	[-]	rainfall coverage in a radar image
WAR_t	[-]	WAR, transformed to a standard normal distribution
x	[-]	Muskingum weighting factor in HBV-IWS
x	[variable]	value in a series of data
x	[-]	state of a system X
x^*	[variable]	estimator of x
$\overline{x}$	[variable]	mean of x
$\overline{\mathbf{x}}$	[variable]	vector of means of **x**
$\tilde{x}_{0.5}$	[variable]	median
$\tilde{x}_{0.75}$	[variable]	upper quartile

Symbol	Unit	Explanation
$\tilde{x}_{0.25}$	[variable]	lower quartile
X	[variable]	any set or system
$\bar{X}$	[variable]	mean of X
$\mathbf{X}(t)$	[variable]	vector of time-series
$X(\mathbf{u})$	[variable]	value of a random field X at location **u**
$X^*(\mathbf{u})$	[variable]	estimator of a random field X at location **u**
$Y(\mathbf{u})$	[variable]	value of a random field Y at location **u**
Z	[mm^6/m^3]	radar reflectivity
$\mathbf{Z}(t)$	[variable]	zero mean transformation of $\mathbf{X}(t)$
β	[-]	curve shape factor in HBV-IWS
β_{space}	[-]	gradient of the averaged power spectrum of a radar image
ΔE	[variable]	variation of energy between two system states
ε	[-]	normally distributed random number
$\boldsymbol{\varepsilon}$	[-]	vector of normally distributed random numbers
ϕ_k	[-]	lag-k auto-regressive parameter
ϕ_k	[-]	phase angle of harmonic k
γ	[variable]	semi-variogram
η	[-]	uniformly distributed, [0,1]random number
λ	[-]	linear weight
μ	[-]	Lagrange multiplier
$\mu_A(x)$	[-]	membership of x to fuzzy set A
ν	[-]	degree of fulfillment of a fuzzy rule
σ^2	[variable]	variance
σ^2	[variable]	variance
σ	[variable]	standard deviation
τ_u	[variable]	shift of a field in u-direction
τ_v	[variable]	shift of a field in v-direction
ω_1	[-]	fundamental frequency
ω_k	[-]	harmonic of order k
ψ	[-]	discharge coefficient
ψ_{max}	[-]	maximum discharge coefficient
ψ_{min}	[-]	minimum discharge coefficient
ψ_{act}	[-]	discharge coefficient assigned to a sub-catchment in FGMOD

Abbreviations

Only those abbreviations used frequently are listed here. Others are explained at the appropriate places in the text.

Abbreviation	Explanation
10AR	proportion of WAR where rainfall in excess of 10.0 mm/h is observed.
200	indicator for radar data transformed with Z-R-relation A = 200, B = 1.6
300	indicator for radar data transformed with Z-R-relation A = 300, B = 1.5
AIC_C	corrected Akaike Information Criterion
Anaprop	anomalous propagation
ANI	anisotropy coefficient.
ANN	Artificial Neural Network
AR	auto-regressive
CDKO	data logging computer at the site of DKOH
CIWS	forecast processor at IWS
Conti	indicator for radar data transformed with continuously updated Z-R-relation
CRI	Classified Rainfall Intensity at time-step t0
CS+1	number of rainfall intensity class shifts from time-step t0 to t+1
CS0	number of rainfall intensity class shifts from time-step t-1 to t0
CS-1	number of rainfall intensity class shifts from time-step t-2 to t-1
CTÜB	forecast processor in Tübingen
Disdro	indicator for radar data transformed with disdrometer-derived Z-R-relation
DKOH	disdrometer Kohltor
DOF	Degree of Fulfillment
DWD	Deutscher Wetterdienst
EDK	External-Drift Kriging
FFT	Fast Fourier Transform
FGMOD	Flussgebietsmodell
ftp	file transfer protocol.
GCM	General Circulation Model
GDU	Gewässerdirektion Ulm
GE10	indicator that only the highest 10% of data were used
GE100	indicator that all available data were used
HBV-IWS	HBV model, modified by IWS

Abbreviation	Explanation
HVZ	Hochwasservorhersagezentrale Karlsruhe
IMF	Image Mean Flux
IMK	Institut für Meteorologie und Klimatologie, Forschungszentrum Karlsruhe
IWK	Institut für Wasserbau und Kulturtechnik der Universität Karlsruhe
IWS	Institut für Wasserbau der Universität Stuttgart
Kriging	indicator for rain-gauge data interpolated with Ordinary Kriging
LAM	Local Area Model
LARSIM	Large Area Simulation model
MCS	Mesoscale Convective System
Merge	indicator for a rainfall field combined from radar and rain-gauge data
Multi	indicator for continuously multiplicatively updated radar data
NBÖB	rain-gauge Böblingen
NMAU	rain-gauge Mauterswiese
NNAG	rain-gauge Nagold
NREU	rain-gauge Reutlingen
NROT	rain-gauge Rottenburg
NSCH	rain-gauge Schnapseiche
NTÜB	rain-gauge Tübingen
NWP	Numerical Weather Prediction
PBEB	river-gauge Bebenhausen/Goldersbach
PHI	angle of anisotropy
PKIR	river-gauge Kirnbach
PLUS	river-gauge Tübingen-Lustnau/Goldersbach
QD	ratio of borderline occurrences in diagonal directions
QV	ratio of borderline occurrences in the horizontal and vertical directions
RC	Spearman rank-correlation coefficient
RKAR	radar at the IMK, Karlsruhe
RMSE	Root Mean Square Error
SBM	String of Beads Model
SCM	Spectrum-Corrected Markov chain model
t+1	indicator for the time-step 10 minutes after forecast point (forecast time-step)
t0	indicator for the time-step of the forecast point (last observation)
t-1	indicator for the time-step 10 minutes prior to forecast point
t-2	indicator for the time-step 20 minutes prior to the forecast point

Abbreviation	Explanation
TTÜB	temperature-gauge Tübingen
UMEG	Gesellschaft für Umweltmessungen und Umwelterhebungen GmbH
WAR	Wetted Area Ratio
WMO	World Meteorological Organization
Z-R-relation	radar reflectivity (Z) - rainfall intensity (R) relation

1 Introduction

The work presented here mainly emanated from a project initiated by the town of Tübingen, named 'Short-term flood-forecasting for the Goldersbach river'. The Institute for Hydraulic Engineering at the University of Stuttgart (IWS) was instructed to develop a flood-forecasting system for the small but repeatedly flood-producing Goldersbach catchment. It should be suited to the operational management of flood-retention basins and serve as a support tool for decision-makers to apply measures for flood-protection in the town of Tübingen. The project started in July 1999, three years later, in July 2002, the system was handed over. However, work continues in improvement of system components, supporting the contractor to become acquainted with the system and finally the development and implementation of an alarm plan to become effective in the case of a flood.

The scope of the project work spanned a great range, from the planning and installation of a telemetered gauge system to the development of techniques for local, short-term rainfall prediction; from the design of database systems for efficient data storage to the fitting and application of rainfall-runoff models; from pouring concrete for the foundations of rain-gauges to programming interfaces for mobile net data transmittal. Indeed, a very enriching experience for those responsible for the project and a comprehensive introduction to all aspects of flood-forecasting. It is the aim of this dissertation to give an overview of the work carried out in the course of the project, with respect to both the engineering and, in greater depth, the scientific aspects. The set-up of the gauge system reflects the specific characteristics of the Goldersbach catchment and leaves little room for generalizations, however the development of the general forecasting scheme, especially the programs for rainfall forecast and rainfall-runoff modeling have been designed with the aim of general applicability, i.e. easy transfer to other sites.

The work is structured in nine chapters. The first, sub-divided in three sections, gives a general introduction to the scope of work. In section 1.1, the motivation and necessity for rainfall and runoff nowcasting in small catchments is described, followed by the conceptual formulation of the goals to be achieved by the project in section 1.2. With the desired aims defined, the principal approach and appropriate methods of resolution are outlined in section 1.3. Chapter 2 is dedicated to general information constituting the conceptual and physical context of the project work. It starts with a brief section of definitions, followed by an introduction to the principal atmospheric processes associated with the formation of precipitation and a description of the function, advantages and limitations of weather radar, the most important means of rainfall observation used in the project. Beyond the physical background, there is also the scientific context. Hence, history and current state-of-the-art of the two fields of research most relevant for this work, namely rainfall simulation and rainfall-runoff modeling, are briefly outlined at the end of the chapter. Where appropriate, further scientific context is given in the introductory sections of chapters 3 through 8. There, each aspect of the flood-forecasting system is explained and evaluated in detail. Final conclusions on the overall system performance and comparisons of desired and achieved results are formulated in chapter 9. The same chapter includes a perspective about further work in the Goldersbach project in particular and in the field of flood-forecasting in small catchments in general, flanked by examples of current-day research directions.

1.1 Motivation

River floods – the term is usually associated with extreme events in major river systems such as the 1993 flood on the Mississippi river or the 1997 Odra flood. While they remain in one's memory due to their elementary power and the feeling of powerlessness they raise, the occurrence and relevance of floods in small catchments, smaller in volume, duration and the number of people directly affected is often somewhat neglected. However, floods in small catchment do occur, they occur fast and they occur without warning, taking people by surprise. The surprise effect and, if one sums up their occurrence frequency over space and time, definitely makes them a threat to life and property not to be taken lightly.

An illustrative example for Southwest Germany is the flood event in the Main-Tauber area, where a thunderstorm event accompanied by severe rainfall forced the Muck- and Brehmbach creeks with a drainage basin area of only 140 km^2 to overflow and caused damages in the order of € 28 Mio. (LFU, 1985). In the Black Forest, the Schuttertal watershed comprising 130 km^2 has had a long history of floods: The town of Lahr, located at the basin outlet suffered flooding in May 1978, July 1980 and May 1983, with overall damages amounting to € 18 Mio. according to WWV (1983). Also triggered by thunderstorms over a catchment of only 80 km^2, the town of Oppenau was surprised by a flood in June 1994, causing damages in the order of € 33 Mio.

Obviously, there is a need for flood protection or warning not only in large, but also in small catchments. The typical approaches of flood protection, however are not always directly applicable to small catchments. Before going into greater detail on this subject, it is helpful to briefly review the range of usual protective measures taken for flood-protection. They can broadly be classified into operational, constructional and organizational measures. The operational class covers alarm plans and early-warning systems. For example, in the Federal State of Baden-Württemberg, Germany, the operational flood forecasting center HVZ provides flood-forecasts for all major river systems in the state. Constructive measures comprise all structures built to either keep water in the main river course (longitudinal dikes) or to retain water in order to spread flood volumes over a longer period of time and thus reduce peaks. All permanent or mobile dams and retention basins belong to this class. Organizational measures cover all infrastructure decisions to assign parts of the landscape to purposeful, harmless flooding, such as polders or floodplains.

Apart from the problems relevant only to small catchments, there are some general limitations of flood protection to be considered. Firstly, especially longitudinal dikes may lead to a treacherous feeling of security: Providing full protection up to their maximum height, any flood exceeding it inevitably releases its entire volume, the effect on the surrounding areas being worse than if the dike had not existed at all. Next, all permanent structures alter to a certain degree the natural spatio-temporal distribution of water in their area of influence, an issue neglected in the past, now growing increasingly important. Finally, almost all decisions with respect to flood protection are based on extreme-value statistics, i.e. the extrapolation of observed, historical flood frequency-magnitude relations under the implicit assumption of stationary conditions.

This assumption however appears increasingly doubtful in recent years, at least in Southwestern Germany, where non-stationarity investigations by Bárdossy (1995) at 13 gauges in Baden-Württemberg revealed increased flood risk at 10 gauges, with the most likely start of non-stationarity in the 1970s. Further research conducted by Caspary and Bárdossy (1995) linked the shift in flood occurrences especially in winter to changes of atmospheric circulation pattern occurrence and persistence. With respect to extreme-value statistics, this leads to dramatic shifts in design floods in recent decades. The 100-year design flood, calculated from the time-series 1932 - 1976 at gauge Pforzheim, river Enz amounted to 368 m^3/s, with uncertainty bounds of ±24%. Extending the series over the presumed stationarity breakpoint to 1999 drastically reduced the probability of the former 100-year flood to a 25 year recurrence probability, with uncertainty bounds of ±19%. Applying only the series after the breakpoint (1976 - 1999) reduced the return period of the same 368 m^3/s (±27%) to a mere 10–year flood! Similar tendencies were observed at the gauge Beuron, river Danube and several others by Caspary (2000) and Caspary (2001). Obviously, the philosophy to design flood protection structures based on extreme-value statistics, providing protection of a certain risk only in the statistical sense to begin with, might be subject to an enlargement of uncertainty bounds if the stationarity assumption is no longer fully valid.

Coming back to the special case of flood protection in small catchments, further aspects have to be considered. As previously mentioned, HVZ at the moment only issues warnings for large rivers. With roughly 1200 municipalities as potential customers in Baden-Württemberg, it is understandable that up to now, HVZ refrains to engage in small-scale flood forecasting. A fact that makes operational flood-forecasting challenging in small catchments is the usually low time to peak and the lack of upstream gauges useful for forecasting purposes. Finally, constructional and organizational measures are often constrained by the lack of space in a small catchment.

All of the above problems apply to the Goldersbach catchment. Encompassing only 75 km^2, the Goldersbach has nevertheless inundated the town of Tübingen-Lustnau several times. In 1955, 1975, 1978 and last in 1987, sudden flooding caused damages that ranged in the order of magnitude of several million Euro (WWA Reutlingen, 1987). Seeking relief the conventional way, several options were investigated but were successively rejected. A relief channel to bypass Lustnau was with € 13.5 Mio. by far too expensive, a system of small retention basins throughout the catchment did not reach the required retention volume but would have significantly altered natural hydrological and hydraulic conditions, the same applied to a the artificial enlargement of the river cross-section throughout the city. A 14-m dam situated close to the city limits, large enough to accept a 100-year flood was rejected due to environmental reasons and public protest.

Finally, a new approach towards coping with floods, resting on three pillars was developed: The first being a flood-forecasting system based on rainfall forecasts and rainfall-runoff modeling. Operated according to the flood-forecast, the second pillar is partial flood retention up to roughly a 30-year flood with a semi-mobile retention basin. The third pillar finally is the direct implementation of protective measures at edifices in endangered areas, also dependent on timely warning. This approach constitutes a certain paradigm shift in the way to cope with floods. From the idea of static 100- or 1000-year flood protection (which in public opinion has the tendency to be mixed with 100% flood protection) to a policy of risk awareness and flexible responses on floods. The advantages of the new approach are that both decision-makers and the public have to be aware of an ever-present flood-risk, which means that in case of emergency, it does not take them by surprise. Also, limiting structural measures to flood protection of lower recurrence intervals or using mobile structures minimizes the impact on natural conditions. On the other side, a prerequisite for successful function is the willingness of all parties involved to regard flood-awareness as a constant duty, not a one-time exercise and the availability of an early-warning for lead times long enough to take all necessary protective measures in the case of a flood.

Aware of that, the town of Tübingen instructed the IWS to investigate the possible lead times achievable by an early-warning system for the Goldersbach catchment. If its feasibility should be proven, such a system suitable for operational use should be developed, serving both the timely and appropriate operation of a flood retention basin, evacuation of the public and execution of protective measures at buildings in potentially flooded areas. As mentioned above, the project was realized in the period from July 1999 to July 2002 and is the basis for this thesis.

1.2 Goals

From the perspective of the town of Tübingen, the project requirements and desired results were clear, i.e. the development of an operational system to forecast floods in the Goldersbach catchment. It should be robust, redundant and suited to the use as decision support system in retention basin operation and execution of evacuation and further protective measures. The anticipated lead time, dictated by the time needed to take action was specified as 6 hours including the delay achieved by basin filling or 3.5 hours to be provided by the forecasting system only.

The desired goals to be achieved from the University's scientific point of view were somewhat more general. Using the example of the Goldersbach project, the general possibilities for flood-forecasting in small catchments should be investigated. The system to be developed should not be tailored exclusively to the Goldersbach catchment, but allow easy adaptation to other sites. To facilitate this, the system should be modular, with individual components easily interchangeable. Furthermore, the underlying philosophy was to develop a forecasting scheme which acknowledges its imminent uncertainties. To realize this, all forecasts should be run as ensembles, thus allowing specification of error bounds to the model output.

Growing familiar with the Goldersbach catchment, namely its rainfall-runoff characteristics, it soon became obvious that the desired lead time of 3.5 hours cannot be achieved by real-time gauge observations only, be it rain- or rivergauges. Additionally, a sufficiently precise rainfall forecast (or rather nowcast) in the order of 2 hours was indispensable. The remaining 1.5 hours of lead time, corresponding to the catchment's time of concentration, could then be provided by rainfall-runoff modeling using real-time rainfall observations and rainfall forecasts. With the principal goal established, the task was then split into several sub-tasks. They are briefly listed in the following. A more comprehensive presentation of goals and approaches is given in section 1.3.

- Select the sources of information necessary for an operational flood forecasting system in a small catchment.
- Install a tele-metered gauge system in the Goldersbach catchment and establish the data transfer from all additional sources of information.
- Develop a database system for efficient storage of and fast access to the data.
- Investigate existing or develop new techniques to optimize the spatial estimation of rainfall combining observations from different sensors.
- Develop a spatially and temporally highly resolved rainfall nowcasting technique to asses the range of possible rainfall developments within the next few hours. To achieve this goal, weather radar data are used.

- Fit a rainfall-runoff model to the catchment that makes use of the high resolution of rainfall input from radar and rainfall interpolation. The model should be tuned to good performance in cases of flood and it has to be able to use rainfall forecast scenarios in addition to rainfall observation as input. The output shall be in the form of a range of possible future discharge developments indicated by error bounds on any desired level. With the system established,
- investigate how much overall lead time can be achieved and quantify the contribution of each individual component. Finally,
- identify and evaluate the sources of error in the system and, if possible, reduce them.

1.3 Approach

The principal layout of the work, including the introductory and concluding sections, has already been presented in the introduction to this chapter. In the following, emphasis is put on the more conceptual and technical components of the forecasting systems. The structure of it is strongly reflected in the contents and sequence of chapters 3 through 8. For easy orientation, the system components, interrelations and respective chapter enumeration are shown in Figure 1.1. Below, each chapter i.e. each component of the overall solution approach is briefly discussed.

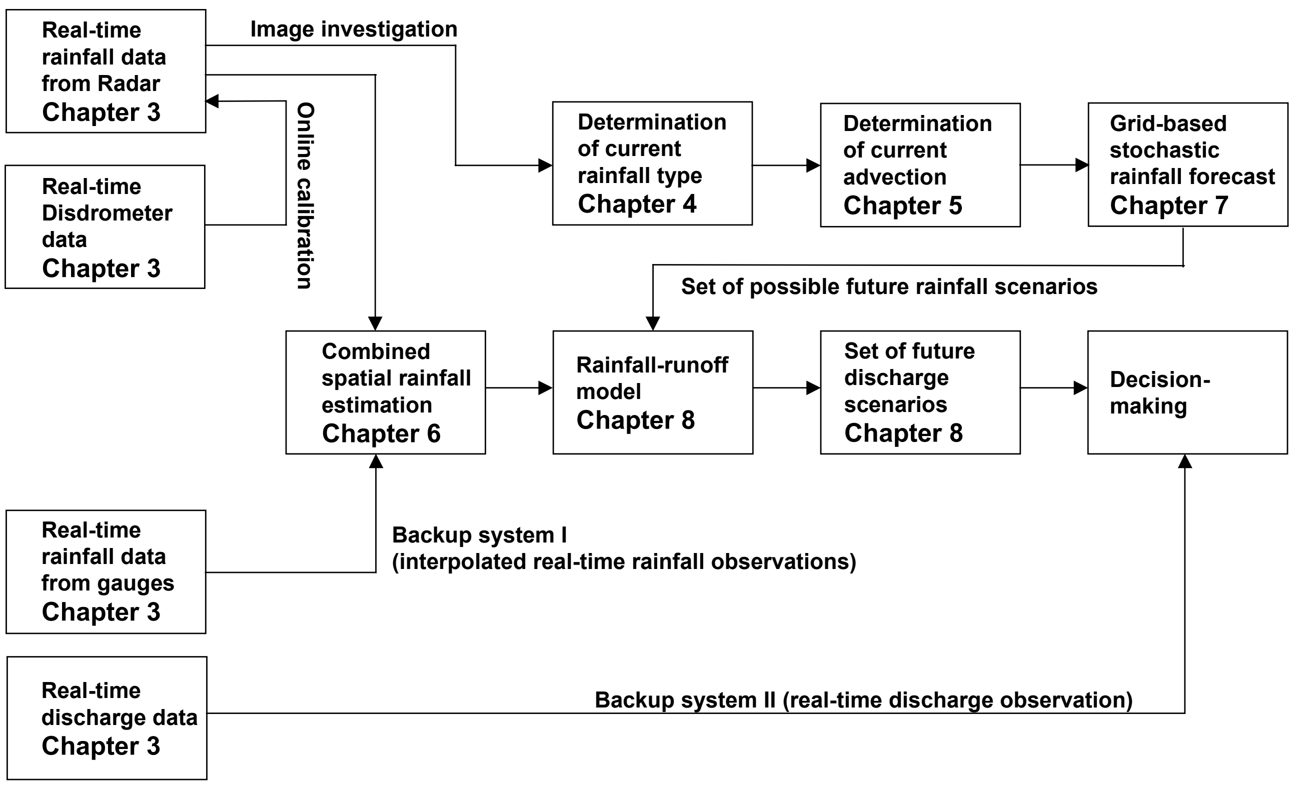

Figure 1.1: Principal structure and components of the Goldersbach flood-forecasting system

Data – Chapter 3

Data are the basis of all modeling, be it simulation or forecasting. Good quality input data are essential as even the most sophisticated algorithm cannot compensate for poor data. In the Goldersbach project, not only data quality considerations were an issue, with the requirements of an operational system in mind, but also data communication and storage played an important role. Hence, considerable time and effort was spent on the selection of gauge types and the necessary spatial and temporal data resolution. Finally, rainfall data were taken from a weather radar, rain-gauges in the federal on-line network and also from three gauges installed directly in the catchment. For reasons of model calibration and operational redundancy, discharge data from three rivergauges in the Goldersbach catchment were also added to the pool of data. After a brief introduction to the catchment characteristics in section 3.1, all components of the gauge network are described in section 3.2, followed by a discussion of data storage issues in section 3.3.

Rainfall type classification – Chapter 4

Investigating rainfall, especially in the unequalled spatial resolution of radar observations reveals its very distinct properties according to the underlying hydrometeorological process of formation. Differences can be identified with respect to persistence, velocity and direction of movement as well as typical rainfall intensities. Clearly, knowledge of the current rainfall type and its typical behavior would be helpful both in the spatial interpolation of rainfall observations as well as in short-term rainfall forecasting. This is attempted in chapter 4. After a brief introduction to the meteorological categories of rainfall, a fuzzy-rule approach to automatically classify radar images according to the prevailing rainfall type is developed and described. Antedating the conclusions given in section 4.3, a sub-division into all meteorological rainfall types was found difficult to achieve. For the purposes mentioned above, interpolation and forecasting, however a distinction into three major rainfall types, stratiform, convective and mixed, was found satisfactory.

Advection estimation and nowcasting– Chapter 5

For local rainfall predictions up to 2 – 3 hours ahead, arguably the most important parameter is rain-field advection. Especially in cases of frontal or stratiform rain, a 'frozen field' advection nowcast is a reasonable estimate of future rainfall. For the Goldersbach project, one estimate of the mean field advection vector was available from the weather radar, exploiting the Doppler effect observable on the emitted and received electromagnetic radar signals. Investigations described in section 5.1 confirmed the applicability of the Doppler advection estimates, however occasional cases of malfunction occurred. For the sake of redundancy, an alternative approach was developed in section 5.1, estimating the shifting vector in-between neighboring radar images through iterative covariance maximization. This method achieved results comparable and even slightly superior to the Doppler estimates but require more computing time. For the operational case, it was then decided to use the Doppler data whenever available, in all other cases the estimates from covariance maximization. In section 5.2, an auto-regressive approach to short-term advection forecasting is proposed. For the very short lead times required for the Goldersbach project, however it was found that a simple persistence forecast was sufficient.

Spatial rainfall estimation – Chapter 6

Spatial rainfall information – with the introduction of weather radar one might have thought that this demand would be satisfied. However, despite its high spatial and temporal resolution in the order of a few hundred meters and minutes, it suffers some quality limitations too strong to be neglected. A brief overview of radar and its sources of error is given in section 2.3. The other option, ground-based point observations of rainfall using rain-gauges, is commonly regarded as more accurate but suffers from its limited spatial significance. Combing the strengths of the two therefore seems a worthwhile thing to do in order to improve the input to rainfall-runoff models. In chapter 6, different approaches for spatial rainfall estimation are investigated. Techniques range from updating Z-R-relations used to transform radar reflectivity observations to rain-rate (sections 6.3 and 6.4) over various kriging techniques described in section 6.5 to a new method termed geostatistical merging (section 6.6). Merging combines a mean field interpolated from rain-gauge observations with the spatial variability of radar data. Based on a multi-objective comparison, conclusions drawn in section 6.7 favor the merging approach.

Rainfall Nowcasting – Chapter 7

As already stated in the above description of goals, only the use of rainfall forecasting in addition to real-time observations reaches the required lead time. According to Obled and Datin (1997), three sources of estimating future rainfall can be thought of: Nowcasting, essentially by extrapolation of radar imagery. This allows the estimation of the spatial distribution of future rainfalls. but it has been recognized that this approach allows extension only over the time of a few hours at best. In mountainous regions, the interference with the relief but also the observation uncertainties over regions affected by masking or ground clutter may further restrict this time range. A second approach is short term mesoscale meteorological modeling. Those models still use grid elements in the order of 50 – 100 km^2 which may not allow a good fit to the contours of the basin of interest. Also, their performance is still limited and their use for small catchments and short lead times may not be thought of for several years. This is also shown by Brath (1997), who found the output of a General Circulation Model (GCM) and a Local Area Model (LAM) for two large-scale flood events in the Po river basin quite different from the rain amounts observed at rain-gauges. Stochastic rainfall scenarios finally are constrained by available real time information. This approach has the advantage that it can be readily implemented while being able to incorporate any new information made available in real time. The crucial assumption is that during a storm, temporal and spatial rainfall patterns will behave as has been observed over past similar events. In real time operation, a rather specific aspect is that the future storm development is constrained by the already observed part of the event. To account for this may be termed 'conditioning on the immediate past' and this effect is typically sensitive over a few hours ahead.

Another look at the same aspect is given by the diagram in Figure 1.2, where the quality of weather forecasts, defined as the product of the accuracy and detail achievable is shown as a function of lead time for three different forecasting methods: extrapolation schemes, meso- and synoptic scale numerical weather prediction. The figure is highly schematic and the stage at which the quality of one technique becomes superior to another will not only change over the years with the development of different methods but also depend on the particular phenomenon being forecast.

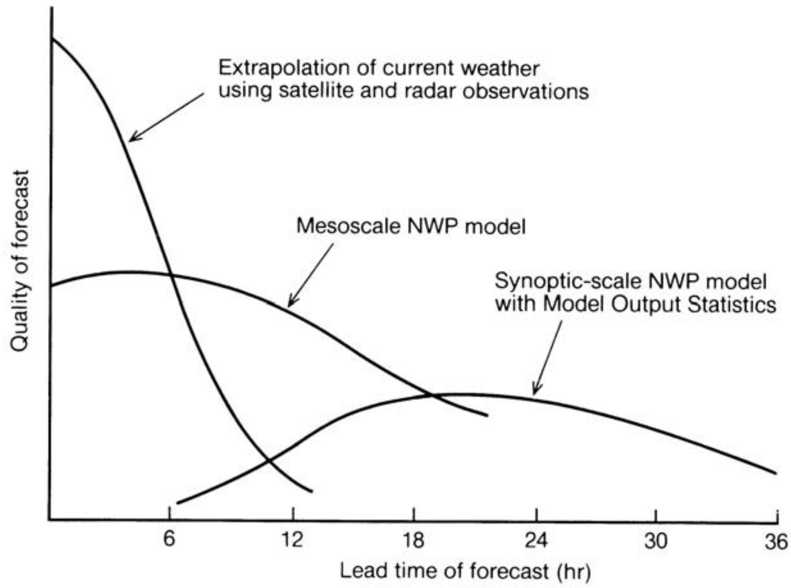

Figure 1.2: The quality of weather forecasts as a function of lead time for three different forecasting methods. (Collier, 1989).

Nevertheless, the above general statements indicate that for the Goldersbach catchment, due to its small size and short time to peak an accurate forecast in the order of a few hours is most relevant. The principal approach was then chosen to be a combination of an extrapolation technique based on the advection analysis and forecast in chapter 5 and a stochastic, hierarchical forecasting technique closely related to the 'String of Beads Model' (SBM) approach by Pegram and Clothier

(2001). In principle, forecasting is done on two scales, the mean development of rain-rate and -coverage in a radar image (section 7.2) and the development of each radar pixel as described in section 7.3. The pixel scale forecast preserves the observed spatial correlation structure of rainfall, shifting and scaling of the forecasted pixel values to match the image parameter forecast ensures a statistically correct large-scale behavior. Applying an auto-regressive approach on image scale and a Markov chain on pixel scale allows fast and easy generation of a large number of equally likely forecast scenarios. Forecasted images are then shifted according to the forecasted advection vector. As outlined in the conclusions (section 7.5), reasonable nowcasts up to a forecast horizon of 2 hours are possible, with the quality dependent on the actual rainfall type.

Flood nowcasting – Chapter 8

The final component of the forecast system is the representation of the catchment's rainfall-runoff behavior with a rainfall-runoff model. Here, two different approaches were pursued. Due to the public interest in the subject of flood-forecasting in small catchments, the Federal State of Baden-Württemberg financially supported the Goldersbach project to fit the rainfall-runoff model FGMOD/LARSIM to the catchment. FGMOD/LARSIM has been in successful operational use for several years at the HVZ. There, it is used to model and forecast the response and flood propagation in larger catchments in Baden-Württemberg. FGMOD/LARISM in calculation mode FGMOD is an event-based, conceptual model in a sense that it estimates certain model parameters from observed discharge hydrographs directly prior to the forecast point and does not continuously simulate water balance components. During calibration and application, it was found that for the Goldersbach catchment with a strong dependency of runoff formation to initial soil-moisture conditions, the model sometimes showed an untimely rise of discharge when the real system was dry, retention potential was high and the observed rise of discharge lagged the triggering rainfall event. Alternatively, the semi-distributed, physically based HBV-IWS model was applied. HBV-IWS is a continuous time model for continuous simulation and takes into account initial system conditions such as soil-moisture. Parameter estimation, calibration and simulation runs are described in sections 8.2 and 8.3, conclusions with respect to the applicability for flood-forecasting purposes of both models are drawn in section 8.6.

To conclude the description of principal approaches to the task of flood-forecasting in the Goldersbach catchment, it is worth taking another look at Figure 1.1. Essential for any operational warning system is to obey the rule of redundancy. As can be seen, three levels of redundancy have been integrated in the system. If the primary basis for rainfall forecasts, weather radar, fails the gain of time due to it drops out, but with the use of real-time rain-gauge observations still the lead time stemming from rainfall-runoff modeling is maintained. If the rain-gauge system should also malfunction, at least real-time rivergauge observations provide an insight into the state of the catchment.

2 General information

The journey of water through different states of aggregation and environments is known as the hydrologic cycle. From evaporation above land and ocean, transportation through air mass convection on synoptic scale, condensation, droplet formation in clouds, precipitation, soil infiltration, surface and sub-surface transport and finally accumulated flow in rivers, it is subject to a dizzying number of physical processes. Due to the limited nature of man's comprehension, the cycle was cut into distinct compartments. 'Distinct' in that context means that each section is homogeneous with respect to a certain measure. Typically, this was either the state of aggregation of water, the environment, a dominant physical law the water is subject to or some measure of scale, either temporal or spatial. Historically, the scientific branches Meteorology, Hydrology and Hydraulics evolved, each developing its own framework of dominating laws, process descriptions and scale definitions.

Accompanying the path of water through many aspects of the hydrology cycle, the Goldersbach project encompasses, to a greater or lesser extent all of the above compartments. It starts with meteorology for rainfall nowcasting purposes, continued by hydrology to describe the rainfall-runoff transformation in the catchment area and finally hydraulics for the propagation of the accumulated water in the channels. Although exciting due to its interdisciplinary nature, this also put a serious constraint on the time available for process modeling in the individual compartments. Nevertheless, it seems appropriate to give a short introduction to the history and state of the art for each of the scientific disciplines with emphasis to the special fields relevant for the Goldersbach project. Starting with section 2.1, the terms and concepts used throughout the report are defined. Then, a brief overview of hydrometeorological processes is given in section 2.2. The subsequent section, 2.3, is devoted to weather radar. It was considered worthwhile including such a chapter as the use of weather radar had and still has a strong influence on many aspects of meteorology and hydrology, especially the formulation of better descriptions of rainfall-forming processes, short-term precipitation forecasting and the evolution from lumped to more distributed hydrological models. Using radar data however requires knowledge of its sources of error and resulting quality limitations. Hence a brief description of the major sources of error is also included in the radar section. It is followed by a historical and formal overview of rainfall simulation techniques in section 2.4. A comprehensive overview of that field could easily fill a book in itself, the overview is therefore very short and arguably selective. Additionally, bearing in mind that for operational rainfall nowcasting purposes mainly stochastical approaches are relevant, the field of large-scale numerical weather description has been neglected altogether. Finally, a short overview of hydrological modeling is given in section 2.5. Additional information on those topics is, where necessary and appropriate, given in the introductory sections of later chapters.

2.1 Definitions and abbreviations

In addition to the list of symbols listed at the beginning, some terms and abbreviations often used in this work are described in this section. Firstly, this is the notion of 'scale' which describes a spatial or temporal extension. Scale limits are often defined by the dominance and meaningfulness of physical processes. In Table 2.1, spatial hierarchies and terminology in the fields of science relevant for the Goldersbach project are listed. It closely follows the description given by Becker (1986).

<table>
<tr><th>Atmospheric Scale</th><th>Hydrological Scale</th><th>Geographical Scale</th><th>Distance [m]</th><th>Area [km²]</th></tr>
<tr><td rowspan="4">[---------- M I C R O ----------]
[-- M E S O --]
γ β α
[M A C R O]</td><td rowspan="4">[--- M I C R O ---]- - - - - - -]
[------ M E S O ------]- - - -]
small large
[--- M A C R O ---]</td><td>Global</td><td>> 10^7</td><td>> 10^8</td></tr>
<tr><td>Regional
Continents,
Regions</td><td>10^7
10^6
10^5</td><td>10^8
10^6
10^4</td></tr>
<tr><td>Choric
River Basins,
Catchments
etc.</td><td>10^4
10^3</td><td>10^2
1</td></tr>
<tr><td>Topic
Hydrotop,
Agricultural
Plot
etc.</td><td>10^2
10
1
10^{-1}
10^{-2}</td><td>10^{-2}

10^{-6}

10^{-10}</td></tr>
</table>

Table 2.1: Classification of scales in hydrology, modified from Becker (1986)

Closely related to the definition of scales in Table 2.1, rainfall forming atmospheric processes can be classified with respect to their spatial and temporal extent. The names and properties of each type is given in Table 2.2, modified from Waymire et al. (1984).

storm structure	synoptic systems	warm fronts and occluded fronts	cold fronts	mesoscale convective systems	supercells	convective cells
horizontal spatial scale	Meso-α	Meso-β	Meso-β	Meso-β	Meso-γ	Meso-γ
horizontal spatial scale [km^2]	> 10^4	10^3 - 10^4	10^3 - 10^4	10 - 10^3	10 - 50	10 - 50
duration scale [h]	> 24	4 -24	4 -24	0.5 – 4	0.5 - 4	0.5 – 1.5
air motions	mixed	stratiform	stratiform	stratiform	mixed	convective
shape	vortex	extended front	extended front	cells arranged along a front	irregular cells	irregular cells
maximum point precipitation intensity [mm/h]	-	20	60	200	300	400
rain spectrum in ripe state	-	widespread, mainly around 5 mm/h	mainly around 30 mm/h	widespread, mainly around 40 mm/h	mainly around 100 mm/h	mainly around 100 mm/h
motion	from West in Northern Hemisphere	with fronts	with fronts	with prevailing air motion	with prevailing air motion	erratic, with wind at mid-cell level

Table 2.2: Rainfall structures in typical extratropical cyclonic storms. Modified from Waymire et al. (1984).

Additionally, some terms often used in literature with differing meanings are specified here to clarify their meaning in the context of this work.

- Forecast: 'A statement of expected future meteorological occurrences' (Parker, 1997). Weather forecasting can be sub-divided into short-, medium- and long-range forecasting, where short-range forecasting is less than about 2 days ahead, medium-range forecasting is 2 days – 2 weeks ahead, and long-range forecasting is months ahead (Collier, 1989). The forecasting techniques developed and applied in this work are only valid for lead times in the order of a few hours and should therefore be referred to as 'Nowcasts'. However, as the term 'Forecast' is much more common, it was used instead. Wherever there is a possibility to mix the two meanings in the text, it is clearly stated which is meant.

- Nowcast: 1. Detailed description of the current weather along with forecasts obtained by extrapolation up to about 2 hours ahead. 2. Any area-specific forecast for the period up to 12 hours ahead that is based on very detailed observation data (Parker, 1997). In this work, the term is used according to the first definition.
- Numerical Weather Prediction (NWP): The forecasting of the behavior of atmospheric disturbances by the numerical solution of the governing fundamental equations of dynamics and thermodynamics, subject to observed initial conditions.
- Pixel: Refers here to one 500×500 m grid-cell in a radar image
- Image: Refers, if not specified otherwise, to a radar image consisting of 256×256 square grid-cells, each 500×500 m in size. The overall image therefore encompasses an area of 128×128 km = 16384 km^2.

2.2 Hydrometeorological Processes

The physical processes relevant for the formation of precipitation occur over a large bandwidth of spatial and temporal ranges. Thus, the following, brief overview of the most important rainfall formation processes in mid-latitudes is structured according to the spatial scale in which they occur (see also section 2.1). For further information about meteorological processes, see for example Hupfer and Kuttler (1998).

2.2.1 Micro scale: Cloud processes

Insights into the processes leading to an enlargement of cloud elements and the release of precipitation have been combined into closed theories of the formation of precipitation, which can be roughly presented in the following manner.

Precipitation formation in water clouds (Bowen-Ludlam Process)

This first elementary process of precipitation formation, due to the mechanisms of coalescence theory, was first described by Langmuir in 1948 and incorporates only the liquid phase. In this process, the 'Langmuir chain reaction' comes into effect for high reaching source clouds. When the drops obtain the critical radius of 3.5 mm (which corresponds to a falling velocity of ≥ 9 m/s), they will be violently deformed during their fall due to high air resistance, and will eventually burst into many smaller droplets. These smaller droplets will again be carried aloft and will significantly increase in size due to condensation and coagulation processes, until they begin to fall once more on reaching the critical radius. These drops then burst into smaller droplets, allowing the aforementioned chain reaction to develop. Eventually a multitude of large drops will have accumulated within the cloud. Only sufficiently large upward movement of air prevents their falling. If the intensity of this upwardly moving air decreases, then a sudden cloudburst of rain occurs.

Precipitation formation in mixed clouds (Bergeron-Findeisen process)

A mixed cloud develops when within a cloud consisting of super-cooled water droplets fixed elements of the cloud are formed by frozen water droplets, or when ice crystals fall into the cloud from ice clouds above (known as the seeding process). This represents a thermodynamically unstable system which changes the existing cloud rapidly into an ice cloud through the evaporation of the droplets and a simultaneous sublimation of water vapor (overdistillation). The size and corresponding downward velocity of these cloud elements rapidly increase to the point of the release of precipitation. If they pass another cloud layer with positive temperatures, then they will coagulate with the cloud drops, causing them to melt and converting them to rain drops. For a less pronounced sleet forming processes, the ice crystals coagulate to form snowflakes, which either arrive at the earth's surface, or fall through warmer air or coagulate with warmer water droplets and fall as rain. Therefore precipitation from mixed clouds can fall either in liquid form (as drizzle or rain) or in solid form (as snow or sleet).

Hail

Hail represents a special form of precipitation. It develops in high reaching storm clouds which have very intense rates of ascent and descent (vertical velocities between 20 to 30 m/s). In this process, super-cooled water droplets attach themselves to ice or snow crystals, until after multiple ascents and descents in the vertical air stream, they fall due to their weight. Corresponding to their method of development, they have a layered structure.

Precipitation formation in ice clouds:

This depends entirely on the rapid growth of ice crystals due to the sublimation of water vapor (diffusion growth) and the coagulation of ice crystals between each other. The precipitation falls to the earth's surface as either ice needles and snow, or as low intensity rain after falling through layers of warmer air. It often evaporates before reaching the surface and can only be seen as streaks in the sky.

2.2.2 Meso-γ scale: Convective cells and supercells

Convective cells develop within air masses of uniform temperature and humidity. If it is destabilized by strong solar radiation it does so from the earth's surface upwards, resulting in intense convection currents. Convective cells are often accompanied by storms and occur predominantly in the afternoon. After these storms are spent, warm summer weather usually resumes. Convective cells are always associated with vertically thick clouds, strong vertical air flows and intense condensation and cloud particle growth processes. Warm, moist air with humid, unstable layers reaching high into the troposphere particularly promotes convective cell and storm development. Convective rainfalls are of high intensity, but usually short duration and limited spatial extension. A characteristic attribute of this type of rainfall is extreme spatial variability. Only in the case of very unstable atmospheric conditions and sufficient moist air masses the formation of long-lived clusters of convective cells (multi-cells) and eventually supercells can occur. Supercells constitute a quasi-stationary multi-cell cluster with enormous rainfall activity and prevail over one area for time-spans exceeding the normal lifetime of a convective cell. Supercells may show a distinct movement that corresponds to the overall direction of air motion (see also Table 2.2).

2.2.3 Meso-β scale: Frontal systems, squall lines and orographic rain

All Meso-β scale precipitation types share the common feature that they are linked to pronounced horizontal air advection and are long lived compared to convective cells. Usually, the driving force behind the movement is a low pressure system or cyclone (see also section 2.2.4 and Table 2.2).

Frontal systems

In a very simplified view, frontal system occur at cyclonic fronts i.e. in the area between cold and warm masses of air, either as a warm front, when warm air slips on top of cold air, or as a cold front when warm air is pushed up by approaching cold air. A cold front provides a higher velocity of rise and therefore rainfall of higher intensity. Compared to convective rainfall, the mean spatial extension and duration is significantly higher (continuous precipitation). Cyclonic rainfall accounts for the largest percentage of the total annual precipitation in temperate latitudes. Cold front storms initiate a dramatic change in the weather with a drastic drop in temperature. The development of warm front storms precede a destabilization of the warm air sliding over colder air.

Squall lines

Squall lines are caused by either the advection of air currents, radiation in higher layers or the convergence of air currents in lower layers of the atmosphere. The atmospheric layer structure can be destabilized by a drop in temperature at high altitudes (dependent on radiation and/or caused by the advection of colder air to these heights). The destabilization can result from warm air advection in deeper layers, or a combination of all these factors. Convergent air flows in lower layers can also result in raising the air, which leads to a destabilization. In all cases, a storm can develop. In the most extreme cases, several storm cells can develop in such a mass of warm air, which tend to form in a line in front of, and parallel to, a cold front. They break with gusts of wind and are therefore called squall fronts or squall lines. Squall lines are associated with very intense and long-lasting rainfall (see also Table 2.2).

Orographic storms

Their development is analogous to that of warm front storms: warm, humid air flows are forced to rise when encountering an obstacle (e.g. a mountain range), raising and destabilizing the thick layers of air and resulting in cooling and condensation. A strong agitation of this air mass can initiate the development of a storm. On the leeward side of the obstacle, the storm clouds resolve themselves once more in the descending air flow. The resulting rainfall is of variable duration and intensity. Due to this orographic effect, the mean height of precipitation in mountainous regions is above average.

2.2.4 Meso-α scale: Synoptic systems

Two types of synoptic systems can be distinguished: cyclones and anticyclones. The term cyclone (depression) refers to an area with a lower air pressure with respect to its surroundings. Similarly, an anticyclone (high pressure system) is an area with a higher air pressure in comparison to its surroundings. From a flow dynamics perspective, cyclones and anticyclones, manifest themselves as air vortices of different dimensions, which rotate around a quasi-vertical axis, with the direction of rotation determined by the Coriolis effect. In the Northern Hemisphere, lows rotate in an mathematically positive sense and highs in negative sense. It should be maintained that in the air layers near the surface a friction conditioned diversion of the wind occurs into the low and out of the high. Cyclones form the frontal systems mentioned in section 2.2.3 and are responsible for most of the rainfall in our latitudes, whereas anticyclones are usually associated with an absence of precipitation. Therefore, further discussion is limited to cyclones.

The simplified life cycle of an ideal cyclone

The typical development of a cyclone (cyclogenesis) in the Northern Hemisphere can be identified by different phases, following one another with a time-lag of about 12 hours. The starting point of cyclogenesis is an undisturbed state at the polar frontal zone, a quasi-stationary front (a region of high gradients). This is superimposed, at a greater altitude, by a strong, uniform west wind. As the quasi-stationary front for reasons connected to flow dynamics cannot remain stable a slight, wave formed deformation occurs in the polar front. With this, the cyclogenesis enters its initial phase. In the initial phase, a slight convergence of flow occurs in the lower layers of the atmosphere, initiating large scale elevation processes. This introduces a fall in air pressure, leading to a cyclonic circulation around the center of the deformation, with the formation of cold and warm fronts. In so doing the cyclone also grows in a vertical direction. Warm and cold fronts border the warm sector of the still young cyclone. The greatest drop in pressure occurs at the surface warm front, close to the apex of the deformation. As a result of this, the young cyclone displaces in the direction, and with the velocity, of the warm air flow. Approximately 24 hours after the initial phase the warm sector has exceeded its maximum radius and starts to become smaller. This phase, characterized by having the strongest cyclonic rotation, is known as the ripe stage. The warm front is overtaken by the cold front (moving faster due to steeper pressure fall in the cold air), causing the warm air to increasingly be found only at altitude. The merging of the cold and warm fronts is known as an occlusion. The occluding cyclone moves considerably more slowly than the young cyclone, and the frontal system can sway around its center. The vertical extent of the cyclone is now so large that its rotation has an effect on the higher troposphere, as well as the lower stratosphere. Even later, in the ageing state, the warm air is completely disconnected from the land by the cold air behind it. With this, the vertical axis, which was previously inclined, becomes steeper, so that a quasi-stationary low develops, reaching high into the troposphere. As the warm air is increasingly pushed upwards by the growing cold air, the original temperature difference disappears, and the primary energy source for cyclogenesis expires. The cyclone enters a closing phase, in which the cyclonic rotation becomes steadily weaker and the low at surface level refills. Finally, the starting point of cyclogenesis is approximately arrived at again (borders between the air masses as a quasi-stationary front).

Weather sequence due to the passage of an ideal cyclone

The typical weather processes at the fronts ensure that the passage of a cyclone is associated with a characteristic succession of weather events. Figure 2.1 shows a summarized version of the weather events associated with the passage of an ideal cyclone. Generally, a difference is made between the forefront weather (usually with a pre-frontal precipitation area around 100 km to 300 km wide), the post-frontal weather (with its traits dependent on the distance from the center of the low) and the rear-side weather (characterized by its relative changeability (post-frontal showers)). Principally, the transition from fore-front weather to post-front weather is characterized by the transition from stable to unstable clouds with unstable precipitation. The precipitation associated with the cold front is characteristically more intense, although generally not as wide, as the precipitation associated with the warm front (the precipitation stops almost directly after the passage of the cold front).

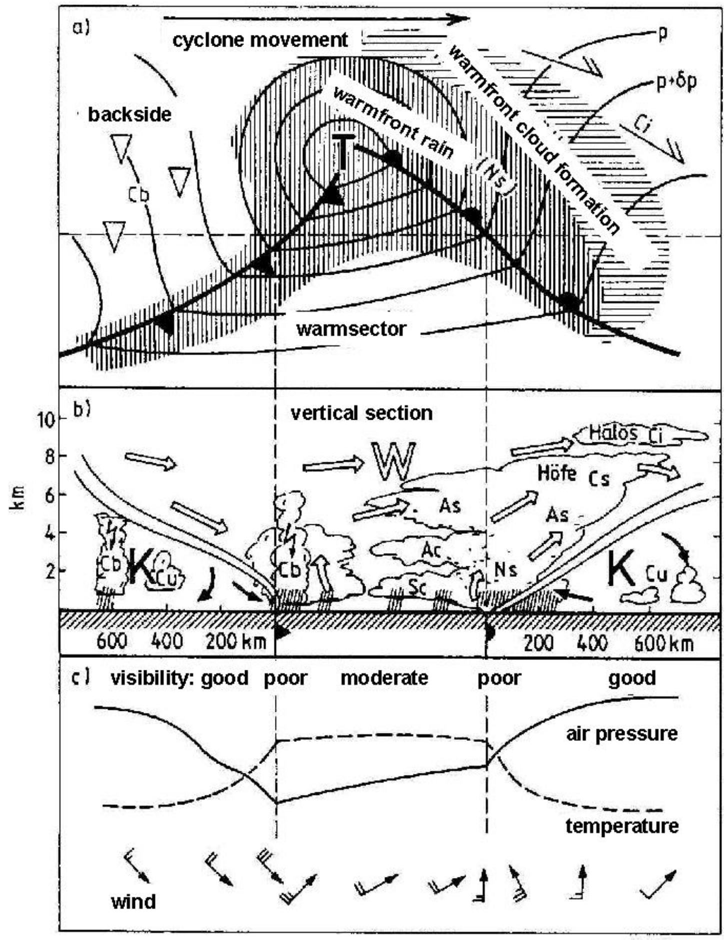

Figure 2.1: Passage of an ideal cyclone, modified from Hupfer and Kuttler (1998)

2.3 Weather radar

Radar (from **Ra**dio **d**etecting **a**nd **r**anging) found its first widespread use in the second world war as an early warning system against hostile aircraft. However, it was observed that under certain circumstances not only aircraft but also water droplets in the atmosphere reflected the emitted radar pulse. This observation, first regarded as an undesired side-effect was later found to be a very effective way of areal rainfall observation. Since then, the use of radar has become increasingly common in the meteorological and hydrological community, especially in mesoscale meteorological research. The advantages of rainfall observation compared to the common rain-gauge observations are obvious: Radar provides insight into rainfall patterns with unequalled spatial resolution of a few hundred meters, with one radar covering an area of roughly 40.000 km^2, whereas gauges sample the spatio-temporal rainfall patterns with good accuracy and high temporal resolution, but only at one point in space. Or, as Fujiyoshi (2001) puts it: 'Precipitation is a metamorphosis process from water vapor to liquid through particle state. Radar is the unique tool to see the interesting process that connects atmosphere and land surface, that is, meteorology and hydrology.'

Until the development of satellite imagery in the 1960s, radar provided the main source of data detailing the structure and behavior of mesoscale weather systems. The increasing availability and range of satellite data have in no way diminished the need for weather radar. Indeed, satellite systems, together with the development of Numerical Weather Prediction models, have sharpened the need for data that radar networks can supply. Also, for rainfall nowcasting for flash-flood warning systems is hardly possible without radar. Therefore, it seems worthwhile to give a short introduction to the possibilities and limitations of weather radar in hydrology, starting with basic radar theory, possible sources of error and their relative importance in section 2.3.1 and finally a brief overview of the current state of radar use in hydrometeorology in section 2.3.2. A more comprehensive introduction to this topic is given in Collier (1989) and Gysi (1995).

2.3.1 Radar Theory

Radar, a remote sensing device as satellite imagery obtains information about precipitation indirectly. Therefore, the observed quantity must be transformed to a reasonable rainfall estimate. This is usually done using rain-gauge observations, although the direct comparison is problematic due to the different scales and places of observation of the two devices.

Measurement principles

Radar precipitation measurement uses the fact that microwave range radiation is reflected by water droplets (and also by snow and ice) in the atmosphere. A short pulsed signal (the pulses are approximately a microsecond long and 3 milliseconds apart) is emitted from the radar dish in a conical beam with an angle of approximately 1.5°). The dish rotates around a vertical axis (azimuth angle) and changes its angle to the horizon (elevation angle) with each revolution. The emitted electromagnetic waves are between 1 - 10 cm in length, their frequency ranging from 3 to 30 GHz. A fraction of the power of these electromagnetic waves is reflected back by the precipitation to the emitter, which also acts as a receiver. From the strength of the back-scattered radiation, conclusions can be drawn about the quantity of precipitation in the investigated volume, from the time-lag between emitting and receiving about the distance from the target to the radar station. From the actual azimuth and elevation angles at signal emission, and the reflection time, the position of the examined precipitation volume can be exactly determined. Using the radar equation, the reflectivity can be calculated through the back-scattered radiation.

$$Z = \frac{P_B \cdot r^2}{C \cdot k^2} \tag{2.1}$$

where:

Z	[mm^6/m^3]	reflectivity
P_B	[W]	back-scattered radiation
r	[m]	target distance
C	[$W{\cdot}m^5/mm^6$]	radar coefficient
k	[-]	hydrometeor reflection factor

The hydrometeor reflection factor k is dependent on the hydrometeor's form, size and orientation, also on the type of precipitation (water, ice , snow). Parameter k is an empirical value, it typically ranges from k = 0.964 for rain to k = 0.456 for dry snow. Z is often defined in dB*Z* units where

$$dBZ = 10\log_{10}(Z) \tag{2.2}$$

Now, the precipitation intensity in the scanned pulse volume can be estimated from the reflectivity using the relationship

$$Z = A \cdot R^B \tag{2.3}$$

where:

Z	[mm^6/m^3]	reflectivity
R	[mm/h]	rainfall intensity
A	[-]	empirical constant
B	[-]	empirical constant

This equation is termed reflectivity-intensity relation or briefly Z-R-relation. In the following, the short form will be used for it. A and B vary from event to event, according to the type and size spectrum of the hydrometeors. Usually the data is averaged through comparison with ground-measured precipitation data, or long established annual average values are employed. Marshall and Palmer (1948) introduced the first relations between radar reflectivity and rainfall intensity, in the following decades a great number of additional relations followed, see for example Collier (1989), DWD (1998), IMK (1999) and Sanchez-Diezma et al. (2001). Table 2.3 gives an incomplete summary of typical Z-R-relations frequently used.

meteorological condition	A	B
drizzle	140	1.5
stratiform rain	200 - 250	1.5 – 1.6
convective rain	300 - 500	1.4 - 1.5
average summer relation	300	1.5
average winter relation	200	1.6
DWD average	256	1.42
Marshall-Palmer average	200	1.6

Table 2.3: Constants A and B of the Z-R-relation for different meteorological conditions

Sources of error

The sources of error when estimating rainfall from a weather radar are manifold. Generally, they can be classified into 4 distinct classes, which will be described separately in the following. The relative importance of the error sources described is often difficult to quantify and may differ under various conditions and amount to systematic and random differences from rain-gauge measurements as large as 100% or more (Smith et al., 1996)! Nevertheless, where possible the sources of error are mentioned along with possible measures to eliminate or at least reduce them. Since the use of radar the procedure of error elimination or in other words radar calibration has been generalized in its meaning. It is now more than just measuring the receiver transfer function but to make measurements to be able to interpret and believe the results of radar. This definition extension from power to reflectivity to rainfall measurements as the success criteria now brings in the radar equation, attenuation corrections – gas and rain, wet radomes and even vertical profile corrections. It brings in meteorological, physics and algorithm issues such as climatology, the Z-R-relationship and adjustment algorithms (Joe, 2001).

Errors due to the radar system

The radar system can cause bias in the rainfall estimate if the radar system losses and the antenna gain are not known precisely. Seo (1997) suggests that errors of that kind can be identified in radar-radar coverage overlapping areas. Another possible source of erroneous rainfall estimates is the grid conversion. According to Sharif et al. (2001), the way the spherically sampled radar data are transformed on a (usually rectangular) grid can, especially at greater ranges, influence the rainfall associated with a watershed on ground level to a significant degree. This was also observed by DWD (1998), who found that repeated conversion from polar to cartesian coordinates causes unwanted smoothing of the data.

Radar measurements not related to rainfall

Measurements of radar not related to rainfall can happen when the beam is reflected at ground level ('ground clutter'). Usually this is easily detected, e.g. using high pass Doppler filters. Sometimes other obstacles in the atmosphere such as flocks of birds or dust can also cause anomalous observations.

Errors due to non-representative sampling space

The single most important source of error is the fact that usually the radar pulse volume is located far above the area of interest (Seo, 1997). Firstly, to avoid ground clutter areas shadowed by rising ground can, especially at greater distances from the radar site only be sampled at high elevation. Secondly, due to the earth's curvature a radar signal emitted horizontally at ground level will reach an altitude of 780 m, 100 km from the emission source. Unfortunately, rainfall exhibits a strong non-uniform vertical reflectivity gradient, thus reflectivity observed at an altitude must not be closely related to rainfall observed at ground level. Those range-dependent biases mirror the vertical reflectivity profile including Bright Band enhancement in the melting layer (or 0° isotherm) and diminishing reflectivity above. Because ice crystal/ particle concentration above the 0 °C isotherm is only very weakly correlated with rainfall below the cloud base, radar rainfall data beyond the range where the base tilt intercepts the 0 °C isotherm have only a very limited ability to delineate the spatial distribution of rainfall on the ground. In the case of low-topped storm, radar may fail to observe it completely. This problem is extremely difficult to deal with, algorithmic correction may not be practical. The same applies to evaporation when, especially in dry-air environments, over-estimation occurs due to evaporation of raindrops below the cloud base. Another possible source of error due to sampling at the wrong place is anomalous propagation (Anaprop). Anaprop occurs when an emitted beam is reflected at obstacles at a distance such that it returns to the receiver after a complete emission-reception cycle of the radar has been completed. The obstacle is therefore supposed at an erroneously close distance of the radar. Both clear-air and precipitation-embedded Anaprop occur frequently. Anaprop can be identified using frequency shifting information from the Doppler effect. Altogether, errors of the gross order of 20% must therefore be taken into account in the determination of the precipitation intensity due to a non-representative sampling space.

Errors due to the indirect measurement of rainfall

The original radar-observed back-scattered radiation undergoes two conversions to obtain the desired rainfall rate. Both conversion are error-prone.

Firstly, the back-scattered radiation observed by the radar is transformed to reflectivity applying the radar equation. If the simplifying assumptions underlying the radar equation are not fulfilled, the conversion can falsify the observation. According to Crozier (1986), the most important assumptions are:

- The scattering precipitation particles in the target volume are homogeneous dielectric spheres whose diameters are small compared to the wavelength.
- The pulse volume is completely filled with randomly scattered precipitation particles.
- The reflectivity factor Z is uniform throughout the sampled pulse volume and the sampling interval.
- The phase of all particles is the same (either all water or all ice).
- Multiple scattering is negligible.

Secondly, the selection of the correct Z-R-relation is critical for the accuracy of the rainfall estimate. As shown in Table 2.3, Z-R-relations may change between seasons, rainfall types or even during the course of a rainfall event. Hail can, due to its very high reflectivity, lead to a huge over-estimation of rainfall if it is not detected and accounted for by an appropriate Z-R-relation. Currently hail is dealt with by simply capping apparent radar rain-rate at a fixed value. Biases due to wrong Z-R-relations can be identified and removed by applying long-term comparisons, over a large area, between radar and rain-gauge network derived rainfall accumulations, and/or the application of real time Z-R specification procedures.

Even if one succeeds in removing all of the sources of error mentioned above, residual random errors will persist. They are caused by temporal, spatial and height sampling, variations in the Z-R-relation and quantization. Jordan et al. (2001) have investigated the importance of these errors at catchment scale using a stochastic space-time model of radar measurement errors. Random errors caused by temporal and spatial sampling, variations in the vertical reflectivity profile, variations in the Z-R-relation and quantization have been included. The dominant influence on random errors in radar rainfall measurement was shown to be the height of the radar beam over the catchment. Proportional standard errors from the above stochastic error sources for 1-hour temporal and 64 km^2 spatial accumulation, with the catchment at a distance of 80 km (beam height 1.77 km) amounted to 0.65, for 10 minute accumulation 0.83.

Finally, it should be borne in mind that for radar applied to flood hydrology, the critical issue is the accuracy of the rainfall measurement at spatial and temporal scales that drive catchment response (in a temporal regard, the catchment's time of concentration), so random radar biases on small temporal or spatial scales might have no harmful effect on catchment flood prediction.

2.3.2 Use of weather radar in hydrology

It has already been stated at the beginning of this chapter that since the 1940s, radar has been used in almost all fields of hydrometeorology. The fields of application are often closely linked to each other, nevertheless they can be sub-divided into 4 main groups, namely precipitation measurement, precipitation nowcasting, flood forecasting and hydrometeorological studies. Radar data are used on a wide range of spatio-temporal scales, from micro-radar observations in a 20 km range to continental radar networks and from flood-forecasting for sewer systems with 30 minutes of lead time to long-term studies of rainfall processes. The following summary is a brief overview of this range of applications and will point to chapters that treat individual aspects in greater detail.

Precipitation measurement

First of all, radar serves the estimation of rainfall, either on its own or, more often, in combination with rain-gauges. Radar data, although sometimes erroneous in magnitude, have the great advantage that they provide a coherent image of spatial rainfall patterns, which, especially in case of small-scale convective events and/or coarse rain-gauge networks might be missed altogether. Beven and Hornberger (1982) found in experiments with a densely gauged catchment that the spatial pattern (location and size) of rain, even in hydrologically homogeneous areas, strongly influenced peak timing, peak values were less strongly influenced and flood volume was barely effected. In non-homogeneous areas, the influence of the rainfall pattern on the flood volume might be also considerable. The catchment investigated had a size of 287 km^2, and it is clear that the conclusions drawn from it are even more relevant for smaller catchments. The resulting need for spatially distributed rainfall information that corresponds to the findings of Wilson et al. (1979) can be met by radar. To mitigate the sometimes large discrepancies of radar to rain-gauge observations, which are often regarded as indisputable, numerous techniques have been developed that try to approach radar to rain-gauge measurements. Among those methods, summarized comprehensively by Foufoula-Georgiou and Krajewski (1995) are extensions of the area-time integral (Doneaud et al., 1994), matched probability distribution of radar and rain-gauge observations (Rosenfeld et al., 1993; Chen et al., 2001), Co-kriging and other geostatistical methods such as Krajewski (1987) and, most widely used, methods to adjust radar observations by rain-gauge-derived multiplicative or additive factors as done by Collier (1986) or DWD (1998) or by adjustments in the Z-R-relation to match rain-gauge observations (DWD, 2001).

However, even sophisticated methods merging rainfall observations from different devices are limited by the quality of the input data. Therefore, as Zawadski (1984) summarized: 'The accuracy of radar estimates at ground will only be improved by addressing the various sources of error in a painstaking and a meticulous manner'. Ways to achieve this goal recently investigated with promising results are, among others, the multi-parameter use of radar including differential reflectivity and differential phase shift (Gorgucci et al., 1994). More detailed information about spatial rainfall estimation can also be found in chapter 6.

Weather radar networks

With the recognition of radar's usefulness in rainfall observation and prediction, several large radar networks were established: NEXRAD (Next Generation Radar) in the USA (see for example NEXRAD, 1986), in the United Kingdom a network of weather radars have been installed, originating from the DWRP (Dee Weather Radar Project), see Ryder and Collier (1987). In Germany, the German Weather Service established a network consisting of 16 radar stations, started in the 1980s, completed in 2000. In numerous other countries (France, Switzerland, Hungary, Canada, Japan and others), weather radar networks have been or are being established. In a second step, triggered by the obvious trans-boundary extension of weather phenomena, international co-operation and data exchange was and is being established. Starting with the COST-73 (Co-operation in Science and Technology) weather radar networking project, the international exchange of radar data in Europe has been started and is continuously enlarged (Collier, 1989). Complementary, small, close-range but low-cost micro radar systems have been developed that can be used as a local substitute or addition to larger radar system for precipitation estimation (Nagaya and Hara, 2001).

Precipitation forecasting

Radar not only provides detailed information about the current rainfall patterns in the range of the radar, it also facilitates or enables to a certain extent the prediction of the development of those patterns in the future. Nakakita et al. (1996) classified radar-based short-term rainfall prediction methods into three categories: Those that extrapolate the movement pattern of a horizontal rainfall distribution (Bellon and Zawadski, 1994; Dixon and Wiener, 1993), those that use the principles of water balance and thermodynamics with a conceptual rainfall model such as Zawadski et al. (2001) and those that either use the full set of conservation equations at the mesoscale or use a method that reduces the grid size of Numerical Weather Prediction models (Takada et al., 2001). In chapter 7, the issue of rainfall nowcasting using radar is further investigated.

Flood forecasting

Ultimately, the improved rainfall observation and forecasting possibilities offered by radar have lead to a better prediction of floods, especially in small catchments suspect to flash-floods from short yet intense convective rainfall events. Starting from the smallest and most rapidly responding of catchments, urban sewer systems, Quirmbach et al. (1999) have successfully applied weather radar for rainfall nowcasting with a 30-minute lead time to optimize the joint operation of urban drainage systems and sewer treatment plants. For larger, natural catchments, Borga and Creutin (2000) have summarized that recent years have proved the applicability of weather radar data for flood monitoring and nowcasting in combination with distributed hydrological and hydraulic models. For small to midsize catchments, Moore et al. (1993) have investigated the utility of radar-derived rainfall forecasts in rainfall-runoff models. Nine catchments ranging from 30 to 750 km^2 were investigated using three different rainfall-runoff models and rainfall forecasts obtained from the HYRAD (Moore et al., 1994a) and FRONTIERS (Moore et al., 1993) projects, and a conditional Markov chain model. It was found that the use of radar rainfall forecasts consistently increased the probability of detection of an exceedence threshold for issuing a warning. This is partly supported by DWD (2000), where the mean daily and hourly areal rainfall over watersheds from radar and rain-gauge networks was assessed. In case of rain-gauge network densities equal or lower than catchment size, radar always provided better results. For watersheds larger than ~ 1000 km^2, the high-resolution rainfall information of radar does not perform better than rain-gauge network interpolation. See chapter 8 for a more comprehensive review of flood forecasting using rainfall-runoff modeling and the related benefits from radar.

Hydrometeorological studies

Last but not least radar provides an insight in the spatio-temporal development of rainfall unequalled by rain-gauge systems, dense as they might be. This has led to a better understanding of rainfall processes and enabled the investigation, verification, limitation or falsification of assumptions stated about rainfall, such as Taylor's hypothesis (Taylor, 1935) or the fractal behavior of rain-fields (Lovejoy and Mandelbrot, 1985). Other fields of interest such as return period analysis of rainfall events or probable maximum precipitation estimation have also gained from the use of radar.

2.4 Rainfall Simulation

Rainfall is the most important driving force behind all hydrological processes in watersheds. The knowledge of its spatio-temporal distribution on different levels of aggregation is of great importance for a range of different design and research purposes. For the assessment of available water power, long-term means are relevant, for flood protection extreme value distributions of rainfall have to be known, in agriculture, seasonal rainfall distributions determines sowing, irrigation and harvesting schedules. For flash-flood forecasting, short yet precise estimates of rainfall rates over small areas are crucial, on the other end of aggregation, knowledge about expectable long-term fluctuations of rainfall regimes, namely the assessment of climate change effects are also of great public and scientific interest.

The description of precipitation is therefore a central topic in hydrology (Bárdossy, 1998). Two principal approaches can be distinguished: dynamic and stochastic. Due to their usually high computing requirements, dynamic weather and rainfall simulation has been possible only since the development of advanced yet affordable data processors.

Generally, dynamic (numerical) models of rain are based on a set of partial differential equations describing conservation of mass, momentum and energy. These equations are solved numerically at every time-step and at each gridpoint of the model domain. As stated by Johnson et al. (1993), the accuracy of rainfall predicted by such models is largely dependent on their capability to jointly simulate the distribution of mass, temperature and water vapor. Several models are currently in use, e.g. the 'Lokalmodell' of the DWD or the National Center for Atmospheric Research Mesoscale Model (NCAR-NM5).

Stochastic models have been used to describe rainfall for many decades. Evolving with the availability of data, they were first developed to describe point-processes based on rain-gauge observations. While annual and monthly precipitation amounts could satisfactorily be modeled with simple auto-regressive moving average (ARMA) processes, the intermittent property of rain on daily or shorter time-scales made modeling a difficult task. But even with elaborate models the limitation to point-processes remained unsatisfying, as rainfall's nature is spatial. Later, supported by satellite imagery and radar observations, rainfall modeling progressed considerably when it shifted to the spatial description of the rainfall.

In that context, the work of Waymire et al. (1984) was a benchmark in many aspects. Firstly because it marked the transition between the old and new model philosophies, and secondly because it was one of the early works that introduced the hierarchical concept in rainfall modeling, which will be discussed later. The principal idea was to describe rainfall structure in extra-tropical cyclonic storms as hierarchical, stochastic point-process at several scales: Synoptic storms on the Meso-α scale, large meso-scale rain areas on the Meso-β scale and rain cells on the Meso-γ scale (Table 2.1 and Table 2.2). In the model, rainfall was still treated 'the old way' as a point-process, the innovation was to subsequently spread the point rainfall over the relevant area. In the following years, a multitude of spatial rainfall models were developed. Another approach typical for that period to be used in connection to satellite remote-sensing of rainfall was proposed by Bell (1987). For each pixel in the gridded model domain, rain occurrence probability was assumed to be spatially homogeneous and to follow a log-normal probability distribution. Generating rain-fields in Fourier space, the (isotropic) spatial covariance field of observed images was reproduced. Temporal evolution of the fields was, with exponentially decreasing correlation, modeled by a Markov chain. The log-normal distribution used by Bell was often recommended as a convenient representation for the probability distribution of radar-derived rain-rate (Crane, 1986). It is advantageous in that it permits to deal with spatial covariance in a conventional way. Other distributions, such as the hyperbolic for high rain-rates proposed by Lovejoy and Mandelbrot (1985) require more careful application.

From the great variety of different scopes in hydrology, over time an equally high number of different modeling approaches for rainfall behavior on various different spatio-temporal scales emerged. On a large integration scale, Doneaud et al. (1994) found that the fractional area of a radar image showing rainfall above a certain threshold is strongly correlated with area-averaged rainfall. This was later supported by Onof and Wheater (1996), who reported that series of consecutive rainfall coverages for a given area are strongly correlated. The same was found true for the logarithmic transforms of coverage and mean areal precipitation depth. On that scale, auto-regressive integrated moving average (ARIMA) models suitably modeled spatial coverages upon the knowledge of areal rainfall depth. For flash-flood forecasting, other, mainly advection-based approaches were developed and are discussed in detail in chapter 7.1. They were to a greater or lesser extend all based on the frozen field hypothesis by Taylor (1935), which implies that the correlation in time is equivalent to that in space if time is transformed to space in the mean direction of storm movement. Onof et al. (1996) found Taylor's hypothesis to be valid for durations of up to ~ 40 minutes, dependent on the size and mean life cycle of the rain structure regarded.

But beyond the diversification in different model approaches, splitting rainfall description into very distinct classes of scale, the countercurrent scale-invariant approach was also developed. Scale invariance implies that both small- and large-scale statistical properties are related to each other by a scale changing operator involving only the scale ratio. The beginning of this new direction was marked by a paper of Schertzer and Lovejoy (1987). They argued that the basic properties of rain are best understood in terms of coupled anisotropic and scaling cascade processes. They demonstrated how rain-fields can be modelled by fractional integration of the product of appropriate powers of conserved but highly intermittent fluxes. Ever since, scaling models have evolved from fractal geometry for rain areas, to mono-fractal fields, to multi-fractals, to generalized scale invariant models to universal multi-fractals. Brief summaries of these developments can be found in Gupta and Waymire (1993). Showing that fluctuations in rainfall fields measured by weather radar satisfy the condition of self-similarity, Menabde et al. (1997) developed a model to simulate rainfall by multiplicative cascades. The results exhibit good statistical and visual agreement with the measured data. However, the issue of estimating fractal properties from real rain-fields remains difficult and usually models are only able to reproduce certain properties of the rain-field such as spatial or temporal properties or 'realistic looks'. It should also be borne in mind that the notion of scales is man-made. As Bruen (1997) puts it, 'Nature itself does not have a problem with scale. The molecules of sea water dance without distinction to tidal waves, tsunamis or ripples. Scale problems in the water sciences arise from man's efforts to understand the behavior of water, to model it and to predict its future behavior. In order to understand scientists have been forced to classify, defining individual processes and making useful but sometimes artificial distinctions between them. This has been necessary and proved extremely useful when examining small and well defined fields of water science. However, scaling problems have arisen with the increasing tendency to expand the scope of scale-typical phenomena and the availability and use of a wider and more diverse range of sources of information, particularly from different scales'.

Alternative approaches to stochastic rainfall analysis include the introduction of wavelets (Kumar and Foufoula-Georgiou, 1993). Wavelet transforms offer a method for decomposing a process into 'atoms' which are localized not only in frequency but also in space. Pavlopoulus and Kedem (1992) introduced the diffusion model, models of Markovian type have been proposed by Gregory et al. (1993), additional meteorological information such as global circulation patterns have been incorporated in rainfall models by Bárdossy and Plate (1992). Another model for rainfall simulation, based on the Metropolis-Hastings algorithm and Simulated Annealing directly incorporates the properties of rain to be reproduced by the model in an objective function (Bárdossy, 1998). A further, more comprehensive review of advances in rainfall modeling, estimation and forecasting is given by Foufoula-Georgiou and Krajewski (1995).

The radar-based 'String of Beads Model' for rainfall simulation and short-term forecasting developed in South Africa by Pegram and Clothier (2001) has had a major influence on the rainfall model developed for the Goldersbach catchment (see chapter 7). In fact, large parts of the methodology have, with modifications, been incorporated. Due to its importance to the project, it will be briefly introduced in the following section.

2.4.1 The String of Beads Model

The following introduction to the 'String of Beads Model' is mainly extracted from Clothier and Pegram (2001), further reading is also provided by Pegram and Clothier (2001).

The 'String of Beads Model' is a stochastic rainfall model based on the combined observations of a large network of daily rain-gauges and an S-band weather radar situated near Bethlehem, South Africa. It was designed as a means to simulate rainfall over a wide range of spatial and temporal scales and with two important tasks to perform. The first is the simulation of long sequences over many years. The primary variables of interest in that context are the mean rainfall rate over the area (IMF, short for image mean flux) and the percentage of the total area which is covered by rainfall (WAR, short for Wetted Area Ratio). The second task to which the model can be adapted is to give short-term forecasts (nowcasts) of future rainfall for use in real-time flood forecasting with a lead time of one or two hours ahead. The model name 'String of Beads Model' already indicates its hierarchical structure: The 'String' is a sequence of alternating dry and wet periods, its simulation concerns event arrival and duration as well as the event advection vector. Then each wet period, the 'Bead', is simulated in greater detail, namely the temporal evolution of image-scale parameters WAR, IMF and β_{space}, with β_{space} being the gradient of the radially averaged two-dimensional power spectrum of radar images. The pixel scale simulation concerns the spatial distribution of rainfall on the simulated images. Each of these 3 modeling stages will be discussed in turn in the following. Here, the term 'event scale' refers to one spell of continuous rainfall observable on a sequence of radar images. 'Image scale' refers to one radar image in the sequence of usually 128×128 km in 1 km grid resolution, updated every 5 minutes. The final and lowest level of the hierarchy is the 'pixel scale' which refers to one gridpoint of a single radar image.

Event-scale simulation

Two independent sets of event scale statistics are pseudo-randomly generated in this first stage of the 'String of Beads Model', the event cumulative advection vector and the event arrival, duration and intensity statistics.

Data analysis revealed that there is no significant dependence structure in the durations of consecutive wet and dry spells. The wet and dry spell durations can thus be alternately sampled from two mutually independent processes. Following the ideas of Haberlandt (1998), both are modelled with an alternating renewal process. The resulting output on event scale is in the form of a binary sequence of alternating wet and dry spells, the 'String'. From this, it is possible to infer pseudo-random statistics pertaining to the average intensity of the events, namely mean and standard deviation of the event WAR and IMF distribution.

In a separate pseudo-random process, depending on the month, a constant event advection direction and speed are simulated by randomly drawing from observed cumulative density functions for bearings binned in 16 sectors and wind speed.

Image scale simulation

The second stage of simulation uses the event scale parameters, given as output by the first stage, to generate pseudo-random time-series of image scale parameters for each event. Three image scale parameters are required in order to simulate a single image and these are WAR, IMF and β_{space}. At present β_{space} is kept to a constant 2.5. The main process used in this stage of simulation is a bi-variate auto-regressive process to model the WAR and IMF time-series. Owing to the fact that the auto-regressive process is pseudo-random, there is no way to control the finishing state of the time-series simulation. This presents a problem as a rainfall event is defined as a period during which WAR exceeds 1%, consequently it must start and finish with WAR at 1% or less. The solution is to simulate two bi-variate AR processes for each event, one in the forward and one in the reverse direction and to combine them using a linear weighing function.

Pixel scale simulation

The third and final stage of simulation accepts the event advection and image scale parameters output by the first and second stages and simulates 2-dimensional images at the pixel scale consistent with those parameters. There are two main underlying processes in this stage, a uni-variate, auto-regressive process and a two-dimensional power-law filtering process. The first generates temporally correlated, pseudo-random fields of pixels and the second imposes a realistic spatial correlation structure on the fields. The auto-regressive parameters describe the temporal relationship of consecutive pixels in a normalized Lagrangian reference frame. After image generation, they are shifted according to the mean event advection vector calculated on event scale. The next step is to power-law filter each of the above generated, temporally correlated noise fields using the constant β_{space}. The result is a sequence of temporally and spatially correlated fields. The final process is then to scale and shift each field to achieve the desired WAR and IMF image scale statistic of the second stage of simulation.

Forecasting using the String of Beads Model

The auto-regressive processes used in the 'String of Beads Model' afford a limited forecasting ability. This requires knowledge of previous radar images, the number depending on the order of the auto-regressive process to simulate both WAR and IMF. Any desired number of scenarios can be run to forecast the future development of WAR and IMF, the most unfavorable can then be used in the subsequent pixel-scale forecast. Using the number of previous radar images necessary for the pixel scale auto-regressive process, a number of forecast scenarios can be generated or the single, mean, expected development can be calculated by setting the random shock term in the auto-regressive process to zero. The forecasted images are then shifted according to the prevailing advection vector. So far, forecast lead times up to an hour achieved satisfactory results, this leaves room for improvement using more sophisticated wind estimates and forecasts.

2.5 Rainfall-Runoff modeling

Rainfall-runoff models are mathematical representations of physical processes occurring in a watershed, mainly with regard to the spatio-temporal distribution of water in it, in particular the transformation of rainfall to discharge. A rainfall-runoff model generally has five components, including system geometry, input, governing laws, initial and boundary conditions and output (Singh, 1995). The processes in a model include all of the hydrologic processes that are considered relevant for the formation of the system output.

Since the development of the Stanford Watershed Model in 1966, there has been a proliferation of watershed models. This activity has been fuelled by ever-expanding computer power and growing capability to observe, store, retrieve, and manage hydrologic data. The models are of different types and were developed for different purposes. Nevertheless, many of the models share structural similarities, because their underlying assumptions are the same and can therefore be categorized. Models are classified with respect to their process description as deterministic, stochastic, conceptual or mixed. Deterministic models try to represent the spatio-temporal distribution of water in a catchment by a correct description of each physical process involved, which usually implies a very fine-scale, 3-dimensional model resolution in the order of decimeters. Fully stochastic models describe the system behavior by the laws of probability, distribution functions and mutual interdependencies of the processes of interest. Virtually no models are fully stochastic, but mixed models exist where some parts are described by the laws of probability and other parts are fully deterministic. Conceptual models apply simplified mathematical process descriptions describing the mean system behavior on a scale larger than the underlying physical processes. Doing so also exploits statistical process properties, conceptual models can therefore be regarded as a combination of deterministic and stochastic model approaches.

Considering the spatial and/or temporal resolution, models can also be sub-classified into distributed and lumped models. A lumped model is in general expressed by ordinary differential equations taking no account of spatial variability of system components. In most lumped models, processes are described by differential equations based on hydraulic laws or by empirical algebraic equations. An example of a lumped model is HEC-1 (Hydrologic Engineering Center, 1981). Distributed models take an explicit account of spatial variability of system components. Examples of distributed models are SHE (Abott et al., 1986a, 1986b) and LARSIM (Bremicker, 2000). Models using only a few distributed components while the majority is still lumped, due to measurement constraints or for the sake of keeping the number of parameters small are termed semi-distributed. Well-known examples of semi-distributed models are TOPMODEL by Beven et al. (1995) and the HBV model developed in Sweden by Bergström and Forsman (1973). This classification is related to the type of process description in the model: The full representation of all physical processes requires high resolution of the model space, while stochastic and conceptual models are applicable in a coarse grid domain.

Graham (2000) points out that the differences between conceptual and physically-based hydrologic models are becoming more and more fuzzy as the two approaches tend to converge. Conceptual models are becoming more physical at the same time that physically-based models use conceptual approaches as a means of overcoming a lack of fully-distributed physical data (Beven, 1996; Refsgaard, 1996).

3 Data

This chapter gives an overview of the various sources of data used in the project. This not only includes information about the nature and characteristics of the Goldersbach catchment necessary for modeling purposes, but also all on-line radar, rain-gauge, waterlevel and temperature data from own and extraneous sources. In fact, the set-up of the rain- and rivergauge system required a much larger portion of the project time as originally expected. While the installation of the gauges in the catchment was relatively straightforward, the data transmittal caused most problems. The transmittal of radar data and rainfall information from gauges operated by the UMEG company via ftp (filer transfer protocol) was relatively stable from the beginning, but access to the own stations was not as easy. Located directly in the catchment without access to the telephone lines, the only option was the mobile network. To establish a reliable gauge connection for data transmittal via the mobile net took time, the support of the local phone company and finally directional antenna. Although installation of measurement devices and data transmittal networks is not very challenging or pioneering from the scientific point of view, it is the basis for all further processing and should therefore be given suitable time and consideration. Even the best forecasting algorithm cannot make up for erroneous or missing data.

In section 3.1, general information about the study area with special emphasis on its rainfall-runoff behavior is given, then all components of the gauge network are described in section 3.2 followed by some aspects of data storage in section 3.3, with the latter being especially relevant for the huge amount of radar data that had to be stored in an efficient yet easy-to-access manner.

3.1 The study area

The Goldersbach catchment is a low-altitude, hilly, almost completely forested area situated in the sub-atlantic temperate climatic zone in the south-western part of central Europe (Figure 3.1). It is shadowed by the hills and mountains of the Black Forest to west, the main weather direction, and consequently shows annual precipitation and runoff rates below the German average. The Goldersbach catchment drains to the river Ammer and finally to the Neckar just inside the city limits of Tübingen. Due to its relatively natural state, it was declared a nature park in 1970 and been the subject of several studies, the last and most comprehensive conducted in the course of research project financed by the German Research Foundation (DFG) in the period from 1978 – 1982. The aim of the project was to closely investigate all components of the hydrologic cycle in forested areas with the example of the Goldersbach catchment. Fortunately, the project results were summarized very elaborately by Einsele (1986), an invaluable source of detailed hydrological information for the current project. The following general introduction to the catchment with emphasis on its rainfall-runoff behavior is, unless stated otherwise, based on Einsele (1986).

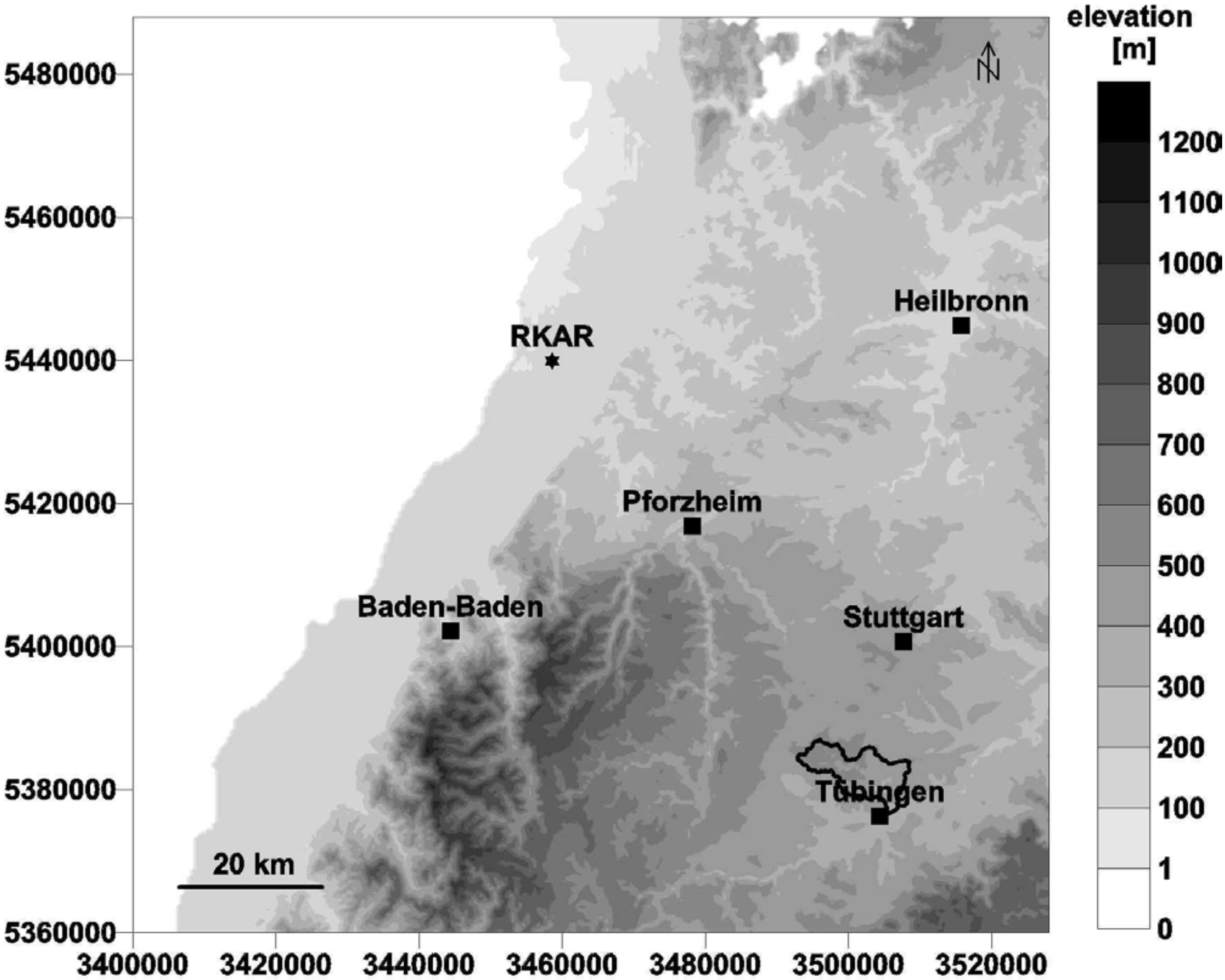

Figure 3.1: Southwest Baden-Württemberg with the Goldersbach catchment and the radar site labeled RKAR. Map limits are the limits of the radar data used.

Regarding the geological and morphological situation, the Goldersbach catchment, situated in Triassic Keuper hills, represents a type of landform which is characteristic of large areas in Southern Germany. The rock sequence in the catchment is dominated by clayey and marly mudrocks as well as by carbonate-cemented or silica-cemented sandstones of upper Triassic or lower Triassic age. As a result of two tectonic graben structures, strike and inclination of the beds differ considerably from the general situation in the South German cuesta landscape. Erosion has formed plateaus at three different stratigraphic levels: in the Stubensandstein, Rätsandstein, and Lias Alpha beds. The consequent streams of the Goldersbach system cut 100 to 150 m deep into these plateaus. The resulting deep and relatively narrow valleys are visible in the digital terrain model shown in Figure 3.4. Slopes steeper than 3° comprise 59% of the total basin area, intermediate slopes between 7 and 15° prevail in 25% of the catchment. The steepest slopes (> 15°) make up 14% of the total area and have been developed chiefly in the Keuper sandstones. Some of the valleys show a distinct asymmetry, with the steeper slopes facing south-west and west.

The prevailing soil types of the cuesta landscape of the Goldersbach catchment strongly reflect the lithology of the aforementioned parent rocks. Additionally; most hills are covered by solifluction mantle as shown in Figure 3.2. While the components differ locally, two-layer soil types with a clayey, poorly permeable sub-layer are widespread. The upper layer thickness generally ranges from 30 to 40 cm, with extremes from 0 to 60 cm.

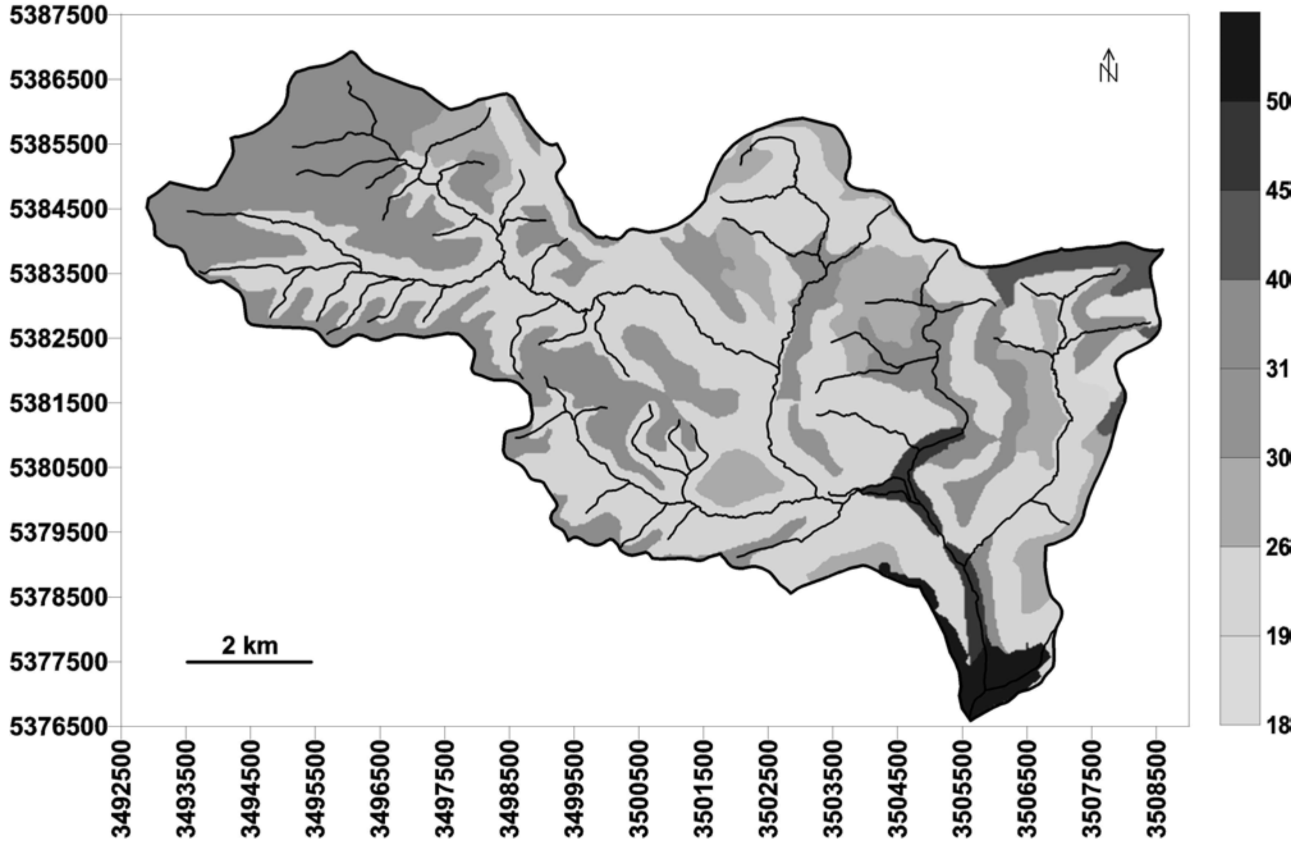

Figure 3.2: Soil types in the Goldersbach catchment taken from soil classification map Baden-Württemberg BÜK 2000 published by LFU Baden-Württemberg. Soil type classification according to German Soil Science Society (AG Boden, 1994).

18: Peolosoles and Rendzines from Solifluction
19: Pelosoles and Brownsoils from Solifluction
26: Parabrownsoils from Loess
30: Brownsoils from Solifluction and Debris
31: Brownsoils from Solifluction
40: Pseudogleye from Loess
45: Alluvial soils
50: Urban areas

At present, 86% of the Goldersbach catchment are forested. Prior to the interference of man, the forest was a sub-montane broadleaf forest with beech and oak as the predominating species, now it contains a mixture of 44% deciduous trees and 56% conifers. The distribution of soils as well as the vegetation cover strongly influences the relative contribution of each component of the hydrologic cycle. The long-term mean annual precipitation in the Goldersbach catchment amounts to 745 mm. With only 196 mm of total runoff, a high mean annual evapotranspiration rate of 549 mm is observed. While surface or direct runoff on predominately sandy soils is relatively low (about 45 mm/year), it increases to 90 mm/year in areas dominated by clayey soils from Keuperian marly and Liassic beds. Depending on the vegetation cover, evapotranspiration rates also significantly deviate from the mean: The annual consumption of coniferous trees (mainly Norway spruce) amounts to 650 mm, while on beech stands, it is usually in the range of 500 mm and shows significant differences in its annual cycle (see also Table 8.4).

With respect to its runoff response to rainfall, the Goldersbach catchment shows a peculiar behavior strongly influenced by the stratified nature of its soil types. Debris layers over clayey sub-layers act as a natural drainage system, which quickly absorbs rainfall and efficiently transports it just below the surface to the receiving stream. This leads on the one hand to a fast and complete interflow drainage of upper and intermediate slopes in the near-surface soil layers but hardly any surface runoff. On horizontal plateaus with less pronounced drainage forcing however, the large water holding capacity of the upper soil layers leads to considerable rainfall retention before a rise in discharge can be observed. Consequently, the degree to which the catchment responds to rainfall is strongly dependent on initial soil-moisture conditions, a fact supported by artificial irrigation tests conducted on 9 test sites in the catchment. Irrigating with an intensity of 100 mm/h, surface runoff only occurred when the soil reached its saturation point. In general, no differences in runoff characteristics could be detected between soils in coniferous, broadleaf or mixed forests. Surface runoff generally increased as the water content of the soil prior to rainfall became higher. When the initial water content was low, all soil types could absorb a minimum of 150 mm of precipitation before any surface runoff was detected. Variation in the runoff rates was high between the different soil types under dry initial conditions, but these differences decreased when the soils were wet. With increasing initial soil-moisture, the influence of the relief on runoff formation decrease steadily. Comparison of experimentally determined minimum water percolation rates with 100-year recurrence precipitation rates indicated that surface runoff in the Goldersbach catchment is extremely rare. Instead, it appears that the most important flood-producing discharge component is fast interflow.

As discussed later in the rainfall-runoff modeling sections 8.2 and 8.3, the strong dependency of the runoff response on initial conditions and a sudden discharge rise once a certain soil-moisture threshold has been reached was difficult to reproduce by a rainfall-runoff model. While originally the investigation of floods had not been a subject of the project described by Einsele (1986), the occurrence of a 100-year flood in 1987 led to a closer investigation of flood-favoring conditions in the catchment. All noteworthy rainfall-runoff events in the period 1975 until 1983 were analyzed with respect to the runoff coefficient and the initial soil-moisture deficit, which revealed a strong dependency among the two. For the 100-year flood in May 1978, the overall initial precipitation losses amounted to 20 – 50 mm. Evapotranspiration and interception contributed by about 5 to 10 mm, 10 to 30 mm were necessary to saturate the upper, coarse-grained soil layer according to its local field capacity. Additional 5 to 10 mm were lost due to infiltration into deeper soil layers. According to this information, the runoff hydrograph reacted on the rainfall only after the considerable amount of 20 to 50 mm of rain had already fallen. This value of course is dependent on the initial soil-moisture deficit but indicates a high retention potential of the catchment in case of dry initial conditions. The direct runoff coefficients of two pairs of similar rainfall events in Table 3.1 further support the strong dependency of flood occurrence or non-occurrence on initial conditions. For two rainfall events in 1980 and 1978 of roughly 100 mm each, the runoff coefficient varied from 5% to 30%! The same applies to two lesser events in 1978 and 1983.

Event	P [mm]	D_i [mm]	$\Sigma\ Q_d$ [mm]	ψ [-]
07. – 19.10.1980	100	72	5.2	0.05
22. – 24.05.1978	108	0	35.5	0.30
07. – 08.08.1978	46	65	4.3	0.09
08. – 09.04.1983	43	0	23.0	0.50

Table 3.1: Rainfall sums, initial soil-moisture deficit, direct runoff and runoff coefficient of 4 rainfall events in the Goldersbach catchment, from Einsele (1986)

P: Rainfall sum
D_i: initial soil-moisture deficit
$\Sigma\ Q_d$: direct runoff sum
ψ : direct runoff coefficient = $\Sigma\ Q_d / \Sigma\ N$

However not only the magnitude of runoff, but also the timing exhibits significant dependency on antecedent conditions, a fact that also led to considerable difficulties in the calibration of the rainfall-runoff models. The response times of the Goldersbach catchment as the time between first rainfall and resulting discharge rise has been investigated by Ludwig (2001) for the observations at gauge Bebenhausen PBEB (shown in Figure 3.4) and are listed in Table 3.2. The values compared to other catchments are unusually high and heterogeneous, which indicates that the catchment has a high retention potential which in case of low initial soil-moisture can significantly delay runoff response or oppress it completely. This is emphasized even further when the response times are compared to the catchment's concentration time according to Kirpich, which, with a flow length of 21 km and a mean slope of 4% to PBEB amounts to only 2.3 hours, a period considerably shorter than the observed lags.

Event	Response time [h]
April 1994	6
June 1995	4
July 1996	10
February 1997	14
October 1998	9

Table 3.2: Catchment response times as time between initial rainfall and runoff response at gauge Bebenhausen (PBEB) for historical flood events, from Ludwig (2001)

To summarize, the Goldersbach catchment shows a very willful runoff behavior. Tame and with low runoff rates during most of the year, even in the case of large amounts of rain when it falls on dry soil, it can under (un-)favorable conditions produce high and fast-rising floods with fast interflow as the predominant component, and surface runoff almost never occurring. All major historical floods, where considerable amounts of rain fell prior to the actual event support this. A hydrological model to adequately model the system's behavior should therefore take initial soil-moisture conditions into account.

3.2 Gauge network

The data used in the Goldersbach project come from a number of different measurement devices operated by several organizations. In addition, various techniques of data transmittal had to be used. Owing to that heterogeneity of data sources, considerable time had to be spent to establish the gauge system including data transfer and storage in a reliable and redundant way. In this section, an overview of all system components is given together with a brief excursion into data storage. A summary of all gauges and other system components is compiled in Table 3.3, additional information is given in sections 3.2.1 through 3.2.4.

ID	full name	see in	x- coordinate [m]	y-coordinate [m]	elevation [m]
RKAR	Radar Karlsruhe	Figure 3.1	3458600	5439900	148
DKOH	Disdrometer Kohltor	Figure 3.3	3497554	5386364	507
NMAU	Rain-gauge Mauterswiese	Figure 3.3	3506912	5381478	420
NSCH	Rain-gauge Schnapseiche	Figure 3.3	3501794	5384440	519
NNAG	Rain-gauge Nagold	Figure 3.3	3479300	5381040	380
NBÖB	Rain-gauge Böblingen	Figure 3.3	3501106	5394840	445
NREU	Rain-gauge Reutlingen	Figure 3.3	3515400	5372370	385
NROT	Rain-gauge Rottenburg	Figure 3.3	3498150	5371390	336
NTÜB	Rain-gauge Tübingen	Figure 3.3	3504400	5376300	330
NTÜB	Temperature-gauge Tübingen	Figure 3.3	3504400	5376300	330
PLUS	Rivergauge Lustnau	Figure 3.4	3505646	5376794	324
PKIR	Rivergauge Kirnbach	Figure 3.4	3505624	5379137	342
PBEB	Rivergauge Bebenhausen	Figure 3.4	3503235	5380224	375

ID	devices installed	operated by	measurement principle	observed quantity	Δt [min]
NMAU	gauge, modem, data logger	IWS	weighing type	rainfall [mm/h]	10
NSCH	gauge, modem, data logger	IWS	weighing type	rainfall [mm/h]	10
DKOH	disdrometer, PC, modem	IWS	optical	rainfall [mm/h] reflectivity [mm^6/m^3]	10
RKAR	C-Band Doppler Weather Radar	IMK	electromagnetic	reflectivity [mm^6/m^3]	10
NNAG	not known	UMEG	weighing type	rainfall [mm/h]	30
NBÖB	not known	UMEG	weighing type	rainfall [mm/h]	30
NREU	not known	UMEG	weighing type	rainfall [mm/h]	30
NROT	not known	UMEG	weighing type	rainfall [mm/h]	30
NTÜB	not known	UMEG	weighing type	rainfall [mm/h]	30
TTÜB	not known	UMEG	weighing type	temperature [°C]	30
PLUS	gauge, modem, data logger	IWS	pressure probe	waterlevel [m]	10
PKIR	gauge, modem, data logger	GDU/IWS	float	waterlevel [m]	10
PBEB	gauge, modem, data logger	GDU/IWS	float	waterlevel [m]	10

ID	location	purpose
CTÜB	Tübingen	central forecast processor
CIWS	IWS	computer for system development
CDKO	Site of DKOH	data logger and mobile net connector for DKOH

Table 3.3: Components of the Goldersbach catchment observation and forecasting system. For abbreviations, see the table 'Abbreviations' in the introduction. For locations see Figure 3.1, Figure 3.3 and Figure 3.4.

3.2.1 Rain-gauges

Being a wholly subsidiary daughter of the Federal State of Baden-Württemberg, UMEG maintains a large network of on-line accessible climate observation stations throughout the state. The network was established as an on-line accessible refinement of the gauge network maintained by DWD. Both the DWD and UMEG stations are of the weighing type and observe precipitation in 1-minute, 0.01 mm resolution. The advantage of the weighing principle is that precipitation is observed regardless of its state of aggregation by the weight increase in the collector. This allows all-year operation without the danger of malfunction due to freezing. Another advantage over other precipitation measurement principles is that no wetting and evaporation losses occur.

Five of those stations are located in a 20 km range of the Goldersbach catchment and are useful for rainfall interpolation over the catchment. Their locations are shown in Figure 3.3. Data is normally transmitted once per day from UMEG to CTÜB and CIWS (see Table 3.3) via ftp in 30-minute resolution. On request, data transmittal can be effected in steps of one hour. This is especially desirable in cases of extreme rainfall events with flood-producing potential.

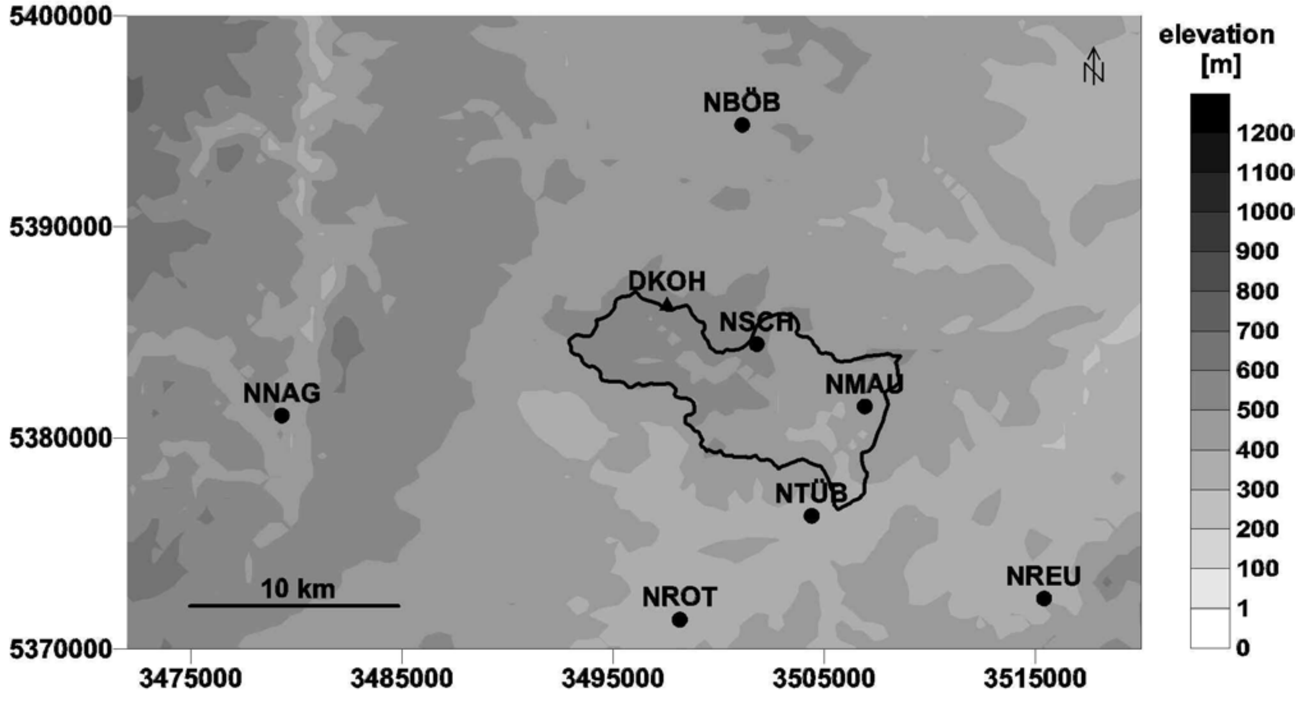

Figure 3.3: The rain-gauge and disdrometer network in and around the Goldersbach catchment

With all UMEG stations placed around, but not inside the catchment, it was necessary for the improvement of rainfall interpolation to install rain-gauges directly in the catchment. Financed by the project, altogether 3 additional rain-gauge were installed as shown in Figure 3.4: DKOH, NMAU, NSCH. The disdrometer DKOH, a special type of rain-gauge is explained in the following section, the other gauges are of the weighing type similar to the UMEG gauges. Data from NMAU and NSCH have 0.01 mm resolution and are stored in 10-minute intervals.

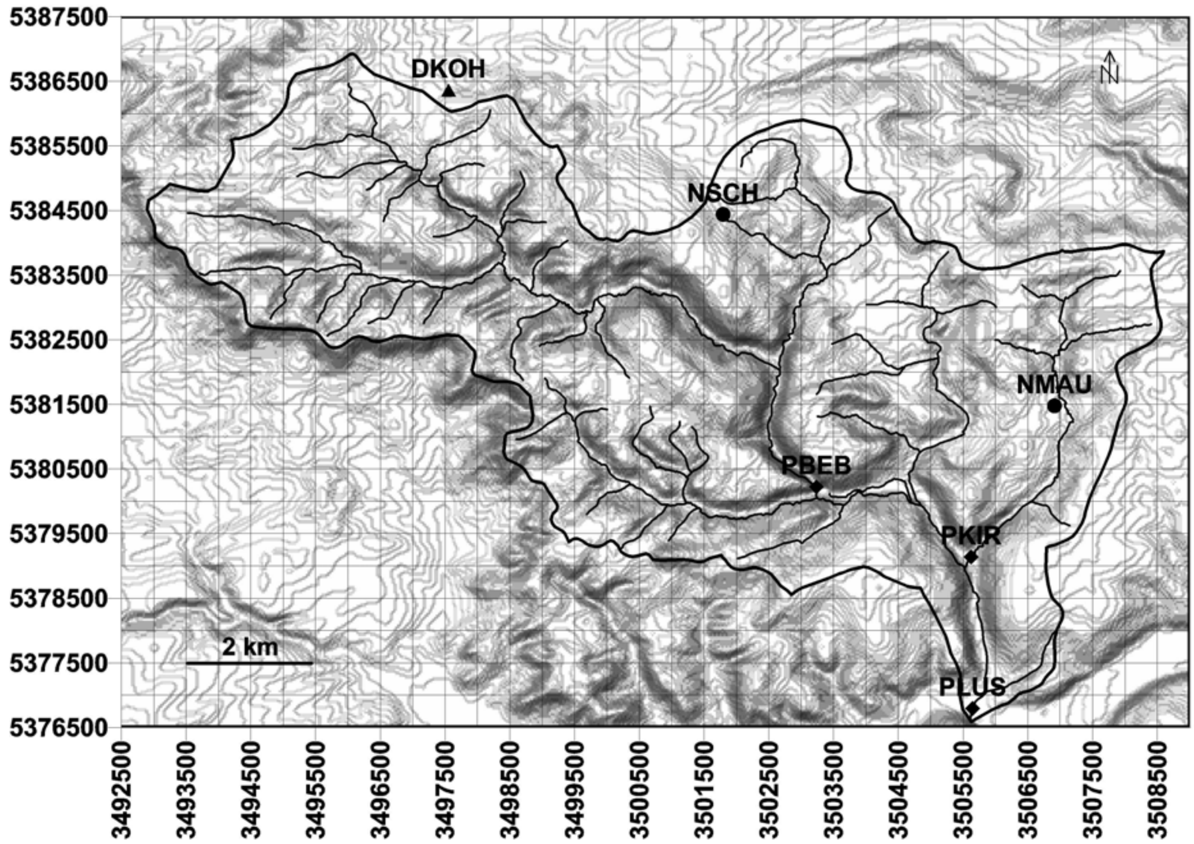

Figure 3.4: The rain-gauge and water-level gauge network and the radar pixel grid in the Goldersbach catchment

At first glance, selection of the gauge locations mainly along the north catchment boundary does not appear to be very representative of the area, however possible sites were difficult to find. Firstly, there are only few sufficiently large non-forested areas in the catchment, which is an essential requirement for a gauge site. Second, as the whole Goldersbach catchment was declared a nature protection area in 1974, no access to phone lines for data transmittal existed inside the catchment with the exception of the village of Bebenhausen. The only remaining option for data transmittal was then to rely on mobile net access. However, again due to its nature protection status forbidding the erection of receiver towers, dense forest cover and deeply encised valleys, net access coverage in the catchment is very patchy and many of the preferred gauge sites had to be rejected. On the few remaining options, the gauges were erected. Even then, after a few months of operation it showed that with normal antenna, remote connections could not always be established due to insufficient transmitter power. Replacing them with directional antenna providing 12 dB antenna gain finally ensured the desired reliability of data transfer. As an example, the site situation at NMAU is shown in Figure 3.5. The rainfall collector is protected from animals by a fence, a few meters away is the casing containing the batteries and the modem, nearby the mast with the directional antenna is visible.

Figure 3.5: Weighing-type rain-gauge NMAU with data logger and directional antenna for mobile net data transfer at site Mauterswiese

3.2.2 Weather radar

The radar data used in this project were taken from a C-Band Doppler weather radar operated by the Institute for Meteorology and Climatology (IMK) Karlsruhe. As can be seen in Figure 3.1, the radar and the Goldersbach catchment are roughly 70 km apart, a distance in which the radar data can still be considered accurate enough for quantitative use. Fortunately, no major shadowing effects due to topography occur, as the direct connection between the radar site and the catchment slips through the lowland gap between the heights of the Black Forest in the South and the Kraichgau rim in the North (see also Figure 3.1). The radar was designed as an operational research radar and has been in operation since January 1994. The scanned range is up to 240 km, for quantitative use of the radar data however the range is limited to 120 km. The raw radar data are in 1° polar coordinate azimuth resolution and 500 m radial increments and are taken at 16 elevation angles between 0.4° and 30° in 10 minute intervals. Transformed with two season-dependent Z-R-relations (A = 300, B = 1.5 for April through September, and A = 200, B = 1.6 for October through March), the raw data are projected on a terrain-following grid 1500 meters above ground in 500 meter resolution, also in 10 minute steps. The grid location can be seen as a square mesh in Figure 3.4. Exploiting the Doppler effect, the radar also provides the mean vertical wind profile in a 50 km range. Several operational calibration procedures are applied to maintain the quality of the radar products. Data from 105 rain-gauges in a range between 6 to 120 km from the radar are used for continuous multiplicative adjustment: A shadowing correction for areas not visible by the radar is used: the observed values above are extrapolated into the shadowed areas using a standard vertical reflectivity profile.

Lastly, an automatic profile correction is applied to suppress Bright Band error and under-estimation in case of snowfall: The presence of a Bright Band in the raw data is identified as strong reflectivity gradient circular around the radar location (when the radar beam enters the Bright Band elevation, sudden reflectivity changes occur). Then the elevation and thickness of the Bright Band is identified. A correction profile based on this information or, in the absence of Bright Band structures, the vertical temperature gradient taken from two ground-based thermometer measurements at 100 and 200 m above ground at the radar site is selected and used on the raw data. More technical data are given in Table 3.4 and IMK (1999).

Specification	
Frequency	5.62 GHz
Transmitted power	255 kW
Beam width	at –3 dB: 0.98°
Gain	44.7 dB
Pulse Repetition Frequency	250 – 1200 Hz
Pulse width	0.85 and 2.0 microsec
Doppler capability	± 48 m/s
Polarization	horizontal
Clutter suppression	IIR high pass Doppler filter
Sensitivity	-104 dBm

Table 3.4: Technical data of the IMK weather radar

3.2.3 Disdrometer

As already mentioned in section 3.2.1, a special type of rain-gauge known as a disdrometer was installed in the Goldersbach catchment. A disdrometer measures the rate of precipitation and distribution of particle size and velocity. Also it identifies the type of precipitation such as drizzle, rain, sleet, hail, snow and mixed precipitation according to WMO table 4680 which is shown in graphical form in Figure 3.6. The measurement principle is such that an infrared laser generates a shallow and broad horizontal radiation band. After passing through the atmosphere, the radiation is focused onto a photodiode line. Hydrometeors falling through the measurement area cause variations in the detected radiation intensities. A digital signal processor (DSP) calculates particle size and velocity and categorizes the precipitation into different classes. The advantage of a disdrometer over conventional rain-gauges is that from the particle size distribution, the radar rainfall reflectivity can be inferred. This makes the disdrometer a useful tool to determine a Z-R-relation with data from only one gauge and to use it as a locally valid transformation function to be used on radar-derived reflectivity data as discussed in section 6.4.

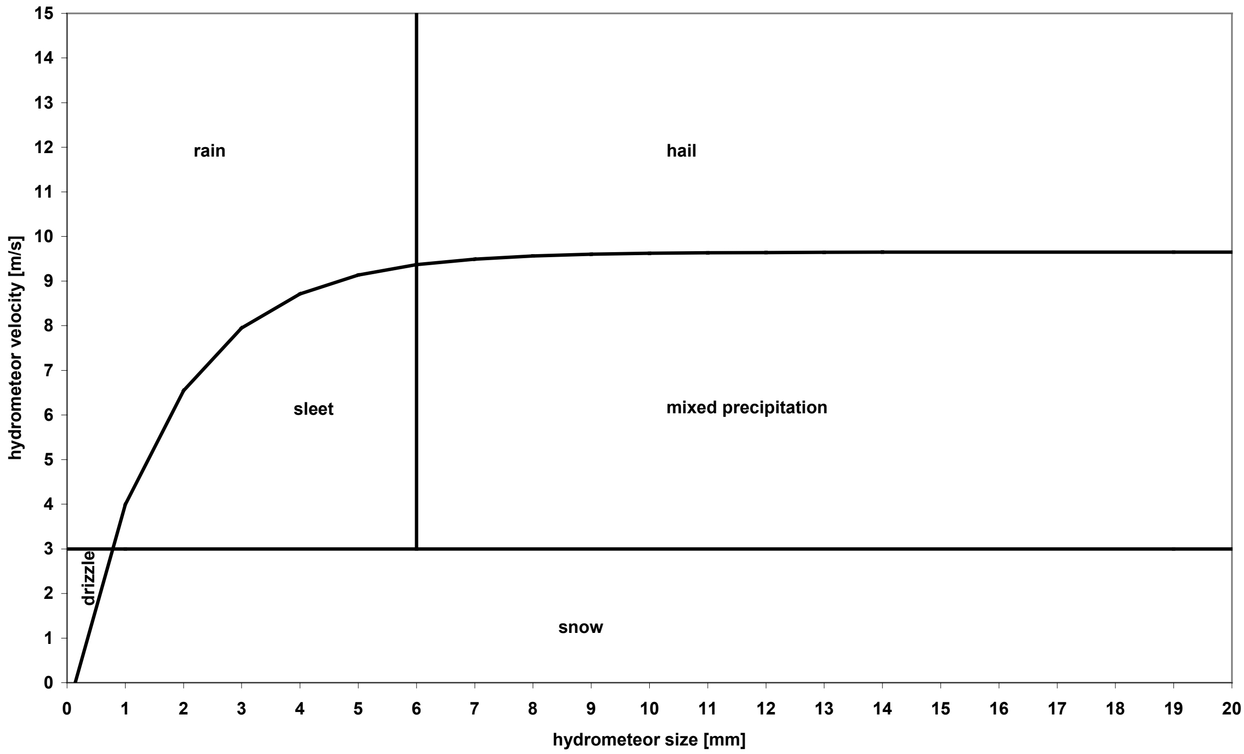

Figure 3.6: Precipitation classification using hydrometeor size and velocity according to WMO table 4680

The device used for the Goldersbach project, PARSIVEL M300, was developed at the IMK and at the time of purchase only available as a prototype. Specifications are listed in Table 3.5, further information on disdrometers is also given by Löffler-Mang and Joss (2000). Due to its relatively high energy consumption, it had to be installed at a place with continuous power supply which was finally found at the site of a youth camp at the northern catchment limit (Figure 3.4 and Figure 3.7).

Unfortunately, during use it was found that the device did not always operate properly and improvements of the measurement techniques were necessary. This disabled the originally intended use for operational radar data calibration. Nevertheless, the disdrometer principle has great potential to improve and combine both rainfall and radar measurement in future.

specification	
transmitter wavelength	780 nm
measuring area	48.6 cm^2
range of particle sizes	0.25 – 25 mm
range of particle velocities	0.1 – 20 m/s
range of precipitation rate	0.01 – 999.99 mm/h
range of radar reflectivity	-9.999 – 99.999 dBZ

Table 3.5: Technical data of the PARSIVEL M300 disdrometer

Figure 3.7: Disdrometer DKOH located at the youth camp Kohltor

3.2.4 Rivergauges

In Baden-Württemberg, the local water authorities operate and maintain an extensive rivergauge network, among them two in the Goldersbach catchment: PKIR at the outlet of the Kirnbach sub-catchment and PBEB at the Goldersbach, about halfway down the catchment (Figure 3.4). The gauges are of the ordinary float-type and record on paper. With the permission of the GDU, an additional, battery-operated digital data logger was installed at each site along with a modem and directional antenna for mobile net data transmittal. In addition to the two existing gauges, a third, PLUS, was installed just before the confluence of the Goldersbach into the Ammer river in Tübingen-Lustnau to obtain information of the overall catchment discharge (Figure 3.4). Due to a wide channel geometry and resulting low water levels of usually only a few centimeters, a gauge of the bubble-in type was installed. Here, the water level is estimated indirectly from the pressure necessary to force air bubbles out of a submerged tube. All gauges record the waterlevel in 10-minute intervals and 1 mm resolution.

The rivergauge data had, at times, to be used with care for several reasons. Firstly, the waterlevel-discharge relations at each site are (especially for the high flow cases) based on only very few observations and introduce uncertainties in the order of several cubic meters per second to the observations. In addition, gauge observations were at times falsified by human impact. The Goldersbach catchment is a very popular weekend destination and playing children have repeatedly blocked the Kirnbach above the site of PKIR with dams, which may have been a lot of fun, but led to erroneous high waterlevel recordings.

3.3 Data storage

Apart from observation and transmittal, effective data storage is an important prerequisite for modeling. Optimally, data are stored consuming as little storage space as possible while allowing random and fast access. Especially at the example of the radar data the importance of optimal data handling becomes evident: One radar image consists of 350×350 grid values. With an image completed every 10 minutes, 6.438.600.000 pieces of information have to be stored per year. If each pixel value is represented by a 32 bit floating point precision value, the necessary storage space amounts to 25.7 Gigabyte. For analysis and modeling, any piece of information must be accessed quickly. Those requirements are only sub-optimally fulfilled when data are stored in files, much better performance is achieved with database storage. Databases store information with minimum storage space and optimum accessibility when they are established according to the three rules of normalization:

- 1st rule of normalization: A table is in first normal form when all attributes (fields) are elementary (no further sub-division possible)
- 2nd rule of normalization: A table is in second normal form when it is in first normal form and each field not containing the primary key has a full functional dependency on the primary key. The primary key is a field or set of fields that unambiguously identifies any record in a table.

- 3^d rule of normalization: A table is in third normal form when it is in second normal form and all fields not containing the primary key are independent.

For all data except the radar, databases were established in MS Access 97. Although limited in performance, MS Access 97 allows easy data handling and export to other programs and was therefore favored where the amount of data did not require more sophisticated solutions. For the radar data, a database was established first with Oracle for Linux, then Oracle 8i for Windows. As primary key, the radar ID in combination with the time-stamp of the radar images was chosen. The header information of each image was stored in an extra table, the matrix of grid rainfall values was split in fields (grid columns) and records (grid rows). Indices were assigned for both the time-stamp and the rows of the radar images to allow fast searching with respect to both time and position. To speed database requests up further, the tables were divided into 3-month partitions. Although the conceptual and programming work to implement the databases and additional tools to read the original, ASCII-file formatted radar data into the database and to do database maintenance work took considerable time and effort, in the long run it paid off. Requests including years of radar data and the whole radar image can be performed in a reasonable time (a few minutes), more specific information such as a section of a single radar image are retrieved in the order of time of one second.

4 Rainfall type classification using Radar

In the early days of weather radar use for rainfall estimation, usually one mean Z-R-relation derived by Marshall and Palmer (1948) was used for reflectivity transformations (see Table 2.3). Doing so implicitly assumed the raindrop size spectrum, which is an important factor influencing reflectivity, to be constant. However, this soon was found to have left room for improvements. When Joss et al. (1968) observed half a year of rainfall simultaneously with a vertical pointing radar, four rain-gauges and one disdrometer, large variations of the Z-R-relation parameters from the standard relation were observed. While B proved to be mainly a constant of 1.5, A varied according to the rainfall type between 50 for drizzle and 1000 for thunderstorms. Furthermore, for each rainfall type, A was approximately log-normally distributed.

Using disdrometer data sampled under a completely different climate, Reddy et al. (2001) also observed a clear seasonal dependence in Z-R-relation in India corresponding to the monsoon periods.

Obviously, Z-R-relations are dependent on the rainfall type because each type possesses a characteristic drop-size spectrum originating from the rainfall-forming process. Waldvogel (1975) found that in warm clouds where the Bowen-Ludlam-process (see section 2.2.1) is predominant, drop-size distributions tend to be mono-disperse, in cold clouds favoring the Bergeron-Findeisen-process (also section 2.2.1), exponential spectra dominate. This clearly shows in mean Z-R-relations from individual rainfall events triggered by different rainfall-forming processes. Small values of B indicate mono-dispersity, large values stem from wide (exponential) spectra. Large values A belong to large-drop events such as thunderstorms, low values A result from drizzle rain.

Based on those and other findings pointing in the same direction, much work has been carried out to determine rainfall-type specific Z-R-relations. The approaches can be broadly classified in two main directions: The first assumes perfect knowledge of the current rainfall type from cloud physics and meteorological considerations and tries to fit Z-R-relations to each of the rainfall types, while the second assumes no a priori knowledge of the rainfall type, but classifies rainfall into types according to the observations made by radar and disdrometer. Fortunately, results from both approaches usually 'met in the middle' with fairly identical classifications and related Z-R-relations, if classification was limited to a few different types.

Joss and Waldvogel (1970), pursuing the observation-based approach found that rainfall can be classified by the vertical reflectivity profile of the rain-field or the drop-size distribution. Less promising was a seasonal or geographically related variation of the Z-R-relation. Chen et al. (2001) sub-divided rainfall into convective, stratiform and mixed types using the vertical reflectivity profile of radar to estimate rainfall-type specific Z-R-relation. The major distinctive feature they based the classification on was the occurrence of high reflectivity in the vertical profile: Profiles with high reflectivity only at Bright Band elevation were considered stratiform events, profiles with high reflectivity spread over all elevations were considered convective rainfall. Another approach was followed by Nagata et al. (2001) who described the spatial variability of rainfall fields by the slope of the scaling Fourier power spectra and the spatial intermittency parameter. Based on those parameters, a 2-D cluster analysis allowed an image characterization into convective, mixed and stratiform rainfall types.

Going one step further Sanchez-Diezma et al. (2001) showed the necessity of considering both the variation of the Z-R-relation as a function of rainfall type and the correction for the distance from the radar by the vertical profile of reflectivity to improve radar-based rainfall-runoff modeling. They compared modelled discharge from generated 3-dimensional rainfall fields and, based on those, fields degraded with simulated errors. The simulated hydrographs showed that the rainfall-runoff process is fairly insensitive to non-systematic errors of the rainfall field, if the mean error is not significant. Range-related radar errors produced different effects for convective and stratiform rainfall events. In the convective case, large scatter but no bias, in stratiform cases bias due to Bright Band presence. In a second step they used different Z-R-relations according to rainfall type: A = 300, B = 1.4 for convective events and A = 200, B = 1.6 for stratiform events which resulted in close resemblance of the degraded fields and the reference field and consequently in improved rainfall-runoff modeling results.

Although the radar data for the Goldersbach project were already seasonally adjusted for the rainfall type using different Z-R-relations for summer and winter, it was considered useful to adjust the radar data according to the current rainfall type to further improve rainfall estimation and rainfall-runoff modeling results. The approach was to use expert knowledge of the current, meteorological rainfall type, mainly based on synoptic analysis and determine which properties extractable from a radar image were suited to discriminate those types in a fast and reliable manner. The rainfall types considered are explained and illustrated in section 4.1 along with the image properties tested. In section 4.2, an automated, fuzzy rule based classification technique is presented and results are shown. Conclusions drawn are summarized in section 4.3.

4.1 Meteorological rainfall types and distinctive features

As previously indicated, the first step towards radar-based rainfall classification was to select meteorological rainfall types to be classified. It should be borne in mind that this classification is mainly based on cloud physics, i.e. the rainfall-producing processes occurring in clouds, the manner of air mass movement (e.g. predominately vertical in case of convection or horizontal in the case of frontal systems) and the synoptic scale conditions. All of the above properties are more or less encrypted in a radar image and can be decoded only to a certain degree. The classification was, with some modifications, mainly based on the rainfall types described in Table 2.2. Synoptic systems were excluded from the classification as the radar image used was simply too small for detection of meso-α scale features. As it was tried to do classifications based on individual images without temporal considerations, supercells and convective cells were grouped due to their close resemblance on individual images; differences only show in their temporal behavior. Additionally the rainfall type 'shower' which incorporates pre-frontal showers, warm-sector rainfall and post-frontal showers was introduced. This was considered important as although showers can be associated with one particular front, their properties differ significantly from the actual frontal rainfall. Finally, the neutral rainfall type 'no rain' with obvious properties was introduced to complete the set of rainfall types for automated rainfall classification. Typical examples of all rainfall types are shown in Figure 4.1 a) through f) and are explained in detail in section 2.2.2 and 2.2.3. Some additional features mainly observable in radar images are given below.

a) Convective cells and Supercells

Convective cells develop from a radiation-induced convective rise of local moist air masses and are usually associated with thunderstorm events. Their life-span is in the order of one hour but rainfall intensities are extreme. Convective cells are usually round to oval in shape and show no or erratic movement. Under unstable atmospheric conditions, one cell may trigger the formation of new cells in its close vicinity, leading to multi-cell thunderstorms. Supercells only occur under very dynamic atmospheric conditions and may live for several hours, propagating with the prevailing wind.

b) Mesoscale convective systems (MCS)

A detailed description of MCS or squall line genesis is given in section 2.2.3. MCS persist for several hours and show a distinctive, uniform movement. MCS, as the name 'squall line' indicates are of oblong structure and are of considerably larger areal extension than convective cells but only slightly less extreme in rainfall intensities.

c) Cold fronts

Cold fronts are in the ideal case narrow, band-like structures that persist for several hours, moving along with a uniform and usually high velocity. Those characteristics vaguely relate them to MCS, but rainfall intensities in cold fronts are usually much lower, up to a maximum of roughly

50 - 60 mm/h. Also, cold fronts may at times have a much larger areal extension with large areas of less intensive rain in the wake of the leading front.

d) Warm fronts

Warm front rainfall, triggered by the propagation of warm air masses leads to widespread, low intensive rainfall that may at times cover the whole radar range and persist longer than 24 hours. Intensities rarely exceed 20 mm/h and no clear form can be assigned to the warm front fields.

e) Showers

Before the passage of a warm front or in the warm sector in-between fronts or after the passage of a cold front, a patchwork of scattered low-intensive showers with irregular shapes can occur. All of the above shower types are covered by the term shower here, as without prior knowledge of the current state of the warm front, warm sector and cold front succession it is very difficult to distinguish them.

f) No rain

This is the easiest case for classification and is only listed for reasons of completeness.

a) Convective cells 22.08.96 13:10

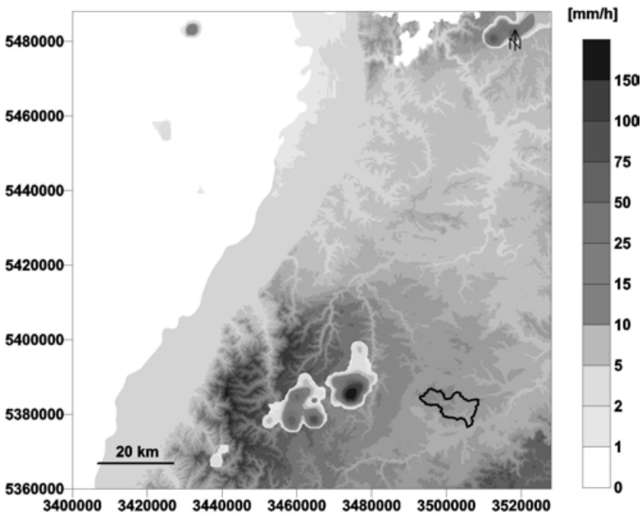

b) Mesoscale convective system 07.06.98 14:30

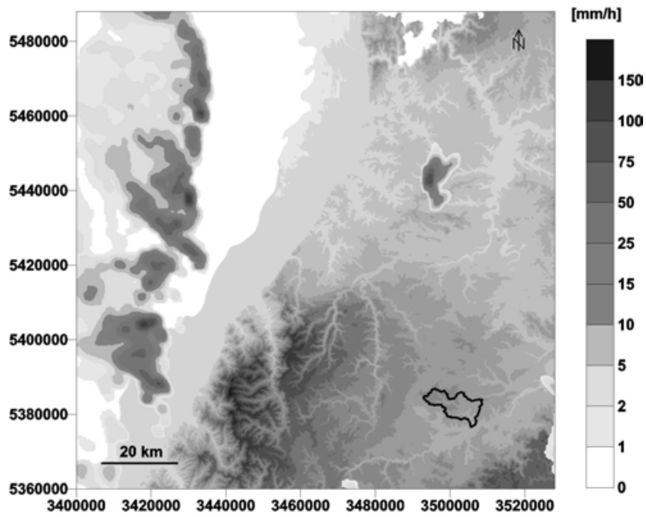

c) Cold front 29.10.98 13:40

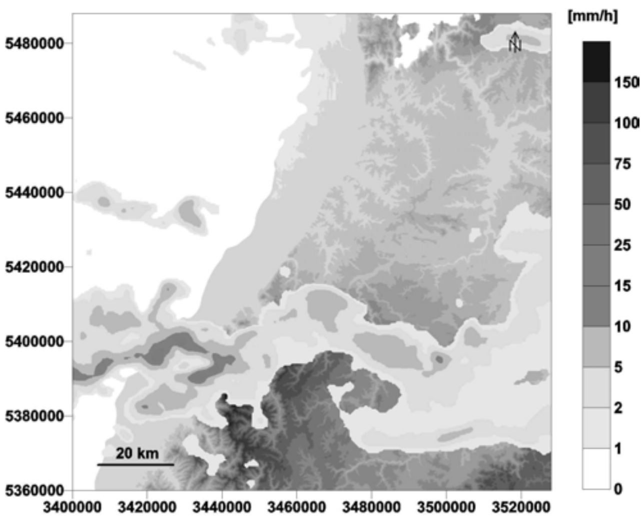

d) Warm front 29.10.98 06:40

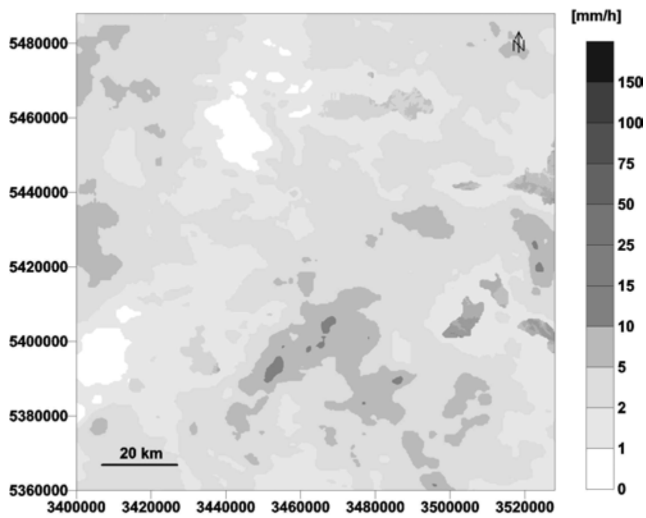

e) Showers 15.03.01 09:00

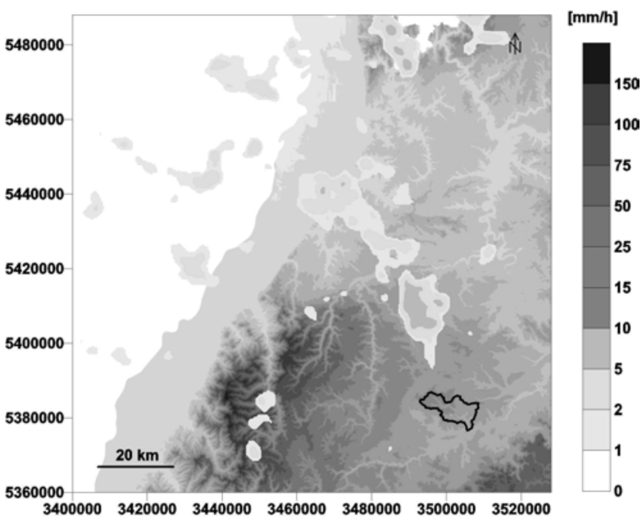

f) No rain

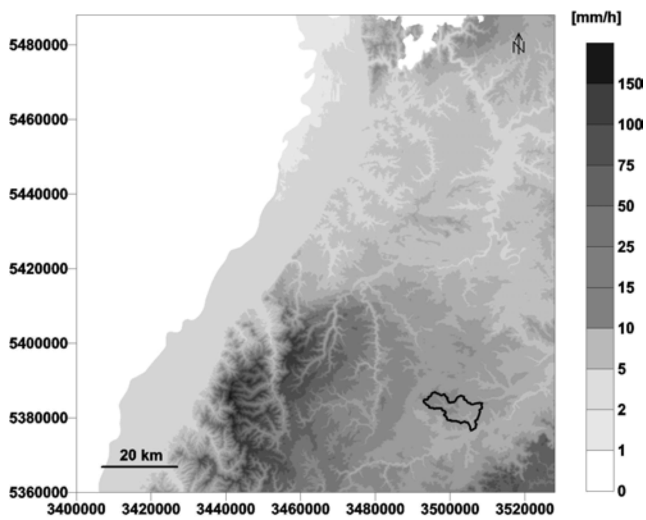

Figure 4.1: Meteorological rainfall types seen by weather radar

Following discussions with Gysi from the Forschungszentrum Karlsruhe and experiences from the 'String of Beads Model' (Pegram and Clothier, 2001), a selection of parameters useful for image classification was compiled. None of the parameters require any information other than the current radar image and describe mainly the rainfall coverage and intensity structure and the shape of the rainfall fields observable in the image. In detail, those are:

- WAR: Wetted Area Ratio, defined as the proportion of the image experiencing a rainfall rate in excess of 1.0 mm/h
- IMF: Image Mean Flux, or average rainfall rate in [mm/h] over the whole image, including the zero-rainfall pixels
- 10AR: Proportion of the wetted area (defined by WAR) where rainfall in excess of 10.0 mm/h is observed.
- QD: Ratio of the number of borderline occurrences in the two diagonal directions of the accumulated neighborhood matrix such that QD ≤ 1.
- QV: Ratio of the number of borderline occurrences in the horizontal and vertical directions of the accumulated neighborhood matrix such that QV ≤ 1.
- ANI: Anisotropy coefficient, defined as the product of QD and QV. The more the features in a radar image resemble circles, the more ANI approaches 1, the more oblong the features are, the more ANI approaches zero.
- PHI: Angle of anisotropy, indicating the directions of the longest extension positive counter-clockwise, with 0° indicating vertical, 90° indicating horizontal structure

While WAR, IMF and 10AR are straightforward in calculation and meaning, QD, QV, ANI and PHI require some explanation. Their derivation is based on Neighborhood analysis (Jähne, 1997): Each cell **X** in a grid is surrounded by 8 neighbors (UL indicating Upper Left neighbor and so on) as shown in Table 4.1 a with their respective sample rainfall intensities given in Table 4.1 b. If the borderline of a rain-field is defined as the transition from rainfall intensity values below to above a certain threshold (here it was set to 10 mm/h) between adjacent cells, for each grid-cell the existence and location of a rain-field border along the cells limits can be determined. With the rainfall intensities given, a rain-field border is located between the center **X** and neighbors **UL** and **ML**. Therefore, the borderline occurrence matrix in Table 4.1 c contains zeroes except for the upper and middle left neighbor. Summing up all neighborhood matrices in a radar image, where each pixel is once the center pixel, the accumulated borderline occurrence matrix of the image can be calculated. This matrix has the following properties:

- It is point-symmetrical to the center.
- If the image contains mainly circular structures, the accumulated values of UL and UR as well as UM and MR are almost identical (the border of the rain-field has the same length in all directions). If, however, the image contains longish structures, the neighborhood values in the direction of the long structure axis will be large, while in the direction of the short axis, they will be small.
- The ratios of the accumulated borderline matrix QD = UL/UR if UR>UL (or UR/UL if UL>UR) and QV = UM/MR (or vice versa) will be close to 1, if circular structures in the image prevail; they will be close to 0 if mainly longish structures occur. The same applies to the product of the two relations, ANI = QD·QV which can then be regarded as an integral measure of the predominant rain-field shape.

PHI is simply calculated as the weighted mean of the four principal directions: Vertical (0°), horizontal (90°) and the two diagonal directions (45° and 135°). The weights assigned are the inverse, normed neighborhood values, so PHI indicates the direction of the longest extension of the prevailing structure in the radar image, starting at 0° for vertical structures and positive counterclockwise orientation.

a)			b)			c)		
Neighborhood matrix			Rainfall intensities			Borderline occurrence		
UL	UM	UR	0	12	13	1	0	0
ML	**X**	MR	9	**11**	15	1	**X**	0
LL	LM	LR	13	12	12	0	0	0

Table 4.1: Sample neighborhood matrix and borderline occurrences on the 10 mm/h level

All parameters were calculated for 22 rainfall events manually classified by Gysi containing a total of 1041 radar images. Some typical parameter time-series for all rainfall types are shown in Figure 4.2 (WAR), Figure 4.3 (IMF), Figure 4.4 (10AR) and Figure 4.5 (ANI). For the single radar images shown in Figure 4.1 the corresponding parameter values are given in Table 4.2. Comparing WAR and IMF, a strong positive correlation seems to exist between the two: the higher WAR, the higher usually also IMF. This was also reported by Pegram and Clothier (2001) and Clothier and Pegram (2001) and verified by own, extensive investigations reported in section 7.2. Due to this mutually similar behavior, in later investigations mainly only WAR was used for classification. Looking at Figure 4.2, it is obvious that an upper border for WAR for rainfall types convective cells and showers exists in the order of magnitude of 20%. Cold fronts and MCS can reach values for

WAR up to 70% for cold fronts and 50% for MCS. The greatest values for WAR up to 100% are only reached by warm fronts, which in turn rarely show coverages below 20%. Clearly, WAR is a very good rainfall type discriminator when applied on the scale of a radar image, here 128 × 128 km. The same applies to 10AR, which was selected among many other threshold values on levels between 5 mm/h and 20 mm/h as the best suited. While showers and warm fronts almost never possess any rainfall intensities in excess of 10 mm/h, convective cells contain a significant percentage of them. Throughout the most of the rainfall event's duration, 10AR exceeds 10%. MCS may contain the same number of highly intensive rainfall cells, but as they are accompanied by areas of less intensive rainfall, the percentage of 10AR does not quite reach the long-term high level persistence associated with convective cells, but can still show values larger than 60% and almost never falls below 10%. Cold fronts range somewhere in-between, sometimes showing zero 10AR occurrences, sometimes up to 30%.

Rainfall type	Date	WAR [%]	IMF [mm/h]	10AR [%]	QD [-]	QV [-]	ANI [-]	PHI [°]
Convective cells	22.08.96 13:10	3	0.75	47	0.91	0.98	0.89	144
MCS	07.06.98 14:30	22	2.24	26	0.86	0.65	0.55	13
Cold fronts	29.10.98 13:40	27	0.93	3	0.94	0.72	0.67	82
Warm fronts	29.10.98 06:40	94	2.67	0	0.93	0.76	0.70	80
Showers	15.03.01 09:00	4	0.14	0	0.87	0.92	0.80	62
No rain	--	0	0	0	--	--	--	--

Table 4.2: Examples of meteorological rainfall types and distinctive features

The shape parameter ANI is a less reliable source of information, at least when regarded isolated without consideration of the previous images. Firstly, ANI shows different results on different intensity levels, and not in all cases is the level chosen (10 mm/h) the most suitable. Secondly, ANI shows considerable fluctuations from one time-step to the next (see Figure 4.5), which makes it difficult and uncertain to do an image to image classification. Despite those difficulties, there is some potential in the shape parameter ANI that can be best seen in the case of the cold front and MCS. Usually of longish structure, they show corresponding low values of ANI and can be distinguished from the more roundish convective and shower cells. The shape parameters for warm fronts should be regarded carefully: When large coverages occur, sometimes the only boundaries in the image are at the range limit of the radar image and around holes in the coherent rain-fields and ANI consequently shows strange values. PHI finally is not a parameter to distinguish meteorological rainfall types, as the orientation of a structure does not tell much about the underlying rainfall type and PHI is only meaningful when considerable anisotropy in the image occurs. Therefore, it was not used as a means of distinction, but could, with low values of ANI indicating the usefulness of PHI, be useful to determine the angle of orientation when for rainfall interpolation anisotropic variograms are used. Looking at the PHI values for the MCS and cold front events in Table 4.2, the angle corresponds well with the angle one would guess from Figure 4.1 b and c.

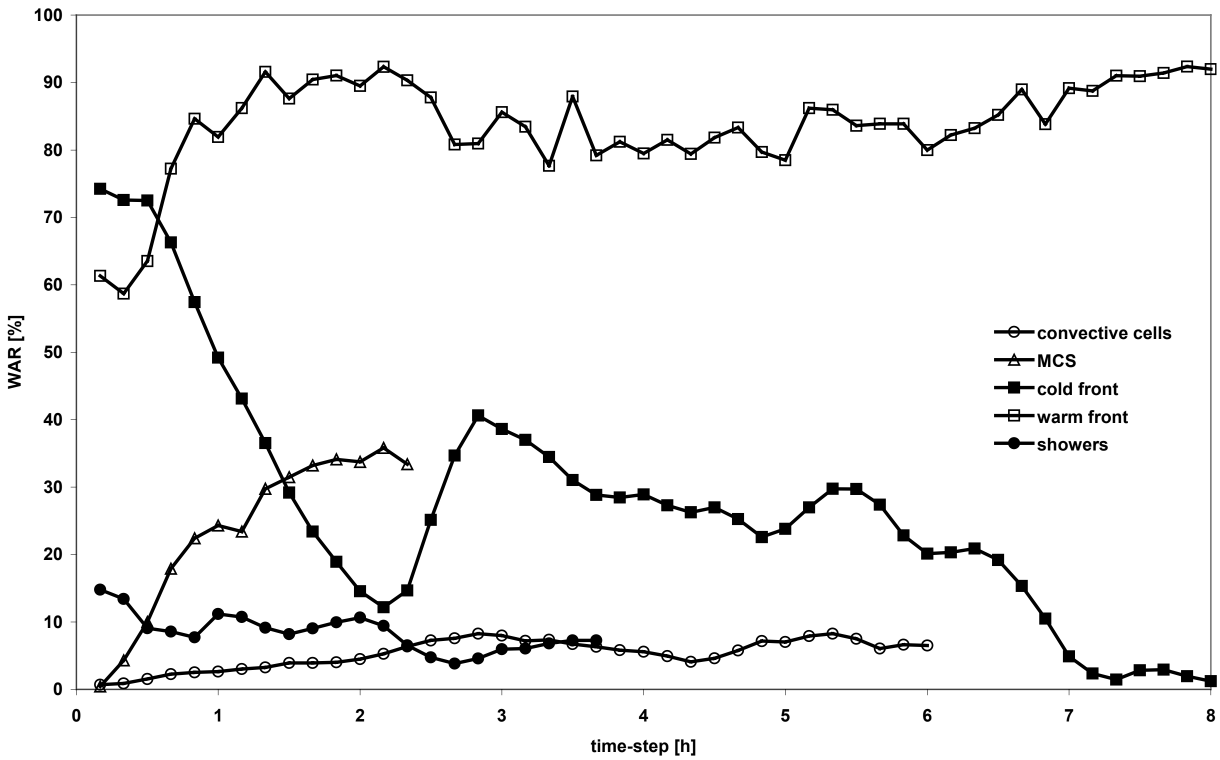

Figure 4.2: Selected WAR time-series for different meteorological rainfall types

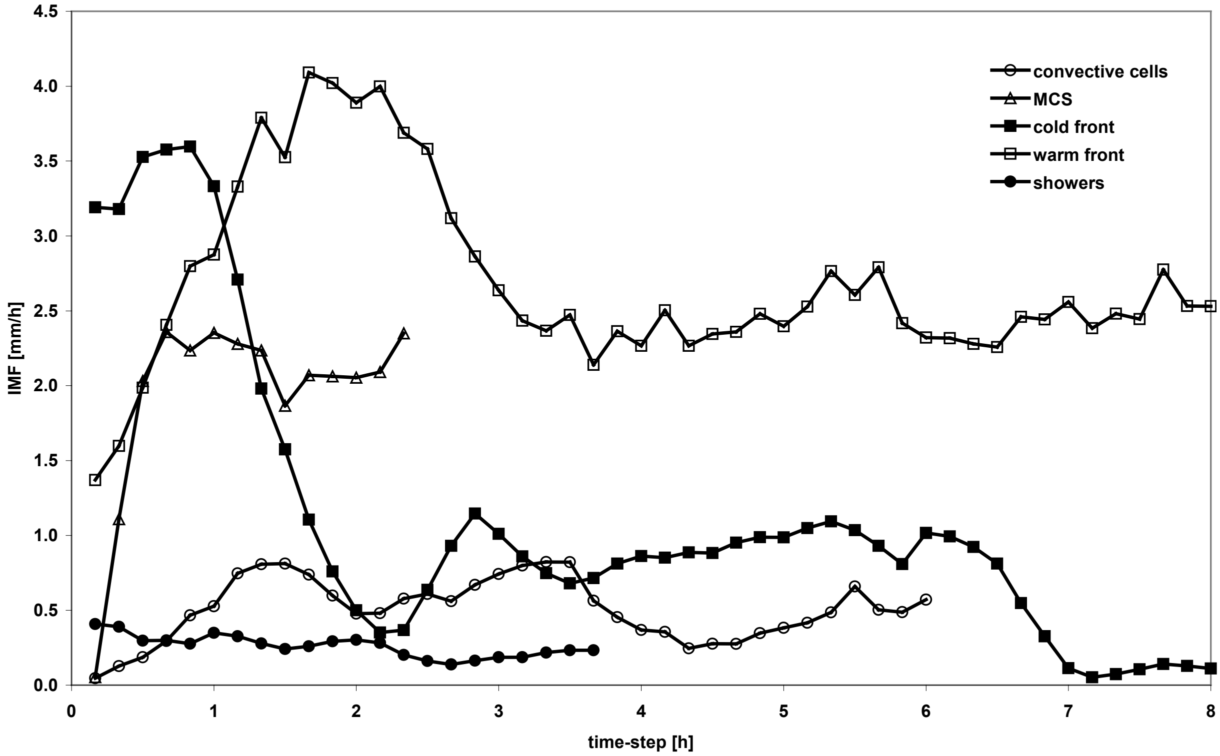

Figure 4.3: Selected IMF time-series for different meteorological rainfall types

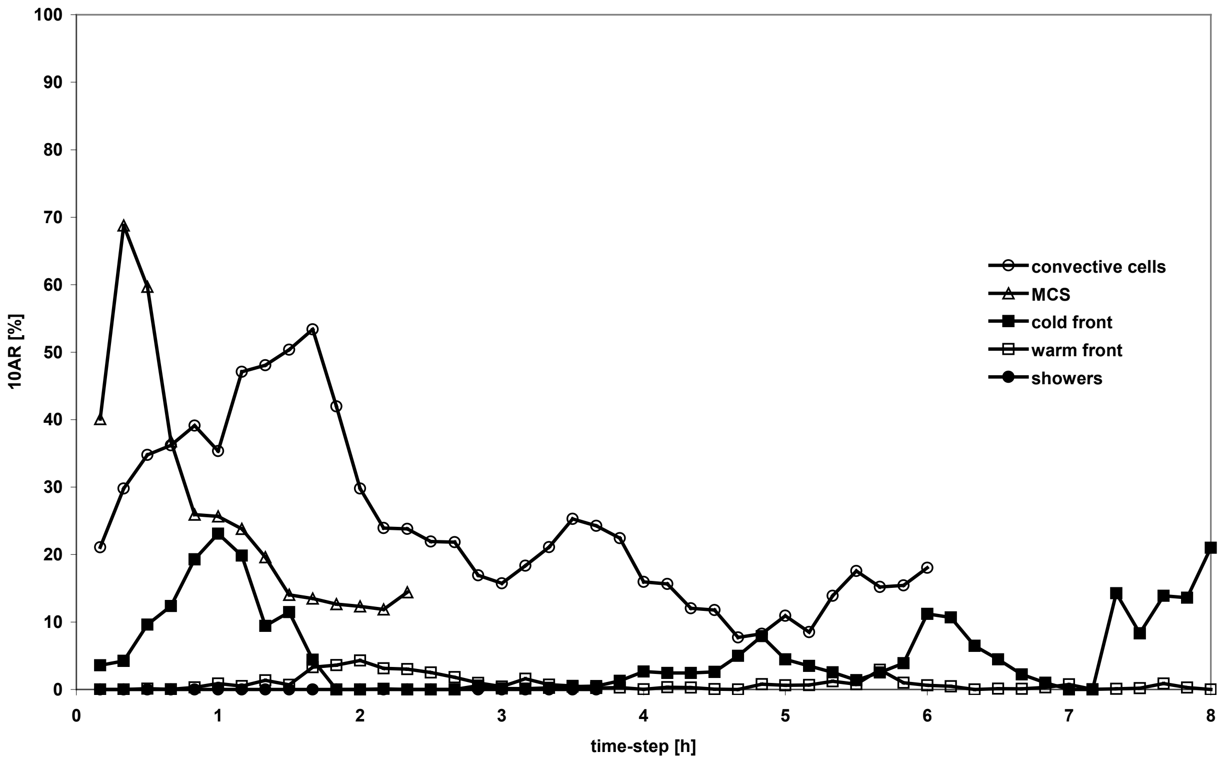

Figure 4.4: Selected 10AR time-series for different meteorological rainfall types

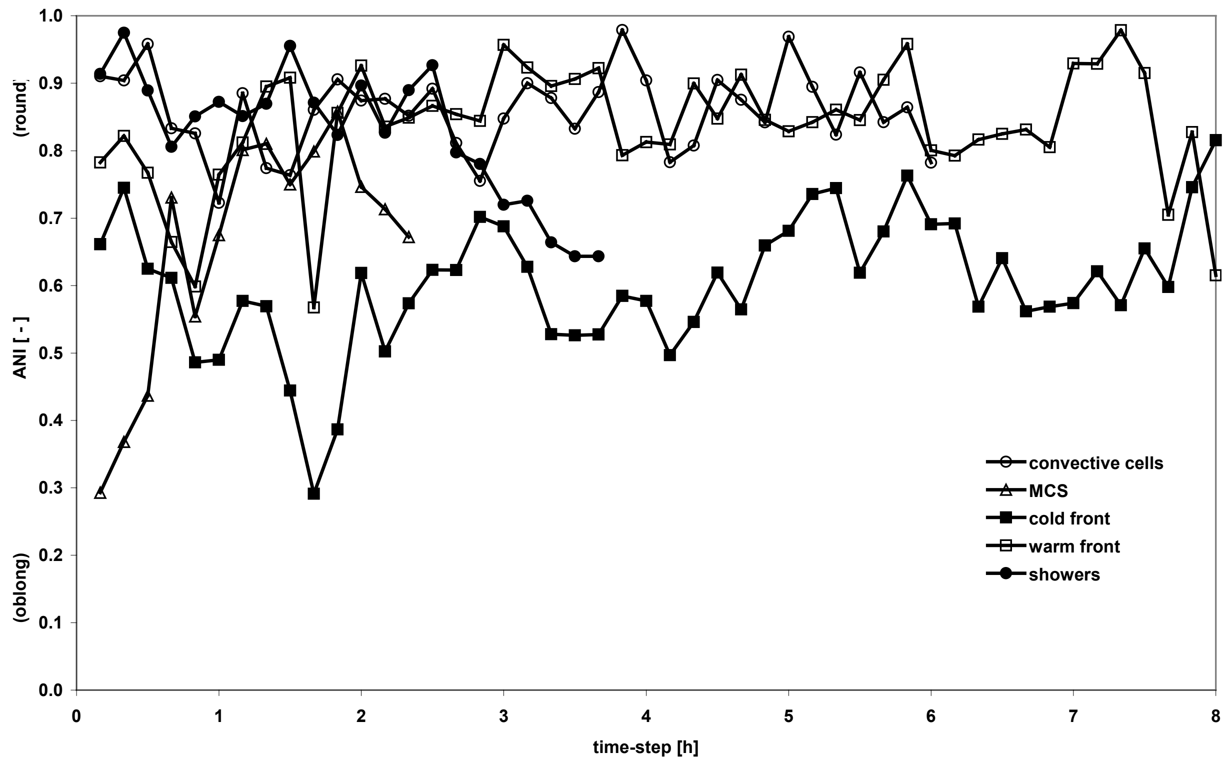

Figure 4.5: Selected ANI time-series for different meteorological rainfall types

4.2 Classification technique and application

From the preliminary analysis of the rainfall types and their respective properties, several conclusions could be drawn regarding their discriminatory power and the resulting requirements for a classification system. Although typical parameter ranges could be specified for each rainfall type, the borders often overlapped and outliers occurred. This is not solely a problem of the appropriate or inappropriate selection of parameters. Even experienced meteorologists are at times unable to assign a single rainfall type to a single radar image, partly because the information contained in the image is not sufficient to allow a clear decision but also because mixed rainfall types frequently occur. A decision system to classify rainfall types from radar images should therefore be able to cope with ambiguous or incomplete data and should allow the incorporation of expert knowledge. Fuzzy logic lends itself well to complex applications with the above requirements and has the additional advantage of easy-to-understand algorithms that enable a common sense validation of each step of the calculation, unlike for example the black-box calculation of neural network approaches. For this reason, a fuzzy rule based classification scheme with a self-optimizing algorithm as described by Bárdossy (2000) was established and applied in section 4.2.1.

4.2.1 Optimized fuzzy rule system classification

'As complexity rises, precise statements lose meaning and meaningful statements lose precision'. This statement by Lotfi Zadeh, the 'father of fuzzy logic' (Zadeh, 1965) refers to the principle of incompatibility that claims that complex systems cannot be explained by algorithms based on conventional mathematics but need to incorporate a mathematical formulation of vagueness. Fuzzy logic is a useful way of doing this, where in short the principle of conventional 'crisp' or singular numbers or sets is given up in favor of vague regions that belong to a certain degree to the original number or set. Fuzzy logic is conceptually easy to understand, flexible and tolerant of imprecise data. It can model non-linear dynamics or relations of arbitrary complexity and can be built upon expert experience. Furthermore, it can be blended with conventional control techniques and is based on natural language. A brief introduction to the fundamentals of fuzzy logic is given in Appendix A4, a more complete introduction to the ever-expanding field of fuzzy logic and fuzzy rule systems can be found in Dubois and Prade (1980), Bárdossy and Duckstein (1995) or Tanaka (1997).

With the fuzzy approach considered suitable for the task, the approach to allocate each radar image to a rainfall type is described below: Firstly, a set of typical rainfall events was classified by Gysi. Upper and lower bounds and typical mean values for each classification parameter (WAR, 10AR) were also estimated by the expert and are listed in the columns labeled 'Expert' in Table 4.3 and Table 4.4. Then, from the set of test rainfall events, the maximum, minimum and mean of each classification parameter was calculated over the whole duration of each event and are also listed in Table 4.3 and Table 4.4. Based on those data, fuzzy sets to represent the typical parameter range for each rainfall type were established. The wet area ratio for convective cells for example, typically shows values between 0 and 8 and may on rare occasions amount to 15%. Consequently, the fuzzy set for WAR values indicating a radar image dominated by convective cells in Table 4.3 shows a maximum membership of 1 between 0% and 8% and linearly drops to zero at a WAR of 15%. For warm fronts, low values of WAR a quite unlikely, while high values up to full coverage of the radar image are frequent. Therefore, the membership function of WAR values indicating a radar image dominated by the presence of a warm front rises from zero to 1 between WAR values of 0% and 40%, then remains at 1 up to a WAR value of 100%, indicating that WAR values in that range can be equally associated with warm fronts. For reasons of simplicity, only triangular and trapezoidal fuzzy sets were used. Due to computing requirements, each trapezoidal fuzzy set was later replaced by a few triangular fuzzy sets covering the same range.

Rainfall type		Test rainfall events 1	2	3	4	5	6	Expert	Fuzzy set
Convective cells	min	0	0	0	2	0	0	0	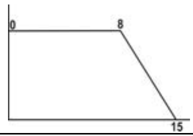
	max	8	6	6	7	4	9	15	
	mean	5	5	2	4	3	6	-	
MCS	min	0	14	28				10	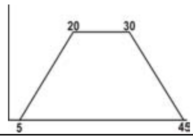
	max	35	46	41				50	
	mean	22	31	34				-	
Cold fronts	min	0	1	16	0			10	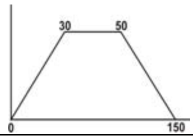
	max	80	74	37	23			50	
	mean	50	33	23	8			-	
Warm fronts	min	59	0	0	0	0	0	25	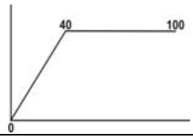
	max	94	88	91	5	47	42	100	
	mean	84	37	63	3	5	16	-	
Shower	min	0	0	0				0	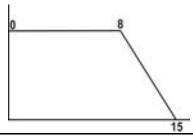
	max	15	8	15				15	
	mean	5	3	7				-	
No rain	min							0	
	max							0	
	mean							0	

Table 4.3: WAR [%] characteristics from test rainfall events and their fuzzy set representation

After establishing the input membership functions for each rainfall type, a system of fuzzy rules covering the whole range of possible input values and all output possibilities, (i.e. each rainfall type) was defined. Here, expert knowledge was again incorporated to establish a reasonable initial rule system for optimization. A fuzzy rule follows in principle the usual scheme IF (criterion) LOGICAL OPERATOR (criterion) .... THEN (consequence). For computing simplicity, only the logical operator 'AND' was used. This does not pose any restrictions, as with the appropriate selection of input fuzzy sets, any logical operation can be represented by a series of 'AND' operations. With the rule system, the answer and the degree of fulfillment (DOF) of each rule in the system could be calculated. Then, the overall rule answer fuzzy set was determined using a suitable algorithm and then defuzzified to the crisp, overall rule system answer. This procedure is described in detail in Appendix A4.

Rainfall type		Test rainfall events 1	2	3	4	5	6	Expert	Fuzzy set
Convective cells	min	8	7	0	11	0	0	10	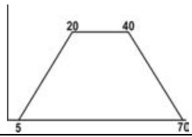
	max	53	33	53	56	39	26	70	
	mean	24	20	39	36	20	11	30	
MCS	min	0	5	7				5	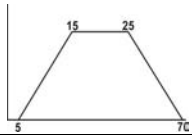
	max	69	37	23				50	
	mean	25	20	17				15	
Cold fronts	min	0	0	0	0			0	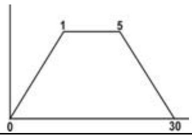
	max	20	23	0	0			25	
	mean	3	5	0	0			5	
Warm fronts	min	0	0	0	0	0	0	0	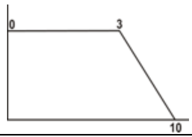
	max	4	4	9	0	2	11	5	
	mean	1	0	2	0	0	1	1	
Showers	min	0	0	0				0	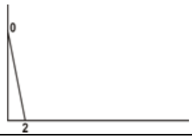
	max	2	0	2				5	
	mean	0	0	2				0	
No rain	min							0	
	max							0	
	mean							0	

Table 4.4: 10AR [%] characteristics from test rainfall events and their fuzzy set representation

For the Goldersbach project, the fuzzy rule optimization program ARASA developed by Bárdossy was applied. It uses fuzzy rules with product inference, weighted sum as rule combination and fuzzy mean for defuzzification. Membership functions of the arguments and the responses can be specified by the user or can be generated by the program using the distribution of the variables in the user specified training data set. Applying ARASA on the training data set which consisted of half of the classified rainfall events described above with the initial rules system from expert knowledge yielded for each time-step a degree of membership for each possible rainfall type. This is superior to a single output assigning exactly one rainfall type to each image: In 'crisp' classification it is unknown whether an image could clearly be associated with a rainfall type or if several rainfall types had similar scores, in fuzzy classification this is known and the radar image can be labeled 'mixed type' or 'ambiguous'. The rule performance was evaluated using a distance measure between observed and calculated values, here the squared and cubed difference between the binary expert classification (one radar image belongs to exactly one rainfall type and has a membership of 1 for this rainfall type, zero for all the others) and the gradual memberships from the rule system classification. Based on the initial rule system and the rule performance expressed by the value of the objective function, the system was optimized with Simulated Annealing using the Metropolis algorithm. The principles of Simulated Annealing as an optimization algorithm are explained in Appendix A1. Here the optimization routine consisted of the following steps: Randomly replace one element of the rule system i.e. replace the membership function for one parameter of one rule by another one from a library of possible membership functions. Calculate the rule system performance over the training data set. If the change resulted in improved performance keep it, if not keep it only with a certain probability that depends on the selected Annealing temperature and the degree of deterioration and decreases throughout the optimization process. Terminate execution when the system has cooled down, i.e. improvement rate is only marginal. Apply the optimized rule system on the validation data set and evaluate the performance.

With the first optimization results it soon became obvious that the best classification was obtained using only WAR and 10AR. IMF, as previously mentioned did not further improve results due to its strong positive correlation with WAR. The incorporation of ANI led in some cases to improvements while worsening others due to its variability and was therefore ignored. In order to find the best rule system, the number of rules was varied from 10 over 12 to 14, the membership functions for all parameters were either predefined (see Table 4.3 and Table 4.4) or automatically chosen by the program to cover the parameter range. Also, some previous system knowledge was added to the rule system optimization by incorporating the WAR and 10AR value of the previous time-step into the set of input parameters. This, however led only to marginal improvement and was therefore not further considered.

4.2.2 Results

From the variety of options tested, the best image to image rainfall type classification was achieved with a system consisting of 14 rules, implying that for each rainfall type several rules exist. A library of 11 and 9 triangular membership functions for WAR and 10AR respectively was used, based on the membership functions obtained from expert knowledge. The output was represented by 6 membership functions in the range of [0,1] and the square difference between expert and fuzzy classification was used as the objective function.

Comparing the two classifications on the validation data set in a contingency table (Table 4.5) indicates a good agreement between the manual and automated classification schemes. From a total of 494 images, 63% were assigned to the same rainfall type and can be found on the main diagonal, while 37% were misclassified. This is a considerably improvement to a completely random classification where on average only one 1/6 or 16% of the images would be properly classified. Taking a closer look at the misclassifications, the largest amount of confusion occurred between cold fronts, warm fronts and showers, with showers being misclassified as cold fronts occurring most frequently. This is somewhat comforting, as even in manual classification it is not always clear when in the course of frontal propagation the transition from frontal to shower type should be made. Also border effects complicate the distinction between warm and cold front or shower types when for example a warm front is entering or leaving the radar image and is therefore only partially visible. A surprisingly low number of convective cells and MCS were misclassified, presumably because their image characteristics are unique.

Expert classification / Fuzzy rule classification	Convective cells	MCS	Cold fronts	Warm fronts	Showers	No rain
Convective cells	**60**	-	6	-	1	-
MCS	-	**33**	9	2	-	-
Cold fronts	5	1	**49**	29	66	-
Warm fronts	-	3	27	**41**	-	-
Showers	1	-	7	13	**97**	-
No rain	1	-	-	2	10	**31**

Table 4.5: Contingency table of expert vs. fuzzy classified radar images with respect to rainfall type. Total number of images classified: 494.

Figure 4.6 provides a slightly different view of the agreements and discrepancies of the two classification schemes. The validation time-series, composed of a series of independent, expert-classified rainfall events is indicated by a line. The sudden transition from one rainfall type to the next where one event was attached to the next is visible as a jump in the line. The fuzzy classification is plotted with dots. Comparing the line and the dots supports the findings from the contingency table: The most obvious misclassifications occurs in the case of showers, but it can be seen that they do not occur completely at random, but with a certain persistence in occurrence and absence. Looking at the radar images of misclassified shower events (not shown here) all featured relatively high shower activity and were optically easy to confuse with a lacerated front.

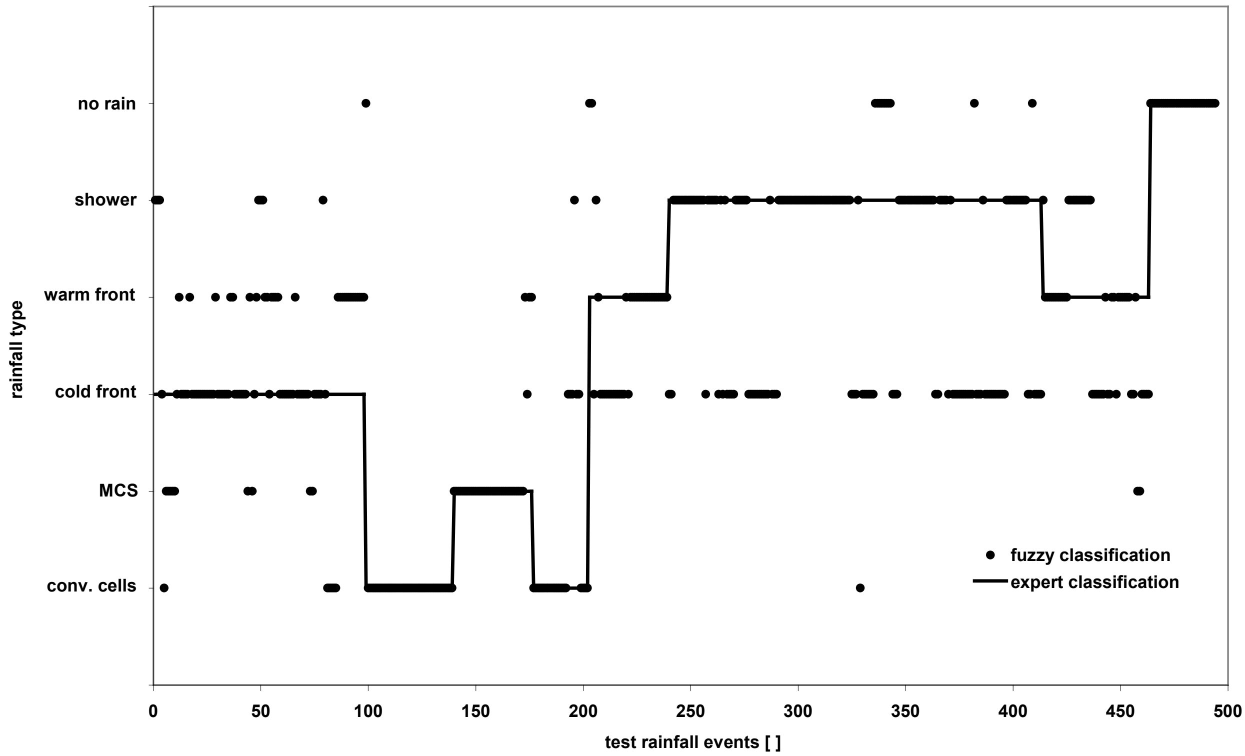

Figure 4.6: Validation time-series of expert vs. fuzzy classified rainfall types

4.3 Conclusions

With the optimized fuzzy rule system presented here, a reasonably reliable classification of individual radar images into 6 meteorological rainfall types is possible. The classification is based on only two parameters, WAR and 10AR which can easily be extracted from a radar image. With the calibration and validation performed only on selected rainfall events combined to artificial time-series it would be desirable to manually classify a long, coherent time-series of radar images and apply the automated fuzzy classification on it to assess its ability to cope with gradual shifts from one rainfall type to the next.

Some further improvement is expected if larger radar images, for example the German Weather Service composite radar image, can be used for classification. On a scale where synoptic features become visible, the additional use of the shape parameters ANI and PHI could be meaningful. This, however, should be accompanied by the introduction of some memory effect such that parameters or classifications in a period of roughly a few hours prior to the current time-step should be incorporated into the classification. Presumably this would lead to a more stable classification but requires further extensive investigations. Additionally the distinction between cold and warm front occurrence could be improved by taking the temporal air temperature gradient observed at the radar site into consideration. In case of a cold front it should be negative, in case of warm air passage it should be positive.

While the results seemed quite promising from a purely meteorological point of view, later investigations with respect to the desired goal of the rainfall type classification, namely the selection of appropriate variograms for rainfall interpolation (see chapter 6) and the type-dependent selection of auto-regressive parameters for forecasting as described in chapter 7 revealed the fact that the classification was too refined. The variograms and auto-regressive parameters did not show large differences between some of the rainfall types, a cruder classification was sufficient. This experience was probably shared by some of the researchers quoted in the introduction to this chapter, who pursued the bottom up approach to classify radar images according to distinctive properties useful in rainfall forecasting and usually restricted their sub-division to three major types.

With this in mind, it was decided to also pool the rainfall types into larger sets of super-ordinate rainfall types which would be more meaningful for short-term rainfall forecasting. Firstly, the long-lived, widespread rainfall type with an isotropic, long-range variogram and high temporal auto-correlation was introduced. Then, in contrast to that, a second type of shorter-lived events with low coverage, a short range variogram and low temporal auto-correlation. For intermediate cases, a mean or mixed type was defined and finally the simple no rain case. In fact, this simple sub-division could be done solely by the value of WAR. Values exceeding 0.5 indicated the widespread rainfall type, values below 0.1 convective types, any values in-between are considered mixed types. In all further investigations, this simple division was used and proved useful.

5 Advection estimation and forecasting using Radar

The evolution of rainfall over a given point in space can be regarded as a combination of two processes: The temporal evolution or 'life-cycle' of a rain-field and the displacement of the rain-field in space, stemming from its movement. Especially in the case of pronounced advection, a reasonable estimate of the advection vector can significantly improve the rainfall forecast over small areas. If the life-cycle of the rain-fields is neglected, the assumption of 'frozen field advection' as stated in Taylor's hypothesis (Taylor, 1935) can be used for the development of simple rainfall forecasting schemes. Taylor's hypothesis implies that the correlation of a moving field in time is equivalent to that in space if time is transformed to space in the mean direction of storm movement. Taylor's hypothesis is applicable in translating processes with relatively weak time-dependence within a moving coordinate system shifted with the mean advection vector. Onof et al. (1996) found that Taylor's hypothesis holds for rain-fields up to ~ 40 minutes, but is dependent on the mean life cycle of the element regarded (cell or larger-scale structure).

Since Taylor, much work has been done in the field of advection estimation, especially fuelled by the widespread and operational use of weather radar systems. Approaches range from the estimation of the image mean field advection using the Doppler effect observed from the emitted and back-scattered radar pulse to advection estimation by maximizing the inter-image covariance through variation of the advection vector.

Whereas previously, due to computer processing constraints, mainly mean field vectors constant over the whole range of the radar image were calculated, research now shifted to a spatially detailed description of the wind field due to the topography-atmosphere interaction and the incorporation of rotation and shear of the wind field. So far, this has been done with encouraging results, however it has been found that increased complexity of the wind field does not necessarily add to its quality. In a study of the improvement in forecasting resulting from higher order extrapolation procedures, Tsonis and Austin (1981) found negligible improvement of skill even in elaborate non-linear extrapolation schemes. Indeed, many such schemes gave much worse results than linear position extrapolation.

Comparing various methods of wind field estimation, Kitano et al. (2001) reported that the field averaged wind velocity provided by a Doppler weather radar using the VVP (Volume Velocity Processing) method proved suitable to short term rainfall forecasting and outperformed field advection vectors from a pattern matching algorithm. Seed (2001) compared two displacement schemes for rain-field advection: the first method assumed a single field displacement vector derived by a pattern-matching algorithm to maximize inter-image correlation. The second derives a field of displacement vectors thereby allowing for rotation and shear along with linear displacement. Especially in the case of complex advection patterns, the simple advection scheme was outperformed by the spatially distributed approach. Sugimoto et al. (2001a) estimated the horizontal wind and divergence pattern using a volume of radial velocity data collected with a single Doppler radar. The goal was to retrieve a mesoscale (20 - 200 km) wind field based on the Extended Volume Velocity Processing (EVVP) method. While the classical VVP assumes spatial linearity of the true wind field, most orographic and convective storms are accompanied by a non-linear wind field. The EVVP was shown to be adequate to allow spatially highly resolved wind fields, with divergence and convergence zones that provide better precipitation nowcasting results than an assumed uniform wind field for the whole radar image.

With the requirements of an operational rainfall forecasting system in mind, namely robustness and redundancy, two independent wind field estimation schemes were investigated in this project. Firstly, the files containing the radar data also included in the header the mean field advection vector derived from Doppler analysis, secondly an estimation scheme based on covariance maximization was developed. Briefly summarized, it was found that both methods provided similar results and could therefore be used alternatively. For the sake of simplicity and computational speed, only mean field vectors were calculated.

Finally, based on the wind field estimates, a short-term forecast scheme based on an auto-regressive process was developed to forecast the wind field to a horizon of about two hours. All investigations were performed on a 13 month data set of radar images from 01.03.00 – 30.03.01.

5.1 Advection estimation

5.1.1 Advection estimation using the Doppler effect

Each radar image provided by the IMK included the angle and velocity of the mean rain-field displacement vector estimated at an elevation of 800 - 1500 above ground in a range of 50 km around the radar site. Applying the Doppler principle for the estimation of the rain-field displacement vector can provide different results according to the elevation range the data are sampled in. In a sensitivity analysis on the influence of elevation when estimating displacement vectors, performed with wind data from May to September 2001 it showed that between the original elevation and a new elevation of 1300 – 3200 above ground in the same range a mean velocity difference of 2.8 m/s along with a mean directional difference of 33.4 ° occurred. At higher elevations, the decreasing influence of topography results in stronger wind in more westerly directions, approaching the geostrophic wind direction. Another aspect of the Doppler-derived wind estimate worth mentioning is that it was not always available and therefore, despite the good quality of the wind estimate, alternative techniques were necessary.

For easier handling, the original data were transformed to shifting vectors in East-West direction, indicated DX, positive for vectors from West to East and North-South direction, indicated DY, positive for displacement vectors from North to South. The values of both directions are approximately normally distributed, as shown in Figure 5.1, ordered around a mean of 1837 m/10 min in easterly direction and 6378 m/10 min in southerly direction. Therefore, the usual wind direction is Northwest. The standard deviations are 3837 m/10 min and 4674 m/10 min for East-West and North-South directions, respectively. The two distributions are only weakly positively correlated, with a correlation coefficient of 0.21, consequently, for later forecasting purposes, the two quantities were treated separately.

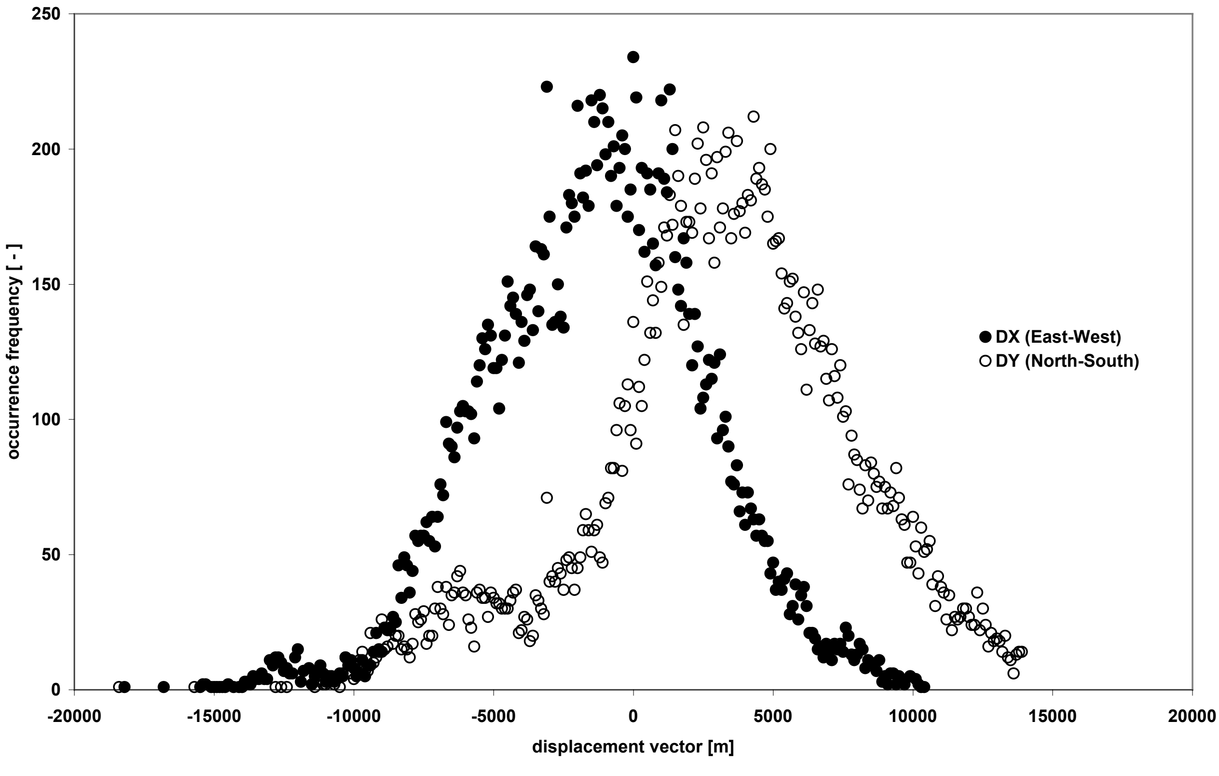

Figure 5.1: Binned occurrence frequencies of wind displacement vectors DX, DY from Doppler analysis, March 2001. Bin width: 100 m/10 min

Although the Doppler wind estimate in general was in good agreement with the displacement inferred from visual radar image inspection and features high auto-correlation, the following plausibility tests were performed

- Reject clear-air echo wind estimates from radar images without rain (WAR = 0).
- Reject wind estimates with a differential angle change from the previous to the current image larger than 45°.
- Reject wind estimates with a differential velocity change from the previous to the current image larger than 10 m/s.

Further information about the quality of the Doppler wind estimates in comparison to the covariance maximization scheme are given in section 5.1.3.

5.1.2 Advection estimation using Covariance maximization and Simulated Annealing

As previously mentioned, due to problems in the radar data processing the Doppler wind estimates were not always available and at times contained unrealistic results. As an alternative, a simple yet fast scheme based on the maximization of inter-image covariance was developed. In conventional notation, the covariance between two radar images described by two matrices **M** and **N,** shifted in their relative position by the advection vector (u,v) is calculated according to (5.1).

$$\mathrm{COV}(\mathbf{M},\mathbf{N},u,v) = \frac{1}{(U \cdot V) - 1} \sum_{j=1}^{U} \sum_{k=1}^{V} \left(\mathbf{M}_{j,k} - \bar{\mathbf{M}}\right) \cdot \left(\mathbf{N}_{j+u,k+v} - \bar{\mathbf{N}}\right) \tag{5.1}$$

where:

COV(**M,N**,u,v)	[$mm^2/10\ min^2$]	2-dimensional covariance between images **M, N**, shifted by (u,v)
U	[-]	size of a radar image in the first dimension
V	[-]	size of a radar image in the second dimension
M, **N**	[mm/h]	matrices of radar rainfall intensities
$\bar{\mathbf{M}}$, $\bar{\mathbf{N}}$	[mm/h]	mean matrix rainfall intensities

Applying different shifting vectors in the X- and Y-direction to represent the rain-field displacement in time between the two image 'snapshots', one will ultimately find the vector resulting in the maximum inter-image covariance which can be regarded as the best estimate of the mean field advection vector. Although straightforward, this is extremely time-consuming if one bears in mind that a radar image consists of 122500 pixels and a possible range of shifting vectors from –100 to 100 m/s would require 40000 covariance calculations for each image pair. To mitigate this problem, several steps were taken. Firstly, the covariance calculation was performed on the Fourier-transformed data, which greatly reduced calculation time. For further information, refer to

Appendix A3. Secondly, starting with the last plausible and verified wind information as an initial estimate (for plausibility tests and verification, see section 5.1.3), Simulated Annealing was used. While other techniques such as gradient methods suffer from the risk of converging to local minima in the objective function field, Annealing accepts negative changes in the objective function with continuously decreasing probability. The Annealing algorithm is explained in detail in Appendix A1. For wind optimization, an initial temperature of 0.083 with a temperature decrease rate of 0.77 was found to provide the fastest converging algorithm. That means that at the beginning, a deterioration of the objective function of 0.1 is accepted with 30% probability, at the end a deterioration of only 0.01 is also accepted with 30% probability. The initial displacement vector range around the initial estimate was set to 50 pixels and a range decrease rate of 0.77, consequently the range cools to 3 pixel at the end of the optimization. It was found that a constant number of 100 iteration steps resulted in stable i.e. repeatable vector estimates in an acceptable time.

In general, the algorithm worked very well, especially in cases of pronounced rainfall in the radar images and the estimates coincided well with the Doppler wind information. For cases of low rainfall coverage or rain-fields entering the image, however, gross errors occurred at times. Therefore, a combined wind estimation procedure was developed to jointly use both sources of information as described in the next chapter.

5.1.3 Combined advection estimation

As the true mean wind field is neither known nor observable and consequently validation of a wind estimation method against it is not possible, the best criterion (apart from visual intercomparison of observed and calculated rain-field displacements in radar images) to assess the quality of the two wind estimation techniques is to consider their relative differences. Also, if the two methods should be used alternatively in operational forecast, it is important to draw similar results from both methods to ensure continuity in the wind forecast. For reasons of simplicity, the term 'root mean square error' in this chapter is used for the root of the mean squared deviations between the two estimation methods and not, as usual, for a measure of deviation between an observed, 'true' quantity and a simulated approximation.

Comparing the two advection estimation methods revealed several points. Both methods usually agree well when the inter-image covariance of both the Doppler and the Annealing wind vector estimation exceed a value of 0.5. This can clearly be seen in Figure 5.2. Below the reference covariance (here arbitrarily chosen to be that of the Annealing wind estimate) of 0.5, the difference between wind vectors in the X-direction from the Doppler and Annealing method show a large scatter, beyond 0.5 the differences narrow significantly, the same also applies for DY (not shown). Figure 5.3 points in the same direction: Again plotted against the Annealing covariance are the root mean square errors of the DX- and DY-shifting vectors between the two estimation methods. The smaller the error, the more similar are the advection estimates of the two methods. This does not evaluate the quality of either technique in comparison to real observations, only the comparability of the estimation methods .In addition, the root mean square error of the estimation covariances of the two methods is plotted. The estimation covariance can be regarded as a 'goodness-of-estimation' indicator, the root mean square error of the two estimation covariances as before indicates the comparability or non-comparability of the two estimation methods. Again, beyond the threshold of 0.5 the wind estimate errors of both methods have reached a lower limit of about 10 pixels or 5000 m, below 0.5 large errors occur. The same applies for the mutual quality criterion, the root mean square error of covariances. Furthermore, the cumulative displacement vectors of the two methods, literally seen as the course of a virtual balloon are shown in Figure 5.4. In general, both methods agree quite well, however the course of the 'Doppler balloon' is very smooth, while those of the 'Annealing balloon' shows at times sudden changes in its course. Regarding the plotted covariance values of the Annealing estimates, it is obvious that the jumps occurred always at times of very low covariance (indicated by oval areas). Consequently, wind estimates of the Annealing as well as the Doppler method should be rejected when showing only small covariances.

In conclusion, the following procedure for combined wind estimation was established:

- On all wind estimates, both Doppler and Annealing derived, perform a plausibility control and verification. Data are plausible when the wind velocity is within [0,100] m/s and the wind angle is in the range of [0, 360] °. Data are verified when the differential angle change from the previous to the current image is ≤ 45° , the velocity change is ≤ 10 m/s and the covariance ≥ 0.5. Data can only be verified with previous images that are also verified.
- If available and verified, use Doppler data to avoid time-consuming Annealing optimization, otherwise estimate wind with Annealing.
- For forecasting purposes, only use plausible and valid data. If not available (poor wind estimate of the previous wind fields), use the latest plausible and valid data. Due to the high auto-correlation of wind, this provides a better result than new, but poor estimates).

In the case shown in Figure 5.4, the final wind estimate is exactly equal to the series of the doppler wind estimate, as there were always plausible and valid doppler wind estimates available (a lucky case).

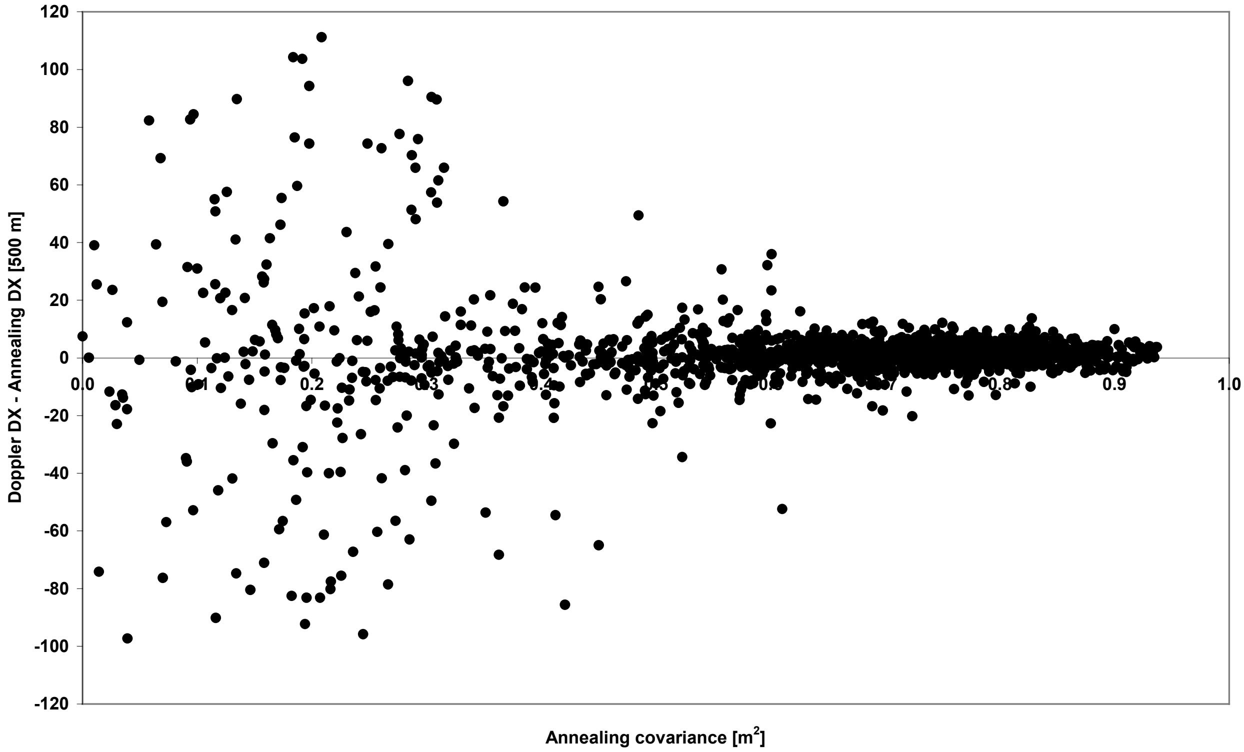

Figure 5.2: Differences of Doppler and Annealing X-direction wind estimation vs. Annealing covariance from 01. – 31.03.01

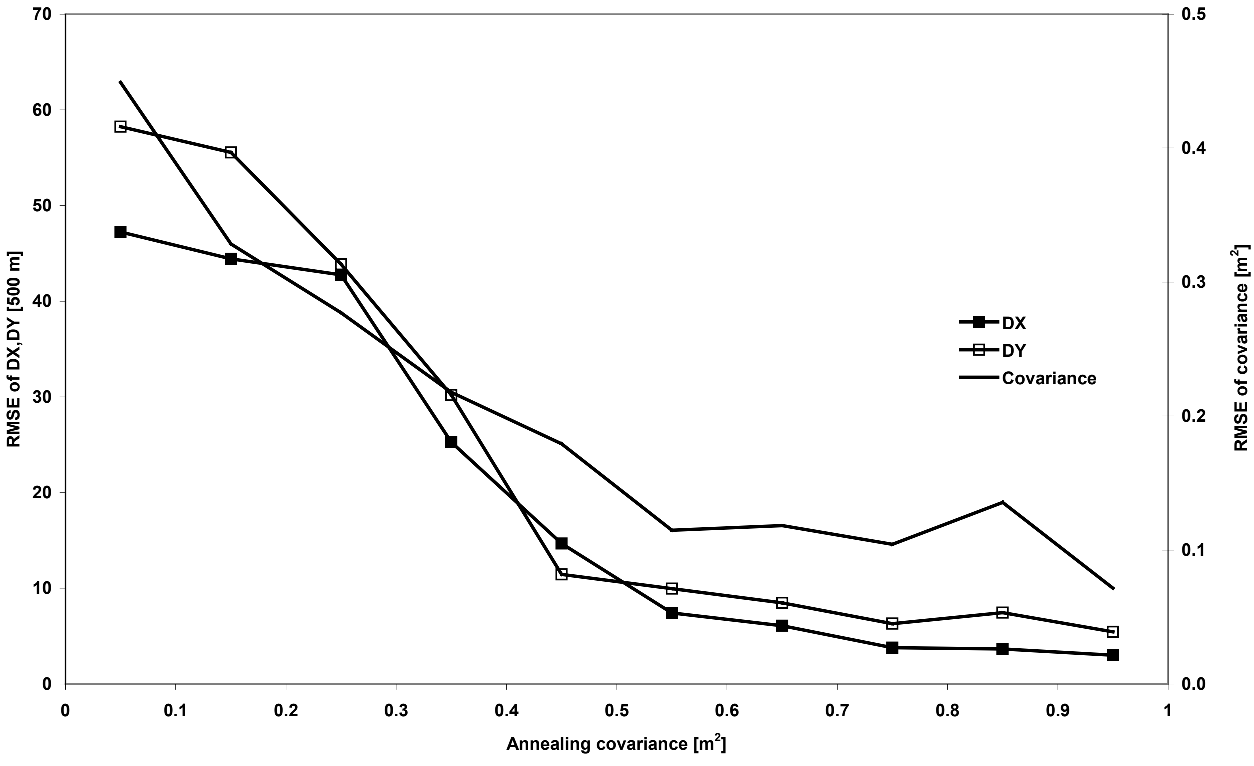

Figure 5.3: RMSE of Doppler DX and Annealing DX, Doppler DY and Annealing DY, Doppler covariance and Annealing covariance vs. Annealing covariance from 01. – 31.03.01

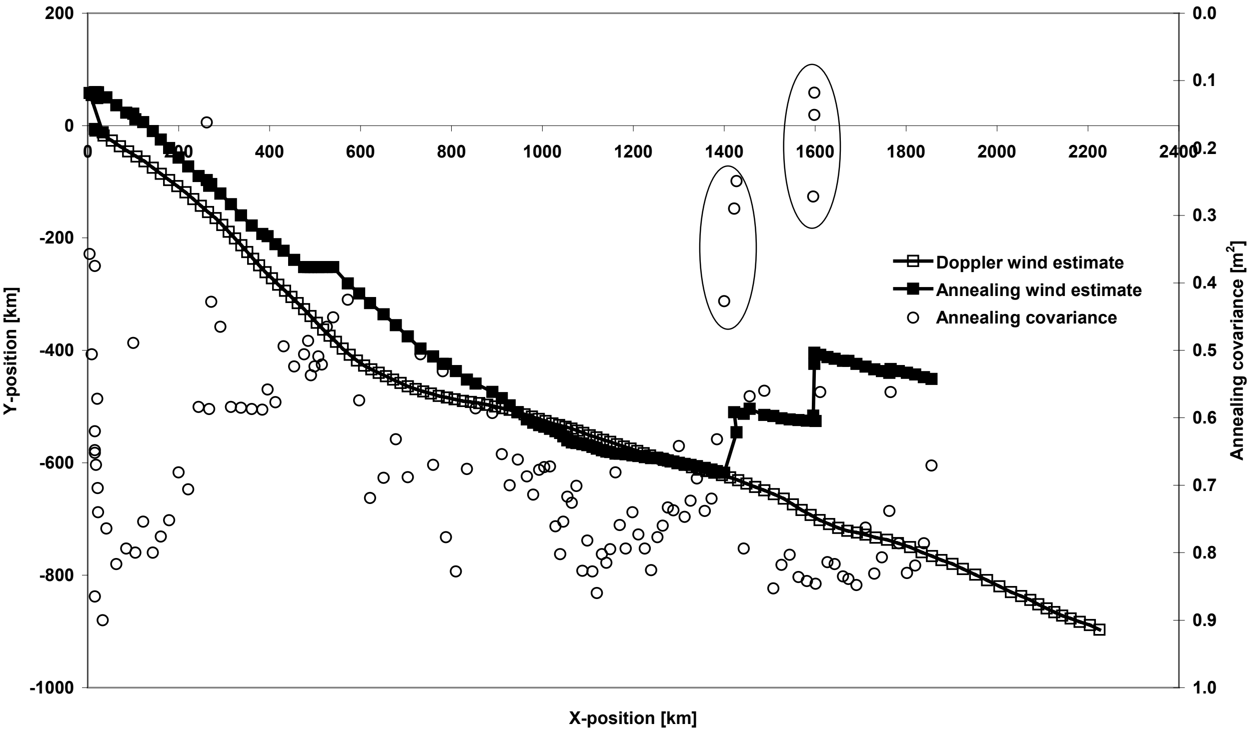

Figure 5.4: Cumulative wind displacements using the Doppler and Annealing wind information and Annealing inter-image covariance from 12.03.01 08:00 – 13.03.01 05:10

5.2 Advection forecast

With a reasonably reliable source of wind estimates in real time as described in section 5.1, the second step was to forecast or rather nowcast the mean wind field for the desired forecast horizon. With the low correlation of the displacement vectors in the X-direction and Y-direction, a simple auto-regressive scheme for each direction individually was applied instead of a multi-variate process. The underlying assumption of an auto-regressive process is stationarity, i.e. the series mean μ is assumed to be the same for each interval of the series. As shall be seen in the conclusions at the end of this chapter, this assumption in combination with the high auto-correlation of the observed wind field lead to a marginally worse forecast performance of various AR(k)-processes than a simple extrapolation of the last observation into the future (persistence).

The general auto-regressive model of order k, or AR(k) model, is

$$x_{t+1} = \overline{x} + \sum_{i=1}^{k} \phi_k \bullet (x_{t-i+1} - \overline{x}) + \varepsilon_{t+1} \tag{5.2}$$

where:

k	order of the auto-regressive process
x_{t+1}	forecast of x at time-step t+1
ϕ_k	lag-k auto-regressive parameter
$\overline{x}$	mean of series x
ε_{t+1}	random component at time-step t+1

The anomaly for the next time point, x_{t+1} - $\overline{x}$ is a weighted average of the previous k anomalies plus a random component ε_{t+1}, where the weights are the auto-regressive coefficients ϕ_k. Estimation of the k auto-regressive parameters is most easily done using the set of equations relating them to the auto-correlation function as calculated in (5.3), which are known as the Yule-Walker equations. These are given in (5.4).

$$r_k = \frac{\sum_{t=1}^{T} \left[(x_i - \overline{x}) \bullet (x_{t+k} - \overline{x}) \right]}{\sum_{t=1}^{T} (x_i - \overline{x})^2} \tag{5.3}$$

where:

r_k	[-]	lag-k auto-correlation
T	[h]	length of the time-series

$$\begin{array}{ccccccccc} r_1 & = & \phi_1 & + & \phi_2 r_1 & + & \cdots & + & \phi_k r_{k-1} \\ r_2 & = & \phi_1 r_1 & + & \phi_2 & + & \cdots & + & \phi_k r_{k-2} \\ \vdots & & \vdots & & \vdots & & & & \vdots \\ r_k & = & \phi_1 r_{k-1} & + & \phi_1 r_{k-2} & + & \cdots & + & \phi_k \end{array} \tag{5.4}$$

The ε values are mutually independent, with zero mean and variance σ^2_ε. Generally it is assumed that ε follows a Gaussian distribution. A simple approach for estimating σ^2_ε is to estimate ϕ_k using (5.4), compute the time-series ε_{t+1} from the data rearranging (5.2) and then to compute the ordinary sample variance of these ε values.

In order for the stationarity assumption to be true, the auto-regressive parameter of a AR(1) process must satisfy $-1 \leq \phi \leq 1$ (Bras and Rodriguez-Iturbe, 1993). For an AR(2)-process to be stationary, its two parameters must satisfy the constraints

$$\begin{aligned} &\phi_1 + \phi_2 < 1 \\ &\phi_2 - \phi_1 < 1 \\ &-1 < \phi_2 < 1 \end{aligned} \tag{5.5}$$

From the 13-month series of wind estimates used, only those periods were selected where at least 6 consecutive values were available to calculate the auto-regressive parameters for both the X-direction and Y-direction as given in Table 5.1. The very high values of ϕ_1, regardless of the order of the process indicates that the mean radar image advection in the temporal resolution of 10 minutes is highly temporally correlated, almost all of the series history information is contained in the previous value. Also, for the AR(1)-and AR(2)-process, the constraints according to (5.5) are fulfilled, and they can be regarded as stationary.

AR( ) -order	1		2		3		5	
	DX	DY	DX	DY	DX	DY	DX	DY
Φ_1	0.953	0.962	0.859	0.888	0.856	0.887	0.856	0.887
Φ_2			0.098	0.076	0.072	0.063	0.071	0.062
Φ_3					0.029	0.015	0.019	-0.001
Φ_4							0.012	0.009
Φ_5							-0.001	0.009

Table 5.1: Auto-regressive parameters for DX- DY-forecasts of different order 01.03.00 – 30.03.01

With a range of models to choose from, the question arises which model is best suited to the data. From the literature, the optimal order of an auto-regressive model can be chosen by minimizing the Corrected Akaike Information Criterion (Hurvich and Tsai, 1989) which is defined as

$$\begin{aligned} &AIC_C = T \log\left(\frac{SE}{T}\right) + \frac{T(T+k)}{T-k-2} \\ &SE = \sum_{t=1}^{T} E_i^2 \end{aligned} \tag{5.6}$$

where:

AIC_C	corrected Akaike information criterion
T	length of time-series
k	order of the AR(k)-process
E_i	error between observed and AR(k)-modelled values
SE	sum of squared errors ε_i over the series

Obviously, the higher the order of a process, i.e. the more information it requires, the higher AIC_C will be if all other values remain constant. The AIC_C therefore allows to balance an increased model performance against the increase in information necessary for it.

According to the information criteria calculated for each AR(k)-process and a simple persistence scheme with an assumed process order of 0 as given in Table 5.2, the AR(5)-process performs best and should therefore be selected. It should be borne in mind, however, that the AIC_C is based on the forecast one step ahead only and different conclusions might be drawn if several forecast time-steps are considered.

AR( )-order	Persistence	AR(1)	AR(2)	AR(3)	AR(5)
AIC_C DX	89639	89790	86016	82939	77255
AIC_C DY	88561	88839	85139	82047	76238

Table 5.2: Corrected Akaike Information Criterion for Persistence and different order AR-models from 01.03.00 – 30.03.01

In Figure 5.5, the RMSE of observed wind displacement vectors in the X-direction and forecasts for different models and different lead times are plotted and quite an opposite impression is given. Note that the forecast is a mean forecast, neglecting the random shock term of the process. While the forecast performance at lag –1 also favors the AR(5)-process, the simple persistence scheme outperforms the others with an increasing forecast horizon. This may seem astonishing at first glance, but can be explained by the non-stationary properties of wind for periods in the hour to day range compared to annual means. While the annual mean of the wind field will remain constant over several years, the mean wind regime over a few days or hours may significantly differ from this mean. The persistence forecast remains unaffected by this, keeping the last value of the actual wind regime, while all the auto-regressive models are drawn towards the long-term mean. The same behavior and similar forecast performance was observed for the forecast in the Y-direction.

In conclusion, for the time being, the wind forecast is performed with simple persistence. Alternatively, AR( )-processes of higher order or methods to include the current mean wind field like ARMA models have some potential to improve the forecast. Then the random forecast component can also be included and, instead of a single forecast for each time-step, scenarios of forecasts could be calculated. Further investigations are needed here.

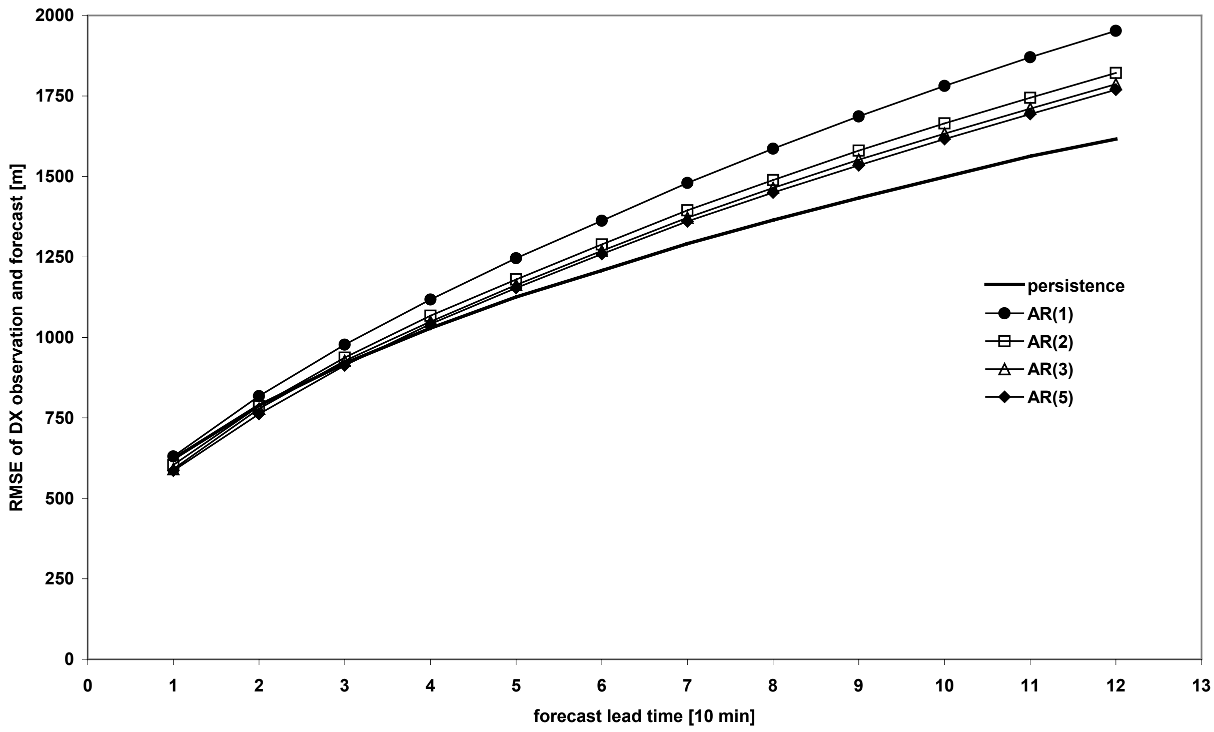

Figure 5.5: RMSE of wind forecast in the X-direction from 01.03.00 – 30.03.01

6 Spatial rainfall estimation

Rainfall is a temporally and spatially highly heterogeneous process. This is a simple truth, however it has been neglected in hydrology for a long time, mainly because no possibility existed to observe this heterogeneity, which in turn was partly due to the lack of appropriate models and computing power to represent it in rainfall-runoff modeling.

Before the introduction of weather radar to hydrological purposes, the best spatial estimate of rainfall possible was the interpolation of point rainfall observations from rain-gauges which resulted in a more or less smooth field of rainfall. This was particularly unfortunate as rainfall measurement and forecast was identified as the dominating source of error in flood forecasting (Moore, 1996).

With the introduction of weather radar, especially the understanding of spatial rainfall behavior, took a quantum leap, triggering a multitude of new rainfall modeling approaches. It seemed to be a logical and straightforward thing to do then to join the advantages of both measurement sources, rain-gauge and radar. The long-used and trusted rain-gauge observations were considered as the 'ground truth', while the spatial information contained in a radar image was regarded as being superior to an interpolated rain-gauge field.

Unfortunately, for several reasons the task proved to be not as straightforward as one would have liked: Firstly, rain-gauges are not as accurate as commonly believed. Wilson and Brandes (1979) reported that the undercatch in strong thunderstorms can amount to as much as 20 - 40%. This undercatch by the rain-gauges may explain the general trend in the data of smaller storms experiencing more under-estimation by radar relative to gauge accumulation. Also, in more recent times, Smith et al. (1996) reported on the same issue that the differences between radar and rain-gauge observations due to random and systematic errors can amount to 100% and more. Clearly, errors of that order of magnitude cannot be accounted for by simple adjustment techniques. But not only the rain-gauge observations are subject to error, as already described in section 2.3.1, radar observations suffer from a multitude of random and systematic errors that are difficult to quantify and reduce.

Secondly, a major source of discrepancies between radar and rain-gauge stems from the different spatio-temporal sampling properties. Rain-gauges measure ground precipitation at one point in space, while radar measures volumetric rainfall in the atmosphere at an altitude depending on the radar tilt and the distance from the radar.

Those large differences of the spatial resolution between rain-gauge and radar measurements prevent any straightforward comparison of the observed quantities. In a fair number of cases, e.g. low-level storms, radar can miss the rainfall event observed by rain-gauges altogether due to beam overshooting. In an effort to quantify the error from the different sampled quantities, Ciach and Krajewski (1999) and Ciach et al. (2001) assumed that the radar-rain-gauge difference variance can be explained by two independent causes: the error of the radar area-averaged rainfall estimate and the area-point error originating from the resolution difference. A procedure to decompose these components was proposed. The results show that the area-point component is a dominant part of the radar-rain-gauge difference over short time-scales and remains significant in accumulation times of up to 4 days.

With an awareness of these problems, the question is how radar and rain-gauge data can be compared or used in combination at all. Under the simplifying assumption that the two devices sample from the same physical quantity, the minimum rain-gauge network density for acceptable comparison was and is frequently investigated. In an assessment of mean areal rainfall over watersheds from radar and rain-gauge networks, the German Weather Service (DWD, 2000) found that in case of rain-gauge network densities equal or lower than the catchment size, radar always provides better results. For watersheds larger than approximately 1000 km^2, high radar resolution does not perform better than rain-gauge network interpolation due to the smoothing effect of the catchment.

Vieux et al. (2001) report that the number of rain-gauges necessary to calibrate radar data depends on the storm depth and the accuracy desired. For the Illinois river basin (2400 km^2), ten gauges achieved an accuracy within ±15% margin of error for storm depths of about 40-60 mm.

Despite the problems outlined above, many techniques to jointly use both data sources and combine their advantages have been developed, from simple to more sophisticated methods. They can be broadly classified into four classes: simple multiplicative adjustment of the radar data, geostatistical approaches, techniques to reduce radar-specific errors with the help of rain-gauge data and other approaches.

Multiplicative adjustments are the simplest and oldest combination techniques and are, especially in operational flood-forecasting purposes the most widely used. Despite their crude simplifications, they usually provide satisfying results if the rain-gauge network density is sufficiently high and the requirements with respect to spatial and temporal resolution are not too high. Collier (1986) adjusted hourly C-band radar rainfall data in a range of 75 km by 5 rain-gauges and multiplicative 1-hour correction. He found that this significantly improved rainfall estimates at other rain-gauge sites. The procedure was found to reduce both bias and random error to a degree dependent on the actual rainfall type; more for frontal rainfall with or without Bright Band effects, less for convective rainfall. Moore et al. (1994b) pursued a similar attempt with rain-gauge data from 30 rain-gauges and a network density of 120 km^2 per gauge. They applied a mean correction factor over all gauges and alternatively gauge-specific correction factors which were then interpolated. The overall improvement against uncalibrated radar was 22%. If only convective events were considered, the improvement reduced to 11.5%, considering only stratiform cases improved the result by 35%. In further work, Moore (1996) used the cross-validation technique to show that the increase of network density does not lead to a proportional reduction of estimation error. Increasing the number of stations to 40 in the above catchment only led to a marginal improvement. Also, he found that the calibration quality is event dependent and that the error increases with rainfall intensity. The German Weather Service (DWD, 1998) also uses a multiplicative adjustment of daily radar data sums, interpolating the gauge-specific adjustment factor by inverse distance interpolation, although it is known that the correction factors sometimes are much too large, especially in low-rain cases. Last but not least, Seo and Breidenbach (2001) proposed a procedure to real-time correct radar-rainfall estimates with a radar-rain-gauge ratio multiplier. The estimation procedure is solved via a variant of exponential smoothing. The procedure yields the unbiased minimum-error-variance solution under inclusion of a memory span of observations. This memory span is variable. It was found that the method was superior to a simple mean field bias correction.

The second group, geostatistical methods were developed to account for the different sampling properties of radar and rain-gauge, whereas the multiplicative methods were usually developed in the operational flood-forecast context. Krajewski (1987) developed a Co-kriging model to combine radar and gauge data. This implied the assumptions that the rainfall field is second-order stationary and has ergodic properties and that the rain-gauge errors are random, uncorrelated in time and have zero mean. Despite these assumptions, the method can be regarded as superior to simple multiplicative adjustments as it accounts for the different sampling techniques of the data. It is also worth mentioning that the rain-gauge data were block-kriged on the radar grid and then co-kriged with the radar data that were also kriged by surrounding grid values to account for the different sampling spaces. Seo et al. (1990a, b) used Universal Kriging to combine radar and rain-gauge data, Goovaerts (1999) conducted an extensive cross-validation comparison of different rainfall interpolation techniques using rain-gauge data and a digital elevation model. The methods evaluated were the Thiessen polygon, Inverse square distance, non-linear regression with elevation and rainfall, Simple Kriging, Ordinary Kriging with varying local mean, External-Drift Kriging and Co-kriging. Here, advanced Kriging techniques outperformed other techniques, making use of the spatial correlation of rainfall and the correlation of rainfall and elevation applying Co-kriging. Co-kriging turned out to be the most demanding method as several semi-variograms had to be inferred and jointly modelled, however the additional complexity did not pay off in the form of better results compared to simpler Kriging techniques.

Rain-gauge data were not only used directly for the adjustment of radar data but also provided insight into radar-inherent errors. As a consequence, further development in radar technology led to improved radar rainfall estimates. Borga et al. (1997) split radar bias in two categories: A range-dependent and mean field bias. The range-dependent bias was corrected using the radar's vertical reflectivity profile while the mean field bias was corrected multiplicatively using rain-gauge data. Following the same approach, Hossain et al. (2001) adjusted radar data for a range dependent mean field bias. This significantly improved the radar rainfall estimate and as a consequence rainfall-runoff modeling accuracy. In terms of runoff volume, the reduction in uncertainty with bias adjustment ranged from 2% to 40%, for time to peak from 4% and 20% and for the peak runoff it was about 44%. Suffering like Borga from strong, range-dependent radar rainfall errors in mountainous regions, Gabella et al. (2001) developed a radar rainfall estimation technique where the observed variability of the radar to rain-gauge measurement ratio is accounted for by using a weights multiple regression as a function of three independent variables: the distance from the radar, the ground elevation above sea level and the minimum height a meteorological target must reach to be visible on the radar. The technique was applied to an alpine region using one C-band radar and 44 rain-gauges and reduced the resulting mean error from radar under-estimation from 27.7 mm to 13.9 mm.

Also trying to mitigate radar rainfall under-estimation at far ranges, DWD (2001) applied rainfall type dependent Z-R-relations. Despite some improvement, radar adjustment with rain-gauge observations was still much more effective than applying only type-dependent Z-R-relations without consideration of rain-gauge observations.

Apart from the methods presented above, a multitude of other, unconventional methods to combine radar and rain-gauge data have been developed. It is impossible to give an exhaustive overview here, but some interesting approaches will be briefly discussed. Matsoukas and Islam (1999) developed an alternative radar rain-gauge fusion methodology, based on Artificial Neural Networks (ANN). Unlike other techniques such as multi-variate analysis that fails to account for the different sampling characteristics of the two sensors and also for that what is measured by each sensor does not correspond to the same physical quantity or Co-kriging where second-order stationarity and ergodicity must be assumed or estimation techniques such as Kalman filtering that have to assume known error characteristics, ANN's are model free estimators which do not imply any conceptualizations. The input for the neural network are radar pixel and rain-gauge values and their respective coordinates. The network training was then performed in two steps, first on the radar data, then with the same weights on the rain-gauge data, thus the rain-gauge data were preserved at gauge locations. The procedure outperformed Co-kriging and provides a more robust estimate of rainfall at ungauged sites.

Another interesting approach that accounts for the different sampling characteristics of radar and rain-gauge is the window probability matching method (WPMM) used for spatial rainfall estimation by Amitai et al. (2001). They compared rainfall intensity distributions from rain-gauges, radar and satellite observations calculating probability density functions and equalized them by adjusting A and B in the Z-R-relation. Finally, Kun et al. (2001) proposed a new method to improve radar data with rain-gauge observations combining Kalman filtering and variational analysis in a self-adaptive way to estimate the system noise variance and the observation noise variance.

With the abundance of possibilities to combine radar and rain-gauge data outlined above only fragmentary, the main aim of the work presented in the following chapters was to apply, evaluate and compare a selection of existing procedures to the rainfall observations available in the Goldersbach catchment. For reasons of generality, standard procedures such as constant Z-R-relations as well as multiplicative and Z-R-relation updating techniques were applied along with geostatistical methods such as Kriging using only rain-gauge values and External-Drift Kriging joining radar and rain-gauge values. Furthermore, a method to merge radar and rain-gauge observations by exploiting their particular advantages was developed and could be shown to outperform the other approaches. All of those methods will be explained in detail after some preliminary data analysis and the introduction of the test statistics used for intercomparison. After the individual method assessment, a multi-objective decision approach is used to intercompare the method performances over a range of events, rainfall intensities and weights assigned to the different statistics.

6.1 Preliminary data analysis

For the analysis, data from 5 rain-gauges with 30-minute sums, 2 rain-gauges with 10-minute sums, 1 disdrometer with 10-minute sums and radar data with 10-minute sums from 15.12.00 - 03.10.01 were available. Unless stated otherwise, the radar data were transformed to rainfall intensity using a standard Z-R-relation with A = 300 and B = 1.5. The rain-gauges are distributed over an area of roughly 2500 km^2, resulting in an average gauge density 1 per 300 km^2. In the Goldersbach catchment itself, however, the gauge density is much higher with 3 gauges per 75 km^2 or 1 per 25 km^2.

Comparing the rain-gauge and radar data revealed a soberingly high number of discrepancies as shown in Table 6.1 for station NNAG, which is also reflected in the low value of the Spearman rank-correlation coefficient of 0.54 over all data excluding the times with mutual zero rainfall observation. The rank-correlation was calculated rather than the standard Pearson correlation coefficient due to the highly skewed distribution of rainfall intensities. Listed are all instances where either the radar or the rain-gauge observed no rain while the other did and the instances of mutual non-zero measurements. The vast majority of the time, where both devices observed zero rainfall, were excluded. The number of observations is given as a percentage of all observations considered, the sums are given as a percentage of the observed rain-gauge sum. The most noticeable observation is the extremely high number of zero radar, non-zero rain-gauge observations, which amounts to 54.9% of the observations and 22.2% of the rainfall sum. The opposite case is comparatively rare and amounts to only 4.6% and 2.8% of the rainfall sum.

Bearing in mind that the rainfall sum from radar over the whole 10-month data set, averaged over the stations was 578.4 mm, the mean rain-gauge observation in the same period was 727 mm, the radar under-estimation which amounts to 20.4% can be explained with the above findings not only by an inadequate Z-R-relation but also a high number of simple zero rainfall observations of radar. Fortunately, this is mainly the case for low-intensity rainfall. If only the sub-set of the largest 25% of rain-gauge rainfall intensities (the percentage taken from all non-zero rainfall observations) is considered (see also Table 6.1), the number of radar misses reduces to 9.4% containing 8.0% of the rain-gauge sum. Possible explanations for this observations could be low-level rainfall not detected by radar or observation errors on the rain-gauge side. Further possible explanations are spatial disagreement of radar and raingauge observation due to wind displacement of the falling rain and threshold effects of both the radar and raingauge measurement principle.

A possibility to improve agreement between radar and ground rainfall occurrence is to not use just one, but an inverse-distance weighted mean of the 9 neighboring pixels above the respective ground station. Table 6.2 shows the different results for March 2001 at NMAU. The 9-pixel average reduces the number of zero radar rainfall observations by 6.1%, added equally to the correct pairs that increase from 58.3% to 61.8% and the zero rain-gauge rainfall cases. That means that using the averaged 9-pixel value has some potential to increase agreement between the two data sources, however the improvement is not overwhelming. For further investigations, usually only the 9-pixel approach was applied.

In an attempt to find further structure in the observation differences, individual rainfall events such as the one shown in Figure 6.1 were investigated. The timeseries of rainfall observed at a point by a raingauge and the respective pixel rainfall of the radar are shown. The cases of principal disagreement of the two series, i.e. when the radar shows zero rain and the raingauge does not and vice versa are indicated by black dots above and below the x-axis. However, various assumptions of the structure of differences such as a tendency for increased occurrence at the beginning or end of events due to the wind-induced horizontal displacement of rainfall on its way from the radar-observed height to ground could not be verified. The differences seem to occur quite randomly with the exception that they are related to rainfall intensity.

From this the question arose about the manner of comparison of the two data sources. Should one compare all cases with at least one device showing a non-zero value or only the cases where both devices indicate rain? The different methods for spatial rainfall estimation should not be evaluated with respect to their performance including an error known to be stemming from the different sampling volumes, but only in the cases where both devices can be assumed to sample from related physical quantities i.e. rainfall occurring at an elevation and on the ground. This also leaves the evaluation unaffected from possible, later improvements of radar rainfall estimation. In later investigations, usually two cases were considered: One where only the rain-gauges had to show non-zero values and a second where both the rain-gauges and the radar observations had to be non-zero. In the result tables, those cases are indicated with 'Radar data ≥ 0' and 'Radar data > 0', respectively. For the reasons mentioned above, the final method comparison was done based on the mutual non-zero rainfall observations only.

		All data		Largest 25 %	
Radar [mm/30 min]	Rain-gauge [mm/30 min]	Number [%]	Sum [%]	Number [%]	Sum [%]
> 0	= 0	4.6	2.8	2.1	1.2
= 0	> 0	54.9	22.2	9.4	8.0
> 0	> 0	40.5	77.8	90.6	92.0

Table 6.1: Differences between rain-gauge and radar observations at 1 pixel (Z-R-relation A = 300, B = 1.5) at rain-gauge NNAG, 30-minute sums, 15.12.00 – 03.10.01

		1 pixel		9 pixel average	
Radar [mm/10 min]	Rain-gauge [mm/10 min]	Number [%]	Sum [%]	Number [%]	Sum [%]
> 0	= 0	7.6	8	10.2	8.1
= 0	> 0	34.1	19.5	28	15.1
> 0	> 0	58.3	80.5	61.8	84.9

Table 6.2: Differences between rain-gauge and radar observations at 1 and 9 pixels (Z-R-relation A = 300, B = 1.5) at rain-gauge NMAU, 10-minute sums, 01. – 31.03.01

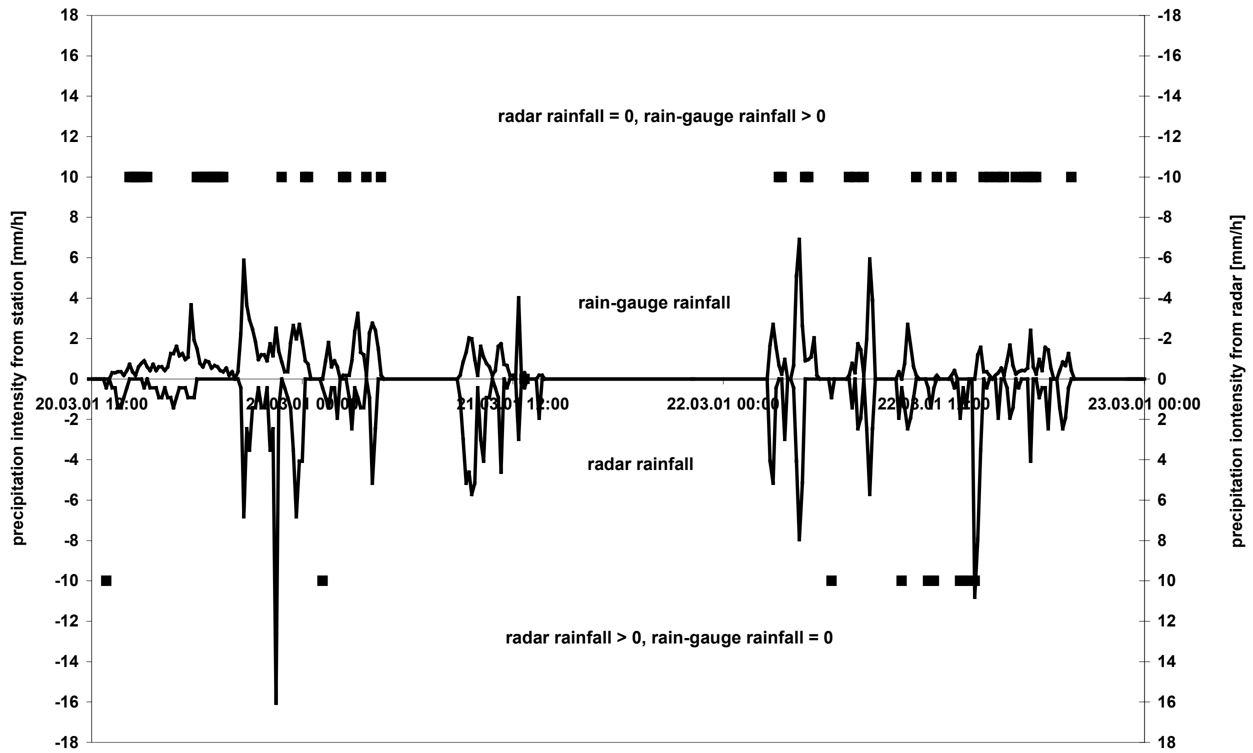

Figure 6.1: Differences between rain-gauge and radar observations (Z-R-relation A = 300, B = 1.5) at rain-gauge NMAU, 10-minute sums, 20.03.01 12:00 – 23.03.01 00:00

6.2 Quality criteria

All evaluations were performed on 10-minute accumulations of the data. This was done as the radar and two stations observed rainfall in real 10-minute resolution. The data from the stations with 30-minute resolution were evenly split into three 10-minute intervals. Separate investigations for all data (15.12.00 – 03.10.01), March 2001 and June 2001 were done. March 2001 was an unusually wet month. In Switzerland it was in many places, (e.g. Bern) the wettest ever recorded March, in Southern Germany the long-term mean rainfall sum for March of 39 mm at station Stuttgart-Schnarrenberg was well exceeded with a sum of 100 mm in March 2001. June 2001 likewise was a wet month, although not as extreme as March. As in flood forecasting, the main interest is to correctly represent the highly intensive rainfall events, statistics were taken not only for the whole data set, but also on different levels of rainfall intensity. They are indicated as follows:

- GE100: Statistics are calculated using all data where rain-gauge observations were > 0.
- GE10: Statistics are calculated using all data where the rain-gauge measurements equal or exceed 0.9063 [mm/30min], which is the rainfall value at 90% cumulative frequency.

The statistics calculated for the method intercomparison were the rainfall sum ('Sum'), the relative sum error ('Error Sum') as the absolute difference of observed and interpolated rainfall sum divided by the observed sum, the standard deviation ('Standa') and relative standard deviation error ('Error Standa') being the absolute difference of observed and interpolated rainfall standard deviation divided by the observed standard deviation, the Spearman rank-correlation coefficient ('RC') and the root mean square error ('RMSE') between observed and interpolated rainfall values. All statistics were calculated using the cross-validation technique, which works as follows: From the set of rain-gauges, leave away one. Using the remaining gauges and the desired interpolation method, estimate rainfall at the location of the station set aside. Compare the estimated with the observed series. Then add the station back and omit another one and estimate rainfall at the new set-aside location and so forth for all stations. Calculate statistics over the whole time-series and all stations. This method was applied to all interpolation methods with the exception of radar data and constant Z-R-relations (cases '300' and '200'), where radar-derived rainfall was directly compared to the rain-gauge observations.

Altogether, a set of a principal interpolation methods with various individual variations were used and will be described in detail in sections 6.3 through 6.6. For easy identification, the following abbreviations for the different methods are used:

- 300: Radar data transformed with a standard Z-R-relation (A = 300, B = 1.5)
- 200: Radar data transformed with a standard Z-R-relation (A = 200, B = 1.6)
- Disdro: Radar data transformed with disdrometer-derived, continuously updated Z-R-relation
- Conti: Radar data transformed with continuously updated Z-R-relation from rain-gauge comparison
- Multi: Radar data transformed with a standard Z-R-relation (A = 300, B = 1.5) and continuous multiplicative updating from rain-gauge comparison.
- Kriging: Rain-gauge data interpolated with Ordinary Kriging.
- EDK: Rain-gauge data interpolated with External-Drift Kriging. External drift are radar data transformed with a standard Z-R-relation (A = 300, B = 1.5).
- Merge: Combination of the mean rain-gauge-kriged field superimposed with the deviations of the radar data from a mean kriged radar field. Radar data are transformed with a standard Z-R-relation (A = 300, B = 1.5).

6.3 Rainfall estimation using static and updated Z-R-relations

With the availability of weather radar data, one of the simplest approaches to estimate spatial rainfall is the use of the radar rainfall estimation from radar reflectivity applying a static Z-R-relation as described in section 2.3.1 or, slightly more complex, a continuously updated Z-R-relation with rain-gauge data as a 'true' reference quantity upon which the relation can be updated. Both approaches have been pursued and are explained in section 6.3.1 and 6.3.2.

6.3.1 Rainfall estimation using static Z-R-relation

Two constant Z-R-relations regularly used by the radar operators in Karlsruhe were investigated. Those are the most commonly used Marshall-Palmer relation A = 200, B = 1.6 and the standard relation applied to the Karlsruhe radar data A = 300, B = 1.5, see also Table 2.3.

The cross-validation results are shown in Table 6.3 and Table 6.4. Regarding the mutual non-zero cases, both standard relations strongly over-estimate the rainfall sum for the whole range of rainfall observations ('GE100') by 31% and 59% respectively, with better agreement being achieved for extreme rainfall ('GE10') by 14% and 8% respectively. However, the second most important evaluation criterion, RMSE increases strongly for extreme rainfall. Regarding the variability of the rainfall values expressed by the standard deviation, both methods over-estimate the observed standard deviation by roughly 30%, indicating that the rainfall observed by radar is too variable. Comparing both standard relations, the standard Karlsruhe relation suits the observations slightly better than the Marshall-Palmer relation and is therefore used as the standard radar rainfall transformation throughout this work.

Level	Radar data	Sum			Standa			RC	RMSE
		Obs	Intpol	Error	Obs	Intpol	Error		
		[mm]	[mm]	[%]	[mm]	[mm]	[%]	[-]	[mm]
GE100	≥ 0	4014	3503	0.12	0.24	0.27	0.21	0.54	0.28
GE10	≥ 0	1847	1292	0.29	0.52	0.57	0.26	0.18	0.70
GE100	> 0	2691	3503	0.31	0.31	0.37	0.27	0.37	0.39
GE10	> 0	1526	1292	0.14	0.53	0.60	0.29	0.13	0.71

Table 6.3: Cross-validation results between observation 'Obs' and interpolation 'Intpol' for rainfall estimation using radar data and a constant Z-R-relation A = 300, B = 1.5, 10-minute sums, 15.12.00 – 03.10.01

Level	Radar data	Sum			Standa			RC	RMSE
		Obs [mm]	Intpol [mm]	Error [%]	Obs [mm]	Intpol [mm]	Error [%]	[-]	[mm]
GE100	≥ 0	4014	4234	0.11	0.24	0.31	0.33	0.54	0.30
GE10	≥ 0	1847	1507	0.18	0.52	0.63	0.33	0.18	0.73
GE100	> 0	2691	4234	0.59	0.31	0.40	0.37	0.37	0.43
GE10	> 0	1526	1507	0.08	0.53	0.65	0.35	0.14	0.74

Table 6.4: Cross-validation results between observations 'Obs' and interpolations 'Intpol' for rainfall estimation using radar data and a constant Z-R-relation A = 200, B = 1.6, 10-minute sums, 15.12.00 – 03.10.01

6.3.2 Continuous updating of Z-R-relation

The idea behind the continuous updating of the Z-R-relation to convert radar reflectivity observations to rainfall intensity is the fact that the Z-R-relation is highly dependent on the drop-size distribution in the radar pulse volume, which can be associated with the current rainfall type. A mean constant Z-R-relation is not able to account for this. An updated estimate of the Z-R-relationship with previous observed radar data and simultaneous ground measurements for the current time-step implicitly considers the current rainfall type and should therefore perform better than a constant relation. For the estimation of A and B, two different approaches were used. The first follows the standard method to derive A and B from simultaneous radar reflectivity and rain-gauge rainfall observations: Transform reflectivity and intensity to log-log space and find A and B as the axis intercept and slope of the linear regression line that best represents the functional relation between Z and R. The second is a simple optimization approach: Vary A and B to minimize the sum error between the rain-gauge rainfall sum $R_{rg,obs}$ and the radar rainfall $R_{radar,obs}$. For both methods, only those previous Z-R data pairs were used where both values were non-zero. To find the optimum estimation algorithm, a number of variations were tested:

- The influence of the number of previous time-steps to use for the optimization of the current Z-R-relation. The time-slots ranged from 30 minutes to 1, 2, 6, 12 and 36 hours. The interpolation quality increased significantly up to a time-slot of 6 hours, for longer periods no change could be observed. Therefore for further investigations, the time-frame was kept constant to 6 hours.
- As not always for every time-step of the previous 6 hours, non-zero data pairs are known, two ways were pursued with respect to the number of data used. The first was to simply use the number of non-zero data-pairs available, which consequently meant a variable number of data considered in subsequent optimizations. Secondly, the number of Z-R data pairs was always

filled up to a constant number. The missing values were randomly drawn from a library of Z-R pairs following the standard Z-R-relation A = 300, B = 1.5. The idea was to keep the number of values for optimization always constant and introduce a bias towards the standard Z-R-relation in case of sparse data. However, this only increased model complexity and did not improve the results.

- Different objective functions were tested for the optimization. Not only squared, but also cubed and quadrupled differences of the rain-gauge and radar rainfall differences were tested. The optimization of the cubed absolute differences resulted in the best relations, especially for intense rainfall. Compared to the linear regression approach in log-log space, the optimization performed slightly better and was therefore favored in further calculations.
- For the optimization, the parameter spaces for A and B were varied according to recommendations given by Doelling et al. (1996). A range of 200 - 400 with increments of 10 for the choice of A, and a range of 1.5 - 2.5 and 0.1 increments for B was found to be the best trade-off between estimation quality and computing time. Expanding the ranges merely prolonged calculation but did not improve results.

In summary, the best agreement between observed and radar-derived rainfall was found with the Z-R-relation optimization in a 6-hour timeslot and the cubed difference between radar and rain-gauge rainfall as the objective function. However, using 7 stations for the estimation of the optimal Z-R-relation for the 8^{th} resulted in 8 different Z-R-relations for each time-step. Only if the differences of the 8 relations for one time-step are small, can the estimation method be considered stable and a mean relation obtained from all 8 stations in the operational case can be regarded as representative for a larger area. To evaluate the variability of the individual Z-R-relations from cross-validation, a standard Z value of 1000 (equivalent to a rainfall intensity of 2.23 mm/h with the standard Z-R-relation A = 300, B = 1.5 relation) was transformed to rainfall using the relation leading to maximum and minimum rainfall for each time-step. Furthermore, the mean rainfall of all 8 relations as a reference value was calculated. The results are shown in Table 6.5. The deviation from the mean value in the maximum as well as in the minimum case are small enough to consider the estimation of the Z-R-relation only weakly dependent on the rain-gauge used and therefore representative for a larger area including ungauged places.

	Exponent 2		Exponent 3	
	Sum [mm]	Error [%]	Sum [mm]	Error [%]
Mean	1797	--	1811	--
Max	1862	3.6	1753	3.5
Min	1740	3.1	1955	3.2

Table 6.5: Mean, maximum and minimum radar rainfall estimations from 8 cross-validation cases, using Z-R updating, summed over the test-period for different exponents of the objective function, 10-minute-sums, 15.12.00 – 03.10.01

It can be deduced from the interpolation results in Table 6.6 that optimizing the Z-R-relation performs well over the whole range of rainfall intensities but tends to under-estimate the extremes. Also, the variability of rainfall observed at the rain-gauges is not fully reproduced but tends to be too low. Compared to the results from the constant Z-R-relations, the overall rainfall estimation has improved while for the extremes, the constant Z-R-relation performs better.

Level	Radar data	Sum			Standa			RC	RMSE
		Obs [mm]	Intpol [mm]	Error [%]	Obs [mm]	Intpol [mm]	Error [%]	[-]	[mm]
GE100	≥ 0	4014	2767	0.31	0.24	0.20	0.19	0.55	0.23
GE10	≥ 0	1847	986	0.46	0.52	0.43	0.23	0.22	0.62
GE100	> 0	2691	2767	0.10	0.31	0.26	0.23	0.40	0.30
GE10	> 0	1526	986	0.34	0.53	0.45	0.25	0.20	0.61

Table 6.6: Cross-validation results between observations 'Obs' and interpolations 'Intpol' for rainfall estimation using radar data and a continuously updated Z-R-relation A = 200 - 400, B = 1.5 – 2.5, time-slot 6 hours, exponent of objective function: 3, 10-minute-sums, 15.12.00 – 03.10.01

6.3.3 Multiplicative correction of radar data

Instead of updating the Z-R-relation for each time-step, the much more common approach of multiplicative radar data adjustment was also investigated. The adjustment factor is simply the ratio of the rainfall sum observed by the rain-gauges and the rainfall from radar applying the standard Z-R-relation of A = 300, B = 1.5. The method ensures that the rain-gauge and radar rainfall sum over a given period are equalized. As in the case of the Z-R-relation updating, the timeslot to calculate the adjustment factor was varied. Again, a depth of 6 hours was found to be optimal and as before, for one time-step the cross-validation procedure yielded 8 different factors from the individual optimization for each group of 7 rain-gauges. As shown in Table 6.7, the differences between the maximum, minimum and mean factor for each time-step summed over the whole period are considerably larger than the variations from the individual Z-R-relations. This indicates that the adjustment factor cannot be regarded as being as spatially homogeneous as the Z-R-relation. Overall, the mean adjustment factor amounted to 0.95, which means that the standard Karlsruhe Z-R-relation over-estimates overall rainfall, a fact that can also be seen in Table 6.3.

	Sum [mm]	Error [%]
Mean	2203	--
Max	2398	8.8
Min	2021	8.2

Table 6.7: Mean, maximum and minimum radar rainfall estimations from 8 cross-validation cases, using multiplicative updating, summed over the test period, 10-minute-sums, 15.12.00 - 03.10.01

As the results of the cross-validation in Table 6.8 show, the multiplicative updating, like the Z-R-relation updating, tends to perform well for all rainfall intensities while under-estimating extreme rainfall, but in contrast to the generally smooth, low variability of the Z-R-relation estimates, the multiplicative updating features a higher standard deviation than observed. This corresponds to the spatial heterogeneity of the multiplier documented in Table 6.7. With regard to rank-correlation and RMSE, the multiplicative updating is outperformed by the Z-R-relation updating.

Level	Radar data	Sum			Standa			RC	RMSE
		Obs [mm]	Intpol [mm]	Error [%]	Obs [mm]	Intpol [mm]	Error [%]	[-]	[mm]
GE100	≥ 0	4014	2892	0.27	0.24	0.26	0.22	0.56	0.25
GE10	≥ 0	1847	1268	0.30	0.52	0.58	0.27	0.26	0.67
GE100	> 0	2691	2892	0.14	0.31	0.36	0.30	0.48	0.35
GE10	> 0	1526	1268	0.17	0.53	0.61	0.32	0.26	0.66

Table 6.8: Cross-validation results between observations 'Obs' and interpolations 'Intpol' for rainfall estimation using radar data and a constant Z-R-relation A = 300, B = 1.5, multiplicative correction from rain-gauge data, timeslot 6 hours, 10-minute-sums, 15.12.00 – 03.10.01

6.4 Rainfall estimation using ground-based Z-R-relations

By observing rainfall and reflectivity at ground level with only one measurement device (thus avoiding the problem that radar and rain-gauge data usually taken to determine Z-R-relations are observed at different places), the disdrometer offers a simple yet elegant way to estimate a Z-R-relation. Furthermore, from the ratio of particle size to fall velocity, a disdrometer offers a possibility to specify the current rainfall type and state of aggregation of precipitation. Enough reason to buy an optical disdrometer for the Goldersbach project and evaluate its possibilities. Unfortunately, the disdrometer used, a prototype, left a lot of room for improvement. According to the developing company, much progress has been achieved since the development of the prototype, partly influenced by the results of the Goldersbach project, in the improvement of sampling algorithms of the disdrometer. However, in short, the measurements taken with the disdrometer were at times unreliable, manifested in random strong over-estimations of rainfall. Consequently, the results were poor. Regardless of this unfortunate result the modus operandi is explained here as the disdrometer's potential to improve radar rainfall estimates is high and it is hoped that with a new product generation performance will increase.

The idea is simple: From a previous timeslot, in this case 6 hours, the current Z-R-relation is estimated from rainfall intensity and reflectivity observed by the disdrometer by linear regression in log-log space and applied on the radar reflectivity observations. If no disdrometer data are available, the standard Z-R-relation A = 300, B = 1.5 is applied. The results are shown in Table 6.9. Despite the occasional strong rainfall over-estimations, the performance of the algorithm was not completely wrong, but performed about as well as a constant Z-R-relation. There is even a slight increase in performance with regard to the reproduction of the observed rainfall sum, although this is accompanied by a slight deterioration of the standard deviation. However, it should be stressed again that the results of this method should be interpreted with caution.

Level	Radar data	Sum			Standa			RC	RMSE
		Obs [mm]	Intpol [mm]	Error [%]	Obs [mm]	Intpol [mm]	Error [%]	[-]	[mm]
GE100	≥ 0	4014	3577	0.11	0.24	0.28	0.25	0.54	0.27
GE10	≥ 0	1847	1374	0.25	0.52	0.62	0.31	0.19	0.70
GE100	> 0	2691	3577	0.34	0.31	0.38	0.31	0.37	0.38
GE10	> 0	1526	1374	0.11	0.53	0.65	0.35	0.15	0.71

Table 6.9: Cross-validation results between observations 'Obs' and interpolations 'Intpol' for rainfall estimation using radar data and a continuously updated, disdrometer-derived Z-R-relation, 10-minute-sums, 15.12.00 – 03.10.01

6.5 Kriging based rainfall estimation

Kriging is a method to estimate linear functions of random fields or point values and was first introduced by Matheron (1971). Kriging is a member of the 'BLUE' (Best Linear Unbiased Estimator) family. The weights assigned to each observed value when estimating at an unknown point are determined using a theoretical covariance function or variogram fitted to the experimental covariance function or variogram from observations. Using Kriging implies the assumption of second-order stationarity or the intrinsic hypothesis which is explained in greater detail in Appendix A2 and in Kitanidis (1997).

Using the Kriging algorithm, several different variations were investigated. The most straightforward approach as described in section 6.5.1 makes use only of the rain-gauge observations and neglects the radar data for the rain-field estimation. With the rainfall type classifications of chapter 4 in mind, two interpolation variations were pursued: One using a mean variogram derived from all data, the other applying three rainfall-type dependent variograms. The sub-division into 3 rainfall types was done according to the simple distinction using the Wetted Area Ratio: 'convective' (WAR < 0.1), 'mixed' (0.1 ≤ WAR ≤ 0.5) and 'stratiform' (WAR > 0.5). Looking at the experimental and theoretical variograms in Figure 6.2 and Table 6.10, the differences are obvious. The 'convective' variogram shows a steep rise in variance at close ranges, while the 'stratiform' variogram raises slowly and in a linear fashion. As expected, the 'mixed' variogram shows an intermediate behavior. All variograms were calculated as mean over the whole time-series with the variogram of each time-step normalized by the standard deviation of the respective time-step to stress the influence of 'smooth' images. For reasons of comparability, the variograms were normalized to a maximum value of 1.

Alternatively, External-Drift Kriging was applied in section 6.5.2, where the radar data transformed with the standard Z-R-relation (A = 300, B = 1.5) were used as drift.

Data used	Variogram	Range [m]	Sill [-]	A [ ]	B [ ]
WAR < 0.1	Gaussian	7200	1.78		
0.1 ≤ WAR ≤ 0.5	Exponential	13500	2.00		
WAR > 0.5	Linear			0.000015	0.1

Table 6.10: Theoretical variograms for three rainfall types 'convective' (WAR < 0.1), 'mixed' (0.1 ≤, WAR ≤ 0.5), 'stratiform' (WAR > 0.5) from rain-gauge observations, 30-minute-sums, 15.12.00 - 03.10.01

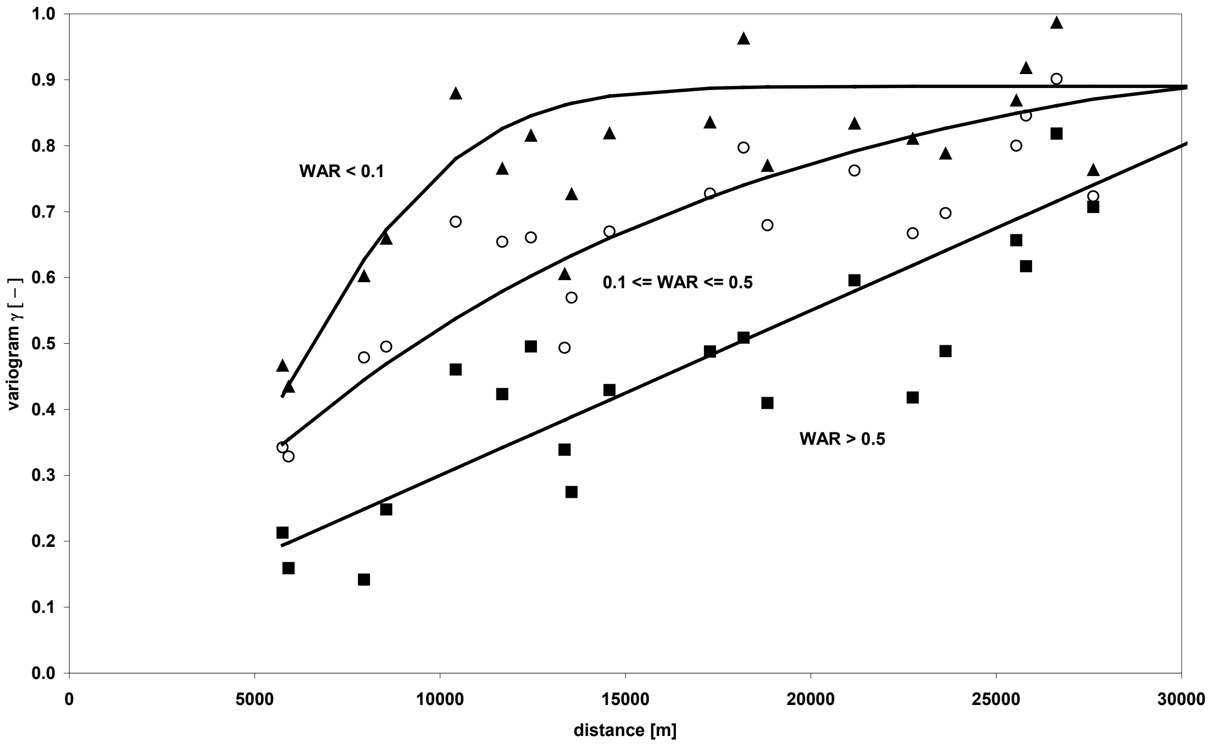

Figure 6.2: Experimental and theoretical variograms from rain-gauge observations for different rainfall types from 30-minute sums, 15.12.00 – 03.10.01

6.5.1 Interpolation of rain-gauge data using Ordinary Kriging

The Ordinary Kriging algorithm, relying only on the rain-gauge data, was not expected to perform very well, except for widespread rainfall events. However, compared to the '300' method (only radar data transformed with a constant Z-R-relation), it performed surprisingly well. Kriging tends to produce very smooth interpolations, which can be seen in the under-estimated standard deviation in Table 6.11 and sometimes misses local intensive rainfall events. This is also visible in Table 6.11, where the overall rainfall sum 'GE100' is much more accurately reproduced than only the intensive rainfall (GE10) sums. With respect to the overall rain, Kriging outperformed the radar data altogether, with respect to the RMSE, it even performed better in the 'GE10' sub-set of rainfall.

Another surprise was the comparison of the two Kriging alternatives, one with a single, the other with 3 WAR-dependent variograms. Despite the distinct differences of the variograms, the interpolation improvement using 3 variograms was only marginal. It must be borne in mind though, that the variogram for convective cases was used in 45% of cases, of which the majority failed to show rain at the stations, the 'stratiform' variogram applied only to 1% of all cases! Consequently, the influence of the two additional variograms was relatively low. Investigating the influence only in the stratiform cases (WAR > 0.5) at least revealed an improvement in the rainfall sum estimation by 2%. This is not overwhelming, but the concept of 3 variograms was retained nevertheless.

Level	Radar data	Sum Obs [mm]	Sum Intpol [mm]	Sum Error [%]	Standa Obs [mm]	Standa Intpol [mm]	Standa Error [%]	RC [-]	RMSE [mm]
GE100	≥ 0	4014	3245	0.19	0.24	0.18	0.22	0.65	0.20
GE10	≥ 0	1847	1151	0.38	0.52	0.38	0.22	0.36	0.56
GE100	> 0	2691	2098	0.22	0.31	0.23	0.24	0.63	0.27
GE10	> 0	1526	977	0.36	0.53	0.38	0.23	0.37	0.56

Table 6.11: Cross-Validation results between observations 'Obs' and interpolations 'Intpol' for rainfall estimation using rain-gauge data and Ordinary Kriging with 3 variograms, 10-minute-sums, 15.12.00 – 03.10.01

6.5.2 Interpolation of rain-gauge data using External-Drift Kriging

External-Drift Kriging can be used if a secondary variable, the so-called drift is available at both the observed and ungauged places and a linear relationship between the drift and the quantity to interpolate exists (see also Appendix A2). Assuming this relationship between the rain-gauge observations and the radar data transformed with a standard Z-R-relation (A = 300, B = 1.5), the radar data were used as drift. Looking at the results in Table 6.12, however indicates that this assumption is not always valid. Although the sum error is quite low, both for the overall and intensive rain, the very large standard deviation and RMSE errors indicate an extreme variability of the interpolated values. A closer look at the time-series of observed and interpolated rainfall at the gauge positions revealed that a small number of cases where radar and rain-gauge data did not coincide at all caused severe rainfall over-estimation and strongly influenced the overall statistics. In an attempt to mitigate this effect, the root of radar rainfall was used as drift, thus reducing the extreme values. However, this led to only a minor improvement. Next, for each time-step the correlation between the rain-gauge and radar data used was calculated and External-Drift Kriging was only performed when it exceeded a value of 0.5. For low correlations and therefore negligible linear relationship between rain-gauge and radar data, Ordinary Kriging using only the gauge data was used. This also improved the results somewhat, but not significantly. Alternatively, elevation was used as External Drift. However, on short aggregation scales below a approximately a day, elevation shows no obvious linear relation with rainfall intensities, so the External-Drift Kriging approach was set aside and is not recommended for the combination of radar and rain-gauge data on short aggregation scales.

Level	Radar data	Sum Obs [mm]	Sum Intpol [mm]	Sum Error [%]	Standa Obs [mm]	Standa Intpol [mm]	Standa Error [%]	RC [-]	RMSE [mm]
GE100	≥ 0	4014	3897	0.15	0.24	0.51	1.25	0.64	0.48
GE10	≥ 0	1847	1582	0.17	0.52	1.30	1.58	0.35	1.28
GE100	> 0	2691	2981	0.20	0.31	0.77	1.61	0.60	0.73
GE10	> 0	1526	1453	0.17	0.53	1.44	1.81	0.38	1.40

Table 6.12: Cross-Validation results between observations 'Obs' and interpolations 'Intpol' for rainfall estimation using rain-gauge data and External-Drift Kriging with radar data and a constant Z-R-relation A = 300, B = 1.5 as drift, 10-minute-sums, 15.12.00 – 03.10.01

6.6 Geostatistical merging of radar and rain-gauge data

Apart from the well-known approaches discussed above, a new method to jointly use radar and rain-gauge data was used. It was developed in discussion with Pegram and Bárdossy. The basic idea is that in general, the rain-gauges are trusted to measure the rainfall sums accurately, but only at discrete points while radar may be mistaken in the absolute values, but provides a trustworthy spatial distribution of rainfall occurrences. The merging is simple and follows the steps in Figure 6.3:

a) The rainfall field is observed at discrete points from rain-gauges ($R_{rg,obs}$).
b) The rainfall field is also observed by radar on a regular, volume-integrated grid ($R_{radar,obs}$).
c) Block-Kriging and the rain-gauge observations are used to obtain the best linear unbiased estimate of rainfall at all ungauged radar gridpoints ($R_{rg,kriged}$).
d) Only the radar pixel values at the rain-gauge positions (or a weighted mean of several neighboring pixels) and the Kriging algorithm are used to estimate the interpolated radar rainfall at each gridpoint ($R_{radar,kriged}$) is applied.
e) At each gridpoint, the deviation c of the observed and interpolated radar value is calculated using a suitable method. At the rain-gauge locations, c is always equal to zero.
f) The field of deviations from e) is applied to the rain-field from rain-gauge interpolation.
g) A rainfall field that follows the mean field of the rain-gauge interpolation while preserving the mean-field deviations from the radar image is obtained.

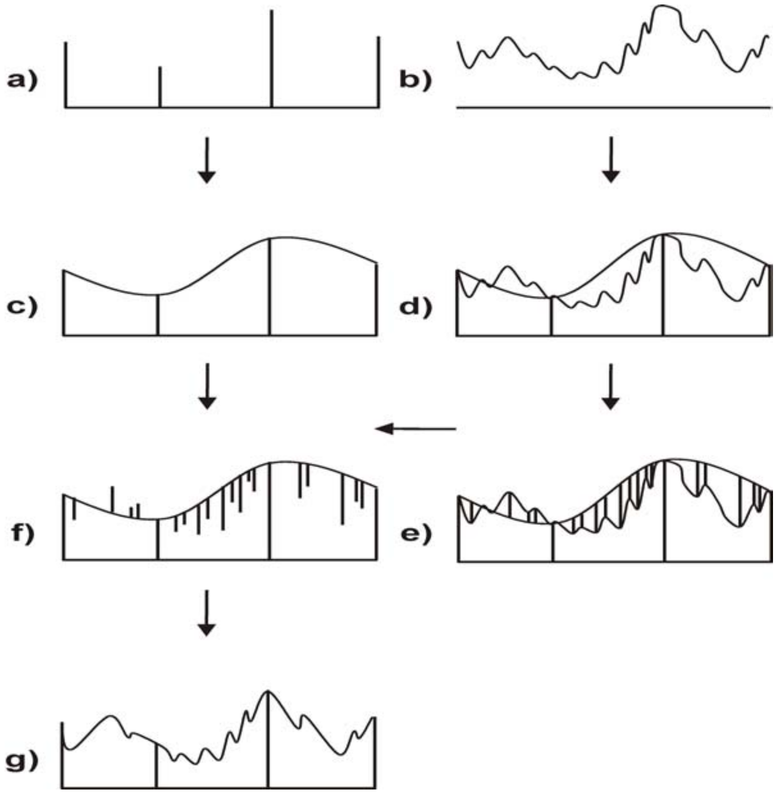

Figure 6.3: Merging rain-gauge and radar data – principal steps

Although straightforward in its principal steps, several additional aspects have to be taken into consideration. Firstly, the variogram to interpolate the radar data must not necessarily coincide with one derived from rain-gauge observations. The radar variograms, again separately for three rainfall types, were calculated from data between 01.03 – 14.05.01. With the radar data given in a 256 × 256 pixel grid, a huge number of possible point pairs to calculate the experimental variogram are available. For the sake of fast computation, only point pairs to a maximum distance of 40 km and in the 4 principal directions (0°, 45°, 90°, 135°) were considered. Again, the variograms were divided by the standard deviation of each time-step and normalized to a maximum value of 1. Looking at the variograms in Table 6.13 and Figure 6.4 shows that with the large number of point pairs used, the variograms became very smooth and the scatter of the experimental around the fitted variogram is very small. Comparing the variograms to those from the rain-gauges (Table 6.10, Figure 6.2) shows good agreement in the short range (5 to 10 km), for far ranges however the variograms differ: While the rain-gauge variograms reach a sill at a range of 15 and 30 km ($WAR < 0.1$, $0.1 \leq WAR \leq 0.5$, respectively), the radar variograms continue to increase beyond the range considered. Secondly, the different sampling characteristics of radar and rain-gauges have to be taken into consideration. While rain-gauges observe rain at one point, the radar rainfall estimate represents the integrated mean over a pulse volume transformed on a grid. To account for this, the rain-gauge data were not point-interpolated on the radar grid center, but block-kriged within the grid limits. The Block-Kriging was done in a straightforward manner: Perform the interpolation for a large number of points (here 100) within the block limits and take the average. Another issue is the area of influence of the rain-gauge observations. From common sense, it is clear that the interpolated rain-gauge field loses its usefulness the farther one has to extrapolate away from the station locations. Therefore, the merged field should increasingly rely solely on the radar observations with increasing distance from rain-gauges. To account for that, the interpolated rain-gauge field can be inversely weighted with the Kriging estimation variance at every gridpoint such that at remote places the original radar image is restored.

The method proposed here has several advantages, namely that the rainfall observation at the rain-gauge locations are preserved in the merged image. Also, the interpolated image combines the two strong points of the original data: the spatial variability of the radar image and the mean field of the rain-gauge data. Furthermore, additional stations can be included without problems

Data used	Variogram	Range [m]	Sill [-]	A [ ]	B [ ]
WAR < 0.1	Expo/Linear	4500	0.65	0.000017	0.41
0.1 ≤ WAR ≤ 0.5	Expo/Linear	5500	0.60	0.000014	0.35
WAR > 0.5	Exponential	10000	0.50		

Table 6.13: Theoretical variograms for three rainfall types 'convective' (WAR < 0.1), 'mixed' (0.1 ≤, WAR ≤ 0.5), 'stratiform' (WAR > 0.5)WAR < 0.1 from radar observations (Z-R A = 300, B = 1.5), 10-minute-sums, 01.03 – 14.05.01

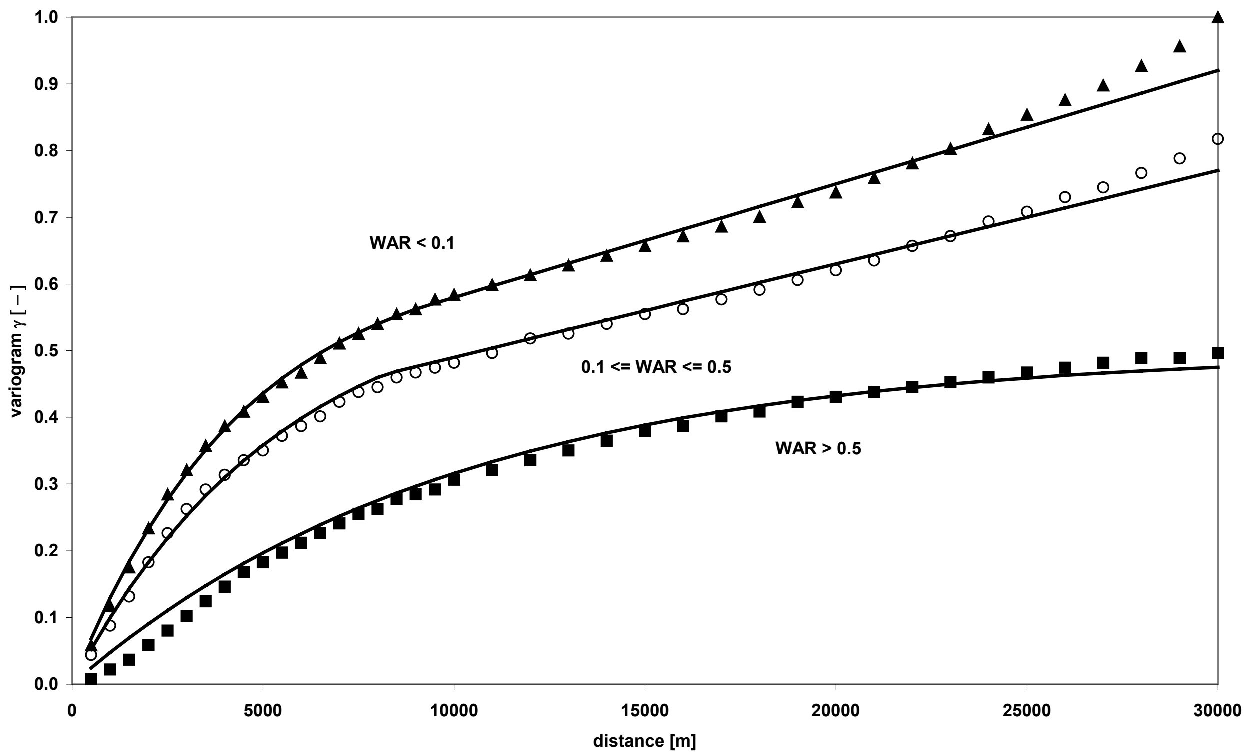

Figure 6.4: Experimental and theoretical variograms from radar observations for different rainfall types from 10-minute sums (Z-R A = 300, B = 1.5), 01.03 – 14.05.01

Applying the merging algorithm revealed the strong influence of the operator to calculate the deviation c on the quality of the result. In a first step, the deviation c_d between the observed and interpolated radar field was calculated as simple difference according to (6.1), the merged field according to (6.2). The results were promising but some under-estimation occurred and negative merged values had to be excluded setting a lower merging limit of zero. Another possibility to combine the fields was to calculate the difference as the quotient c_q of the observed and interpolated radar value according to (6.3) and (6.4). Here, the results strongly over-estimated rainfall and large standard deviation and RMSE errors occurred. The problem was that large errors occurred in low-intensity cases, where the absolute difference between $R_{radar,obs}$ and $R_{radar,kriged}$ was small but the ratio large. Applying this on $R_{rg,kriged}$ led to large errors for $\hat{R}$. If for example $R_{rg,kriged} = 3$ mm/h, $R_{radar,obs} = 3$ mm/h and $R_{radar,kriged} = 0.01$ mm/h then the quotient is 300 and the estimated rainfall R^* amounts to a completely unrealistic 900 mm/h. The last and best option was then to calculate the quotient c_{ln} of the log-values, raised by 1.5 according to (6.5) and (6.6). The logs equalize the observed and kriged radar values somewhat, thus reducing the ratio. The same was attained by adding 1.5 [mm/h] to each value to force the values out of the steeply inclined domain of the logarithm function. As with the difference operator, however, negative values can occur when

$R_{radar,obs}$ or $R_{rg,kriged}$ are small compared to $R_{radar,kriged}$ and have to be avoided by a lower limit of zero for the merged values.

$$c_d = R_{radar,obs} - R_{radar,kriged} \tag{6.1}$$

$$R^* = R_{rg,kriged} + c_d \tag{6.2}$$

$$c_q = \frac{R_{radar,obs}}{R_{radar,kriged}} \tag{6.3}$$

$$R^* = R_{rg,kriged} \cdot c_q \tag{6.4}$$

$$c_{ln} = \frac{\ln\left(R_{radar,obs} + 1.5\right)}{\ln\left(R_{radar,kriged} + 1.5\right)} \tag{6.5}$$

$$R^* = e^{c_{ln} \cdot \ln\left(R_{rg,kriged} + 1.5\right)} - 1.5 \tag{6.6}$$

where:

c_d	[mm/h]	difference of radar pixel and interpolated radar value
c_q	[-]	quotient of radar pixel and interpolated radar value
c_{ln}	[-]	logarithmic quotient of radar pixel and interpolated radar value
$R_{radar,obs}$	[mm/h]	observed radar pixel value
$R_{radar,kriged}$	[mm/h]	interpolated radar value
$R_{rg,kriged}$	[mm/h]	interpolated rain-gauge value
R^*	[mm/h]	merged rainfall estimate

The results of the merging algorithm using the c_{ln} operator are listed in Table 6.14. Although the individual statistics are not exceptionally better than those of other methods, it shows good overall performance and no obvious weaknesses occur as in some other methods. A final and comprehensive comparison was carried out in section 6.7.

For the final creation of the merged rainfall image, the estimated rain-field was masked with a binary-transformed radar field: Wherever the original radar field showed zero values, the merged image was also set to zero, wherever the radar image contained non-zero values, the merged rainfall estimate was kept.

Level	Radar data	Sum Obs [mm]	Sum Intpol [mm]	Sum Error [%]	Standa Obs [mm]	Standa Intpol [mm]	Standa Error [%]	RC [-]	RMSE [mm]
GE100	≥ 0	4014	3922	0.11	0.24	0.30	0.27	0.60	0.25
GE10	≥ 0	1847	1560	0.17	0.52	0.72	0.43	0.37	0.70
GE100	> 0	2691	3172	0.20	0.31	0.41	0.36	0.52	0.36
GE10	> 0	1526	1449	0.12	0.53	0.77	0.51	0.39	0.72

Table 6.14: Cross-Validation between observations 'Obs' and interpolations 'Intpol' results for rainfall estimation merging rain-gauge data and radar data from a constant Z-R-relation A = 300, B = 1.5, r_{ln} method, 10-minute-sums, 15.12.00 – 03.10.01

6.7 Comparison and Conclusion

From the multitude of results for different rain-gauges, different interpolation methods, various evaluation criteria, rainfall intensity levels and time-series, only a few were shown in the previous chapters. Even from those, it is hard to draw a unique conclusion on the ranking of the interpolation techniques. To cope with that, a multi-objective decision system was set up to jointly evaluate the results. Firstly, an individual weight was assigned to each of the rain-gauges considered according to their proximity to the Goldersbach catchment as the rainfall estimation should be best in the area of interest. The weights assigned are: NNAG 5%, NBÖB 8%, NREU 7%, NROT 10%, NTÜB 20%, NMAU 25%, NSCH 25%. Next, different weights were assigned to the statistics calculated. The sum error and RMSE were considered most important and were therefore assigned high weights, the standard deviation error a little less and finally the RC, which fluctuated only within narrow bounds throughout all scenarios was considered the least significant. The exact weights are given in Table 6.15, Table 6.16 and Table 6.17. With the original purpose of the work, flood forecasting, in mind it was considered especially important to correctly reproduce extreme rainfall rather than long-term mean values, consequently low weights between 0% and 30% were given to 'GE100', weights ranging from 70% to 100% to 'GE10'. Finally, as already mentioned in the introductory remarks, three time-series were considered for evaluation: The whole time-series, March 2001 and June 2001. All statistics were normalized to [0,1] with 0 indicating the most favorable, 1 the least favorable value and then multiplied by its individual weight, multiplicatively combined from all relevant weights.

The score and rank of each interpolation method for the three time-series and 3 weighting schemes are shown in Table 6.15, Table 6.16 and Table 6.17. First of all, it shows that throughout all scenarios, merging outperforms the other methods. Kriging performs well in the two wet months

March and June 2001 but proves to be not very good over the whole period. The standard Z-R-relations are outperformed by most other techniques in wet months, not so much because they do not perform well in wet months but because the other, rain-gauge-dependent methods perform better in the case of frequent widespread rain. The intermediate ranks are interchangeable throughout the different time-series and there is no clear advantage of one method over the others. Also it shows that the variation of weight does not have a great influence on the ranking of the methods. Only in a few cases do the different weighing schemes alter the ranking.

All data		Weight [%]		Weight [%]		Weight [%]	
		Score	Rank	Score	Rank	Score	Rank
Intensity weight	GE100	30		30		0	
	GE10	70		70		100	
Statistics weights	Error Sum	40		50		40	
	Error Standa	20		20		20	
	RC	10		10		10	
	RMSE	30		20		30	
300		0.53	4	0.51	4	0.57	5
200		0.47	2	0.44	2	0.47	2
Conti		0.70	7.5	0.74	8	0.71	7.5
Multi		0.56	5	0.56	5	0.53	4
Disdro		0.48	3	0.46	3	0.52	3
Kriging		0.59	6	0.61	6	0.64	6
EDK		0.70	7.5	0.64	7	0.71	7.5
Merge		0.43	1	0.40	1	0.44	1

Table 6.15: Scores and ranks of rainfall interpolation methods applying different objective functions, All data (15.12.00 – 03.10.01)

March 2001		Weight [%]		Weight [%]		Weight [%]	
		Score	Rank	Score	Rank	Score	Rank
Intensity weight	GE100	30		30		0	
	GE10	70		70		100	
Statistics weights	Error Sum	40		50		40	
	Error Standa	20		20		20	
	RC	10		10		10	
	RMSE	30		20		30	
300		0.70	6.5	0.67	6.5	0.74	6.5
200		0.93	8	0.93	8	0.94	8
Conti		0.39	2	0.39	2	0.42	2
Multi		0.47	4	0.46	4	0.48	4
Disdro		0.70	6.5	0.67	6.5	0.74	6.5
Kriging		0.41	3	0.43	3	0.46	3
EDK		0.50	5	0.47	5	0.52	5
Merge		0.37	1	0.34	1	0.38	1

Table 6.16: Scores and ranks of rainfall interpolation methods applying different objective functions, March 2001

June 2001		Weight [%]		Weight [%]		Weight [%]	
		Score	Rank	Score	Rank	Score	Rank
Intensity weight	GE100	30		30		0	
	GE10	70		70		100	
Statistics weights	Error Sum	40		50		40	
	Error Standa	20		20		20	
	RC	10		10		10	
	RMSE	30		20		30	
300		0.84	8	0.86	8	0.84	8
200		0.79	5	0.81	5	0.80	5
Conti		0.82	6.5	0.84	6	0.83	6.5
Multi		0.72	4	0.73	4	0.73	4
Disdro		0.82	6.5	0.85	7	0.83	6.5
Kriging		0.52	2	0.50	2	0.57	2
EDK		0.56	3	0.52	3	0.60	3
Merge		0.50	1	0.46	1	0.53	1

Table 6.17: Scores and ranks of rainfall interpolation methods applying different objective functions, June 2001

Another way to compare performances is to look at selected time-series of rainfall. In Figure 6.5 and Figure 6.6 two rainfall events observed at rain-gauge NMAU were interpolated using all other rain-gauge observations and various interpolation methods. The first image shows rainfall observed in the course of a short, yet intense thunderstorm event. The Kriging time-series displays a typical problem of Kriging in the case of local rainfall. Before the storm actually hits NMAU, intensive rainfall at surrounding stations forces the rainfall estimate at NMAU to an unrealistically high value. Later, when the storm has reached NMAU but has disappeared from the other stations, rainfall is under-estimated due to the same reason. The radar captures the temporal structure of the storm quite well but under-estimates the volume, the same applies for the disdrometer method which found just the standard Z-R-relation for this event. The merging method preserves the temporal storm structure as observed by the radar, but increases the volume a little bit. The next event shows some typical problems of radar rainfall observation in winter. Due to the Bright Band effect, the radar greatly over-estimates ground rainfall, which is also only gradually mitigated by the disdrometer Z-R-relation. As the event was widespread and observed at all rain-gauges, Kriging performs quite well, merging also is able to reduce the radar over-estimation and lower the rainfall estimate close to the observation.

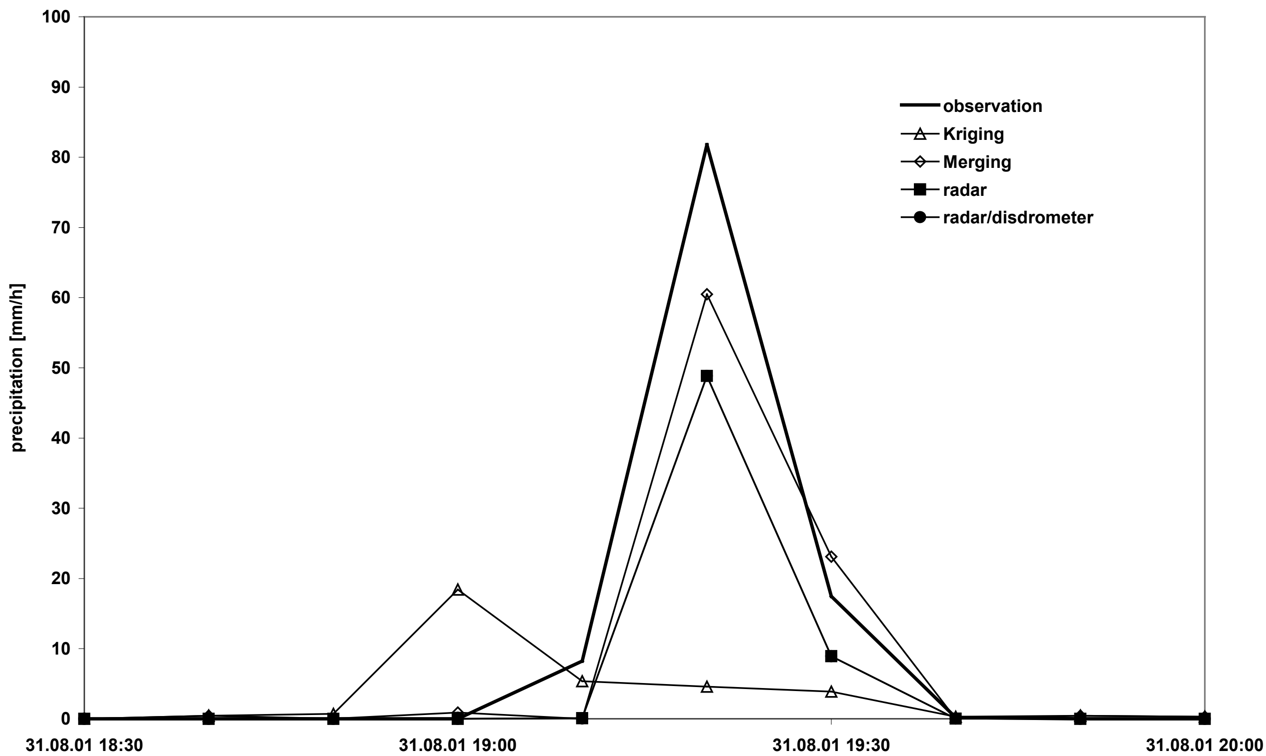

Figure 6.5: Point rainfall estimation at rain-gauge NMAU using different interpolation methods, 31.08.01 18:30 – 20:00

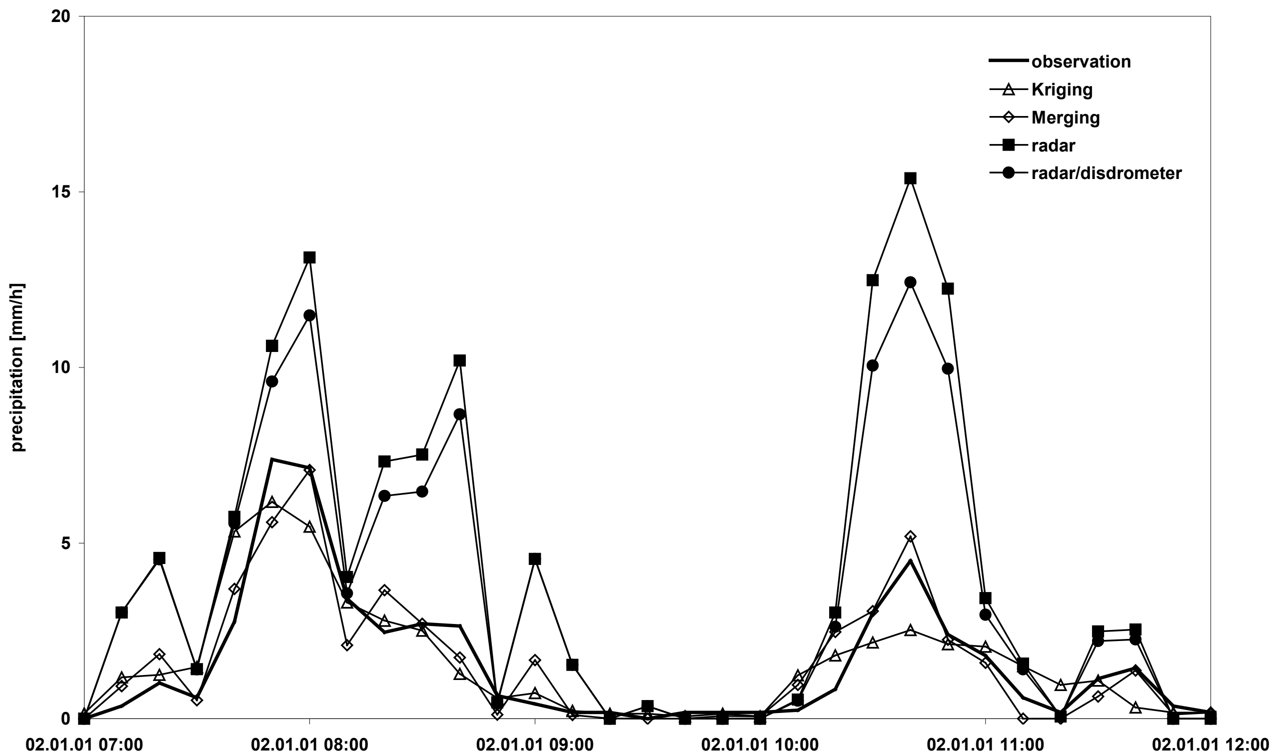

Figure 6.6: Point rainfall estimation at rain-gauge NMAU using different interpolation methods, 02.01.01 07:00 – 12:00

Based on those results, rainfall interpolation for operational use in the Goldersbach project is solely based on merging. Figure 6.7, Figure 6.8, Figure 6.9 and Figure 6.10 again show the observed basic data, intermediate steps and the resulting merged rainfall estimate over the Goldersbach catchment for the thunderstorm event described above. Figure 6.7 shows the kriged rainfall estimate from 8 rain-gauge observations, Figure 6.8 the radar rainfall image at the same time which indicates a small but intensive convective cell over the catchment. Kriging only the radar observations at the 8 rain-gauge location produces Figure 6.9, which shows the same shape as the kriged rain-gauge image, but the mean field rainfall intensity is less. Combining the two with the merging algorithm and masking with the binary original radar image leads to Figure 6.10 which closely resembles the original radar image in shape and relative intensity distribution but has been raised in the overall intensity.

To conclude, merging is a useful tool to combine the rainfall information of different sources in spatial rainfall estimation, however there is still great potential in improving all aspects of the involved data. Even a good combination algorithm cannot make up for poor input data quality. In a key paper published by Zawadski (1984) he summarized this as follows: 'The accuracy of radar estimates at ground will only be improved by addressing the various sources of error in a painstaking and a meticulous manner'.

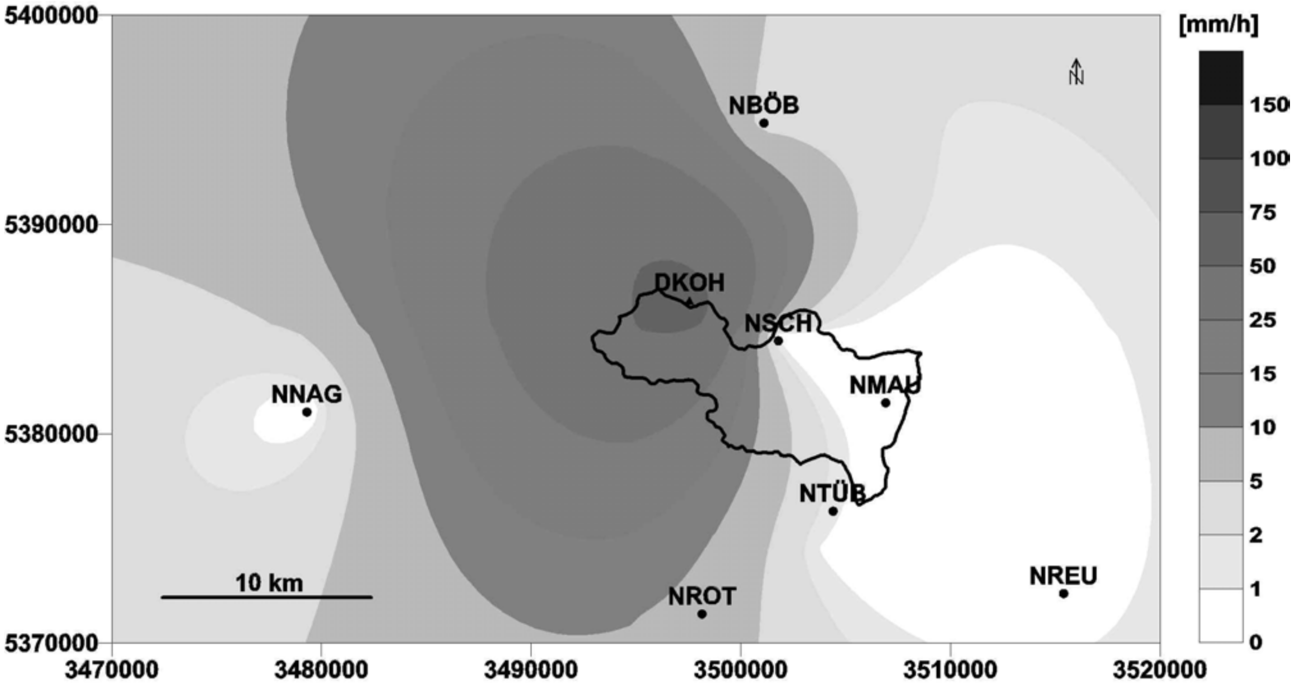

Figure 6.7: Spatial rainfall estimation Kriging, data from 8 rain-gauges, 31.08.01 20:10

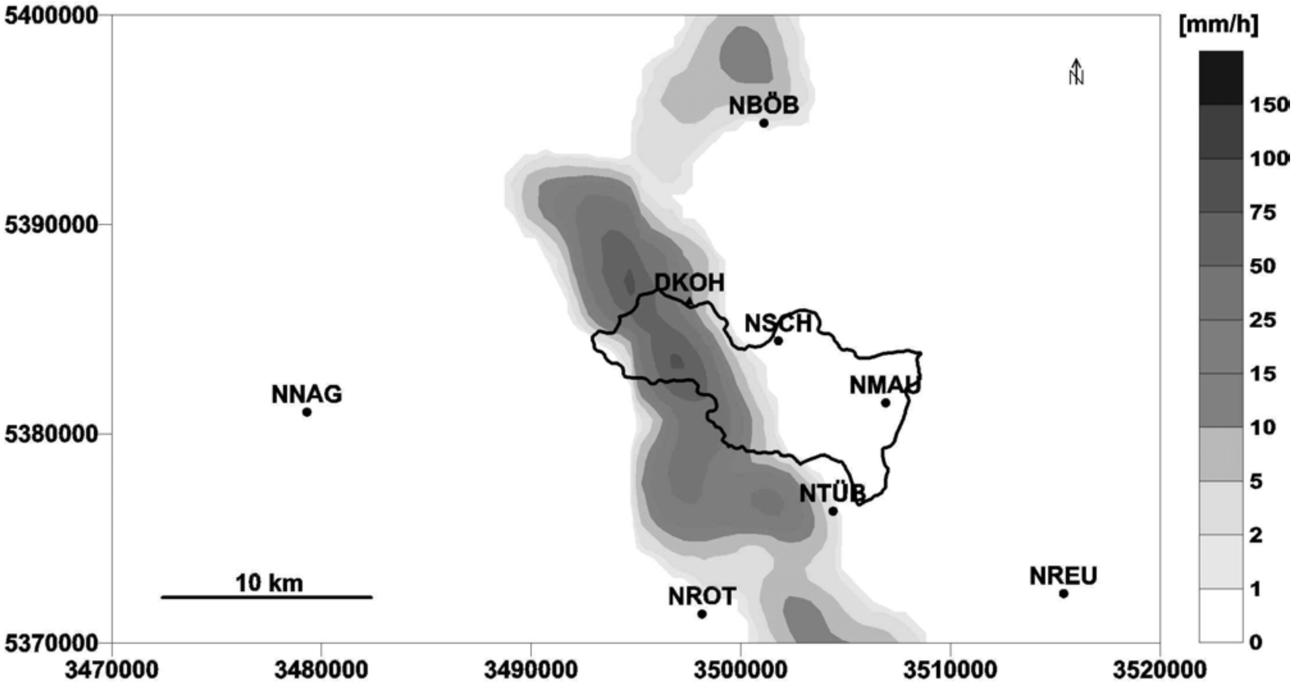

Figure 6.8: Spatial rainfall estimation using radar rainfall (Z-R A =300, B =1.5), 31.08.01 20:10

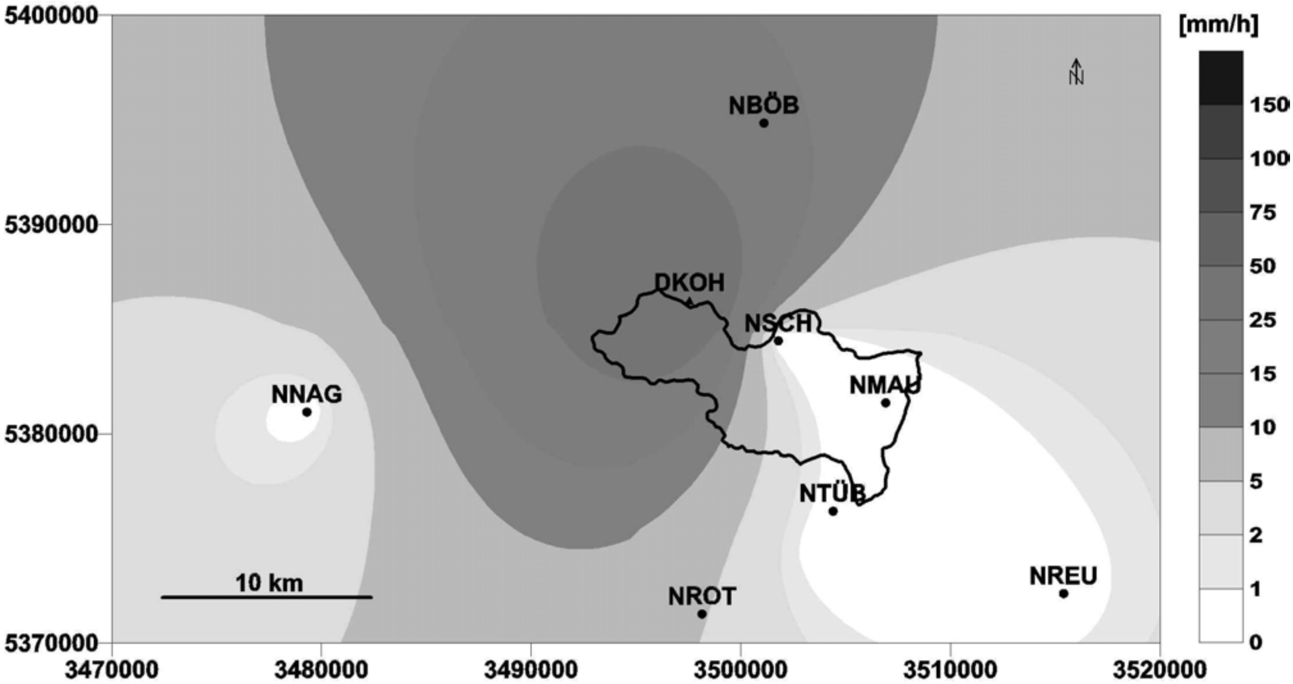

Figure 6.9: Spatial rainfall estimation, Kriging with radar rainfall (Z-R A =300, B =1.5) at 8 rain-gauge locations, 31.08.01 20:10

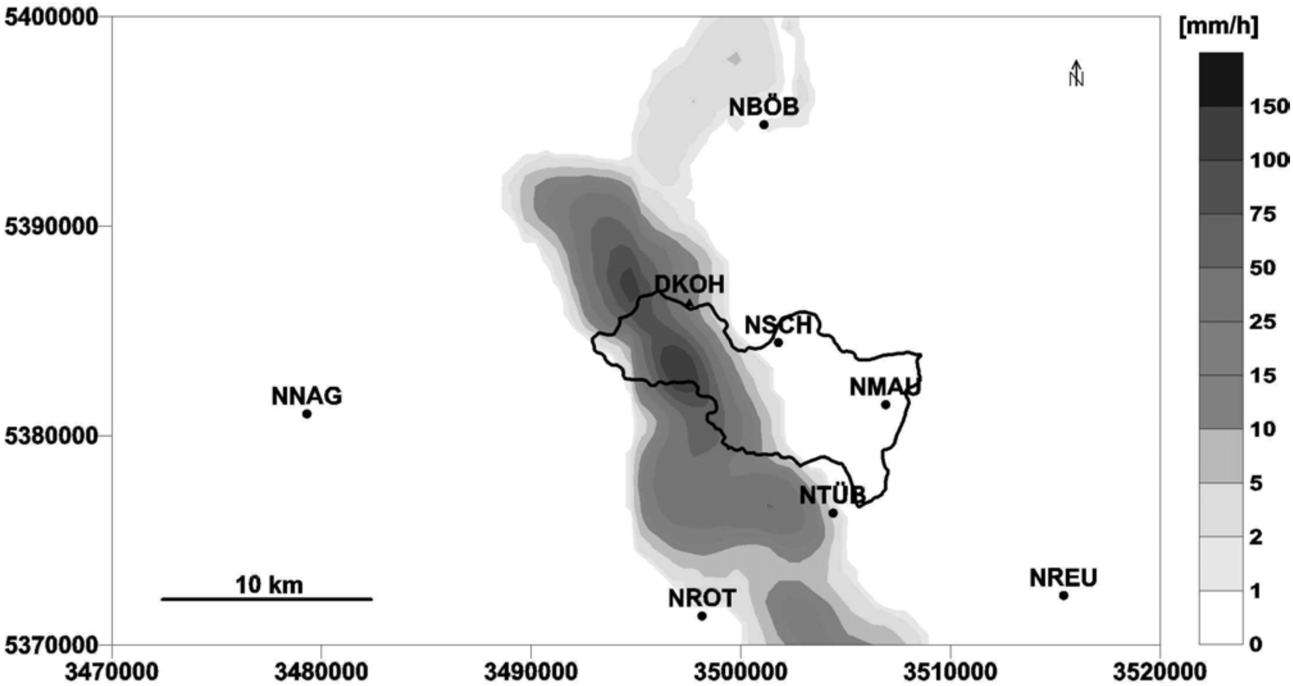

Figure 6.10: Spatial rainfall estimation with Merging, using radar rainfall and rain-gauge data, masked with a binary radar rain-field, 31.08.01 20:10

7 Rainfall forecasting

7.1 Introduction

Quantitative rainfall forecasting is of great interest in hydrology for improved, and with a longer lead time, flood and flash-flood warning systems. While for the flood prediction of large catchments with areal extensions in the order of several thousands of square kilometers and response times in the order of several hours to days, the large scale rainfall forecasts by Numerical Weather Prediction models (NWP) are usually sufficient to at least assess general trends, they fail for small catchments. A reasonable prediction of rainfall in small, fast-responding catchments requires a precise estimation of initial states which is normally only achieved by direct observation and high spatio-temporal forecast resolution. Even then, a satisfying forecast quality is only achieved for forecast horizons of a few hours and hence the term 'nowcasting' was coined for this type of forecast.

The important question about the limits of predictability at various temporal and spatial scales was assessed by many authors. Based on simulation experiments, Islam et al. (1993) suggested that for space-time scales of the order of 2 hours or less, and averages over 2 to 100 km^2, useful predictions are restricted to a 3-hour lead time at best. This system-immanent limit of predictability stems from the partly chaotic nature of the rainfall process and of our limited ability to observe all relevant physical parameters in sufficient resolution. Moore (1995) states in that context that each scale of motion in the earth's atmosphere is associated with an intrinsic finite range of predictability. Whilst the largest scale motion may be predictable several weeks ahead and those at synoptic scales a few days in advance, the motions of convective systems can be predicted only a little more than an hour ahead. Even with detailed observations of the phenomenon in time and space supported by a high level of model description, these limits cannot be breached due to the chaotic nature of atmospheric motion (Lorenz, 1993). According to Austin and Smith (2001), this is presently acknowledged in large-scale NWP, which are usually run in the 'ensemble mode', wherein the governing equations are solved for a number of times with small perturbations in the initial values to quantify the range of possible outcomes based on uncertain input.

With the special data and process description requirements for nowcasting in mind, a multitude of different techniques was developed. Nakakita et al. (1996) classified operational short-term rainfall prediction methods into three categories: Those that extrapolate the movement pattern of a horizontal rainfall distribution, those that use the principles of water balance and thermodynamics with a conceptual rainfall model and those that either use the full set of conservation equations at the mesoscale or use a method that reduces the grid size of Numerical Weather Prediction models.

In the following, a more detailed sub-division into five major classes, including some special cases, was undertaken.

In the times when the principal source of rainfall observation was rain-gauges, a simple statistical approach was developed. Model basis were the empirical, joint distributions of rainfall duration and rainfall sum from long-term observations. Knowing the rainfall sum and duration of an actual rainfall event at a rain-gauge up to present, it was then possible to assess the probability distribution of the remaining duration and volume of the current rainfall event. Klatt and Schultz (1983) developed and applied such a model for operational flood-forecasting in combination with a distributed rainfall-runoff model.

The second and, due to its relative simplicity, currently most popular nowcasting technique are the advection based models. In principle, they use a series of previous radar images to extract a distributed or mean field advection vector from pattern recognition or covariance maximization and extrapolate it into the future, as can be seen in Bremaud and Pointin (1993) or Bellon and Zawadski (1994). This straightforward approach however assumes simple rain-field displacement and does not explicitly account for rain system dynamic evolution, which results in a considerable forecast error. Austin and Smith (2001) commented that the primary reason why advection forecasts fail to achieve universal success does not originate from errors in the forecast advection velocity but is a result of the fact that the spatial rainfall fields exhibit variation in time as well as space, i.e. the precipitation structures of interest undergo internal development as they are advected. Nevertheless, most operational nowcasting is based upon cloud and rainfall pattern advection. Examples of some routinely issued nowcasting alert systems based on field advection are the British GANDOLF and HYRAD project (Moore et al., 1993), the French 'Synergie' and the German MAP project.

A logical step from simple field advection was then to add a means of precipitation structure development to the mere displacement. A multitude of models have been developed, ranging from stochastic to multi-fractal approaches and topography-triggered rain-field development.

The 'String of Beads Model', as explained in section 2.4.1 and Clothier and Pegram (2001) and Pegram and Clothier (2001), in nowcasting mode is a typical example of the stochastic approach. Here, the rain-field evolution is jointly modelled through auto-regressive processes on two hierarchical scales, the (radar-) image scale and the (radar-) pixel scale. On image scale, the coverage and mean rainfall intensity are nowcasted using a bi-variate AR-process, on pixel scale the evolution of each rain-cell is forecasted with an uni-variate AR-process. The forecasted pixel field is then scaled to match the forecasted image scale properties and then shifted using the advection forecast. It should be noted that the pixel forecast includes a spatially correlated random component which is assumed to be isotropic and constant over time.

Seed (2001) also proposed an advanced advection based nowcasting system: S_PROG. In addition to a distributed advection field forecast, it exploits the observation that rain-fields commonly exhibit both spatial and dynamic scaling dependent properties i.e. the lifetime of a feature in the field is on the scale of the feature (large features evolve more slowly than small features) and that features at all scales are present in the field. The temporal evolution of each level in the cascade is modelled using a simple auto-regressive lag-2 model.

Another obvious source of rain-field structural development is the interaction with topography. Kataoka et al. (2001) considered this in a short-term rainfall prediction model based on linear extrapolation. Firstly, a field in which non-orographic fields caused by original meteorological disturbances is derived from a calibrated radar field. Secondly, the movement of the non-orographic field is predicted. Finally, after moving the non-orographic field, the predicted rainfall is estimated taking the orographic effect into account. Up to a lead time of 3 hours, predictions agreed well with observations.

Applying advection techniques in operational nowcasting, forecasters were often not quite satisfied with the results from purely automated forecasting procedures and had the notion that an experienced forecaster could at times outperform them. In an attempt to combine the advantages of both methods, the interactive nowcasting system FRONTIERS was developed in Great Britain by Brown et al. (1994) for operational use. Here, a meteorologist manually defines the principal precipitation structures in a radar image which are then automatically forecasted with respect to size and intensity evolution. The obvious disadvantage of this procedure is the compulsory human presence in the forecast process and the subjective bias of the respective meteorologist on duty which makes it impossible to reproduce results. Although the interactive approach is therefore limited to larger forecasting organizations, good performance justifies its application where possible.

Looking at precipitation as an agglomeration of individual structures rather than a spatially coherent phenomenon, tracking methods as another nowcasting technique were developed, mainly with the forecast of convective events in mind. In general, tracking techniques try, in contrast to the manual interactive systems described above, to automatically identify individual rainfall structures in a radar image. For each element, an analysis of its displacement direction and velocity and its evolution in size and rainfall intensity is performed and extrapolated into the future. Some more advanced systems allow the merging and splitting of elements as well as the birth of new and the decay of existing ones. A typical tracking nowcasting system for lead times of up to 1 hour was developed by Chen and Kavvas (1992). The rain-field is decomposed into single, coherent elements by threshold analysis. The elements are represented by polygon edges and the centroid. A statistical adaptive scheme is used to forecast the changes in each of these elements in time and a polynomial function is used for the forecast of the cells. Birth, decay, merging and splitting are also possible. The composition of these elements forms the complete rain-field with respect to its spatial configuration, location and rain intensity texture at each forecast time-step. Focusing on the nowcasting of thunderstorm cells defined as an area larger than a certain threshold, having intensities exceeding another threshold, Dixon and Wiener (1993) developed the TITAN model. Nowcasting of convective cell position and size is carried out via a weights linear fit of storm track history and allows for merging and splitting. A similar model, SCOUT II, was developed by Einfalt et al. (1990).

While all of the above methods considered the physical processes of dynamic rainfall formation and evolution only indirectly in the form of statistical, empirically derived parameters and are designed for, and limited to, short-range, short-term rainfall nowcasting, completely different approaches originated from the process-oriented description of rainfall. With the poor performance of NWP's for small-scale rainfall nowcasting and the lack of physical justification of the purely stochastic models in mind, physically based, conceptual models tailored to smaller scales were developed as an alternative.

The concept of a simplified representation of rainfall dynamics as a goal, Georkakakos and Bras (1984) proposed a dynamic approach using ground based meteorological observations. The model, typical for most of the conceptual rainfall models, rests on the conservation of mass and momentum laws in which state variables and boundary conditions are parameterized directly in terms of ground variables. In verification studies, it was shown that the model forecasts outperformed persistence and were somewhat better than the pure advection.

A further improvement of conceptual models was obtained by parameter estimation and updating using spatially highly resolved observations, namely from radar and satellite. Georkakakos and Krajewski (1991) first proposed to combine radar observations with physically-based rainfall models. They concluded that under most scenarios of radar data accuracy, adding radar observations results in moderate to significant forecast improvements. Based on the conceptual model of Georkakakos and Bras (1984), both Seo and Smith (1992) and French and Krajewski (1994) proposed real-time rainfall forecasting models which combine radar observations with physically based models of rainfall. The model of Seo and Smith (1992) consists of a physically-based component to estimate the liquid water content and a statistical component to forecast it. For parameter estimation, it includes radar data, but lacks a means of accounting for observation errors. A further development of French and Krajewski (1994) uses both radar and satellite data to predict both convection and advection dynamics. Data sources used for parameter estimation are radar reflectivity, satellite infrared brightness temperature, ground-level air temperature, dew point temperature and pressure. Advantages of this approach include the vertically integrated definition of liquid water content and the objective use of remote sensing observations, the incorporation of physically based representation of convection and advection and the restriction to only two parameters that are related directly to model physics.

Further work was carried out by Zawadski et al. (2001), who assimilated radar data into a physically based, cloud resolving model for rainfall nowcasting up to 1 hour. Here, the near ground refractivity index was used to diagnose a high-resolution, two-dimensional distribution of relative humidity in the mixed layer. The system was a significant improvement compared to nowcasting methods based on Lagrangian persistence.

At that stage, basically three independent rainfall forecasting procedures coexisted, each limited to a certain scale in space and time: Advection-based models performed well in the ultra-short range, physically based, conceptual models in the range of up to a few hours, and NWP's in the range of several hours to days. It then seemed reasonable to combine the three in a hybrid model where NWP parameter estimation is improved by local observations from radar or rain-gauges and NWP output in turn sets boundary conditions for the intermediate range forecasts over small areas.

Nakakita et al. (2001) confirmed that NWP products modified to have a finer scale in lower layers have a potential to be utilized in physically based, short-time rainfall prediction with radar information in a sense that the highly resolved distribution of dynamical indices such as Surface convergence, Shear, CAPE (Convective Available Potential Energy) and Richardson number explain types of generation and propagation of rainfall system quantitatively. Continuing the work of Georkakakos and Krajewski (1991) outlined above, Kozyniak et al. (2001) successfully incorporated data from a NWP into the model of French and Krajewski (1994) to enlarge forecast lead time. In Japan, Takada et al. (2001) developed a model for forecasting rainfall up to 6 hours ahead. The model comprises a meso-scale NWP and a short-term forecasting model based on the kinematic method using radar and rain-gauge data. The NWP is conditioned to observed radar data in a 3-hour pre-event run. The short-term forecasting model is then used to forecast the first 3 hours of rainfall, its output is then used to further configure the NWP for the next 3 hours of forecast. It was found that forecast results up to 6 hours coincided well with observations along with the pleasant property that the model provides a smooth connection of NWP and short-term forecasting model. Sugimoto et al. (2001b) also proved the potential for improved rainfall forecasts with hybrid models by updating a physically based, conceptual rainfall model including thermodynamics and water balance with radar data and forecasts of a Numerical Weather Prediction model by an extended Kalman filter. It is noteworthy that in the model, the conceptual rainfall model parameters are advected, not the rain itself, which allows the incorporation of orographic influences on the rainfall rates. Overall, the stochastic outperformed the merely deterministic method.

While all of the above hybrid models combined NWP and conceptual models, the LAWA work group including the German Weather Service (DWD) and the Federal States of Germany is currently combining all three types of forecasting techniques in the framework of the RADVOR project. The goal is to integrate real-time radar observations into the DWD's numerical weather model 'Lokalmodell' for forecasts of up to 15 hours. Nested within is an advection-based tracking system for local rainfall nowcasts of up to 4 hours. For further information on the topic of rainfall nowcasting, refer to Foufoula-Georgiou and Krajewski (1995) or Collier (1986).

The forecasting approach developed for the Goldersbach project was named SCM model, short for 'Spectrum-Corrected Markov chain'. Its development was influenced by the 'String of Beads Model' (SBM) described above insofar as it also follows a two-step hierarchical modeling approach on the image and the pixel scale. Also, it applies a bi-variate, auto-regressive process to forecast the image-scale parameters. However, to make the model better applicable for nowcasting purposes, several approaches of the SBM were either modified or replaced. The most important change is the use of a Markov chain approach to forecast rainfall on pixel scale instead of the auto-regressive model in the SBM. Secondly, the spatio-temporal variability of rainfall was considered to a higher degree. On image scale, this was achieved by estimating the auto-regressive nowcasting parameters individually for each of the three major rainfall types classified in chapter 4. Then, the idea of a constant, isotropic 2-dimensional Fourier spectrum describing the spatial structure of the rain-field in a radar image was abandoned in favor of an anisotropic, time-variable spectrum estimated from previous radar images. This was considered important, as own observations as well as work by Moszkowicz (2001) indicated that the spatial correlation functions observed from both rain-gauge systems and weather radar are significantly anisotropic.

In section 7.2, the principal steps, parameters and results of image-scale forecasting are outlined, followed by an introduction to the nowcasting approach on pixel scale in section 7.3. Lastly, the two are combined to the SCM model in section 7.4. Using the advection forecast developed in section 5.2, some exemplary short-term forecast results are presented in the same section. Final conclusions are drawn in section 7.5.

7.2 Image-scale forecast

Following the hierarchical rainfall modeling approach of the SBM model by Pegram and Clothier (2001), it was assumed that the development of the integral radar image behavior can be expressed by the image-scale properties WAR and IMF, whose behavior is in turn adequately described by auto-regressive processes. The test data set used for model set-up and forecast evaluation comprises simultaneous time-series of WAR and IMF from 01.03.00 – 31.3.01 in 10-minute resolution, which amounts to 56879 values. The data were checked for consistency using a threshold of permissible change: If the deviation of WAR or IMF from one image to the next exceeded 10%, the values were labeled erroneous. Also, each period of non-erroneous data pairs shorter than 1 hour was excluded to ensure that auto-covariance calculations for different lags were based on similar data sets. After data verification was completed, the time-series split into different data classes as follows: 13% were labeled erroneous, 45% contained mutual zero values, and 42% contained nonzero values. Of the latter, 34% showed WAR values lower than 0.1, only 2% exceeded 0.5. This is important as the sub-division into 3 different rainfall types was based on the WAR series (see also section 4.3). For all further investigations, the zero data pairs were excluded to avoid strong bias in mean values. In the case of zero WAR and IMF, the forecast is trivial and can therefore be treated separately.

For the calculation of WAR and IMF, advection was not taken into consideration. Although this introduces an error due to rain-fields entering or leaving the radar image, with the large size of the image (128 × 128 km) compared to its boundary line it was regarded as negligible.

As already reported by Clothier and Pegram (2001), the series cross-correlation between WAR and IMF is very high. For the data set used, it amounted to 0.90 (excluding zeroes). This suggests to jointly analyze and forecast the two parameters, an approach also taken in the original development of the SBM. Figure 7.1 shows the WAR and IMF time-series of a warm front passage with relatively low rainfall intensities between 20.03.00 08:00 – 21.03.00 08:00. It is obvious that throughout a whole range of rainfall coverages, WAR and IMF behave very similar.

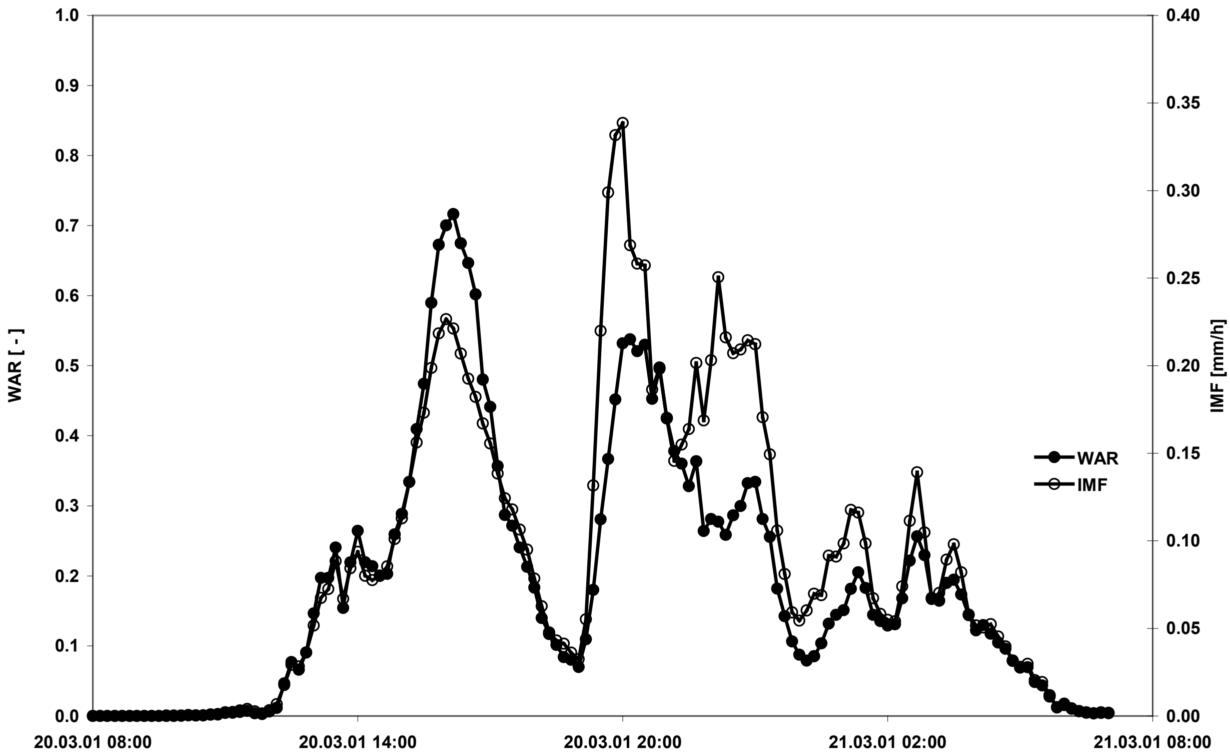

Figure 7.1: WAR and IMF time-series, 20.03.01 08:00 – 21.03.01 08:00

7.2.1 WAR and IMF normalization

Conventional time-series analysis and modeling techniques, including auto-regressive processes have been developed for normally distributed data. The WAR and IMF time-series however are highly skewed, with a majority of low values and therefore had to be transformed to Gaussian space. The transformed series are indicated with subscript 't' (e.g. WAR_t). To facilitate transfer parameter estimation, the transformation was such that the data later followed a standard normal distribution. Excluding the zero values, the range of values to transform was [0.0001,1] for WAR and [0.0001,2] for IMF. The first attempt to base the normalization on only one function for WAR and IMF, respectively was not successful. Consequently, a combination of logarithmic and exponential transfer functions for different parameter ranges was applied. Function parameters were found with an iterative optimization algorithm, minimizing the objective function of moments in (7.1). The objective function reduces to zero in the case of a perfect transformation to a standard normal distribution.

$$\left(\overline{x}^2 + (\sigma - 1)^2 + g_1^2 + g_2^2\right) \mapsto \min \tag{7.1}$$

where:

$\overline{x}$	mean
σ	standard deviation
g_1	skewness
g_2	curtosis

Apart from the parameters optimized in the course of optimization, the statistic d_λ in (7.2) was also calculated, which decreases with increasing transformation quality.

$$d_\lambda = \frac{\left|\overline{x} - \tilde{x}_{0.5}\right|}{\tilde{x}_{0.75} - \tilde{x}_{0.25}} \tag{7.2}$$

where:

d_λ	λ-statistic
$\tilde{x}_{0.5}$	median = 50% quantile
$\tilde{x}_{0.75}$	upper quartile = 75% quantile
$\tilde{x}_{0.25}$	lower quartile = 25% quantile

Furthermore, the Chi^2 test was performed for WAR_t and IMF_t to verify the hypothesis of standard normal distribution.

For WAR, a set of 4 transformation functions displayed in (7.3) was used. Judging from the moments of the transformed series given in Table 7.1, which indicate close agreement with the moments of a theoretical standard normal distribution, the transformation seems successful. Visual comparison of the theoretical, original and transformed empirical cumulative distribution functions in Figure 7.2 also indicates close agreement with the exception of the very low WAR values.

$$
\mathrm{WAR}_t = \begin{cases} -999 & \text{for} \quad \mathrm{WAR} = \text{missing} \\ +999 & \text{for} \quad \mathrm{WAR} = 0 \\ \dfrac{-\log_{\alpha_{5,\mathrm{WAR}}}\left(\dfrac{\alpha_{3,\mathrm{WAR}}}{\mathrm{WAR}-\alpha_{4,\mathrm{WAR}}}-1\right)+\alpha_{2,\mathrm{WAR}}}{\alpha_{1,\mathrm{WAR}}} & \text{for} \quad \mathrm{WAR} \quad [0.0001, 0.0103] \\ \alpha_{6,\mathrm{WAR}} \cdot \mathrm{WAR}^{\alpha_{7,\mathrm{WAR}}} + \alpha_{8,\mathrm{WAR}} & \text{for} \quad \mathrm{WAR} \quad]0.0103, 1] \end{cases} \tag{7.3}
$$

where:

$\alpha_{1,\mathrm{WAR}} = 2.8$ $\alpha_{4,\mathrm{WAR}} = 0.00009$ $\alpha_{7,\mathrm{WAR}} = 0.22$

$\alpha_{2,\mathrm{WAR}} = 3.1$ $\alpha_{5,\mathrm{WAR}} = 3$ $\alpha_{8,\mathrm{WAR}} = -2.15$

$\alpha_{3,\mathrm{WAR}} = 0.999911$ $\alpha_{6,\mathrm{WAR}} = 4.8$

	$\overline{x}$ [-]	σ [-]	g_1 [-]	g_2 [-]	d_λ [-]
WAR	0.076	0.122	2.836	9.728	0.560
WAR_t	-0.001	0.989	-0.138	-0.125	0.008
Standard normal distribution	0	1	0	0	0

Table 7.1: Statistics of original and transformed WAR series and standard normal distribution

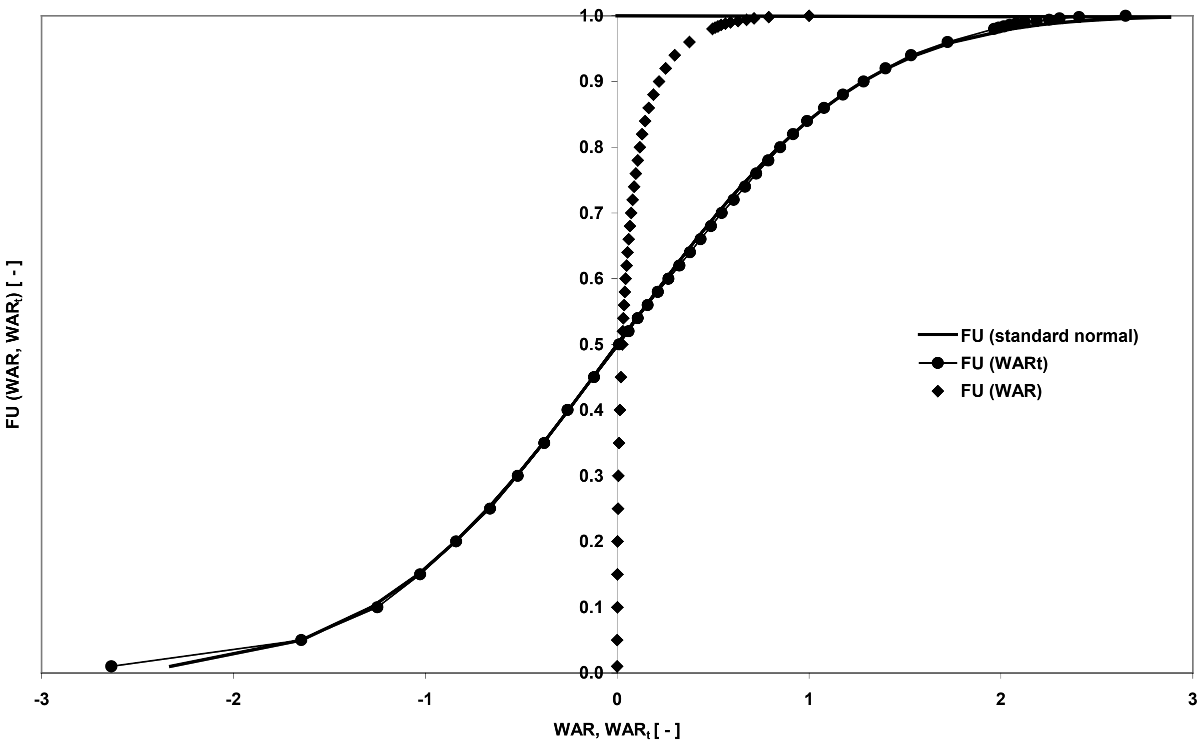

Figure 7.2: Original, normalized WAR and standard normal distribution, 01.03.00 – 31.03.01

The deviation in the low ranges is also reflected in the Chi^2 for WAR_t which was calculated from the data sub-divided into 30 classes. The high value of 249 was almost exclusively due to the contribution of the lowest class. With a permitted Chi^2 value on 50% significance level of 26.3, the hypothesis of a standard normally distributed transformed WAR_t series was obviously rejected. Bearing in mind that the error occurred for very low values of WAR, which are not relevant for floods, the transformation was retained nevertheless.

The same procedure was applied to the IMF-series. Here, a larger number of transformation functions was necessary to achieve acceptable results. The valid data range was split into 5 classes according to (7.4). Using transformation functions from the logarithmic and exponential family, then the function parameters shown in Table 7.2 were determined with the optimization routine explained above. As before, the moments of the transformed sample agree closely with those of a standard normal distribution.

$$
\mathrm{IMF_t} = \begin{cases}
-999 & \text{for} \quad \mathrm{IMF} = \text{missing} \\
+999 & \text{for} \quad \mathrm{IMF} = 0 \\
\dfrac{-\log_{\alpha_{5,\mathrm{IMF}}}\left(\dfrac{\alpha_{3,\mathrm{IMF}}}{\mathrm{IMF}-\alpha_{4,\mathrm{IMF}}}-1\right)+\alpha_{2,\mathrm{IMF}}}{\alpha_{1,\mathrm{IMF}}} & \text{for} \quad \mathrm{IMF} \quad [0.0001, 0.0003] \\
\dfrac{-\log_{\alpha_{10,\mathrm{IMF}}}\left(\dfrac{\alpha_{8,\mathrm{IMF}}}{\mathrm{IMF}-\alpha_{9,\mathrm{IMF}}}-1\right)+\alpha_{7,\mathrm{IMF}}}{\alpha_{6,\mathrm{IMF}}} & \text{for} \quad \mathrm{IMF} \quad]0.0003, 0.0084] \\
\alpha_{11,\mathrm{IMF}} \cdot \mathrm{IMF}^{\alpha_{12,\mathrm{IMF}}} + \alpha_{13,\mathrm{IMF}} & \text{for} \quad \mathrm{IMF} \quad]0.0084, 0.0606] \\
\alpha_{14,\mathrm{IMF}} \cdot \mathrm{IMF}^{\alpha_{15,\mathrm{IMF}}} + \alpha_{16,\mathrm{IMF}} & \text{for} \quad \mathrm{IMF} \quad]0.0606, 0.2062] \\
\alpha_{17,\mathrm{IMF}} \cdot \mathrm{IMF}^{\alpha_{18,\mathrm{IMF}}} + \alpha_{19,\mathrm{IMF}} & \text{for} \quad \mathrm{IMF} \quad]0.2062, \infty]
\end{cases} \tag{7.4}
$$

where:

$\alpha_{1,IMF} = 7$	$\alpha_{6,IMF} = 2.6$	$\alpha_{11,IMF} = 5.4$	$\alpha_{14,IMF} = 5.87$	$\alpha_{17,IMF} = 5.9$
$\alpha_{2,IMF} = -1.4$	$\alpha_{7,IMF} = 4.09$	$\alpha_{12,IMF} = 0.18$	$\alpha_{15,IMF} = 0.196$	$\alpha_{18,IMF} = 0.25$
$\alpha_{3,IMF} = 1.999911$	$\alpha_{8,IMF} = 1.999911$	$\alpha_{13,IMF} = -2.425$	$\alpha_{16,IMF} = -2.56$	$\alpha_{19,IMF} = -2.22$
$\alpha_{4,IMF} = 0.00009$	$\alpha_{9,IMF} = 0.00009$			
$\alpha_{5,IMF} = 3.35$	$\alpha_{10,IMF} = 3.45$			

	$\overline{x}$ [mm/h]	σ [mm/h]	g_1 [-]	g_2 [-]	d_λ [-]
IMF	0.043	0.073	3.745	22.910	0.612
IMF_t	0.000	1.000	0.000	-0.166	0.000
Standard normal distribution	0	1	0	0	0

Table 7.2: Statistics of original and transformed IMF series and standard normal distribution

Looking at the cumulative distribution functions in Figure 7.3 again reveals strong similarities to the WAR transform. In general, agreement with the theoretical distribution is acceptable except for the lower end. Binned in 10 classes, the Chi^2 for IMF_t amounted to 142 which again contradicts the normal distribution hypothesis. With the major part of 112 originating from the lowest class, the transformation was still kept as the closest approximation to a standard normal distribution achievable.

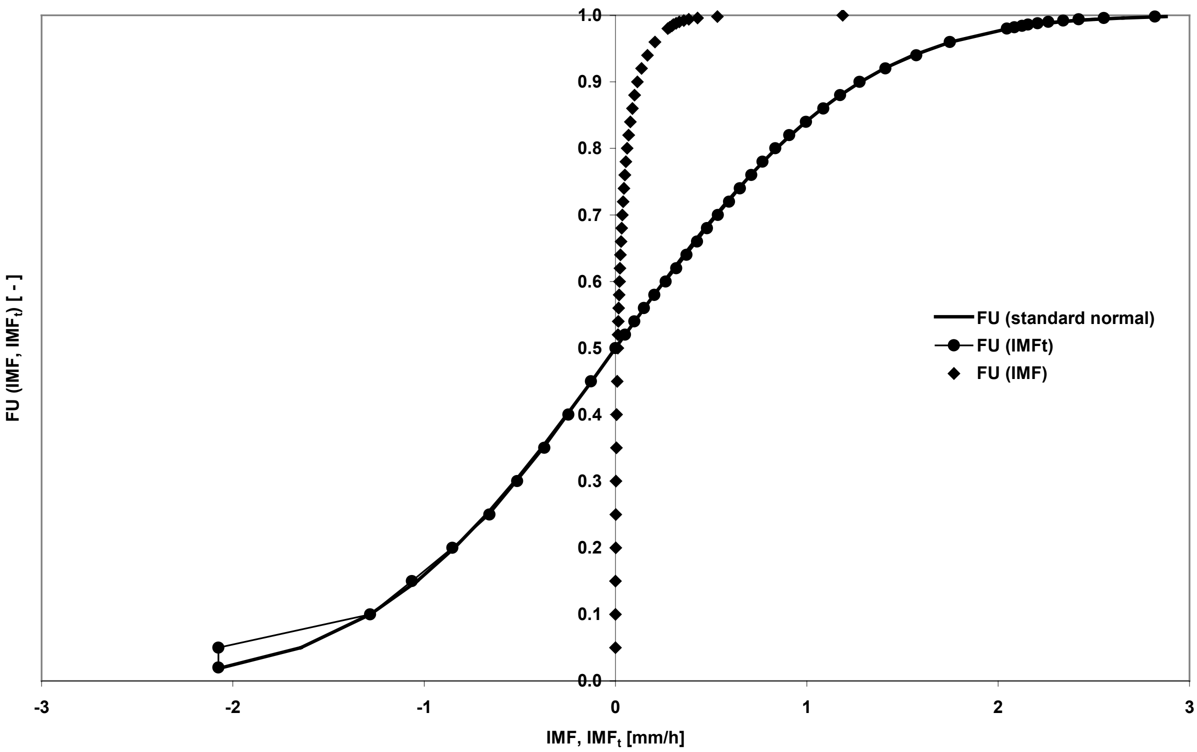

Figure 7.3: Original, normalized IMF and standard normal distribution, 01.03.00 – 31.03.01

7.2.2 Forecast parameter estimation

As mentioned in the introduction to this chapter, the forecast parameters were determined individually for the 3 principal rainfall types expressed by different ranges of WAR outlined in section 4.3. Additionally, for reasons of comparison, the forecast parameters were also calculated for the whole series without the distinction into rainfall types. With the simultaneous simulation of WAR_t and IMF_t, the uni-variate, auto-regressive model expands to a multi-variate matrix representation of the process. While the basic description of auto-regressive processes has been explained at the example of the uni-variate case in section 5.2, a short explanation of multi-variate processes, here at the lag-2 example is given here, following mainly the description in Bras and Rodriguez-Iturbe (1993).

If $\mathbf{X}(t)$ is the vector of normal variate time-series to be jointly modelled, then $\mathbf{Z}(t)$ is the zero mean transform or time-series of anomalies of X(t) according to (7.5).

$$\mathbf{Z}(t) = \mathbf{X}(t) - \overline{\mathbf{x}} \tag{7.5}$$

where:

$\mathbf{Z}(t)$	zero mean transformation of $\mathbf{X}(t)$
$\mathbf{X}(t)$	vector of n different but interdependent time-series
$\overline{\mathbf{x}}$	$n \times 1$ vector of stationary means of $\mathbf{X}(t)$
n	number of variates/ time-series

Working with the anomalies rather than the original series, a bi-variate AR(2) process can then be described by (7.6). The estimated anomaly vector for the next time-step is simply a weighted combination of the last two anomaly vectors and a random component, which shows cross-correlation between the two data vectors, but is uncorrelated in time. The random component ε(t) is assumed to follow a standard normal distribution.

$$\mathbf{Z}(t) = \mathbf{A}\mathbf{Z}(t-1) + \mathbf{B}\mathbf{Z}(t-2) + \mathbf{C}\boldsymbol{\varepsilon}(t) \tag{7.6}$$

where:

A, **B**, **C**	parameter matrices
ε(t)	$n \times 1$ vector of uncorrelated, zero mean, unit variance random components

Using the method of moments approach, Clarke (1973), Salas and Pegram (1977), and others used lag-covariance matrices to identify **A**, **B** and **C**. This requires the calculation of the lag-0, lag-1 and lag-2 covariance matrices, here denoted by $\mathbf{M}_0$, $\mathbf{M}_1$, $\mathbf{M}_2$. Exploiting the unit variance, zero mean and non-auto-correlation of ε(t) as well as the stationary properties of the covariance matrices leads to a set of three simultaneous matrix equations on the three unknown matrices **A**, **B** and **C**. Those are

$$\mathbf{B} = (\mathbf{M}_2 - \mathbf{M}_1\mathbf{M}_0^{-1}\mathbf{M}_1)\cdot(\mathbf{M}_0 - \mathbf{M}_1^{T}\mathbf{M}_0^{-1}\mathbf{M}_1)^{-1} \tag{7.7}$$

$$\mathbf{A} = (\mathbf{M}_1 - \mathbf{B}\mathbf{M}_1^{T})\cdot\mathbf{M}_0^{-1} \tag{7.8}$$

$$\mathbf{C}\mathbf{C}^{T} = \mathbf{M}_0 - \mathbf{A}\mathbf{M}_1^{T} - \mathbf{B}\mathbf{M}_2^{T} \tag{7.9}$$

where

$\mathbf{M_0}$ lag-0 covariance matrix
$\mathbf{M_1}$ lag-1 covariance matrix
$\mathbf{M_2}$ lag-2 covariance matrix
Superscript **T** denotes the matrix transpose, superscript **–1** matrix inversion.

In general, a stationary process without consideration of the random component approaches the series mean with increasing forecast lead time. As can be seen in Table 7.3, the mean of the original and transformed WAR and IMF series for each rainfall type differ considerably from each other. It should be mentioned here that the choice of the best auto-regressive model was only made among a lag-1 and lag-2 model, either uni-variate or bi-variate. This, however, did not pose an unacceptable limit to the possible range of models, as AR(2) models, although reasonably simple, require the fitting of only two parameters in addition to the sample mean and variance of the series but are able to describe a variety of time-series with qualitatively quite different behaviors (Wilks, 1995).

WAR	Mean WAR	Mean WAR_t	Mean IMF	Mean IMF_t
WAR < 0.1	0.024	-0.393	0.014	-0.366
0.1 ≤ WAR ≤ 0.5	0.211	1.201	0.117	1.209
WAR > 0.5	0.630	2.174	0.338	2.217

Table 7.3: Mean values of the original and transformed series WAR, WAR_t and IMF, IMF_t according to different rainfall types expressed by WAR

While this can be expected due to the different ranges of magnitude the mean values are calculated from, the correlation matrices shown in Table 7.4, Table 7.5 and Table 7.6 pertaining to the rainfall types, also reveal different time-series behavior. Here, for easier comprehension, the correlation matrices with values normalized to [0,1] are shown, while for the calculation of **A**, **B** and **C**, the covariance matrices were used.

lag-0	WAR_t	IMF_t
WAR_t	1	0.827
IMF_t	0.827	1

lag-1	WAR_t	IMF_t
WAR_t	0.707	0.696
IMF_t	0.703	0.766

lag-2	WAR_t	IMF_t
WAR_t	0.640	0.642
IMF_t	0.635	0.690

Table 7.4: Lag-correlation matrices for bi-variate WAR_t – IMF_t forecast for WAR < 0.1

lag-0	WAR_t	IMF_t
WAR_t	1	0.739
IMF_t	0.739	1

lag-1	WAR_t	IMF_t
WAR_t	0.990	0.730
IMF_t	0.718	0.965

lag-2	WAR_t	IMF_t
WAR_t	0.986	0.723
IMF_t	0.699	0.926

Table 7.5: Lag-correlation matrices for bi-variate WAR_t – IMF_t forecast for 0.1 ≤ WAR ≤ 0.5

lag-0	WAR_t	IMF_t
WAR_t	1	0.649
IMF_t	0.649	1

lag-1	WAR_t	IMF_t
WAR_t	0.980	0.655
IMF_t	0.588	0.973

lag-2	WAR_t	IMF_t
WAR_t	0.945	0.659
IMF_t	0.518	0.926

Table 7.6: Lag-correlation matrices for bi-variate WAR_t – IMF_t forecast for WAR > 0.5

Looking at the correlation matrices reveals several interesting properties of the joint behavior of the WAR-IMF time-series. Firstly, it can be clearly seen that all series show a strong positive correlation for time-lags of 0, 10 and 20 minutes with the highest persistence tendency for the intermediate rainfall type. Image-scale forecasts on short lead times will therefore be close to a simple persistence forecast, a fact that was later supported by the forecast results, where only at longer lead times the auto-regressive model outperformed persistence. Secondly, cross-correlations between WAR_t-IMF_t and IMF_t-WAR_t series decrease from the convective over the mixed to the stratiform rainfall type. A finding not corresponding to intuition is that the cross-correlations for the stratiform event slightly increase with increasing lag, a fact that lacks a meaningful explanation.

Applying (7.7) to (7.9) on the covariance matrices resulted in stationary processes for the convective and mixed rainfall type, while for the stratiform type, decomposition of $\mathbf{CC}^T$ was not possible due to the unusual cross-correlation behavior (for decomposition problems and solution strategies see Bras and Rodriguez-Iturbe, 1993). As cross-correlations in this case were weaker than in the other two cases, it was then decided to define individual, uni-variate models for WAR_t and IMF_t in the case of stratiform rainfall events.

7.2.3 Results

To summarize the forecasting process on image scale, the procedure is given here step by step: Firstly, transform the image-scale parameters WAR and IMF into the Gaussian variates WAR_t and IMF_t. Then select the appropriate auto-regressive model according to the rainfall type indicated by the current value of WAR. Using the current and previous observations, forecast WAR_t and IMF_t to the desired forecast horizon. To evaluate the mean behavior or general trend of the forecast, do a mean forecast omitting the random component $\varepsilon(t)$ in (7.6). For operational flood forecasting, where upper and lower probability bounds of future WAR and IMF development are important, perform a number of forecast scenarios, now including $\varepsilon(t)$. Here, a set of 100 forecasts was computed and the 90% bounds as the range between 5% and 95% exceedence probability were calculated.

Forecast performance was evaluated using the RMSE between observation and forecast, both for WAR and IMF and different forecast lead times. For reasons of comparison, the RMSE for a simple persistence forecast and an auto-regressive model estimated from all observations (without distinction of rainfall types) was also calculated. The results over the whole 1-year test period are shown in Figure 7.4. In general, the performance of the auto-regressive models is not much better than the simple persistence forecast. At small lead times of up to 20 minutes, persistence is even slightly superior to the 3-rainfall type approach. This somewhat discouraging result was already expected from the auto-correlation matrices, where the high values indicated an almost constant behavior of WAR and IMF. It should however be remembered that this result is only valid for high temporal sampling frequency and short forecast horizons. WAR time-series sampled in 6-hour intervals could presumably be modelled only inadequately by persistence. Comparing the performance of persistence vs. auto-regressive forecast, the latter wins beyond a forecast horizon of about 1.5 hours (WAR) and 1 hour (IMF). This is in contrast to the findings for advection forecast (Figure 5.5) where the simple persistence model remained superior throughout. Considering further that WAR and IMF forecasts should be available as scenario ranges and are of greater importance for larger lead times to asses the long-term rainfall development in contrast to the short time forecasts on pixel scale, it was then decided to keep and apply the auto-regressive model.

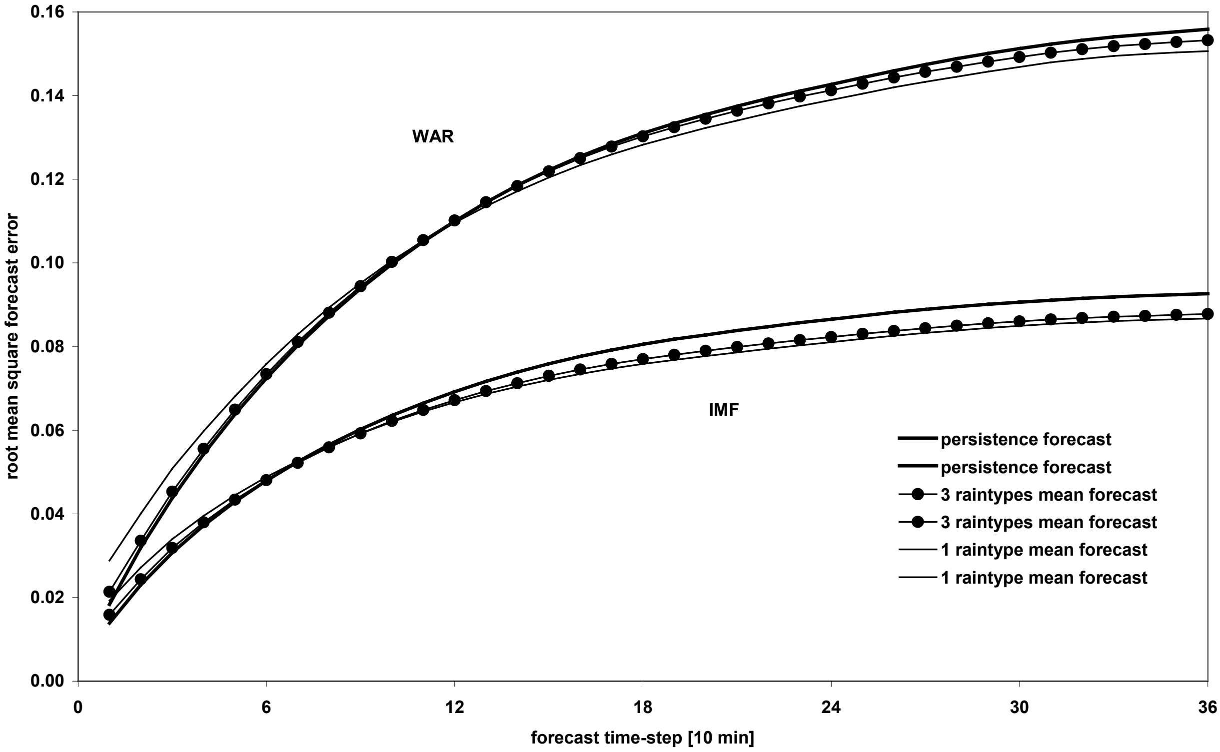

Figure 7.4: Root mean square error for WAR [-]and IMF [mm/h] forecast by persistence and mean auto-regressive forecasts using 1 or 3 rainfall types, for forecast horizons up to 6 hours, 01.03.00 – 31.03.01

Two forecast examples a the test rainfall event in March 2001 are given in Figure 7.5 for WAR and Figure 7.6 for IMF. The time-series of observations is indicated by a bold line. To keep the images concise, forecasts are given for only two points in time, 20.03.01 15:40 and 20.03.01 21:50. The persistence forecast is easily recognized as a horizontal line, simply extrapolating the last observation. The mean forecast (omitting the random component) for the 3-rainfall type forecast captures in both cases the actual trend, but gradually converges to the mean, specific to the current rainfall type, with increasing forecast lead time. The upper and lower 5% exceedence probability limits from 100 scenarios are indicated by thin lines confining the range of possible future developments between extreme increase and decay. Although the range is wide towards the largest forecast horizon, it is still useful in assessing the worst-case development of rainfall on image scale and, as can be seen from the graphs, the real observed development of WAR as well as IMF is always inside or very close to the uncertainty margins. This indicates that the white noise process produces fluctuations around the mean of the correct order of magnitude and that the arbitrarily chosen number of 100 scenarios is a reasonable trade-off between computing time and error range captured.

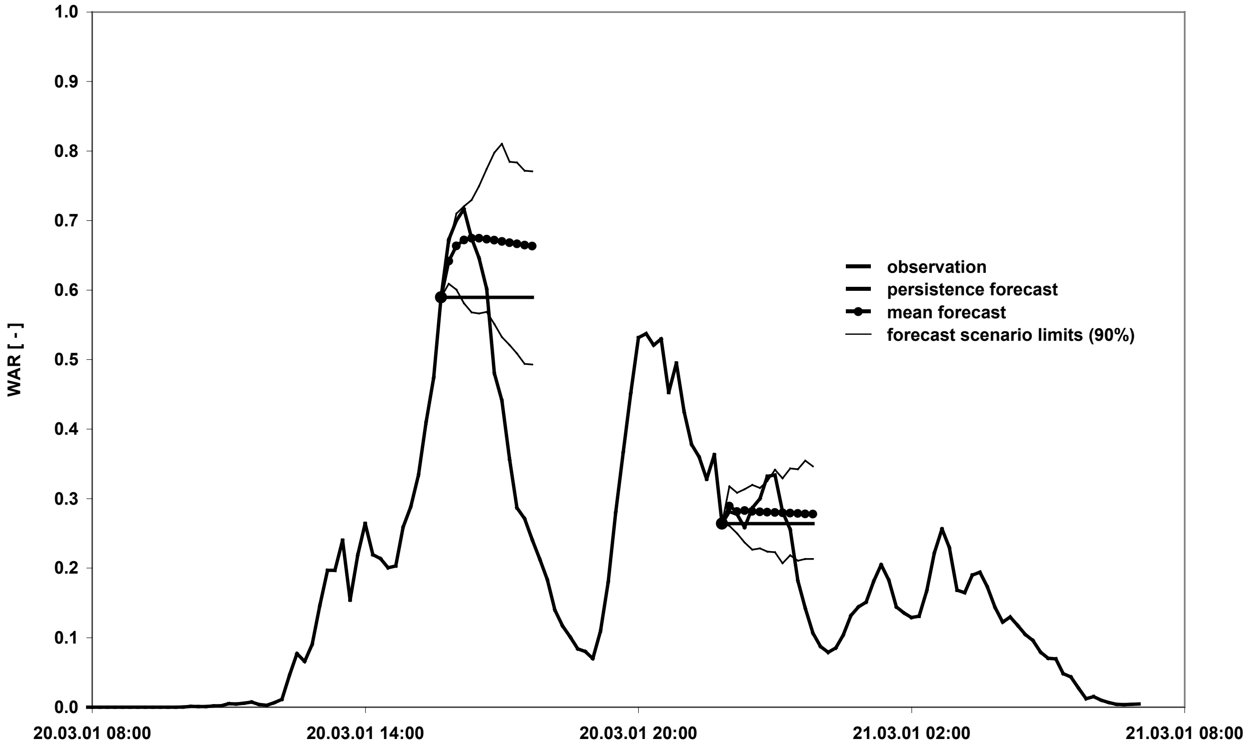

Figure 7.5: WAR time-series, observed and forecasted by persistence, mean forecast and 90% probability limits from 100 forecast scenarios, 20.03.01 08:00 – 21.03.01 08:00

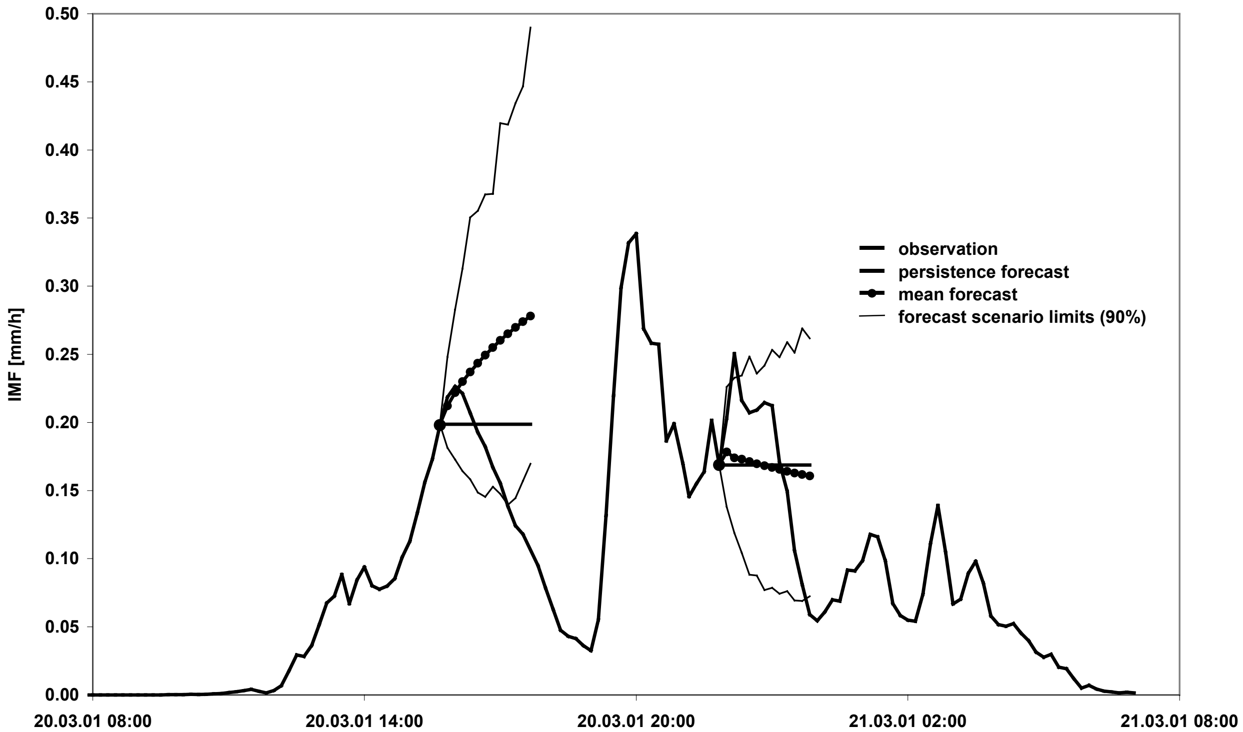

Figure 7.6: IMF time-series, observed and forecasted by persistence, mean forecast and 90% probability limits from 100 forecast scenarios, 20.03.01 08:00 – 21.03.01 08:00

7.3 Pixel-scale forecast

Rainfall nowcasting on pixel-scale is, after the image-scale forecast, the second step in the SCM rainfall forecasting approach. It is based on several principles and assumptions, which are explained here briefly. Firstly, the goal is to predict the temporal evolution of rainfall fields, not of rainfall observed at a fixed point in space. The reason for doing so is that a rainfall field (the term 'rainfall field' is used here in a rather general way for any coherent area in a radar image showing rainfall) may exist over a period of time, although it may change its location according to the current advection. It is believed that the evolution of such long-lived structures is easier to predict than the footprint it leaves at fixed points in space, i.e. the rainfall observation at these points. However, this implies that the advection vector must be known with sufficient precision. It is assumed here that, according to the findings in chapter 5, the mean field advection estimated and forecasted from Doppler observation and covariance maximization is sufficiently precise. A further, related assumption is that the spatio-temporal development of rainfall can be predicted separately over space and time and then combined to the overall forecast. The rainfall field location is predicted with the advection forecast, the temporal development, or 'life-cycle' is predicted with the SCM model.

7.3.1 Principal approach

The first attempt to forecast rainfall on pixel-scale directly followed the approach of Pegram and Clothier (2001) in the 'String of Beads Model', i.e. the application of an auto-regressive process on each pixel. Although this approach is attractive due to its simplicity, several problems were encountered in the process of parameter estimation. Firstly, the transformation and backtransformation of the strongly skewed distribution of radar rainfall observations to a normal distribution and back, a requirement for the application of an auto-regressive process, to a certain degree altered the data. Further, the estimation of auto-regressive parameters requires the calculation of anomalies, i.e. to subtract the mean from each rainfall observation. The question was which mean value to take. While for long-term simulations, a long-term, stationary mean is appropriate, for short-term forecasting this value can differ significantly from the mean of the last few observations and equally the expected mean within the near future. Another point at issue was, whether the mean value should include zero rainfall observations or only non-zero values. As the mean strongly influences the result of the auto-regressive process, after several unsatisfactory attempts, this approach was given up in favor of a Markov chain forecasting approach, which is independent from the mean. It is explained below.

Markov chain theory

Generally, the state of a system invariably changes with respect to some parameter, for example time or space. The transition from one state to another as a function of that parameter, or its corresponding transition probability, may generally depend on the prior states. The most common class of model, or stochastic process, used to represent the transition of system states is known as Markov process, or, for discrete data, Markov chain. If the system can be in a number of n different states, the process is called an n-state Markov chain. The number of previous system states that influence the transition to the next defines the order of the Markov chain. For example, a binary system with only two possible states, where only the last system state is relevant for the transition to the next state is termed a two-state, first-order Markov chain.

Formally, an m-order Markov chain can be expressed as

$$P\left\{x_{t+1} \mid x_t, x_{t-1,} \ldots\ldots, x_1\right\} = P\left\{x_{t+1} \mid x_t, x_{t-1,} \ldots\ldots, x_{t-m}\right\} \tag{7.10}$$

where:

x_{t}-1, xt, x_{t-1}	states of a system X at time-steps t-1, t, t+1
m	Markov chain order

The transition probabilities from one state to the next of an n-state, first-order Markov chain can be written in matrix notation as

$$\mathbf{P} = \begin{bmatrix} p_{1,1} & p_{1,2} & \cdots & p_{1,n} \\ p_{2,1} & p_{2,2} & \cdots & p_{2,n} \\ \vdots & \vdots & & \vdots \\ p_{n,1} & p_{n,2} & \cdots & p_{n,n} \end{bmatrix} \tag{7.11}$$

where:

P	transition probability matrix
$p_{1,2}$	transition probability from system state 1 to system state 2
n	number of possible system states

For m-order Markov chains, the number of rows of the transition probability matrix is n × m, the number of columns remains at the number of system states, n. As the states of a system are mutually exclusive and collectively exhaustive, the transition probabilities in each row of the transition matrix add up to 1.0.

In practice, the transition probabilities are obtained from conditional, relative transition frequency counts in a sufficiently large data set.

For the simulation of a system, the transition probabilities in one row are added up to a cumulative distribution function:

$$\mathbf{P_{cumulative}} = \begin{bmatrix} p_{1,1} & p_{1,1}+p_{1,2} & \cdots & 1 \\ p_{2,1} & p_{2,1}+p_{2,2} & \cdots & 1 \\ \vdots & \vdots & & \vdots \\ p_{n,1} & p_{n,1}+p_{n,2} & \cdots & 1 \end{bmatrix} \tag{7.12}$$

where:

$\mathbf{P_{cumulative}}$ cumulative transition probability matrix

From any initial state x, a state transition can be drawn from (7.12) with a uniformly distributed, [0,1] random number. From the new system state, another state transition can be simulated drawing another random number and so forth to simulate a sequence of system states of any desired length. The same applies to forecasting, where the simulation simply starts from the last observed system state.

The advantages of the Markov chain approach to short-term forecasting are, that no data transformation to a normal distribution is necessary and that no stationary mean value has to be estimated. However, as for the definition of the transition matrix a finite number of system states is required, continuous data such as rainfall intensities have to be classified, which means a loss of information. Also, large data sets are required for transition probability estimations, especially if the system is of high order and/or state.

A more formal and comprehensive treatment of the topic can be found, for example, in Katz (1985) or Wilks (1995).

System state definitions

For the application of the Markov chain approach to rainfall forecasting of each pixel individually, a special definition of system states was defined to both consider the current rainfall type as well as the state of the rainfall field in its life-cycle. Before this is discussed in detail, some abbreviations used throughout the following section are given below.

- t-2: time-step 20 minutes prior to forecast point
- t-1: time-step 10 minutes prior to forecast point
- t0: time-step of the forecast point (last observation)
- t+1: time-step 10 minutes after forecast point (forecast time-step)
- CRI: Classified Rainfall Intensity at time-step t0
- CS-1: number of Class Shifts to get from classified rainfall intensity at time-step t-2 to the classified rainfall intensity as time-step t-1
- CS0: number of Class Shifts to get from classified rainfall intensity at time-step t-1 to the classified rainfall intensity as time-step t-0
- CS+1: number of Class Shifts to get from classified rainfall intensity at time-step t0 to the classified rainfall intensity as time-step t+1 (the forecast)

The simplest transition matrix to simulate the evolution of rainfall would be to classify rainfall intensities into an appropriate number of intensity states and use a sufficiently large series of data to count the rainfall class transitions from one image to the next, thus forming a first-order model. However, this would neglect all but the last observation and consequently any information about the state of development of the rainfall field. Also, characteristics of individual rainfall types would not be considered. As all of the above was assumed to be an important indicator of the future rainfall development, the states of the transition matrix were defined as a combination of several parameters. Firstly, to account for different rainfall types, the image-scale parameter WAR was, as explained in section 4.3, split in to 3 classes to account for convective, mixed and stratiform rainfall types. The class limits are listed in Table 7.7. Secondly, the last observed rainfall intensity, CRI, was used to define the state of the current rainfall situation. In order to limit the number of system states to a reasonable number, the rainfall intensities were classified to 8 classes. From the assumption of approximately log-normally distributed rainfall intensities, the class limits increase exponentially with increasing rainfall intensity (Table 7.7). Finally, the temporal development of rainfall is captured by an analysis of rainfall intensities of the previous 30 minutes. Again, considering the development individually for each rainfall intensity level would have led to a very large transition matrix. Instead, the rainfall intensities at t0, t-1 and t-2 were classified into the previously mentioned 8 rainfall intensity classes, and the number of class shifts from one time-step to the next was calculated. The maximum class shift was limited to ±3, as larger shifts almost never occurred. As a result, the description of the current rainfall state was further refined by 7 classes covering the class shift from t-2 to t-1 and 7 classes for the class shift from t-1 to t0 (CS-1 and CS0 in Table 7.7, respectively).

WAR	
No.	limits [-]
1	[0,0.1[
2	[0.1,0.5]
3	[0.5,1]

CRI	
No.	limits [mm/h]
1	[0]
2	]0,2]
3	]2,4]
4	]4,8]
5	]8,16]
6	]16,32]
7	]32,64]
8	]64,128]

CS-1	
No.	shifts [-]
-3	-3
-2	-2
-1	-1
0	0
1	1
2	2
3	3

CS0	
No.	shifts [-]
-3	-3
-2	-2
-1	-1
0	0
1	1
2	2
3	3

Table 7.7: Classification of the Markov transition matrix input parameters

With the four parameters WAR, CRI, CS-1 and CS0 defining the state of one pixel in a rainfall field, the system was subdivided into a number of $3 \times 8 \times 7 \times 7 = 1176$ possible states. This seems to be a large number, but the huge amount of radar pixel data to calculate the occurrence frequency of each class allows such a refined distinction of states, especially as the system output, i.e. the forecast of the rainfall at the next time-step, t+1, was limited to only 7 classes. As for the input, the output is not a rainfall intensity, but the number of rainfall intensity class shifts between time-steps t0 and t+1. Adding or subtracting the predicted class shift to the rainfall intensity class at time-step t0, provides the prediction of the rainfall intensity class at time-step t+1. If this results in a rainfall intensity class beyond the range of rainfall intensity classes (1 to 8), the predicted rainfall intensity class is limited to either the upper or lower class limit (1 or 8, respectively).

Lastly, a discrete rainfall intensity has to be estimated within the predicted intensity class boundaries. This can be done by randomly drawing a value within the class limits under the assumption of a certain distribution of values. However, for the time being, a simpler method was chosen. The position of the new rainfall value within the limits of the predicted class is assumed to be the same as the rainfall observation at time-step t0 in its rainfall intensity class.

On pixel scale, the Markov chain is applied individually for each pixel in the radar image. This means, however, that by chance, one pixel might experience a rise in rainfall intensity, while its neighbor might at the same time drop in intensity. However, as neighboring pixels in an image have very likely experienced the same history, i.e. they are in the same system state, they usually behave quite similar, drawing the system transition from the same cumulative distribution of state transition probabilities. Still, as will be discussed in section 7.4, the independent development of each pixel leads to a certain dissolution of coherent rainfall fields and requires correction.

Apart from the general advantages of the Markov chain approach outlined above, the special system definition for rainfall simulation had two additional advantages. Firstly, the definition of a zero rainfall intensity class CRI = 1, allows the random development of rainfall fields from 'blue sky', i.e. a transition from zero rainfall to a non-zero value. Equally, the decay of rainfall cells (a transition to rainfall intensity class 1) is possible.

7.3.2 Parameter estimation

The transition probabilities from one rainfall state to the next were calculated from a time-series of radar data in a 256×256 pixel matrix from 01.09.00 – 25.09.01. For each time-step t0, the previous radar images t-1 and t-2 were shifted with the negative advection vector. Thus, the snapshots of each rainfall field at different times, propagating with the advection vector were shifted and 'stacked' on top of one another to investigate their development with time. Excluding all times where the advection estimates were poor (indicated by a cross-covariance lower than 0.5, as explained in chapter 5) or data were missing, a total number of 5371149 valid transitions were observed. Those were not equally distributed over all system state transitions. In fact, 55% of all 1176 possible state transitions did not occur at all. However, 77% of those were associated with the extreme intensity class shifts of ±3. This indicates that such sudden changes in rainfall intensity within a 10-minute period rarely occur. For practical purposes, it was decided that if such a state with an undefined transition probability occurs, the forecast is simply set to the previously observed value.

From the data, the rainfall 'birth rate', i.e. shifts from zero rainfall (CRI = 1) to a non-zero value (CRI > 1) occurred in 4.1% of all cases, and almost exclusively as a shift from CRI = 1 to CRI = 2. The opposite case, cell decay, was observed in 7.4% of all cases. Again, the shift mainly occurred between rainfall intensity classes 1 and 2, now only in the opposite direction.

As the complete transition probability matrix is too large to be shown here, only an exemplary sample is displayed in Table 7.8. The steep rise of the cumulative transition probability for class shift CS+1 = 0 (i.e. no change of rainfall intensity class from t0 to t+1) indicates that on the mean

WAR-level (WAR = 2), a low rainfall intensity class (CRI = 2) and no intensity change from t-1 to t0 (CS-1 = 0), rainfall intensities tend to remain stable in the future.

current system state				CS+1 – rainfall intensity shift to the next system state						
WAR	CRI	CS-1	CS0	-3	-2	-1	0	+1	+2	+3
2	2	0	-1	0	0	0.112	0.817	0.938	0.994	1
2	2	0	0	0	0	0.130	0.908	0.980	1	1
2	2	0	1	0	0	0.246	0.922	0.980	0.998	1

Table 7.8: Sample of the cumulative transition probability distribution matrix for WAR = 2, RI = 2, CS-1 = 0, CS0 = -1 to 1

7.4 Combined forecast – the SCM model

The principal forecast procedures on both the image and the pixel scale were established in the previous sections. Now, they are combined. This not only includes their mere sequential application, but also the incorporation of the advection forecast and some corrective measures to ensure the correct spatial structure of the predicted rainfall fields. The complete forecast procedure, termed SCM model (short for 'Spectrum-Corrected Markov chain') is outlined in section 7.4.1. In section 7.4.2, the model is applied on a 12-hour storm event in March 2001, where both frontal rainfall and intensive rainfall cells, embedded in large rainfall fields, occurred. The forecast quality is evaluated both for individual pixels as well as the mean areal rainfall in the Goldersbach catchment.

7.4.1 The principal steps of the SCM model

The SCM model can be subdivided into 5 steps: advection forecast, image-scale forecast, pixel-scale forecast, correction of the pixel-scale forecast to match the mean spatial structure of the previous radar images, and finally the correction of the pixel-scale forecast to match the image-scale forecast.

Advection forecast

As described in section 5.2, the mean field advection is predicted by persistence, i.e. the last observed advection vector is used for all forecast time-steps.

Image-scale forecast

On the scale of the radar image, two parameters describing the overall temporal evolution of rainfall are predicted. Those are the rainfall coverage, WAR and the mean rainfall intensity in the image, IMF. The forecast is carried out as described in section 7.2.

Pixel-scale forecast

With the pixel forecast, the development of a moving rainfall field, not the development at a fixed point in space is described. Consequently, the radar images at time-steps t-1 and t-2 previous to the forecast time-step t0 are first shifted in the negative direction of the observed advection. Then, following the procedure outlined in section 7.3, a Markov chain is used to individually predict the rainfall development at each pixel. This means that for each pixel in the radar image and each forecast time-step, a uniformly distributed, [0,1] random number is drawn to determine the answer of the transition matrix. Figure 7.7 b) shows an exemplary field of random, uniformly distributed numbers used for the pixel forecast at one time-step.

Spectrum correction

Comparing an observed radar image (shown exemplary for a radar image at 20.03.01 17:50 in Figure 7.7 a), with the 10-minute pixel-scale forecast (Figure 7.7 c), reveals several things. Firstly, although the forecast for each pixel was generated independently from the others, the main rainfall field structure is preserved. However, the large-scale coherence of the field is reduced and a number of isolated, new rainfall cells scattered throughout the image have been produced. Obviously, in terms of frequency analysis, the Markov chain forecast acts as a high-pass filter, decreasing the influence of the low frequencies in the 2-dimensional, spatial Fourier spectrum of the image. In the following section, the 2-dimensional, spatial Fourier spectrum will simply be referred to as 'the spectrum'. In order to establish a spectrum in the forecasted image that is closer to the observed one, a spectrum-correction procedure is applied.

Firstly, the mean spectrum of the radar images observed at t0, t-1 and t-2 is calculated. Information on Fourier transformation and the calculation of spectra is given in Appendix A3 or, more detailed, in Bloomfield (1976). The mean spectrum of the images is calculated as the average of each harmonic over the 3 images. The mean spectrum contains the information of the prevailing spatial structure of rainfall of the previous images. Unlike the constant, isotropic spatial spectrum of rainfall applied in the 'String of Beads Model', the mean spectrum calculated here is continuously updated and consequently reflects the current rainfall structure, including the magnitude and direction of anisotropy, if there was any present.

The mean spectrum can be imprinted on the image produced by the pixel-scale forecast, thus establishing the mean observed spatial structure in it. This procedure is also explained in detail in Appendix A3. Firstly, the forecasted image is transformed to Fourier space and its spectrum is calculated. Then, separately for each harmonic, the ratio of the mean and the forecasted spectrum amplitude is calculated. Each harmonic of the forecasted image is then multiplied by the square root of this ratio, forcing the forecasted spectrum to be identical to the mean spectrum. Finally, the adjusted, forecasted image is transformed back to normal space by the inverse Fourier transform. In Figure 7.7 d), the forecasted image, adjusted to the mean observed spectrum, is shown. Compared to the uncorrected image, the image shows a higher spatial coherence, which resembles that of the observed image.

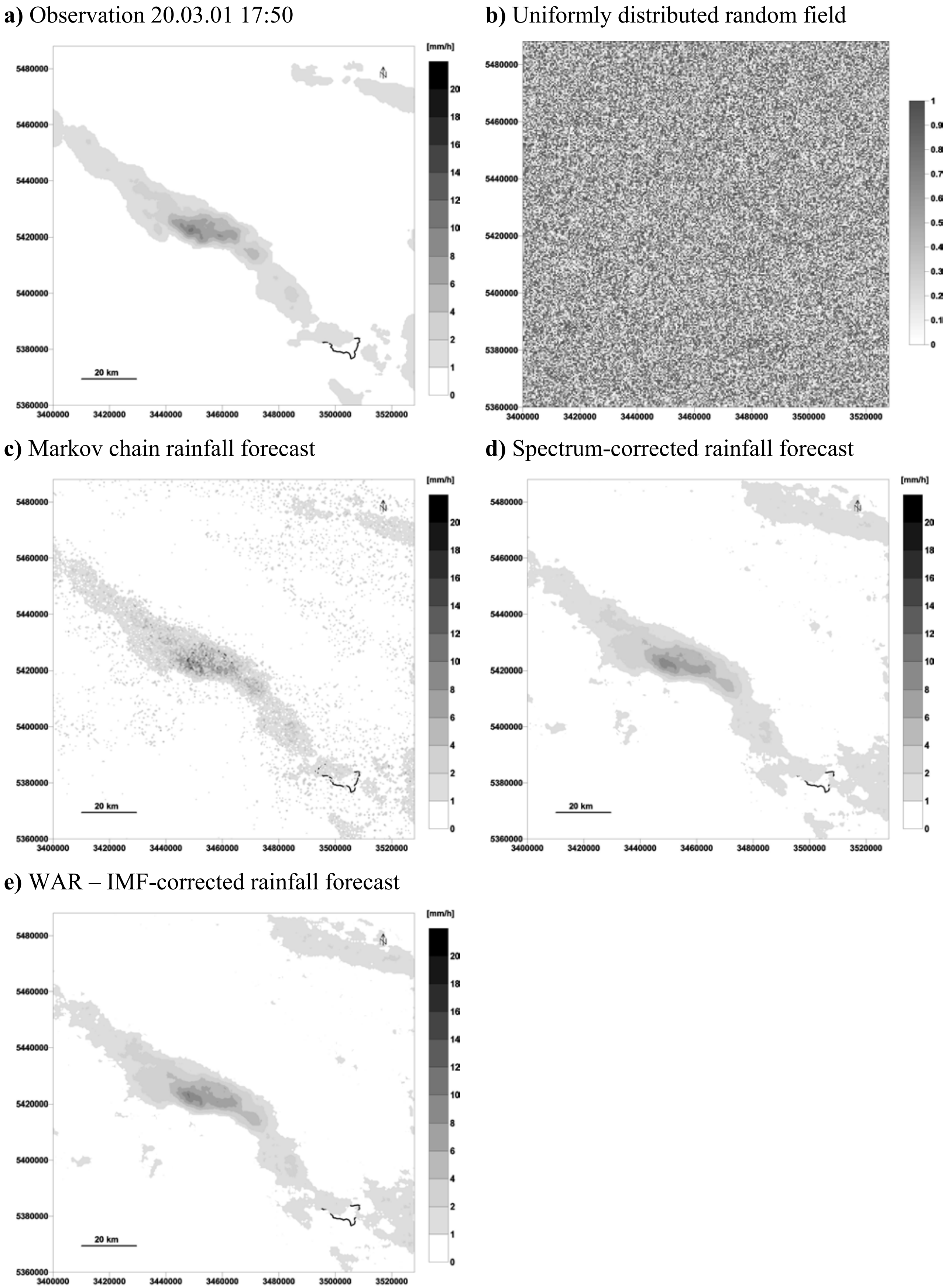

Figure 7.7: Principal steps of the SCM model

WAR-IMF correction

After correction of the forecasted image with respect to its spatial structure, the image is further adjusted to the mean rainfall coverage (WAR) and the mean rainfall intensity (IMF) according to the image-scale forecast. As this is done mainly multiplicatively, the spectrum is almost completely preserved. Firstly, all rainfall intensities in the image are ordered by magnitude. If the number of non-zero values is higher than the predicted WAR-value, all pixels in excess of that number, starting from the lowest value, are set to zero. If the observed number of rainfall values higher than 1 mm/h (the limit for a pixel to be considered as rainfall pixel) is lower than the predicted WAR, the rainfall rate in the required number of additional pixels is raised to 1 mm/h. With the correct coverage established, the mean rainfall rate is then calculated and multiplicatively adjusted to match the predicted mean rainfall intensity. As this might affect the number of pixels showing rainfall intensities larger than 1 mm/h, the image is again corrected for coverage and so forth, until after a number of iterations, both coverage and mean rainfall intensity are sufficiently close to the predicted values. Depending on the predicted WAR and IMF, this correction can significantly alter the forecasted image. If the predicted WAR and IMF are already close to the WAR and IMF of the spectrum-corrected image, however, no large changes occur. This was the case in the WAR-IMF adjustment shown in Figure 7.7 e), which closely resembles the spectrum-adjusted image in Figure 7.7 d).

Finally, the forecasted image is shifted in space according to the predicted advection vector, a 10-minute forecast of a radar image is completed. Taking now the forecasted image as the last 'observation', the whole procedure is repeated for the next forecast time-step until the desired forecast horizon is reached.

As the SCM model is stochastic in nature, any desired number of forecast scenarios can be produced from one initial system state, defined by the last three observed radar images. Computing scenarios is helpful to get an idea about the range of possible, further developments of rainfall and to identify worst-case developments.

7.4.2 Application and results

The SCM model was applied to a storm event in March 2001 which extended over several days. In the course of the event, a 12-hour period from 20.03.01 12:00 – 21.03.01 00:00 showed a very distinct rain-front moving through the range of the radar, followed later by a period of widespread rain with embedded areas of intensive rainfall. Observed sequences of 30-minute duration for both the front and the widespread rain are shown in Figure 7.8 a), b), c) and Figure 7.9 a), b) and c), respectively. In the same figures, in images d), e), f), the corresponding rainfall forecast of the SCM model is shown. Starting with a 10-minute forecast in images d) , the forecast lead time increases in 10-minute increments. Consequently, images e) show a 20-minute forecast, images f) a 30-minute forecast. However, the forecast sequence is only one exemplary realization of many possible rainfall scenarios. It is only due to space constraints that not more forecast scenarios of the same period of time are shown.

Both in the forecast of the frontal system (Figure 7.8) and the widespread rain (Figure 7.9), south-westerly winds prevailed. Consequently, with the continuous propagation of the forecasted rainfall fields, more and more blank pixels at the western and southern border occur, while the forecasted field leaves the radar range in north-easterly direction. After roughly 1.5 hours, it has left the radar range completely; the forecast is reduced to a zero rainfall prognosis.

Looking at the frontal system only, it shows that the SCM model is generally able to reproduce and predict the propagation and development of a frontal system and to preserve its anisotropic, band-like structure. However, comparing Figure 7.8 c) and f), the forecast shows considerably more widespread rainfall as was observed. Also, looking at the sequence of forecasts in images d) through f), the increase of rainfall has occurred instantaneously between 17:30 and 17:40. This can be explained by a sudden rise of WAR and IMF in the image-scale forecast, which forces the image to a certain coverage and mean rainfall intensity. The somewhat exaggerated abruptness of the rainfall intensity transition between image e) and f) suggests that the random component of the WAR-IMF forecast is maybe too large and should be reduced.

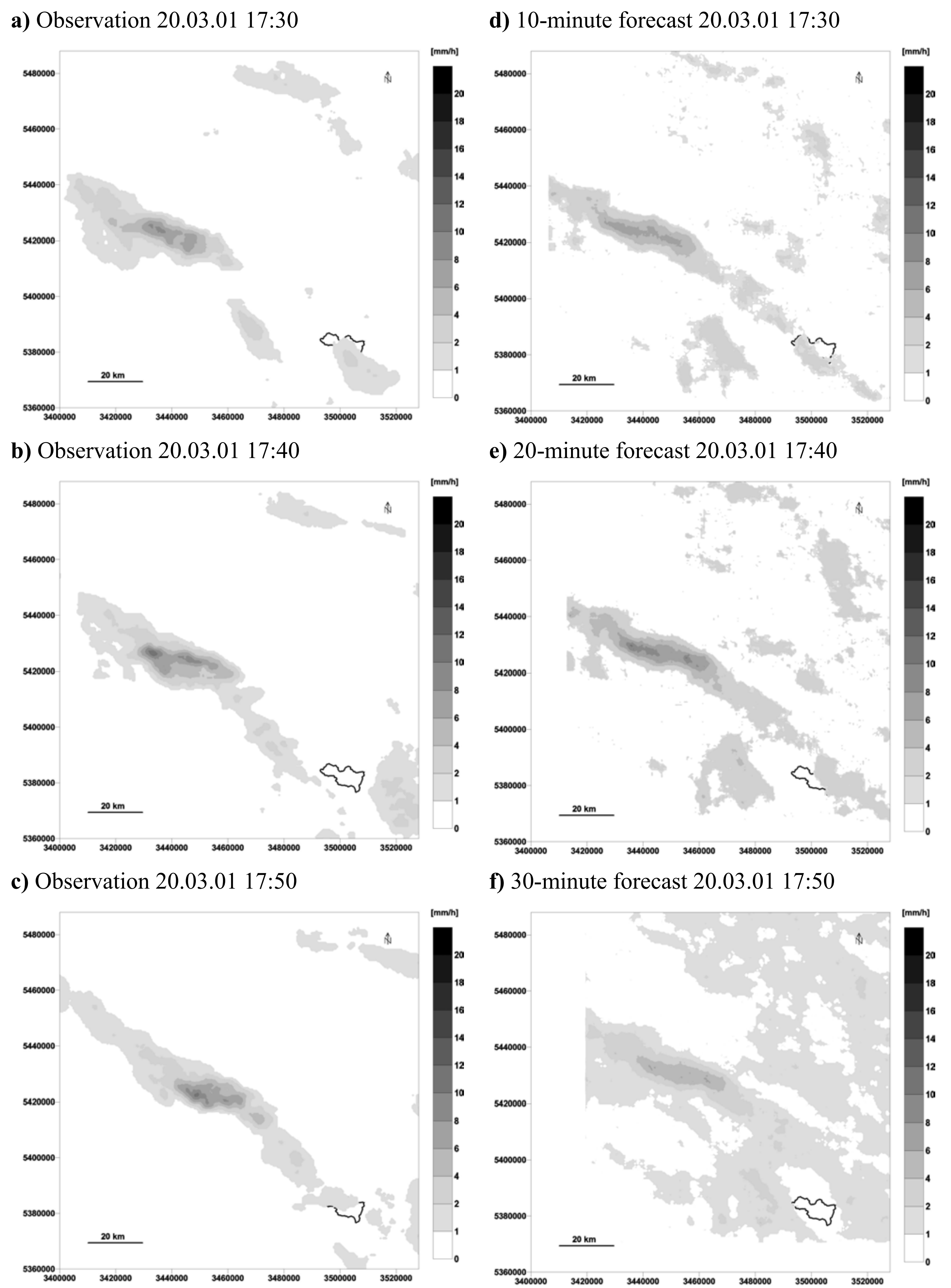

Figure 7.8: Rainfall observations and SCM model forecasts, 20.03.01 17:30 – 17:50

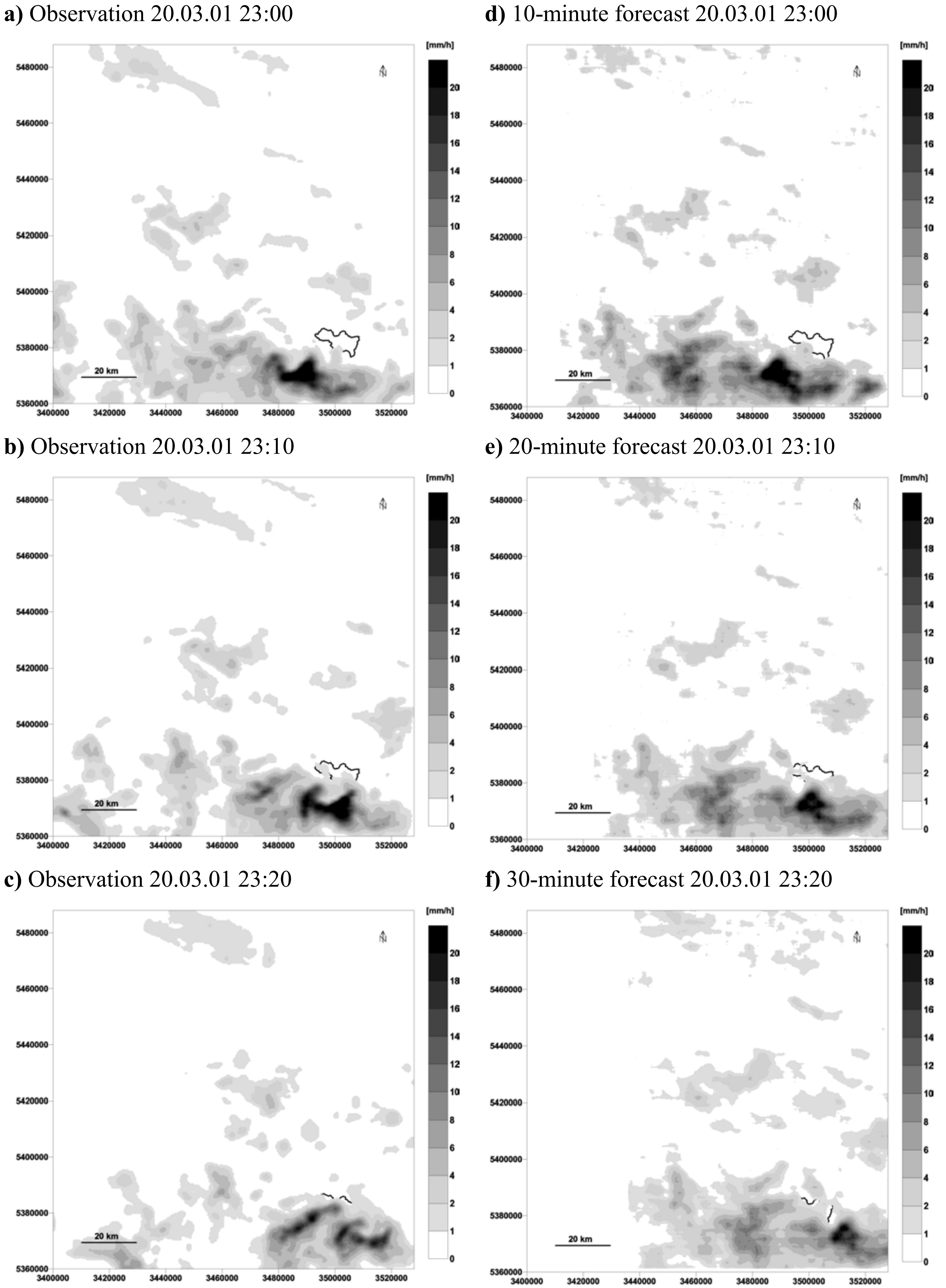

Figure 7.9: Rainfall observations and SCM model forecasts, 20.03.01 23:00 – 23:20

Comparing the observed and predicted rainfall sequence in Figure 7.9 shows that the SCM model is also able to reproduce clustered rainfall systems without clear spatial anisotropy. In the observed images, a somewhat erratic occurrence and decay of small rainfall structures with low rainfall intensities can be observed. Although the SCM model is not able to forecast their exact locations (this would require physically based, cloud-resolving modeling), it correctly reproduces the overall, erratic behavior of the observations. The area of intensive rainfall in the south-eastern corner of the observed images is also visible in the forecasts, moving out of the image in an easterly direction.

From the mere visual comparison of the observed and forecasted images, it can be concluded that the forecasts produced by the SCM model are plausible. However, the question is whether the SCM forecast is really superior to simple forecasting schemes, such as a persistence forecast, where the last observation at a pixel is the (constant) estimate of future rainfall, or a zero-rainfall forecast, where the estimate for each forecast time-step is simply zero rainfall. This question is investigated below, both for the rainfall prediction at individual pixels and for the mean catchment rainfall in the Goldersbach catchment.

In Figure 7.10, the observed time-series of mean rainfall over the Goldersbach catchment for the 12-hour rainfall event 20.03.01 12:00 – 21.03.01 00:00 is indicated by a bold line. Three periods of intensive rain towards the end of the time-series are visible. All of them are approximately of 1 hour duration, the last corresponds to the rainfall clusters visible in Figure 7.9. Also shown are the 10-minute and 60-minute forecasts as time-series: Each time-step of the observation period was considered as the forecast point once. From there, one 10-minute and one 60-minute forecast was produced. The lines in the figure connect the forecasted values from all forecast points, placed at the time-step they were forecasted for. The 10-minute forecast reproduces the observed time-series quite accurately, especially the observed and forecasted periods of intensive rainfall agree in time and magnitude. The 60-minute forecast underestimates the first two periods in magnitude, the third shows good agreement. In general, the agreement of wet and dry spells both for the 10-minute and 60-minute forecast is also satisfactory.

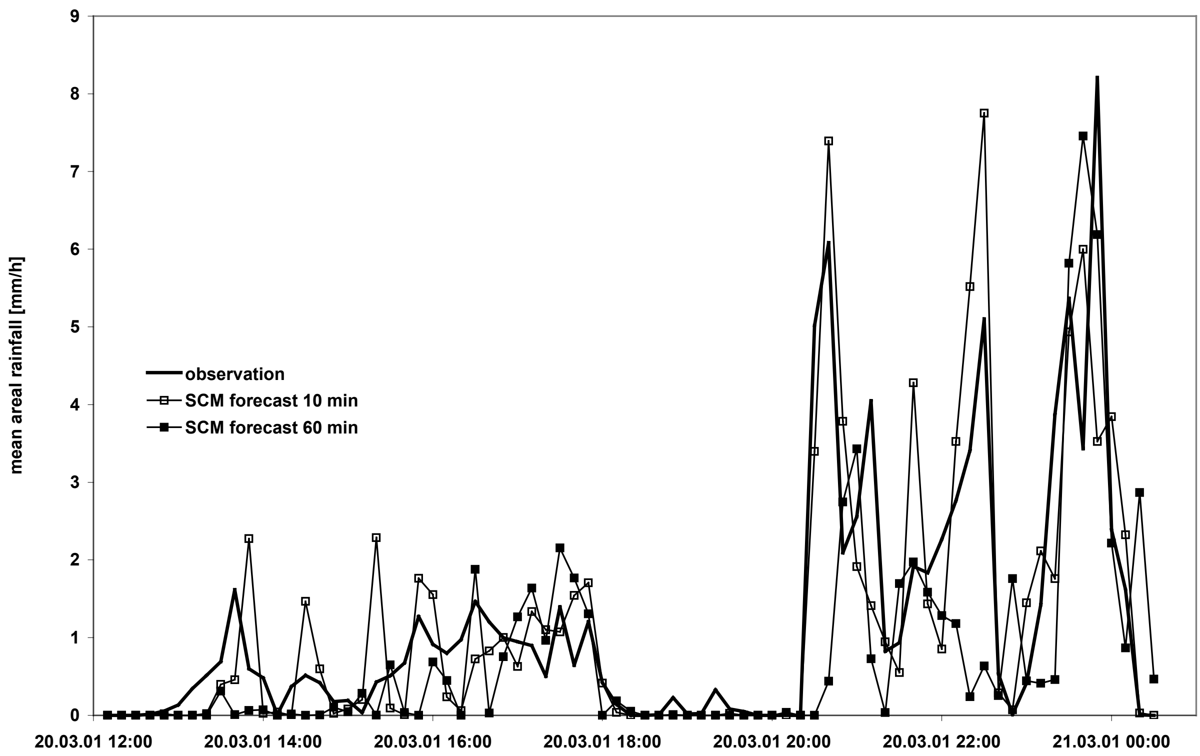

Figure 7.10: Areal rainfall over the Goldersbach catchment, observation, 10-minute and 60-minute forecast using the SCM model. 20.03.01 12:00 – 21.03.01 00:00

In Figure 7.11, the SCM forecast of areal rainfall is compared to a persistence and zero rainfall forecast. The same period of observed rainfall as in Figure 7.10 is shown, as well as the 60-minute SCM forecast and the 60-minute persistence forecast, which is simply the observed time-series shifted by 60 minutes. The zero rainfall is not drawn, but easy to imagine as a horizontal line at 0 mm/h. While the persistence forecast may work satisfactory in the case of long-lasting rainfall events with little variation in rainfall intensities, the prediction for the 3 periods of intensive rainfall fails. Each rainfall peak is, due to the persistence forecast, shifted by 60 minutes and falls in a period of low rainfall observation. As already shown in Figure 7.10, the SCM forecast captures the temporal development of catchment rainfall, although it sometimes underestimates the rainfall magnitudes. Compared the other forecast techniques, it can be regarded as superior. The zero rainfall forecast fails completely and may only outperform a very poor rainfall forecast, or equal any forecasting model in a dry period.

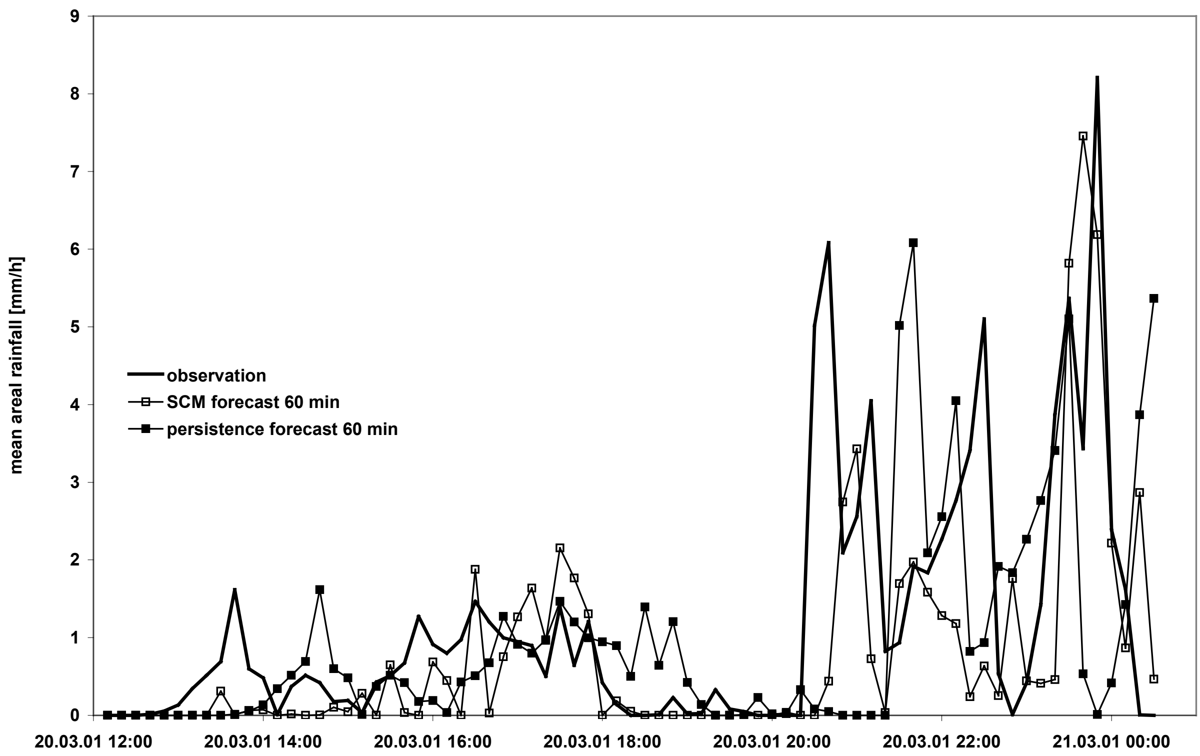

Figure 7.11: Areal rainfall over the Goldersbach catchment, observation and 60-minute forecast using the SCM model and simple persistence. 20.03.01 12:00 – 21.03.01 00:00

Apart from visual intercomparison, the quality of each forecast technique was also evaluated by the RMSE over a range of forecast horizons from 10 to 90 minutes. This was done both for the mean areal rainfall in the Goldersbach catchment (Figure 7.12) and for the observed and forecasted time-series at each individual pixel in the Goldersbach catchment. For the latter, from the 296 mean forecast errors, corresponding to the 296 time-series from each pixel covering the Goldersbach catchment, the mean was calculated (Figure 7.13). Although, due to the averaging effect when calculating the mean catchment rainfall, the RMSE of the catchment rainfall forecast is generally lower than the mean RMSE from pixel rainfall forecast, the general properties of the two statistics are similar. Firstly, the zero rainfall quality remains constant over all forecast lead times, as the observed value is compared to zero for any lead time. Also, the zero rainfall forecast performs worse than the other techniques, which can be explained by the fact that almost the entire observed time-series experienced rainfall. If the forecast would have been performed in a dry period, the zero rainfall forecasts would have been perfect, but so would have been the persistence and presumably the SCM forecast.

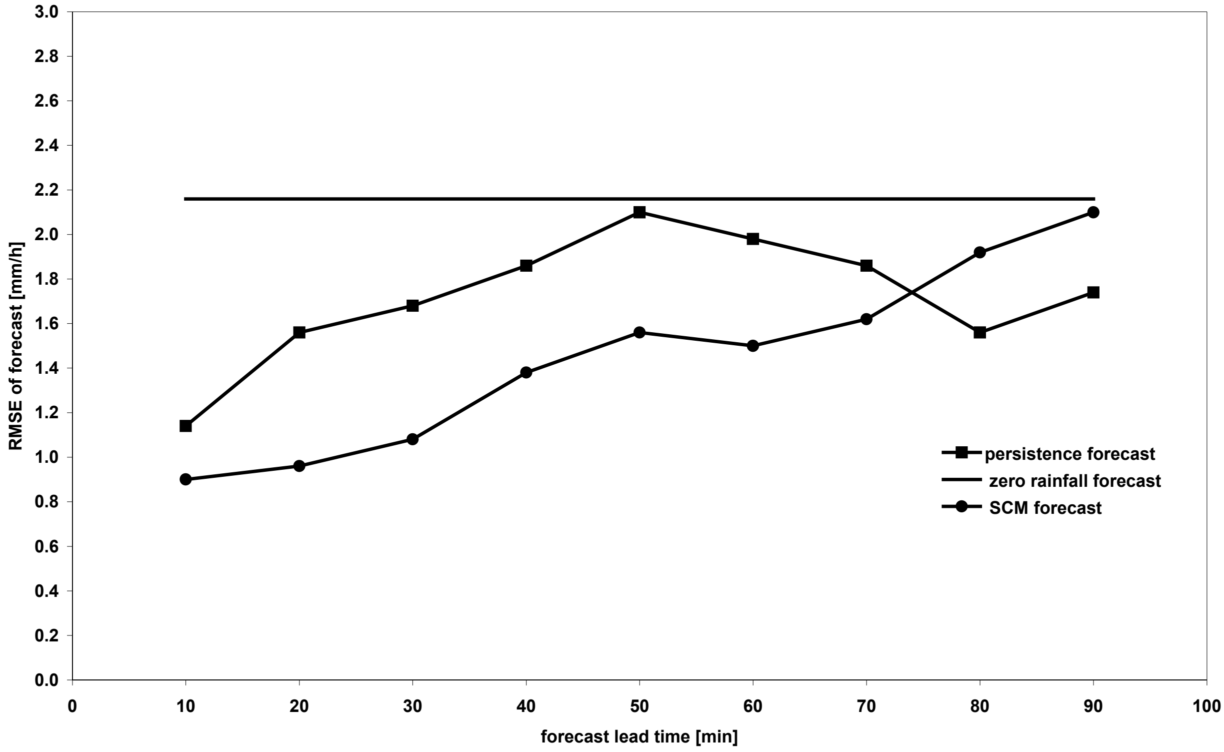

Figure 7.12: Root mean square forecast error of areal rainfall over the Goldersbach catchment using the SCM model, simple persistence and zero rainfall forecast. Forecast lead times from 10 to 90 minutes. 20.03.01 12:00 – 21.03.01 00:00

For short lead times, the persistence forecast performs considerably better than the zero rainfall forecast. At a lead time of 50 minutes, the two are comparable, for larger lead times the RMSE of the persistence forecast reduces again. This seems surprising, but can be explained by the fact that the three intensive rainfall events show a similar duration and occur with a certain periodicity of approximately 1 hour and 15 minutes. When the forecast lead time comes in the range of that lag, one observed period of strong rainfall is considered as the estimate for the following period. Purely by accident, this leads to a good forecast and thus the forecast error is reduced.

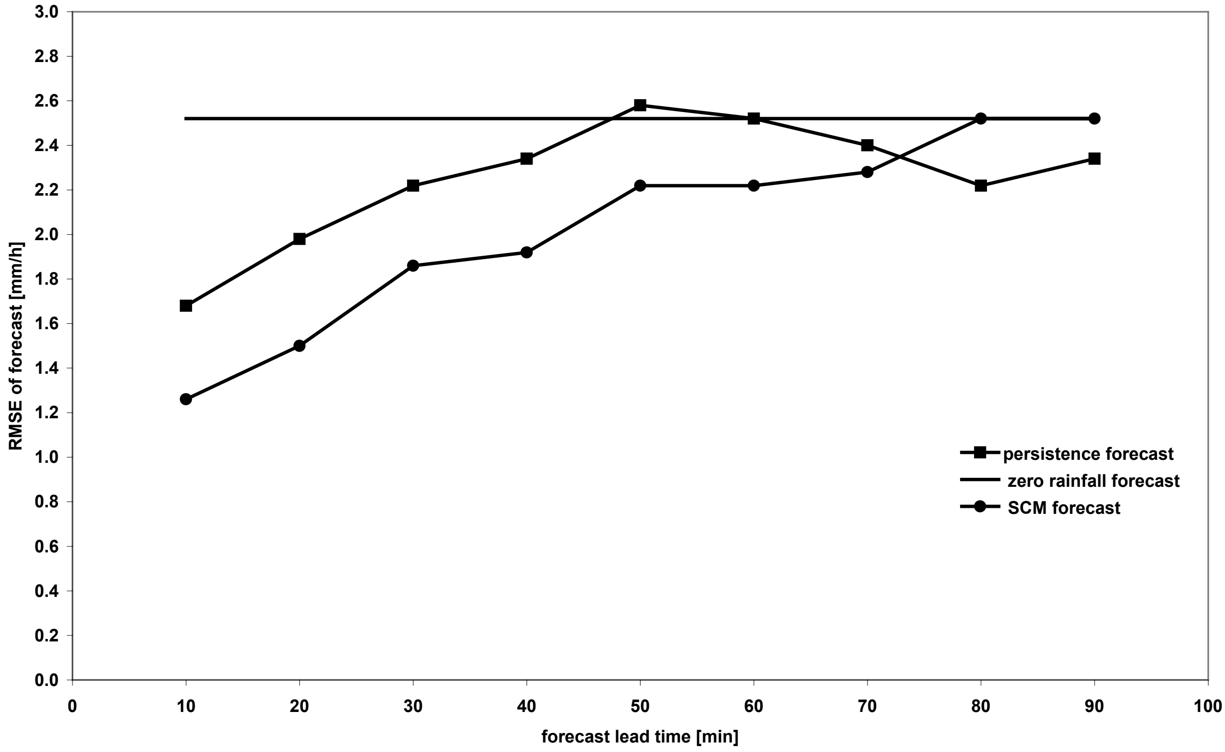

Figure 7.13: Root mean square forecast error, summed over all radar grid-cells over the Goldersbach catchment using the SCM model, simple persistence and zero rainfall forecast. Forecast lead times from 10 to 90 minutes. 20.03.01 12:00 – 21.03.01 00:00

The SCM model forecast performs better than the two other forecasting schemes, with the exception of the accidentally low RMSE of the persistence forecast at 80 to 90 minutes lead time. At a forecast lead time of 90 minutes, the SCM forecast quality approaches that of the zero rainfall forecast and remains on that level. This is due to the limited size of the radar image. As in the observed event, considerable advection occurred, the whole forecast field has left the range of the radar image after 90 minutes, and blank pixels prevail. Presumably, if the radar image would be larger, the SCM model forecast would outperform the other methods for even longer forecast horizons.

Despite this encouraging result, it should be borne in mind that first of all, if the model performs better than the other forecast methods, it does not necessarily mean that it is good enough for the desired application, i.e. accurate flood-forecasting in the Goldersbach catchment. Secondly, the zero rainfall and the persistence forecast are no serious competitors, the model should much rather be compared to other, more sophisticated stochastic, advection-based or numerical forecasting models. Nevertheless, the results are encouraging.

7.5 Conclusions

A stochastic model for short-term rainfall forecasting, or rather nowcasting, has been developed. The model uses radar data in 10-minute resolution in a range of 128 × 128 km on a 500 m grid. It provides a forecast in the same temporal and spatial resolution in the range of the radar field. Presumably, it can also be used to forecast larger fields. The model is termed SCM model, short for 'Spectrum-Corrected Markov chain'. Based on ideas in the 'String of Beads Model' by Pegram and Clothier (2001), the forecast is performed on two scales. The mean coverage and mean rainfall intensity is predicted on the scale of the radar field with a bi-variate, auto-regressive process. The development of each pixel in the radar image is forecasted with a Markov chain, which defines its system states by the current rainfall type, the current rainfall intensity and the development of rainfall intensities of the last 30 minutes. The field of forecasted pixel values is adjusted by a mean Fourier spectrum obtained from previously observed radar images to match the observed spatial structure. Finally, the forecasted field is adjusted to the predicted coverage and mean rainfall intensity of the image and shifted according to the prevailing advection vector. The model can produce forecast distributions, which makes it suitable for the assessment of upper and lower bounds of future rainfall development.

At the moment, the maximum achievable forecast lead time is, in the case of strong advection, in the order of 1.5 hours. This is mainly due to the limited size of the radar image, but also to the limitations of model's predictive power.

Optical verification of forecasted fields and statistical tests of forecast performance compared to simple persistence and zero rainfall models have provided encouraging results. However, further, more rigorous testing is required.

In the next chapter, the model's rainfall forecast scenarios will be used in combination with a rainfall-runoff model to assess its usefulness in flood forecasting.

8 Flood forecasting

8.1 Introduction

One of the first and most important tasks in hydrology has always been to predict the occurrence and development of river floods. With many cities built along major rivers for transportation reasons, people have for centuries taken a vital interest in the behavior of rivers and sought to predict it with various methods.

One of the first approaches was to simply observe upstream gauge readings and relate them to the observations on site. The advantage of this method is its robustness and computational simplicity. It works best for large catchments with meaningful upstream gauges available. For the river Rhine at Kaub, Germany, with an basin area of 103729 km^2, an operational flood forecast of 48 hours using multiple linear regression is possible (Maniak, 1997). However, for smaller catchments with short response times, in the absence of reliable upstream gauge observations, regression techniques fail to provide sufficient forecast lead times, even when current rainfall measurements are included.

The next step to achieve satisfactory estimates of future discharge developments was then to develop simple rainfall-runoff models, taking directly into account the most important flood producing quantity, rainfall, and defining catchment-specific rainfall-runoff transfer functions. The traditional approach to modeling the rainfall-runoff response of a river basin was through a lumped representation, with catchment average rainfall as input. This approach was usually justified if the point of interest was the basin outlet, and it had the advantage that it was well adapted to the classical observation means (rain-gauges and river-gauges).

Commonly, the parameter estimation for those models was achieved through the analysis of observable catchment properties and the calibration on historical events. Depending on the quality of the data used and the appropriateness of the model structure, they generally led to accurate predictions within the range of the calibration data set, but not necessarily for extreme events beyond it. Another limitation of lumped models was relevant in small to medium catchments of up to ~ 150 km^2. Here, usually the individual behavior of every section of the drainage network is relevant in a flood case. Modeling them in a lumped way usually led to insufficient model performance.

The improved availability of spatially distributed data such as radar rainfall, the development of Geographical Information Systems and the shortcomings of lumped models mentioned above, favored the development of distributed, more physically based hydrological modeling (Beven, 2001; Borga and Creutin, 2000). At first sight, the advantages of distributed models were obvious.

Concerning the rainfall input, they were supposed to be sensitive to patterns associated with a given basin rainfall, while in a lumped model, two rainfalls with the same volume but different patterns could only give the same output. With respect to catchment data such as topography or soil types, it was also intuitively believed that increased model parameter distribution would inevitably lead to increased model performance. In short, the underlying assumption during that stage of rainfall-runoff modeling evolution was that distributed models are a priori superior to lumped models. After years of experience with distributed modeling, however, this assumption was generally found to not hold true, mainly because spatial data quality did not support process description in an equally high resolution. Critical voices arose whether a distributed rainfall-runoff model can be really consistent with all different types of information it collects, and if it makes use of such detailed information (Obled et al., 1994).

Research shifted to investigation of adequate relations between input data, processes to be modelled and the desired model output. Assessing the necessary temporal resolution of rainfall data, Obled and Datin (1997) reported that, despite limitations imposed by stability conditions of numerical schemes in the model, it is more often the system itself which specifies its time-scale: if the impulse response of a given system peaks after a time T, then a time-step to describe properly any input should lie between 1/3 and 1/5 of T. Ichikawa et al. (2001) used rainfall simulations at different spatial averaging scales to assess the optimum spatial resolution of rainfall for rainfall-runoff modeling in catchments. For a 52 km^2 catchment they found the minimum resolution before information loss occurred to be 6×6 km, while a 200 km^2 catchment required at least 9×9 km input data resolution. Zhang et al. (2001) used a distributed, conceptual rainfall-runoff model with two-layer soil structure, especially developed for gridded radar data, to compare the performance of lumped and distributed models. They found that the distributed modeling approach yielded much better results than the same model used in lumped mode, especially for spatially variable rainfall events. While this result was generally in favor of distributed modeling approaches, another interesting result was the sensitivity of the distributed model on the individual input components. It showed that the distributed rainfall input significantly improved modeling results, while the parameters representing physical catchment characteristics, estimated from distributed data or used in a lumped way led to comparable results. Consequently, the model was established in a distributed manner to allow for high-resolution rainfall input, but the model parameters were kept lumped. Thus, the number of model parameters was kept small without reducing model performance.

Research studies by Michaud and Sorooshian (1994), driven on small to mid-size watersheds with very dense rain-gauge networks (1 gauge per 5 km^2) also supported the idea to use rainfall data in high resolution. In their area of investigation, the predictability of runoff significantly depended on the accuracy of the rainfall assessment. With gauge densities lower than 1 per ~ 20 - 40 km^2, results significantly degraded. Another work stressing the strong impact of rainfall data quality on rainfall-runoff modeling in small catchments was presented by Borga et al. (1997). Using radar rainfall data, they found that due to the non-linear nature of the rainfall-runoff process, bias in radar measurements can strongly affect runoff calculations. In a study catchment, a radar rainfall bias of 69% caused a bias in resulting runoff volumes of 80%.

Based on the above and many other investigations in recent years, evolution in hydrologic modeling shifted away from the uncritical belief in ever-increasing model performance by increased data and parameter distribution towards a harmonized scale of data, process description and desired model output. It should be borne in mind though, that in principle higher data resolution is always advantageous, if high data quality is maintained and if the appropriate processes are described with the data. In reality, however, especially sub-surface data are often afflicted by huge uncertainties which can, used on a fine grid to model processes on that scale, lead to worse model performance than lumped data used for lumped processes. Consequently, a semi-distributed, conceptual modeling approach which acknowledges data uncertainties by a corresponding degree of averaging and appropriate process descriptions shows good potential for accurate modeling with a manageable number of calibration parameters.

Coming back to the special case of hydrological modeling for flood forecasting purposes, some of the general findings discussed above are especially relevant, while others are only of minor importance. Bearing in mind that for forecasting purposes, the main focus is on the catchment-integrated result, namely discharge at the basin outlet, obviously highly detailed process descriptions of sub-surface water propagation are not relevant, whereas an appropriate spatio-temporal representation of rainfall and soil-moisture conditions and computational speed are important. Those requirements support the aforementioned semi-distributed, conceptual approach. In some cases even lumped models might still be sufficient, but several other, innovative ways have also been proposed.

Dawson and Wilby (1998) developed and applied an artificial neural network (ANN) for flood forecasting with a 6 hour lead time. Preliminary results were comparable in performance to lumped or semi-distributed models, with the additional advantage of ANN's to learn and improve over time. The disadvantage on the other hand is the Black Box nature of ANN's, which does not allow any process evaluation, but only establishes a link between the given input and the desired output.

This is not the case with Fuzzy approaches, where the system transfer function expressed by Fuzzy rules can easily be interpreted by the user. Fuzzy approaches can be referred to as 'grey-box' models in a sense that no numerical reproduction of physical processes is sought, but a conceptual link between input and output is established by optimization on a training data set while a user can still interpret and evaluate each step of the modeling process. Bárdossy (2000) combined on-line available data of various sources in a Fuzzy rule system. Input data used were upstream waterlevels, rainfall observations and rainfall forecasts, the desired output was on-site waterlevels. Using past observations of simultaneous input and output, a Fuzzy rule system was established. Split-sampling and cross-validation methods used to compare the Fuzzy-rule forecast with Wiener Filter and Nearest Neighbor methods favored the Fuzzy-rule approach. Stüber et al. (2000) followed a similar approach to define a Fuzzy-rule system for operational flood forecasting for the town of Trier, Germany.

The flood-forecasting approach for the Goldersbach catchment was two-fold. As the project was considered a pilot study for the feasibility of flood forecasting in small catchments in Southern Germany, the Federal State of Baden-Württemberg financed the calibration of the rainfall-runoff model FGMOD/LARSIM to the Goldersbach catchment by Dr. Ludwig consulting engineers. FGMOD/LARSIM has for several years been in operational use in the flood forecasting center (HVZ) in Karlsruhe and was therefore regarded as being suitable for the purpose. It is an event-based, conceptual model and was fitted to the Goldersbach catchment in a 500 m grid matching that of the radar rainfall data. A detailed description of the model and its performance is given in section 8.2. In short, it was found that due to the strong dependency of runoff on antecedent soil-moisture conditions in the Goldersbach catchment, the event-based model, in cases of low initial soil-moisture, modelled the rising limb of a flood too early.

As an alternative, running the model in its continuous simulation mode, LARSIM, was recommended to base the runoff simulation on estimates of the current soil-moisture conditions. This was considered reasonable, but instead of LARSIM the conceptual, semi-distributed HBV model originally developed by Bergström and Forsman (1973) was used. It was favored as it has had a long history of use and experience at the IWS. This however does not exclude the later application of LARISM and the comparison of the two continuous time models. HBV was also built on a 500 m grid to make full use of the radar rainfall data but, following the findings by Zhang et al. (2001) discussed above, the parameters describing the catchment characteristics were used in a more lumped mode. The principal HBV model structure, parameter estimation techniques and modeling performance are described in section 8.3. In section 8.4, both the FGMOD and the HBV-IWS model are used for flood forecasting under the assumption of a perfect rainfall forecast, i.e. rainfall observations were used as forecast. For the HBV-IWS model, this corresponds to the normal simulation mode, while for the FGMOD/LARSIM model, it differs from normal, i.e. post-event simulation. For forecasts, the optimization of event-specific parameters is performed in a period prior to the forecast point, not throughout the entire event. Using rainfall forecast scenarios output by the SCM model (see section 7.4), both models were finally applied to generate forecast scenarios of a flood event in July 1996 for a lead time of 3 hours. The chapter concludes with a summary and evaluation in section 8.6.

8.2 The rainfall-runoff model FGMOD/LARSIM

The original version of FGMOD (short for 'Flußgebietsmodell') was developed at the University of Hannover as a tool for event-specific simulation and forecast of floods in river basins (Ludwig, 1978). Further developed mainly by Dr. Ludwig consulting engineers, it was found to be well suited to operational flood forecasting purposes, where long-term water balance considerations were not relevant. The program system was then not only chosen by the HVZ for operational use (Homagk and Ludwig, 1998) but was also applied for flood forecasting under different climatic conditions in China (Ludwig, 1989).

While FGMOD performed well for operational flood forecasting in medium to large basins, it had the drawback that the water cycle with its different components was not reproduced, which made it inapt for the assessment of long-term hydrological issues such as land-use modifications or climate change impact. Recognizing this deficiency, the continuous time model LARSIM ('Large Area Simulation') was developed on the basis of FGMOD. This was mainly done in the course of the research project BALTEX, in which Dr. Ludwig consulting engineers was engaged, and a dissertation emanating from it (Bremicker, 2000). FGMOD/LARSIM, which includes both the original FGMOD modules and LARSIM can be applied on both grid-based as well as watershed-delineated basins. For the Goldersbach project with the focus on flood forecasting, the program was used in the event-based calculation mode, which also reduced the necessary input data to rainfall and discharge observations. The catchment sub-division was based on the 500 × 500 m grid of the radar data, so each grid-cell was assigned exactly the rainfall value of its associated radar grid.

As only the event-based modeling routines FGMOD of FGMOD/LARSIM were used here, it is explained here briefly without consideration of the larger framework of FGMOD/LARSIM. It is however referred to by its full name.

8.2.1 Model structure and parameter estimation

FGMOD/LARSIM is in principle a series of rainfall-runoff models for sub-catchments and floodrouting routines for flood propagation in rivers. For most algorithms representing the rainfall-runoff process, different options exist in the model, but for the sake of brevity only those applied in the Goldersbach case are explained.

Effective precipitation

To calculate the partition of precipitation directly contributing to discharge, the discharge coefficient function was used. Here, effective precipitation is calculated by multiplying the amount of rainfall at each time-step with a time-variable reduction factor, termed the discharge coefficient ψ. The discharge coefficient is calculated individually, as a function of interflow, for each sub-catchment. The functional relation is such that the discharge coefficient increases with increasing discharge and reduces in the recession limb of a flood, thus representing the natural saturation of the soil during a rainfall event. Calculation of ψ is done according to the following formula:

$$\psi = \min\left[\psi_{\min} + (\psi_{\text{act}} \cdot \text{BAF}) \cdot \left(\frac{100 \cdot \text{QI}}{3.6 \cdot \text{FT} \cdot \text{TA}}\right)^{\text{CAF}} ; \psi_{\max}\right] \tag{8.1}$$

where:

ψ	[-]	variable discharge coefficient
ψ_{min}, ψ_{max}	[-]	maximum and minimum allowable discharge coefficient
ψ_{act}	[-]	discharge coefficient assigned to each sub-catchment
BAF, CAF	[-]	calibration parameters specific to each sub-catchment
QI	[10^3 m^3]	index for discharge from slow interflow reservoir
FT	[km^2]	sub-catchment area
TA	[h]	calculation time-step

Baseflow

Baseflow can be set to a fixed value or to the minimum discharge observed in the simulation period. For calibration, the latter option was used, while for operational purposes, both options were applied.

Runoff concentration

The runoff concentration in each sub-catchment is calculated with a modified Clark model, which mainly consists of two parallel, linear reservoirs for the fast and slow portion of interflow, respectively. Effective precipitation is separated according to a threshold value: Rainfall above it is assigned to the fast, rainfall below to the slow interflow reservoir. Representing the sub-catchment by a rectangle of the same area, the simplified trapezoidal hydrograph from effective precipitation is used as input into either of the two linear reservoirs. Both reservoir retention constants are connected to sub-catchment geometry through the travel time according to Kirpich: the higher the travel time, the higher the retention constant.

Routing

After flow accumulation in each sub-catchment, discharge is routed in the river system. As with other processes, FGMOD/LARSIM offers a selection of alternative routing techniques, namely the methods according to Williams, a modified Kalinin-Miljukov method and several translation-retention models. To account for the different retention characteristics in the main river bed and the embankments, the routing model according to Williams (1969) was used in the Goldersbach catchment. The river and embankment geometry expressed by river length, slope and position was partly extracted from a vectorized river network map. The cross-sectional data were determined from extreme-value statistics under the assumption of bankful discharge for a two-year return flood. This empirical relation between flood magnitude, recurrence interval and channel geometry was established by Leopold and Maddock (1953) and can be formulated as follows:

$$\begin{aligned} T_H &= 0.349 \cdot HQ_2^{0.341} \\ W_H &= 2.71 \cdot HQ_2^{0.557} \end{aligned} \tag{8.2}$$

where:

T_H	[m]	main channel depth
W_H	[m]	main channel width at bankful flow
HQ_2	[m^3/s]	2-year recurrence flood

From previous investigations in the Neckar catchment, encompassing the Goldersbach catchment, a linear regression between sub-catchment size and the 2-year recurrence flood magnitude was established according to (8.3). Thus, cross-sectional data for the river system was ultimately based on sub-catchment size, if no other, more precise data was at hand.

$$HQ_2 = 0.4794 \cdot A_{sc}^{0.8068} \tag{8.3}$$

where:

A_{sc}	[km^2]	sub-catchment area

As snowfall was, from the evaluation of past flood events, not considered relevant, no snow routine was implemented in the Goldersbach model.

Parameter estimation

Before the optimal estimation of the free model parameters could be performed, a structural representation of the Goldersbach catchment with the principal components of FGMOD/LARSIM, sub-catchments, nodes and rivers had to be configured. As previously mentioned, a grid representation was chosen to match the grid of the radar data. For reasons of comparison, not only the 500 m grid supported by the radar was used, but also a 1 km grid to determine whether the additional information contained in the fine grid results in increased model performance. The main data for sub-catchment delineation were taken from a 30-m digital elevation model based on photogrammetric aerial photography and a vectorized river network based on the topographic maps of Baden-Württemberg. In the case of the 500 m grid as shown in Figure 8.1, altogether 356 elements were needed to reconstruct the basin in FGMOD/LARSIM model space, 60 of which were only needed for linking purposes and featured zero area. The 1 km grid model amounted to 88 elements with 13 connection elements.

With the principal model geometry established and the relevant process descriptors selected as outlined in the previous section, the model was then calibrated by optimization of the free model parameters on simultaneous rainfall and discharge observations from 5 independent flood events in April 1994, June 1995, July 1996, February 1997 and October 1998. The optimization criterion hereby was to minimize the deviation between the observed and modelled discharge time-series for each event, expressed by the difference of the hydrograph centroids, the difference of peak flows, the sum of square errors and the weighted sum of square errors. While most of the free parameters were considered event-independent, others were individually adjusted for each event. Event-independent parameters are:

- Threshold A for sub-division of effective precipitation into the fast and slow interflow component.
- Parameter CAF of the discharge coefficient function
- Retention constant EQD of the fast interflow reservoir
- Retention constant EQI of the slow interflow reservoir
- EKM, EKL, EKR, the roughness coefficients of the main channel and the embankments

Parameters adjusted individually for each event are:

- Baseflow, which was set to the lowest value of the event
- Parameter BAF of the discharge coefficient function

8.2.2 Parameter sets used

Based on the data and techniques described in section 8.2.1, Dr. Ludwig consulting engineers fitted the FGMOD/LARSIM model in event-based calculation mode to the Goldersbach catchment. The sub-catchment delineation based on the 500 m grid is shown in Figure 8.1. All event-independent calibration parameters were identified on the 5 flood events mentioned above.

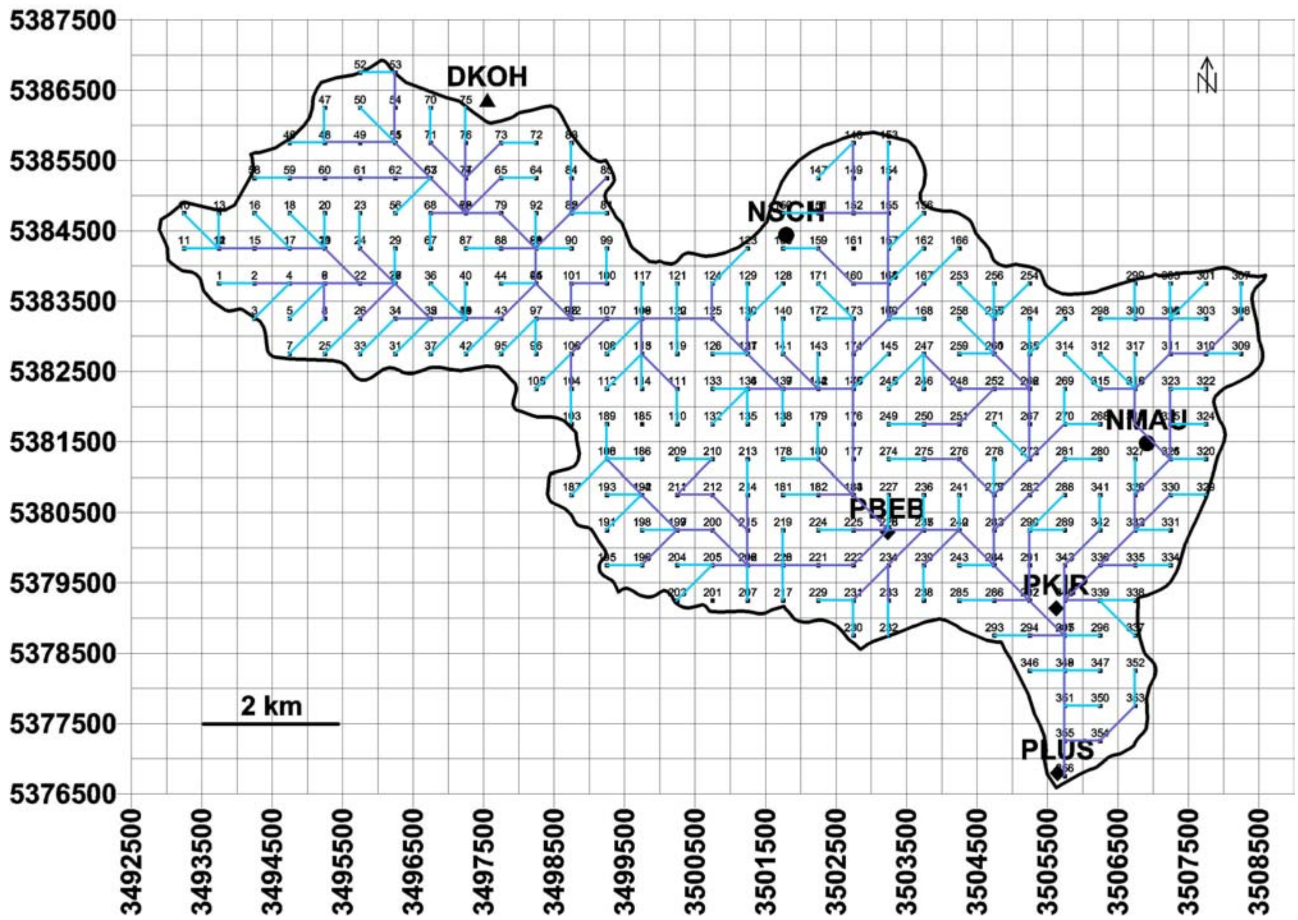

Figure 8.1: River network and basin sub-division according to 500 m grid in FGMOD/LARSIM

Together with the river roughness coefficients, which were assumed constant throughout the catchment, the event-independent parameters are shown in Table 8.1. With the static parameters fixed, the modelled discharge hydrographs for each event were optimized through variation of the event-dependent model parameters. This was done both for the model runs with radar and rain-gauge rainfall data. For each event, the adjusted parameter BAF of the discharge coefficient function is listed in Table 8.2. As only discharge observations of the two gauges PKIR and PBEB were available, CAF was kept constant throughout the entire sub-basin draining to either of the two.

		Parameter for sub-catchment PBEB	PKIR
A	[mm/h]	3	2
CAF	[-]	0.34	0.34
EQD	[-]	30	30
EQI	[-]	200	200
EKM	[$m^{1/3}/s$]	30	30
EKL	[$m^{1/3}/s$]	20	20
EKR	[$m^{1/3}/s$]	20	20

Table 8.1: Event-independent parameters of the 500 m grid FGMOD/LARSIM model

BAF Event	Parameter for sub-catchment PBEB	 PKIR
Rain-gauge data		
April 1994	0.098	0.173
June 1995	0.170	0.190
July 1996	0.196	0.079
February 1997	0.206	0.117
October 1998	0.042	0.045
Radar data		
July 1996	0.216	0.093
February 1997	0.305	0.108
October 1998	0.050	0.063

Table 8.2: Event-dependent parameter BAF of the 500 m grid FGMOD/LARSIM model

8.2.3 Model performance

In this section, the results and conclusions drawn from the calibration runs in Ludwig (2000) and Ludwig (2001) are discussed. The results and the evaluation of the model's ability to forecast the Goldersbach catchment rainfall-runoff behavior with automated estimation of event-specific parameters is discussed in sections 8.4 and 8.5.

Firstly, the comparison of model performance using the 500 m and 1 km grid model revealed no significant advantage of one over the other. The same applied to the evaluation of the differences with respect to the alternative model inputs, radar and rain-gauge data. For both cases, some events were better reproduced while others showed a slight deterioration of results. This is comforting insofar as, according to this result, the techniques developed to jointly use radar and rain-gauge data (see section 6.6) apparently combine two approximately equal data sources. However, it should be mentioned that at times, radar clearly missed the ground-observed rainfall volumes. The most relevant finding that ultimately led to a second, closer investigation of the rainfall-runoff behavior of the catchment by Dr. Ludwig consulting engineers (Ludwig, 2001) was that most calibration events featured a time-lag of the observed and modelled hydrograph in the rising limb, with the modelled discharge responding faster to rainfall. For one exemplary calibration event, a medium flood event in February 1997, this time-lag can be seen in Figure 8.2 between the observed hydrograph at PBEB (the gauge at the catchment outlet, PLUS, was not in use at that time) and the corresponding model output.

The figure also reveals a considerable delay in the order of 12 hours between the beginning of the rainfall event and the related runoff response. This is unusually high, considering the small size of the Goldersbach catchment. It can be explained by the dominance of interflow in runoff formation, which in turn is strongly influenced by initial soil-moisture conditions, a finding already discussed in section 3.1.

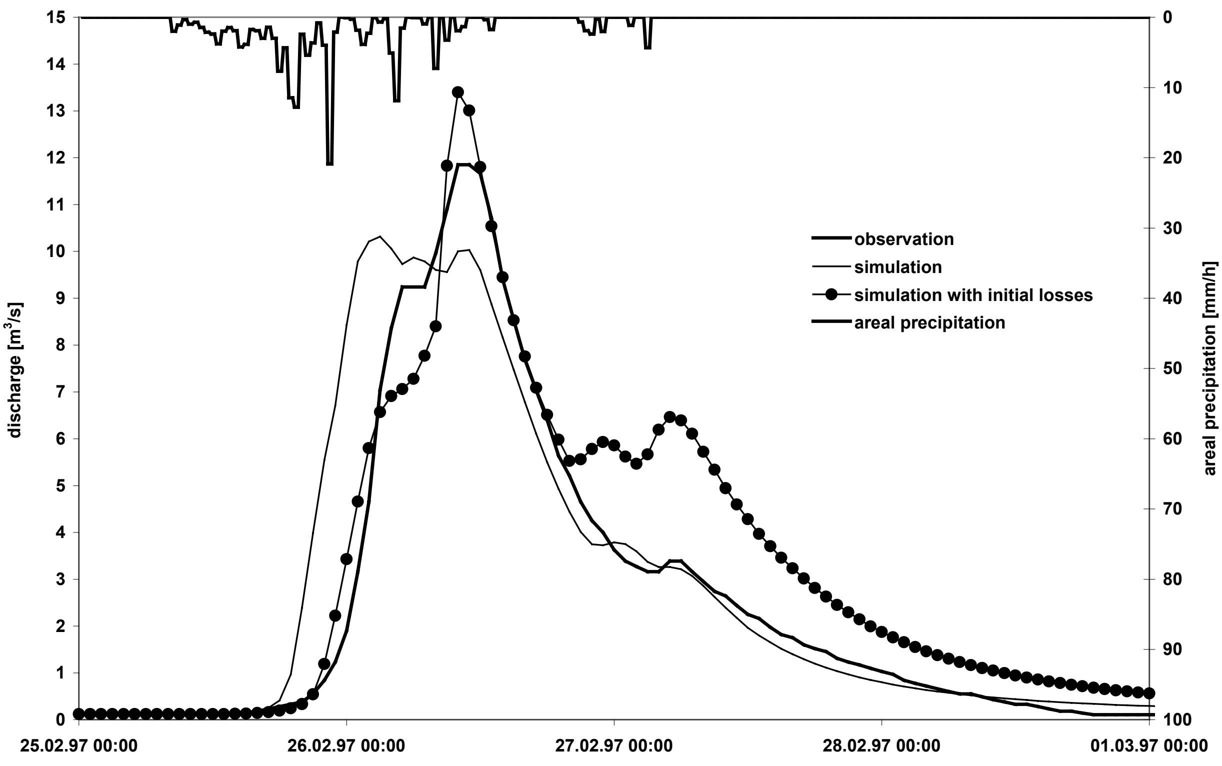

Figure 8.2: Areal precipitation, runoff observations at PBEB and FGMOD/LARSIM simulation with event-specific parameter optimization on 500 m grid with and without consideration of initial precipitation losses, 25.02.97 – 01.03.97

The time-lag between observation and model result was in the rough order of 2 to 4 hours, which was considered too much with a forecast horizon of only up to a few hours anticipated. Consequently, several different approaches to reduce this lag were pursued and evaluated. Replacing the discharge coefficient function used so far by the runoff coefficient method according to Koehler did not improve results and was therefore set aside. Next, a fixed value for baseflow was used rather than the event-specific minimum. Despite the improvement for some cases, a fixed value does not lend itself to operational use where the beginning of a modeling period does not necessarily coincide with a hydrograph that consists of baseflow only. Choosing from the large range of calculation options in FGMOD/LARSIM, the modified Clark approach was used for both the fast and slow interflow reservoir, originally it was used for fast interflow only. This alternative led, as before, to both improvements and deterioration for different events, therefore the old calculation mode was kept and the travel times in the channels were investigated. Controlled by the river bed and embankment roughness coefficients, the wave propagation velocity has, especially in larger catchments a strong influence on flood hydrographs. In the Goldersbach catchment however, the calculated flow velocity for bankful discharge at PBEB was with 2.4 m/s reasonable, which indicated an equally reasonable choice of roughness coefficients. Increasing the roughness by a factor of two, however, led to an only marginal deceleration of flow velocities and reduced the unwanted time-lag only slightly. Obviously, routing was not the problem and yet other ways had to be thought of to get to grips with the issue. The final and most successful measure was then to introduce event-dependent initial rainfall losses for each event. The magnitude of the initial loss could to a certain degree be related to the baseflow prior to the event, which is an estimator of the antecedent soil-moisture. For the 1997 flood event already mentioned, the initial loss rate was set to an average of 6.9 mm over all rain-gauges used. Introducing an initial loss rate for all calibration events also led to a new estimation of event-independent parameters. The new and old values (in brackets) are A = 3.0 (3.0), EQI = 300 (200), EQD = 50 (20). Looking at Figure 8.2, the improvement of the new calibration with initial losses with respect to the time-lag in the rising limb is obvious. Although there is a certain trade-off between the improvement in the rising limb and the deterioration in the falling limb, for operational flood forecasting a correct representation of flood formation has first priority.

However, in the case of full saturation of the catchment, caused by high antecedent rainfall sums prior to a storm, the model performs well even without manual estimation of initial loss rates. This is the case for the last severe flood event in the Goldersbach catchment in July 1987, shown in Figure 8.3. Due to very intensive rainfall on fully saturated soils, very fast interflow and even overland flow occurred in the Goldersbach catchment, which pushed the discharge observed at

PBEB to its peak, only 2 hours after the beginning of the main rainfall event. The model reproduces this generally well. However, in this case the modelled discharge hydrograph even lags the observed by about 45 minutes.

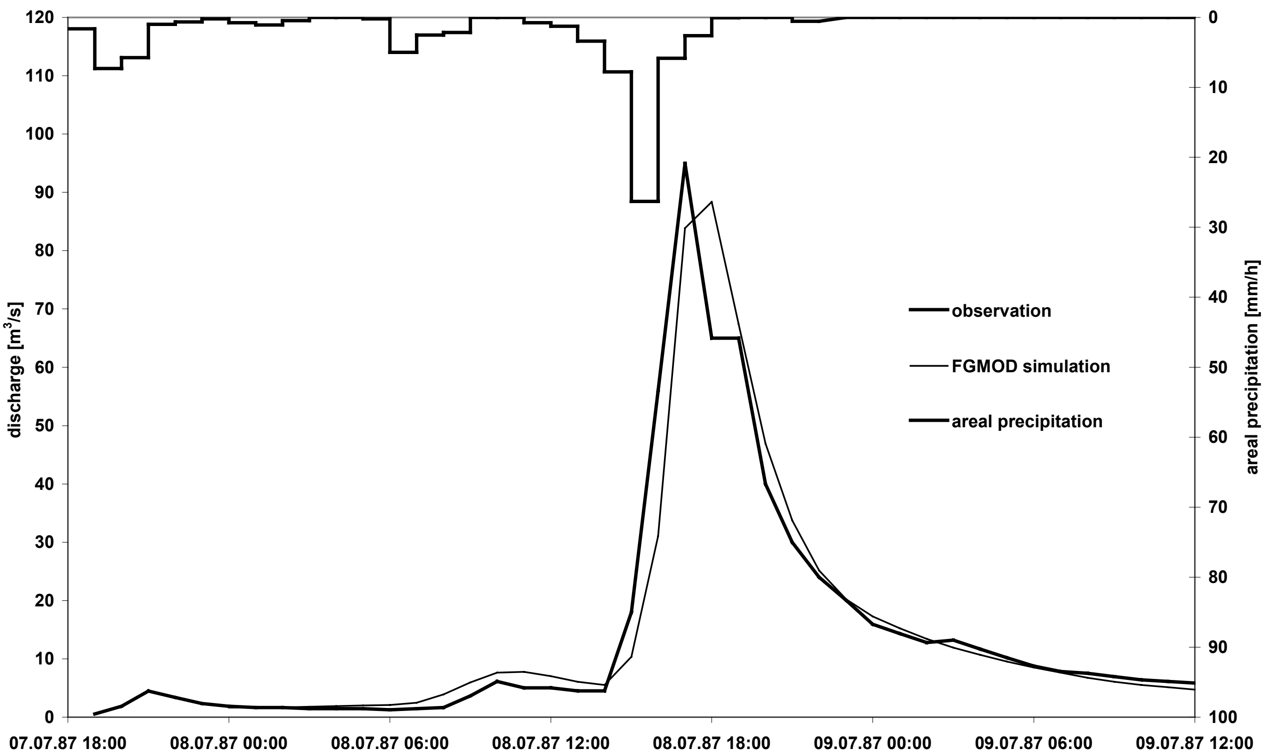

Figure 8.3: Areal rainfall, runoff observations at PBEB and FGMOD/LARSIM simulation with event-specific parameter optimization on 500 m grid, 07.07.87 18:00 – 09.07.87 12:00

Nevertheless, the introduction of an initial loss rate generally effectuated the greatest improvement in model performance, and some relation to the initial soil-moisture conditions could be observed indirectly through baseflow magnitude. The problem, however, was that the magnitude of the initial loss was manually fixed and could not be related to any of FGMOD/LARSIM's parameters to allow for automatic estimation. This is mainly due to the fact that FGMOD/LARSIM in the event-dependent calculation mode can consider the system's initial states only indirectly e.g. via the magnitude of the initial baseflow. Consequently, it was recommended by Dr. Ludwig consulting engineers to apply LARSIM in the continuous time mode, which keeps track of all relevant system states over time. With an own continuous time model, HBV, at hand and years of experience with it, it was decided to calibrate the HBV model to the catchment first, but with the intention to also fit LARSIM in continuous time mode to the Goldersbach catchment later. The principles of the HBV model are explained in section 8.3.1, followed by a detailed discussion of the model set-up for the Goldersbach catchment described in section 8.3.2 and some application results given in section 8.3.3.

8.2.4 Flood forecasting with FGMOD/LARSIM

So far, all simulations were performed a posteriori, i.e. with full knowledge of both the observed rainfall and runoff observations. The estimation of the event-specific parameter BAF was based on the comparison of observed and modelled discharge throughout the entire event. This, however, is not possible in operational flood forecasting. Here, BAF has to be estimated on the rainfall and discharge data available at the present time: As long as the observed discharge is below a threshold of usually three times the mean discharge, a fixed value of BAF, determined from historical events, is applied. If the observed discharge exceeds the threshold, the value of BAF to be used for the forecast is calculated from a period prior to the forecast point, usually the last 6 hours. In the Goldersbach catchment, due to its small size, the period was set to 4 hours.

All discharge forecasts calculated with FGMOD/LARSIM in sections 8.4 and 8.5 are done in forecast mode, i.e. they were based on values of BAF calculated according to the described procedure.

8.3 The rainfall-runoff model HBV-IWS

The HBV hydrological model has a long history and the model has found applications in more than 30 countries. Its first application dates back to the early 1970s (Bergström and Forsman, 1973). Originally, the HBV model was developed at the Swedish Hydrological and Meteorological Institute (SMHI) for runoff simulation and hydrological forecasting, but the scope of applications has increased steadily. The model has also been subject to modifications over time, although the basic modeling philosophy has remained unchanged and can in short be formulated as follows:

- the model shall be based on a sound scientific foundation
- data demands must be met in typical basins
- the model complexity must be justified by model performance
- the model must be properly validated
- the model must be understandable to its users.

The above criteria are neither met by a fully distributed, physically-based model nor a completely stochastic or lumped model. Consequently, the HBV model was developed as a semi-distributed conceptual model. It is semi-distributed insofar as the basin can be sub-divided into hydrologically uniform sub-catchments and further into zones according to elevation, land-use or soil type. The distribution of each sub-catchment into different elevation and land categories however is not spatially fixed. That is, geographical information is taken from actual physical data, but is represented in each sub-catchment only as a percentage of the whole area for that sub-catchment without keeping track of exactly where the percentage is located in space. The model has a number of free parameters, values of which are found by calibration. There are also parameters such as the maximum water storage capacity of the soil and mean monthly evapotranspiration that describe the characteristics of the basin and climate, which as far as possible remain untouched during model calibration. The use of sub-basins opens the possibility to have a large number of parameter values for the whole basin. In decades of use, however, it proved wise to be restrictive in most applications as there is only little variability in parameter values in sub-basins.

Based on the improved HBV-96 version of the original model, a modified version developed at the IWS termed HBV-IWS has been used for the Goldersbach catchment. Showing only slight differences to HBV-96, the following brief introduction to the principal model structure and process representations is mainly based on the description of Lindström et al. (1997).

8.3.1 Model structure

Figure 8.4 shows the principal processes covered by the HBV model and the spatial sub-division of the basin in the model. Input data to the model are precipitation and air temperature in the desired temporal resolution. On the following pages, each model algorithm is explained in detail.

Figure 8.4: Schematic view of the HBV model showing sub-catchment division, snow distribution, elevations and vegetation zones, unsaturated and saturated zones, and river routing. Taken from Graham (2000).

Snow

As with many hydrologic models, the simple degree-day approach is used for snowmelt. Although atmospheric modelers have criticized the degree-day approach for lack of information of proper energy fluxes, it is still recognized within the hydrologic modeling community as an effective means of intercomparison (WMO, 1986). Fergusson (1999) predicted about the future use of snowmelt routines for rainfall-runoff models that '... no one model will dominate the field in ten years' time ... For climate change applications, energy-balance approximations will be used but there is still likely to be much debate over how to distribute the necessary inputs and surface parameters, and how to parameterize sub-grid variability in snow cover'. Excessive data input required for the theoretically superior energy balance approach and the fact that in the Goldersbach catchment all major floods were not snowmelt-induced justified maintaining the simple approach.

Zoning sub-catchments based on elevation allows the individual consideration of snowfall and snowmelt at different heights. Precipitation inputs are then modelled as snow or rain according to the prevailing temperature and a given threshold temperature for snow formation. Thus, snow builds up during sub-freezing periods with temperature lower than T_{crit}.

$$MELT = DD \cdot (T - T_{crit}) \tag{8.4}$$

where:

MELT	[mm]	snowmelt
DD	[mm/(K·day]	degree-day factor
T	[°C]	current daily mean air temperature
T_{crit}	[°C]	threshold temperature

The snow routine of the HBV model has primarily two free parameters that have to be estimated by calibration: DD and T_{crit}.

Interception

In contrast to the original HBV-96, HBV-IWS contains a reservoir to account for seasonally dependent interception by plant cover. Maximum interception values are given for each month according to the plant cover of each zone. Rainfall in excess of the interception retention capacity will be transferred to the soil-moisture and effective precipitation routines, rainfall below the available retention capacity is completely stored. The interception storage is emptied through evapotranspiration.

Surface Runoff generation

HBV-IWS includes a simple routine to account for Hortonian surface runoff occurring due to infiltration excess. Surface runoff occurs when the rainfall intensity exceeds the maximum infiltration capacity of the soil specified by the parameter HYDCON.

Soil-moisture and effective precipitation

Soil-moisture dynamics is a complex process which requires complex models to be described in detail. If the problem is limited to modeling of the effects of soil-moisture on runoff generation on basin scale, the problem can be greatly simplified. Often a bucket approach is chosen to represent the field capacity and thus the storage capacity of the soil. It is clear, however, that this approach is crude and gives a response that is often too categorical. The soil-moisture accounting of the HBV model is based on a modification of the bucket theory in that it assumes a statistical distribution of storage capacities in a basin. This simple assumption has followed the model ever since its introduction and has proved to be very important, as it makes the model independent of scale as long as this distribution function is stable.

The soil-moisture accounting routine is controlled by two free parameters, namely FC and β. FC is the maximum soil storage in the basin and β determines the relative contribution to runoff from a millimeter of rain or snowmelt at a given soil-moisture deficit.

$$P_{eff} = \left(\frac{SM}{FC}\right)^{\beta} \cdot \left(P + MELT\right) \quad (8.5)$$

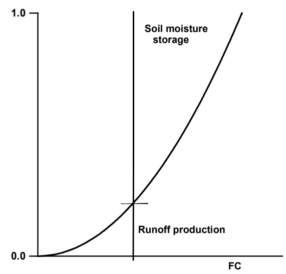

where:

P_{eff}	[mm]	effective precipitation
SM	[mm]	current soil-moisture
FC	[m]	maximum soil storage capacity
β	[-]	curve shape factor
P	[mm]	precipitation

Evapotranspiration

Evapotranspiration forms an important part of the water balance and is a key factor in the interaction between land surfaces and the atmosphere. In spite of the great importance of evapotranspiration it is often regarded as a residual term in hydrologic models.

The evapotranspiration routine in the original HBV model is based on monthly values of potential evapotranspiration as input. In order to improve the model performance when either the spring or summer is much colder than normal and when daily changes of the weather inputs need to be taken in to account, a correction factor based on mean daily temperatures and long-term averages is included according to the following equation.

$$PE_a = (1 + C \cdot (T - T_m)) \cdot PE_m \tag{8.6}$$

where:

PE_a	[mm]	current potential evapotranspiration
C	[1/°C]	empirical parameter
T	[°C]	daily mean air temperature
T_m	[°C]	monthly long term average temperature
PE_m	[mm]	monthly long term average potential evapotranspiration

Furthermore, the current soil-moisture has an important influence on the magnitude of the real evapotranspiration. Only in the case of an optimum water availability, does the actual evapotranspiration equal the potential evapotranspiration. In the model, this is accounted for by a soil-moisture limit PWP, below which the actual evapotranspiration will be linearly reduced due to insufficient water availability.

$$\begin{aligned} E_a &= PE_a \cdot \frac{SM}{PWP} \quad \text{for} \quad SM < PWP \\ E_a &= PE_a \quad \text{for} \quad SM \geq PWP \end{aligned} \tag{8.7}$$

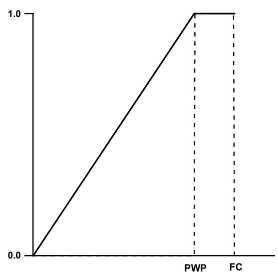

where:

E_a	[mm]	current evapotranspiration
PWP	[mm]	soil-moisture limit for evapotranspiration decrease

The response function

The basin response routine transforms excess water from the soil-moisture routine to discharge in each sub-catchment. The routine consists of two reservoirs. The first reservoir simulates the fast and delayed interflow in the sub-surface, while the lower reservoir represents the baseflow. Both reservoirs are connected in series by a constant percolation rate and are considered linear with a constant recession coefficient. In addition to the regular outlet, the upper reservoir also features a threshold-dependent runoff component: Only if the reservoir level exceeds a certain threshold, fast runoff from the upper outlet occurs. Overall, the response function consists of the following modeling parameters: Three recession coefficients K_0, K_1, K_2, a threshold L and a constant percolation rate K_{perc} between reservoirs.

$$
\begin{aligned}
Q_0 &= \begin{cases} \dfrac{1}{K_0} \cdot (S_i - L) \cdot A_{sc} & \text{for } S>L \\ 0 & \text{for } S \le L \end{cases} \\
Q_1 &= \frac{1}{K_1} \cdot (S_i) \cdot A_{sc} \\
Q_{perc} &= \frac{1}{K_{perc}} \cdot (S_i) \cdot A_{sc} \\
Q_2 &= \frac{1}{K_2} \cdot (S_b) \cdot A_{sc}
\end{aligned}
\tag{8.8}
$$

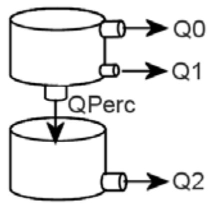

where:

Q_0	[m³/s]	fast interflow
Q_1	[m³/s]	interflow
Q_{perc}	[m³/s]	percolation
Q_2	[m³/s]	baseflow
K_0	[h]	fast interflow storage constant
K_1	[h]	interflow storage constant
K_{perc}	[h]	percolation storage constant
K_2	[h]	baseflow storage constant
S_i	[mm]	interflow reservoir waterlevel
S_b	[mm]	baseflow reservoir waterlevel
L	[mm]	threshold waterlevel for fast interflow
A_{sc}	[m²]	sub-catchment area

Finally there is a transformation function for smoothening of the generated flow. The transformation consists of a triangular weighing function with one free parameter, MAXBAS.

$$Q = g(t, MAXBAS) \cdot (Q_S + Q_0 + Q_1 + Q_2) \tag{8.9}$$

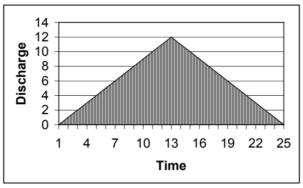

where:

Q	[m^3/s]	current overall discharge
MAXBAS	[h]	duration of the triangular weighting function (Unit Hydrograph)

Routing

After transformation, discharge is routed through the river step by step with the Muskingum flood routing model. It represents a river stretch between two sections using a prism and a wedge storage. After iterative calculation of the two routing parameters K and x, the flood propagation is calculated according to the formula given below.

$$Q_{out}(t_i) = C_1' \cdot Q_{in}(t_i) + C_2' \cdot Q_{in}(t_{i-1}) + C_3' \cdot Q_{out}(t_{i-1})$$

$$C_1' = -\frac{K \cdot x - \left(\frac{\Delta t}{2}\right)}{K \cdot (1-x) + \left(\frac{\Delta t}{2}\right)} \;;\; C_2' = \frac{K \cdot x + \left(\frac{\Delta t}{2}\right)}{K \cdot (1-x) + \left(\frac{\Delta t}{2}\right)} \;;\; C_3' = -\frac{K - (K \cdot x) - \left(\frac{\Delta t}{2}\right)}{K \cdot (1-x) + \left(\frac{\Delta t}{2}\right)} \tag{8.10}$$

where:

$Q_{out}(t_i)$	[m^3/s]	discharge leaving the river stretch at time-step t_i
$Q_{out}(t_{i-1})$	[m^3/s]	discharge leaving the river stretch at time-step t_{i-1}
$Q_{in}(t_i)$	[m^3/s]	discharge entering the river stretch at time-step t_i
$Q_{in}(t_{i-1})$	[m^3/s]	discharge entering the river stretch at time-step t_{i-1}
K	[h]	retention constant of the Muskingum model
x	[-]	weighting factor of the Muskingum model
C_1', C_2', C_3',	[-]	formula parameters

8.3.2 Parameter sets used

Customizing the HBV-IWS model to the Goldersbach catchment consisted of several steps. Firstly, the principal division into sub-catchments and zones, secondly the estimation of parameters reflecting the soil, vegetation and climate conditions in the catchment, finally the optimization of the calibration parameters on historical flood observations. For the first two tasks, the following sources of information were available:

- Digital terrain model of the catchment in 30-meter resolution
- Soil classification map of Baden-Württemberg BÜK 2000
- LANDSAT 1993 satellite image classified according to land-use
- Hydrographic river catalogue, scale 1: 50.000
- Digital hydrographic river catalogue, scale 1: 10.000

An additional, valuable source for the estimation of catchment-specific soil parameters was Einsele (1986). Based on this report, the major geologic, geographic and hydrologic characteristics of the catchment have already been described in detail in section 3.1.

The sub-division of the catchment and structural representation in the HBV-IWS model was quite straightforward. Using the existing rivergauge locations and the major river conjunctions as logical sub-basin delimiters resulted in 11 sub-catchments as shown in Figure 8.5. It was decided to zone each sub-catchment according to the grid of the radar data. Thus, a direct relation of rainfall observations at one radar pixel and rainfall input for one zone was established to make optimum use of the spatial data. One minor drawback was that as a consequence the sub-catchments, composed of square 500 × 500 m zones, showed somewhat unnatural, angular boundaries. This however was not too serious, as the fine grid resolution still permitted a close resemblance between the real and approximated boundaries.

Next, all model parameters directly related to observable physical quantities had to be estimated for all zones and sub-catchments. Following the maxim of keeping things as simple as possible and as complex as necessary, it was attempted to keep the number of different parameters as small as possible while still representing the heterogeneity of the catchment. For soil parameter estimation, this led to a classification of soil types in the catchment (Figure 3.2) into three super-ordinate classes: sandy, loamy and mixed soils. This classification was found sufficiently detailed with respect to the hydrological behavior of the soils by Einsele (1986). Their distribution in the catchment follows a clear east-west direction, with clay prevailing in the east and sandy soils dominating in the west. As a result, soil types, usually assigned individually to the zones could be kept constant throughout each sub-catchment (see Table 8.3). The HBV-IWS parameters FC, PWP and HYDCON describing the soil infiltration and retention potential were directly related to the soil type and are shown in the same table.

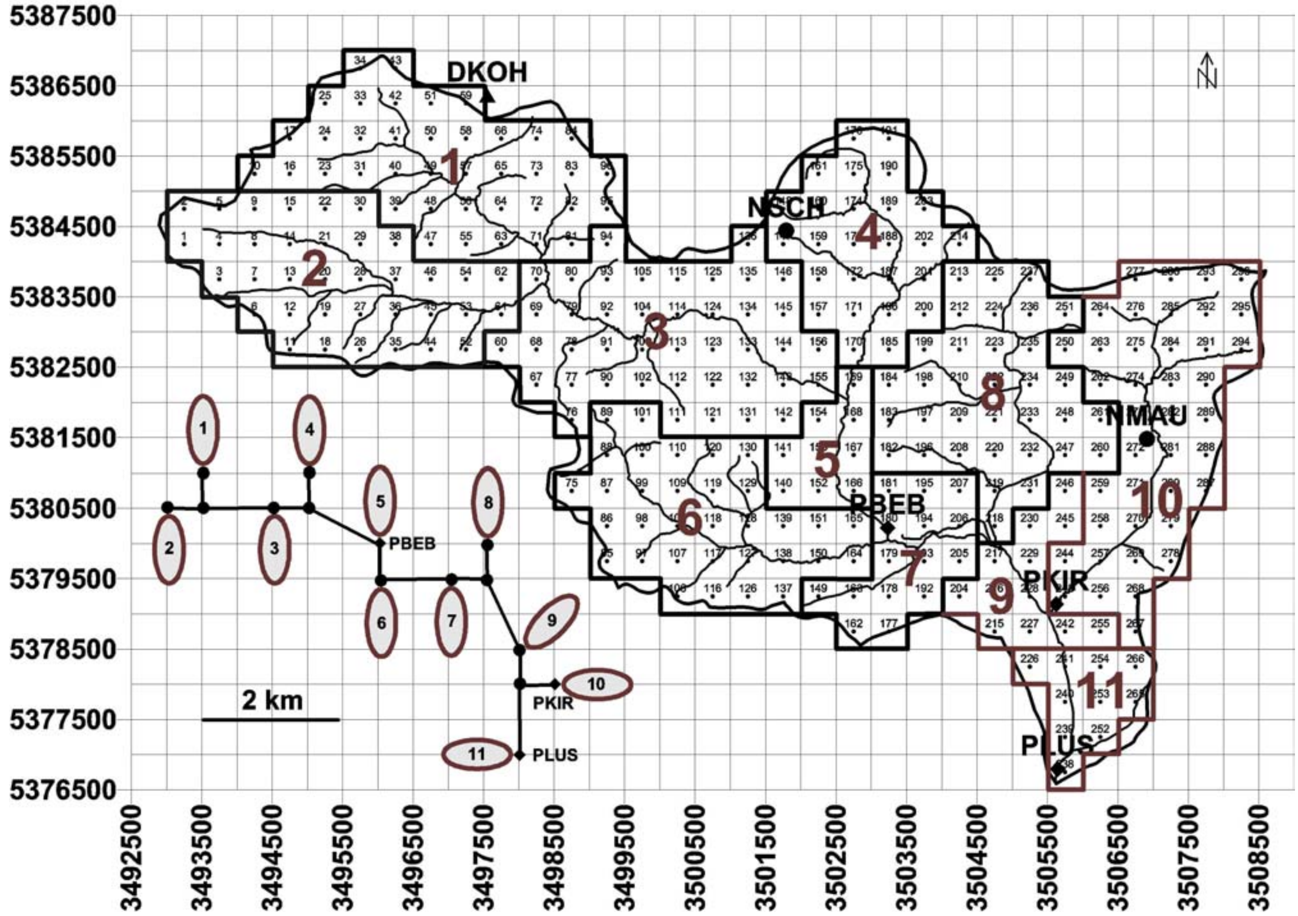

Figure 8.5: HBV model representation of the Goldersbach catchment

Name	ID	A_{sc} [km^2]	Soil type [mm]	FC [mm]	PWP [mm]	HYDCON [mm/d]	Forest [h]
Lindach	1	9.75	sand	170	70	1900	coniferous
Fischbach	2	9	sand	170	70	1900	mixed
Oberer Golderbach	3	10.5	sand	170	70	1900	coniferous
Kleiner Goldersbach	4	6.5	clay	230	90	1500	coniferous
Vor PBEB	5	2.25	sand	170	70	1900	mixed
Arenbach	6	8.25	sand	170	70	1900	mixed
Vor Bebenhausen	7	3.75	mixed	200	70	1600	deciduous
Seebach	8	8.5	mixed	200	70	1600	coniferous
Großer Goldersbach	9	3	mixed	200	70	1600	deciduous
Kirnbach	10	10	clay	230	90	1500	mixed
Vor Lustnau	11	2.5	mixed	200	70	1600	mixed

Table 8.3: Sub-catchments of the Goldersbach catchment in the HBV-IWS model

Next, the LANDSAT 1993 image was used to classify each pixel according to its vegetation cover. As reported in section 3.1, the Goldersbach catchment is almost completely covered by coniferous or deciduous forest and as for the soil types, vegetation remained fairly homogeneous within sub-catchments. Consequently, all zones in a sub-catchment were assigned one vegetation type as listed in Table 8.3. From Einsele (1986) and DWD (1990), mean monthly values for potential evapotranspiration and the volume of the interception storage were taken according to each tree type (see Table 8.4).

	mean temperature	PE_m			interception storage		
		beech	conifers	mixed	beech	conifers	mixed
	[°C]	[mm/d]	[mm/d]	[mm/d]	[mm]	[mm]	[mm]
January	2.0	0.0	0.2	0.1	0.18	3.15	1.40
February	2.3	0.0	0.1	0.1	0.18	3.15	1.40
March	5.4	0.2	0.8	0.5	0.18	3.15	1.40
April	8.0	0.8	2.9	1.9	0.44	3.29	1.61
May	12.2	2.6	4.3	3.5	0.50	3.33	1.66
June	14.2	3.4	4.2	3.8	2.80	4.55	3.50
July	16.3	4.7	4.5	4.6	2.80	4.55	3.50
August	16.1	3.6	3.5	3.6	2.80	4.55	3.50
September	12.0	1.8	2.1	2.0	2.80	4.55	3.50
October	9.3	0.7	0.9	0.8	0.18	3.15	1.40
November	3.3	0.0	0.2	0.1	0.18	3.15	1.40
December	2.1	0.0	0.1	0.1	0.18	3.15	1.40

Table 8.4: Seasonally dependent parameters of the HBV model

The long-term monthly temperature averages in the catchment were calculated from recordings at climate station TTÜB from 1987 - 1991. While this series was sufficiently long to reveal the annual temperature cycle, it was considered too short to infer the long-term mean temperature. From Einsele (1986), the annual mean temperature of 8.6°C in the period from 1951 - 1970 was known and could be used to correct the monthly temperature averages with the ratio of the five-year (9.8°C) and the long-term annual mean. The corrected monthly means are also shown in Table 8.4.

Routing parameters x and K of the Muskingum model for each of the 5 rivers in the HBV-IWS model were calculated with empirical formulas, as unfortunately no simultaneous up- and downstream discharge hydrographs were available for a more precise estimation. The length and slope of each river stretch were taken from the digital terrain model and the river catalogues. From the estimation of the cross-sectional areas under the assumption of bankful discharge at HQ_2 described by Ludwig (2000), river geometry and roughness coefficients were approximated. The retention constant K was then calculated as quotient of water volume in each river stretch and discharge corresponding to HQ_2. Due to the lack of data, the non-stationarity parameter x was approximated according to the relation

$$x = \frac{v}{v + 1.7} \tag{8.11}$$

where:

x	[-]	non-stationarity parameter of Muskingum model
v	[m/s]	flow velocity for representative discharge

In agreement with the rule of thumb that for natural rivers, x usually takes a value of 0.3, results from the above formula were close to this value. Hence, x = 0.3 was fixed for all rivers. K values were in the order of magnitude of 30 minutes ±15 minutes.

The remaining parameters were either drawn from experience or determined by calibration on historical events. For snowmelt, evaporation and effective precipitation separation, the following values were known as reasonable and also worked well in the Goldersbach catchment: $T_{crit} = 0$ [°C], $DD = 2.4$ [mm/(K·day)], $C = 0.1$ [1/°C], $\beta = 4$ [-]. All remaining parameters describing the retention and translation behavior of the catchment were found by optimization on the events already used by Ludwig (2000) in Table 8.2. Only the October 1998 event was excluded due to doubts concerning data accuracy. Calibrating on the remaining events yielded the parameters in Table 8.5.

Name	ID	L [mm]	K0 [h]	K1 [h]	K_{perc} [h]	K2 [h]	MAXBAS [h]
Lindach	1	12	2	13	100	1500	3
Fischbach	2	12	2	13	100	1500	3
Oberer Golderbach	3	12	2	13	100	1500	3
Kleiner Goldersbach	4	12	2	13	100	1500	3
Vor PBEB	5	12	2	13	100	1500	2
Arenbach	6	12	2	13	100	1500	3
Vor Bebenhausen	7	12	2	13	100	1500	2
Seebach	8	12	2	13	100	1500	3
Großer Goldersbach	9	12	2	13	100	1500	2
Kirnbach	10	12	2	13	100	1500	3
Vor Lustnau	11	12	2	13	100	1500	2

Table 8.5: Sub-catchments of the Goldersbach catchment in the HBV-IWS model

8.3.3 Model performance

It is the old problem of rainfall-runoff modeling for flood forecasting, that the extreme events one would like to calibrate on are firstly rare and secondly poorly documented. This also applies to the Goldersbach catchment. Only two major flood events (1978 and 1987) have been observed and documented. However, in the case of the 1978 flood, peak discharge estimates from different sources for rivergauge PLUS ranged from 54 m^3/s to 84 m^3/s! This was considered to leave a little too much room for interpretation, hence only the 1987 event was used to evaluate the model's ability to reproduce extreme events. Even there, rainfall and runoff data were only available in 1-hour resolution.

Nevertheless, the observed and modelled hydrographs of the 1987 flood event are shown in Figure 8.6. In general, the model performance is comparable to FGMOD/LARSIM (see Figure 8.3). Similar to the hydrograph produced by FGMOD/LARSIM, the modelled discharge response to the intensive rainfall lags the observation in the order of 45 minutes, but is able to reproduce the magnitude of peak discharge and the flood volume.

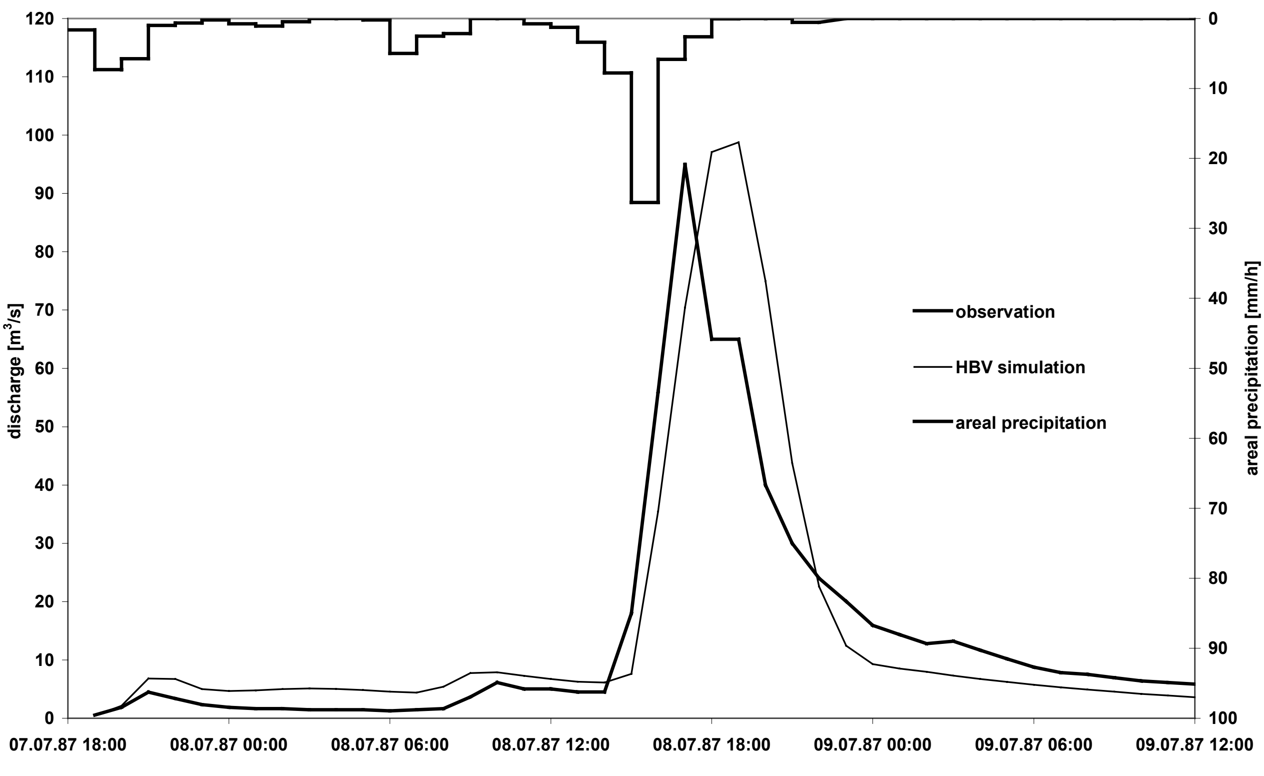

Figure 8.6: Areal rainfall, runoff observations at PBEB and HBV-IWS simulation, 07.07.87 18:00 - 09.07.87 12:00

Despite the satisfactory result, it was observed that the modelled discharge hydrograph is strongly dependent on antecedent soil-moisture conditions. The available time-series of reliable, simultaneous rainfall and discharge observations in the catchment, however, are at the moment too short to assess the model's ability to reproduce the long-term dynamics of system states and processes such as soil-moisture or evapotranspiration. This means that in the long run, the model performance could be limited by long-term biases not observable with the available data. Here, further work is necessary.

Therefore, at the moment, no clear advantage of one of the two rainfall-runoff models over the other can be stated. As a consequence, both were incorporated in the flood-forecasting system for the Goldersbach catchment and can be used alternatively.

8.3.4 Flood forecasting with HBV-IWS

Using HBV-IWS for flood forecasting purposes is straightforward. The only difference from normal simulation mode is that in addition to rainfall and temperature observations, forecasts of those quantities are used. The procedure of rainfall forecasting has been explained in chapter 7, for temperatures, simply the last observed value is used as forecast. This is considered to be reasonable as during the forecast period of only a few hours, usually no significant temperature changes occur. Furthermore, only in the case of snowfall does temperature have a direct impact on flood magnitudes, in all other cases it only influences it indirectly and delayed via evapotranspiration. In operational flood-forecasting, the final state of the system (soil-moisture, reservoir volumes) is stored and used as initial condition for the next. Thus, all model parameters are continuously simulated and provide estimates of the prevailing state of the catchment. As no further modeling techniques are used for forecasting apart from those already applied in normal simulation mode, it is clear that model performance is mainly dependent on the quality of the forecast input data. In other words, all quality differences between simulation and forecast can be ascribed to the quality of the input data.

8.4 Flood forecasting using rainfall observations

In this section, both the FGMOD/LARSIM and the HBV-IWS rainfall-runoff model are used to forecast discharge, based on observed rainfall in the forecast time. Strictly speaking, this is not a forecast, as observed data are used as model input for the forecast. The difference to the model applications described in section 8.2.3 and 8.3.3 is however that now, the calibration parameter BAF in FGMOD/LARSIM is not estimated using the rainfall and discharge observations of the entire event, but only a period prior to the forecast point, as discussed in section 8.2.4. For the HBV-IWS model, there is no change.

In order to assess the performance of the rainfall-runoff models, not influenced by the quality of the rainfall forecast, the observed data are used as 'perfect rainfall forecast'. Again, the extreme event in July 1987 is used as an example.

In Figure 8.7, the 'perfect areal rainfall forecast' (the rainfall observation) is drawn. The forecast point (indicated by a black dot) was placed at 08.08.01 13:00, directly before the start of the intensive rainfall event that triggered the flood. The forecast lead time was set to 6 hours. In case forecasted rainfall scenarios are used, this would be too long for a reliable prognosis. Using observed data, however, allowed the long lead time.

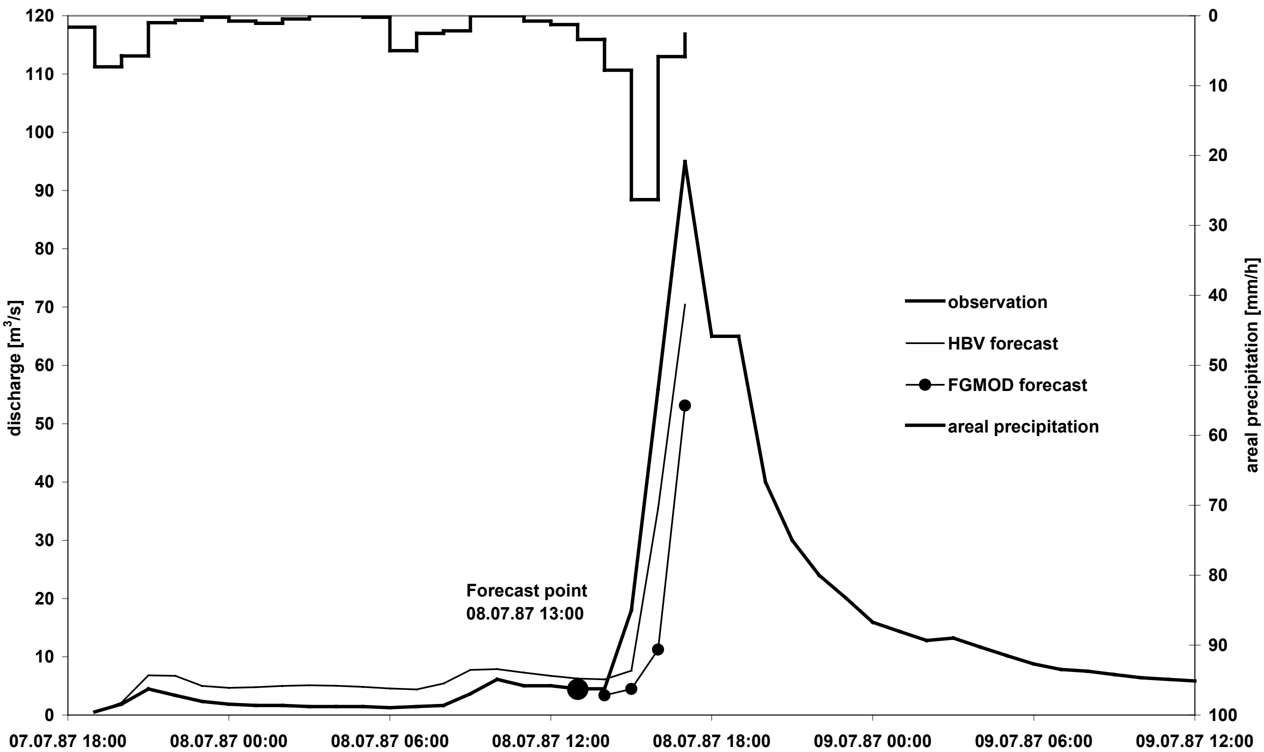

Figure 8.7: Observed areal precipitation, discharge forecasts at PBEB from FGMOD/LARSIM and HBV-IWS using observed precipitation. Forecast point: 08.07.87 13:00, forecast duration: 6 hours

The discharge hydrograph forecasted by HBV-IWS equals that of Figure 8.6, as it is based on the same input data. The forecast produced by FGMD/LARSIM however looks different; now BAF has been optimized only in the 4-hour period prior to the forecast point.

Both models produce an acceptable 6-hour forecast. Although both share the problem of the delayed rise of the discharge hydrograph, both rise with roughly the slope of the observed rising limb. At the end of the forecasting period (08.07.01 17:00), the HBV-IWS model forecasts 70 m^3/s, FGMOD/LARSIM 53 m^3/s. This is less than the observed peak discharge of 95 m^3/s occurring at that time, but as both forecasted hydrographs started to rise later than the observed one, it can be expected that they will continue to rise to a delayed, but comparable value. In fact, the peak discharge of HBV-IWS occurred at 08.08.01 18:00 and amounted to 97 m^3/s (see Figure 8.6). Compared to the modelled hydrograph in Figure 8.3, the FGMOD/LARSIM forecast is now more delayed, but still can be expected to produce a peak flow forecast in the same order as the observed.

To conclude, both rainfall-runoff models provide reasonable runoff predictions for a 6-hour forecast horizon, under the assumption of a perfect rainfall forecast. Now, it remains to be seen whether the models, using predicted instead of observed rainfall, are also able to produce reasonable estimates of future discharge, and if so, up to which forecast horizon. This is investigated in the following section.

8.5 Flood forecasting using rainfall forecast scenarios

In this section, the complete rainfall-runoff forecasting procedure developed for the Goldersbach catchment is applied on a medium flood event in July 1996. Unfortunately, the 1987 event cold not be used, as no radar were available. The gauge at the catchment outlet, PLUS, was not yet in service in 1996, thus the discharge forecast had to be evaluated on the data of PBEB.

As already stated in section 1.2, the principal approach to flood-forecasting here is of probabilistic nature, i.e. no exact, single-valued prognosis for each forecast time-step is sought, but rather to provide upper and lower bounds of possible, future developments of rainfall as well as discharge. Thus, starting from the last observations at the forecasting point, an ensemble of rainfall forecasts was produced and used as input for the rainfall-runoff models. Here, the size of the ensemble was limited to a number of 10. This is mainly due to time constraints in operational forecasting. As it was envisaged to update the forecast every 10 minutes in cases of extreme rainfall (which includes also the retrieval of data from the gauges, calculation of secondary data such as advection and so forth), unfortunately no more than 10 runs can be performed in the time-frame available. However, a higher number of scenarios would certainly provide statistically more meaningful statements.

The flood event discussed here (see also Figure 8.8 and Figure 8.9) occurred between 08.07.96 00:00 and 09.07.69 06:00, with a peak of ~ 25 m^3/s occurring at 08.07.96 17:20. While the rainfall data from the radar were available in 10-minute resolution, the observations at PBEB were only recorded in hourly steps, hence the step-like rise of the observed discharge hydrograph, labeled 'observation' in the figures. The flood peak was reached in two steps, caused by two sequences of rainfall. Starting in the evening of the 7th of July, approximately 47 mm of rain (labeled 'areal precipitation' in the figures) fell until the 08.07.96 10:00, forcing the discharge at PBEB up to

~ 12 m^3/s. Additional 20 mm of rain were observed until 08.07.96 14:50, which led to the peak discharge. For reasons of simplicity, both the observed and the forecasted rainfall is not given for individual radar pixels, but as mean areal rainfall in the Goldersbach catchment.

The SCM model was applied to produce the required ensemble of rainfall scenarios. Again, for reasons of visibility, they are not shown. Instead, the lower (90%) and upper (10%) exceedence probability limit for areal rainfall, calculated from all forecast scenarios is displayed. They are labelled '90% rainfall scenario limit' and '10% rainfall scenario limit' in the figures. Taking a look at them reveals that the peak rainfall, observed at 08.07.96 14:20, is predicted by about 30 minutes too early. For this event, no Doppler advection data were available, and the advection estimation and forecast was based on the covariance maximization technique (see section 5.1.2), which over-estimated the real rain-field propagation. This is unfortunate, but nevertheless, the maximum rainfall intensity and the rainfall duration is adequately predicted. As already discussed in section 7.5, the maximum lead time for rainfall forecast is in the order of 1.5 hours. Beyond, simply zero rainfall is predicted.

Using the forecasted rainfall scenarios as well as two simple rainfall forecasting schemes, namely zero rainfall and persistence (extrapolation of the last rainfall observation), both the FGMOD/LARSIM and the HBV-IWS rainfall-runoff models were used to produce discharge forecast scenarios. The results for FGMOD/LARSIM are shown in Figure 8.8, those produced by HBV-IWS in Figure 8.9. The lines in both figures are uniformly labeled: 'simulation' refers to the runoff simulation, based on observed rainfall and discharge measurements prior to the forecast point. The forecast point itself is indicated by a black dot. From there, several discharge scenarios branch off. The curve labeled 'zero rainfall scenario' indicates the discharge forecast based on the assumption of zero rainfall beyond the forecast point. 'Persistence rainfall scenario' labels the discharge forecast using the rainfall observation at the forecast point as forecast for the future. The discharge hydrographs resulting from the 10 rainfall forecast scenarios are presented in a simplified form: The lower (90%) and upper (10%) exceedence probability limit for discharge at each forecast time-step, labeled '90% discharge scenario limit' and '10% discharge scenario limit', respectively. Finally, to visualize the general tendency of the discharge forecasts, the mean of all scenarios is drawn ('mean discharge scenario').

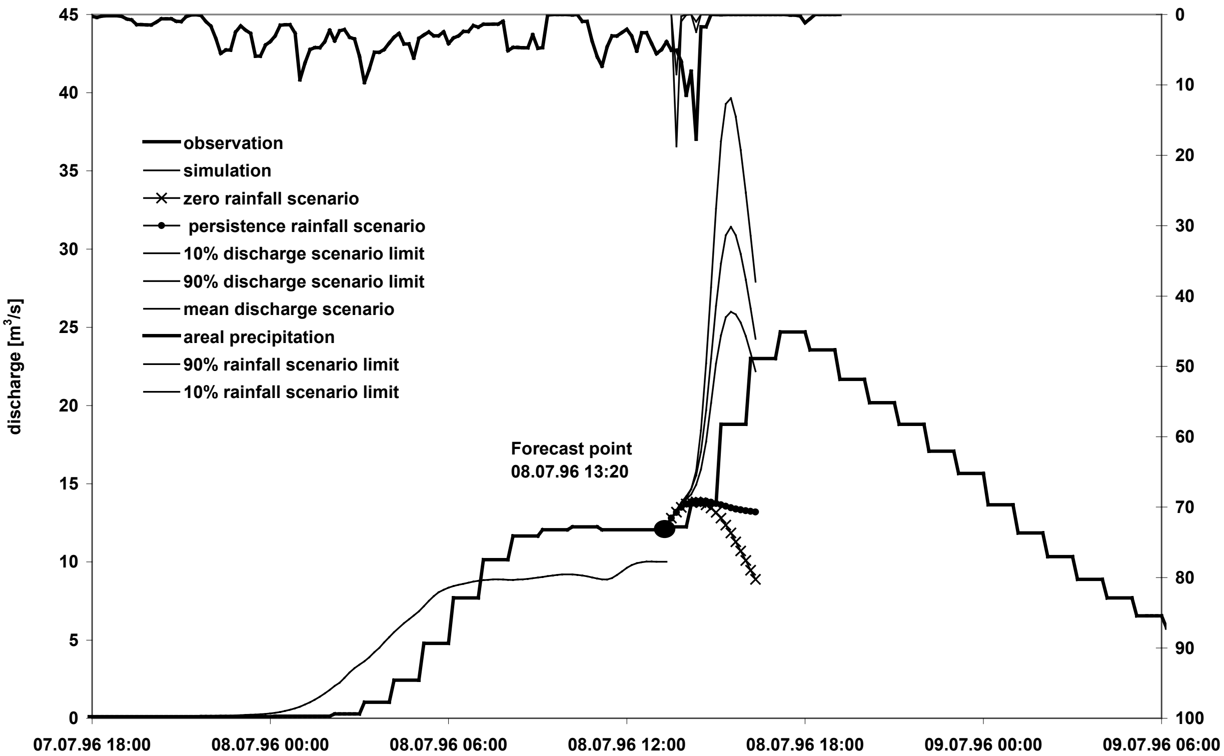

Figure 8.8: Observed areal precipitation, rainfall forecast scenarios, discharge simulation and discharge forecast scenarios at PBEB from FGMOD/LARSIM, using rainfall forecast scenarios. Forecast point: 08.07.96 13:20, rainfall forecast duration: 1.5 hours, discharge forecast duration: 3 hours

At first, the discharge simulated and forecasted by FGMOD/LARSIM (Figure 8.8) is discussed. The simulated discharge hydrograph starts to rise too early, a typical problem discussed in section 8.2.3, and, at the forecast point, does not completely reach the observed discharge. However, it is reasonably close. Then, in a period of 6 hours prior to the forecast point, the event-dependent parameter BAF is estimated for the use in the forecast period. The forecast scenarios, starting off from the last observed discharge value, rise and reach their respective peaks too early. This, however is not a problem of the rainfall-runoff model, but, as already mentioned, a problem of the rainfall forecast. The peak values range from 26 to 39 m^3/s, with a mean of 31 m^3/s. This is somewhat exaggerated, as the observed peak is with 25 m^3/s at the lower limit of the forecast range. Still, the forecast scenarios provide a better estimate of the peak magnitude as those provided by the zero rainfall and persistence forecast, which reach a maximum of 14 m^3/s at most and then decline.

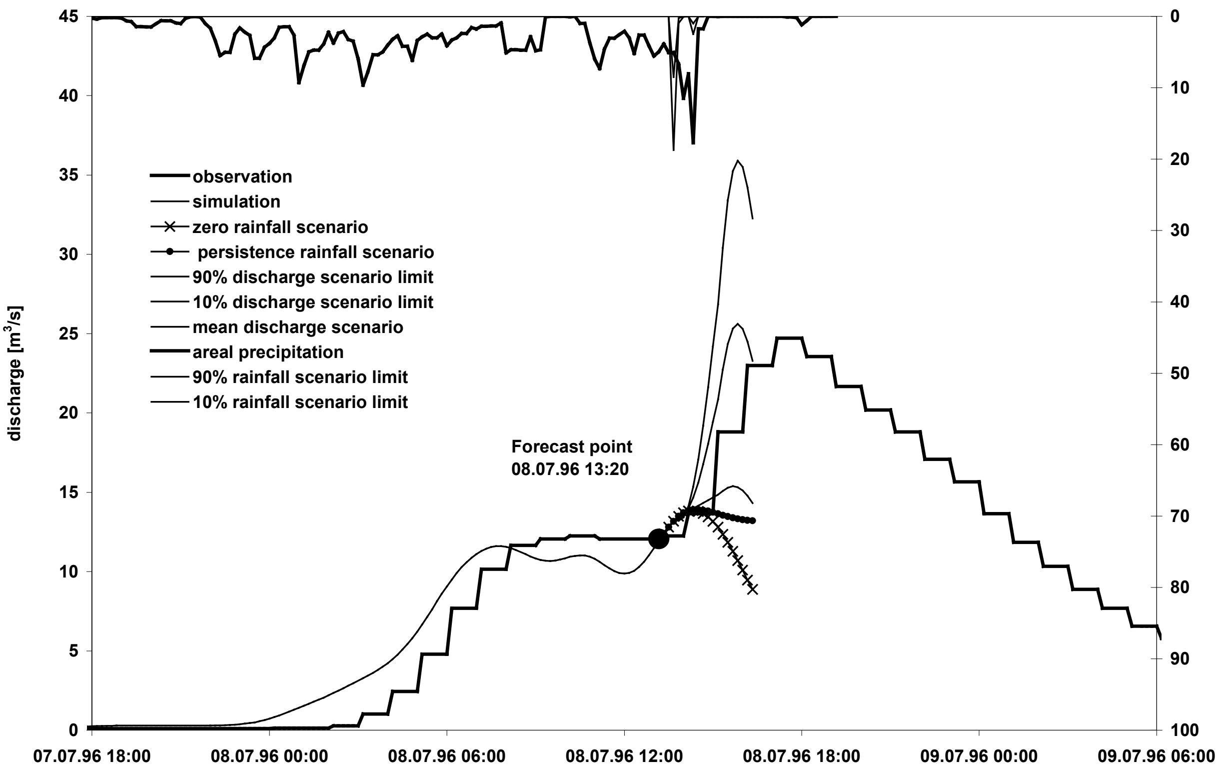

Figure 8.9: Observed areal precipitation, rainfall forecast scenarios, discharge simulation and discharge forecast scenarios at PBEB from HBV-IWS, using rainfall forecast scenarios. Forecast point: 08.07.96 13:20, rainfall forecast duration: 1.5 hours, discharge forecast duration: 3 hours.

Applying the HBV-IWS model provides, for this particular event, a better discharge forecast than FGMOD/LARSIM. As can be seen in Figure 8.9, although the simulated discharge also starts to rise too early, it reaches the observed discharge at the forecast point. Then, again due to the rainfall forecast, all discharge forecasts reach their peak about 1.5 hours too early. But now, the bandwidth of possible peak values ranges from 15 to 35 m^3/s, with a mean of 25 m^3/s. This corresponds well to the observed peak of 25 m^3/s. As before, the zero rainfall discharge forecast and the persistence discharge forecast are not able to reproduce the rise of the flood.

It should be stressed that the above forecasts all emanate from one forecast point, and results could look different for forecasts calculated for other periods of time. If a forecast would have been calculated at 08.07.96 08:00 (the time where the observed discharge reaches its first level of 12 m^3/s), for example, the persistence forecast would presumably also have provided a reasonable discharge forecast. However, the forecast point 08.07.96 13:20 was chosen as it is the critical time for decision-making: The observed discharge has already risen to a considerable value, and any action towards flood management is dependent on the knowledge whether the discharge will continue to rise or will drop again.

Altogether, both rainfall-runoff models were able to produce reasonable forecasts of the peak magnitude about 3 hours in advance, using rainfall scenarios valid in the order of 1.5 hours.

8.6 Summary and conclusion

In chapter 8, two rainfall-runoff models were fitted to the Goldersbach catchment and tested with respect to their suitability for short-term flood forecasting using rainfall forecasts. The first, FGMOD/LARSIM, is an event-based model and has been in operational use at the HVZ for several years. The second, HBV-IWS, is a continuous time model. Both models were applied in a grid-based mode matching the radar data to make full use of their spatial resolution, while keeping the model parameters lumped to avoid over-parameterization.

According to Ludwig (2000), for the storms investigated in the course of model calibration, no difference in model accuracy between the use of radar data in 500 m and 1 km resolution was observable. Moore et al. (1994c) also developed a grid-based rainfall-runoff model tailored to the use of radar data, using model parameters in a lumped way. They found that only in the case of convective rainfall events of limited areal extend did the model outperform approaches with a higher state of spatial averaging. This corresponds to the above findings, nevertheless the fine grid resolution was maintained to increase agreement of the catchment boundaries in nature and in the model.

Both models were calibrated on historical events. Due to the high dependency of runoff production on initial soil-moisture conditions in the Goldersbach catchment, the event-based model FGMOD/LARSIM, in cases of low soil-moisture conditions prior to an event, sometimes simulated the rising limb of the flood too early. However, all major floods in the catchment occurred in combination with high initial soil-moisture conditions. For those cases relevant for flood-forecasting, FGMOD/LARSIM performed well. An alternative would be to use the model in its continuous time mode, LARSIM, to keep track of relevant initial system states. This would have the additional advantage of greater independence from the river-gauge recordings, which in event-based mode are required for parameter estimation. The gauge data available in the Goldersbach catchment are, according to GDU (personal communication), at times not reliable.

Calibration of the HBV-IWS model was also successful, however it would be desirable to evaluate the long-term dynamics of its water-balance components such as soil-moisture or evapotranspiration on longer time-series. This is important, as runoff occurrence in the catchment is strongly dependent on soil-moisture conditions and hence its correct evolution over time. A new approach to provide estimates of soil-moisture directly from observations, not from indirect balance calculations, is at the moment pursued by the Institut für Wasserbau und Kulturtechnik, Universität Karlsruhe (IWK). In the Goldersbach catchment, a cluster of online-accessible soil-moisture probes was installed in an area of high soil-moisture dynamics. It is now investigated to which extend parameters of the HBV-IWS model can be related to and updated by on-site observations of soil-moisture.

Validation of both models was performed on observations of the last extreme flood in the Goldersbach catchment in 1987. In general, it has yielded satisfying results. For FGMOD/LARSIM, validation has been done in both a post-event mode, where the event-specific model parameter BAF was optimized with data of the entire event, as well as the forecast mode, where parameter optimization was done in a period prior to the forecast point.

Finally, both models were applied on a flood event in July 1996, with rainfall forecasts provided by the SCM model. The rainfall forecasts were accurate with respect to the observed rainfall intensities, but too early with respect to timing. The rainfall forecast horizon was 1.5 hours. Beyond, zero rainfall was predicted. Using the rainfall forecast ensemble, upper and lower bounds for the development of discharge were calculated by both rainfall-runoff models. Further, the mean expected development was indicated by the average of the discharge scenarios. It was shown that both models, in combination with the rainfall forecast, provide reasonable discharge estimates for up to ~ 3 hours and outperform forecasts based on zero rainfall or persistence rainfall assumptions. However, due to data limitations, so far no long-term statistics of model performance and forecast quality could be calculated. Further work is planned in this context.

9 Summary and perspective

This chapter is dedicated to a look around: into the past, to the origins and scope of the work presented here, into the present, a review of the goals achieved and methods developed, into the near future, necessary and desirable further work in the Goldersbach project, and finally a glance into the far future, the long-term goals in short- and medium range rainfall and flood forecasting.

The past

The work presented emanated from the project 'Short-term flood-forecasting for the Goldersbach river'. Initiated by the town of Tübingen, the goal was to develop a flood-forecasting system for the 75 km^2 Goldersbach catchment. It should be suited to the operational management of flood-retention basins and serve as a support tool for decision-makers to apply measures for flood-protection in the town of Tübingen. The anticipated lead time, dictated by the time needed to take action was specified as approximately 3.5 hours. Due to the small size and the rainfall-runoff characteristics of the Goldersbach catchment, the desired lead time could not be achieved by real-time river-gauge and rain-gauge observations only. The principal approach was then to develop a weather radar-based, short-term rainfall forecast valid for roughly 1.5 hours, and to use these forecasts in combination with real-time rainfall observations in a rainfall-runoff model to gain 3.5 hours of lead time.

The present

The goals and principal approach established were translated into several deeds. The first step was to establish a gauge system in the Goldersbach catchment and to establish a data transmittal and data storage system to retrieve and store data from 8 rain-gauges, 3 river-gauges and a Doppler weather radar.

Then, a radar-based rainfall type classification technique was developed to consider the unique properties of different rainfall types in interpolation and forecasting. Based on two variables, the rainfall coverage in a radar image and the fraction of rain in excess of 10 mm/h, a fuzzy rule system was developed which distinguishes 6 meteorological rainfall types. As this was found to be too refined for the desired purposes, the distinction was given up in favor of the three rainfall classes 'convective', 'mixed' and 'stratiform', defined only by the rainfall coverage.

Especially for short-term rainfall forecasting, knowledge of the current advection is crucial. Therefore, two independent wind field estimation schemes were investigated. Firstly, the mean field advection vector derived from Doppler analysis, secondly an estimation scheme based on covariance maximization. It was found that both methods provide similar results and can be used alternatively. Based on the wind field estimates, a short-term, auto-regressive forecast model was developed for a horizon of about two hours. As the comparison of the auto-regressive forecast to simple persistence favored the latter, finally the last observed advection vector was simply extrapolated to the desired forecast horizon.

With several sources of rainfall observations available, namely radar and rain-gauges, it seemed reasonable to combine the advantages of both: the spatial resolution of radar and the presumably precise measurement of rain-gauges. Several approaches were investigated, including standard applications such as constant Z-R-relations as well as multiplicative and Z-R-relation updating techniques. Further, geostatistical methods such as Kriging, External-Drift Kriging and a new method termed 'Merging' were applied. Merging preserves the mean rainfall field estimated by rain-gauge observations but imprints the spatial variability of the radar image on it. Applying a multi-objective decision technique for evaluation and comparison favored the Merging approach.

A short-term rainfall forecasting model named 'SCM model', short for 'Spectrum-Corrected Markov chain' was developed for the Goldersbach project. Based on radar data, it follows a two-step hierarchical approach on the scale of an entire radar image and individual pixels in an image. A bi-variate auto-regressive process is used to forecast the image-scale parameters rainfall coverage and mean rainfall intensity. The individual development of each pixel in the radar image is forecasted with a Markov chain, which defines its system states by the current rainfall type, the current rainfall intensity and the development of rainfall intensities over the last 30 minutes. The field of forecasted pixel values is adjusted by a mean Fourier spectrum obtained from previously observed radar images to match the observed spatial structure. Finally, the forecasted field is adjusted to the predicted coverage and mean rainfall intensity of the image and shifted according to the prevailing advection vector. The model can produce any number of forecast scenarios, which makes it suitable for the assessment of upper and lower bounds of future rainfall development. On the anticipated forecast lead time of 90 minutes, forecasts from the SCM model were shown to outperform simple persistence and zero rainfall forecasts.

Finally, two rainfall-runoff models were fitted to the Goldersbach catchment and tested with respect to their suitability for short-term flood forecasting. The first, FGMOD/LARSIM, is an event-based model, the second, HBV-IWS, is a continuous time model. Both models were used in a grid-based mode matching the radar data to make full use of their spatial resolution, while keeping the model parameters lumped to avoid over-parameterization. Using rainfall forecast ensembles generated by the SCM model, upper and lower bounds for the development of discharge were calculated. It was shown that both models, in combination with the rainfall forecast, provide reasonable discharge estimates for up to ~ 3 hours and outperform forecasts based on zero rainfall or persistence rainfall assumptions.

The near future

Now, with an operational rainfall and flood-forecasting system developed, two major tasks have to be solved in the near future. The first is to hand the system over to the contractors and to accompany the first time of use. The second is the improvement of system components. As with most other fields of science, rainfall and runoff forecasting is an evolutionary process, and the more time one has spent in this field, the more obvious the shortcomings and limitations of one's own developments become and the more ideas one has to overcome them. However, bearing in mind the final purpose of flood forecasting, namely to provide lead time for protective measures and evacuation, it becomes obvious that the greatest benefit cannot be achieved by a slight improvement of the forecast model, but to ensure the proper function of the alarm chain, in which the forecast model is nothing but one component. For the relatively new issue of flood forecasting in small catchments, so far, at least in Baden-Württemberg, no standard procedures exist to implement alarm plans. For larger catchments, the HVZ is the competent and responsible institution that issues warnings to the public, but they are unable to provide detailed warnings for the multitude of smaller catchments. New ways of co-operation between communities and the HVZ have to be sought, which leave the day-to day work associated with the operation and maintenance of a local flood-warning system to local organizations, but make use of the knowledge of experienced forecasters in the HVZ.

Apart from this more organizational point of view, from the scientific perspective, several aspects of the modeling and forecasting process could be improved. Firstly, as especially in the case of strong advection, the rainfall forecast is limited by the size of the radar image, it would be desirable to include data from several radar stations, combined in a large field, into the model.

For the improvement of radar observations, the idea of simultaneous observation of rainfall rate and radar reflectivity with one gauge, the disdrometer, is still appealing. As the somewhat discouraging results so far were mainly due to the prototype character of the gauge used, it is believed that with a new generation gauge, a local calibration of radar data can be achieved.

A more 'down-to-earth' issue is the real-time updating of soil-moisture conditions for rainfall-runoff modeling. As already discussed in section 8.6, a research project currently conducted in the Goldersbach catchment by IWK investigates the potential of real-time, spatial, soil-moisture measurement for parameter updating in rainfall-runoff models. As the soil-moisture conditions, especially in the HBV-IWS model, strongly influence the runoff simulation, a great potential for improvement is anticipated from this approach.

Finally, it would be very desirable to evaluate the performance of the forecasting system both on long-term series of rainfall and runoff observations in the Goldersbach catchment and in comparison to other, existing forecasting systems. For other systems such as TITAN (Dixon and Wiener, 1993, WDSS (Eilts et al., 1996), CARDS (Meteorological Service of Canada), CHYD (Keenan, 1999), SPROG (Seed and Keenan, 2001), such competitions were already organized during the Sydney 2000 Forecast Demonstration project (Fox et al., 2001). However, the assessment of forecast performance must not necessarily be limited on the pure evaluation of algorithms. It is also important to assess the performance of the complete alarm chain, including the forecaster, decision-makers and participating institutions such as the police. Krzysztofowicz (1993) developed a theoretical framework of forecast systems for small to medium catchments and a Bayesian theory of such a system. The term 'system' in this context refers to the monitor, the forecaster and the decider. The framework allows to model statistically the performance of the monitor and the forecaster, and based on this, formulate optimal decisions and determine the performance of the entire system.

The far future

Beyond the aforementioned, immediate tasks to be done in the Goldersbach project, the broader perspective in the field of rainfall and flood forecasting is addressed here. The selection of topics, namely integrated meteorological modeling and new observation techniques, is arguably incomplete and influenced by the author's subjective view. Nevertheless, it is believed that advances in those fields can significantly contribute to the improvement of quantitative precipitation forecasts at temporal and spatial resolutions suitable for input to hydrological flow forecasting models operating on catchment and urban scales.

Currently, two disparate approaches are used operationally for short- to medium range weather forecasting: systems based largely on radar/ satellite extrapolation, which have great skills over an hour or so, but declining accuracy for longer durations (see also Figure 1.2). Numerical Weather Prediction (NWP), based on solving the fundamental equations of motion of the atmosphere, is clearly more appropriate for prediction on scales of 6 to 12 hours. Neither technique performs well in the intermediate range (Austin and Smith, 2001). Presumably, lower meso-scale NWP models should have something to offer, particularly at lead-times in the order of 3 to 12 hours, to use in a fine-scale rainfall forecasting model. Large-scale prediction could provide an opportunity to determine if the broader conditions are favorable for storm initiation, development or decay, acknowledging that processes of precipitation formation operate over continuous spatial and temporal scales (Kozyniak et al., 2001). The challenge then is to construct a hybrid system that makes use of the skill of nowcasting over short periods to nudge or guide a mesoscale meteorological model so that the combined system can improve the accuracy of quantitative precipitation forecasts into the 3 to 12 hour domain. To achieve this, the following are important:

- Forecast products, particularly those for hydrological applications, must be statistical in nature. This is both to reflect the chaotic structure of the underlying dynamic processes and to account for the possibility of unresolved structure due to sparse observation data sets.
- Objective scoring schemes should be used at matched spatial and temporal resolutions to determine optimum forecasting schemes for a given application. This will also allow the determination of the resolution at which the transition should be made from an extrapolation scheme to a mesoscale numerical model.
- Most important is the incorporation of information provided by observations and short-range forecasts into mesoscale models. This will involve the development of techniques to update NWP systems to remain in concordance with the real time measurements of precipitation and others parameters.

Attempts to develop such hybrid NWP/ image extrapolation systems to improve the short-range precipitation forecast accuracy, were already conducted during the 1980s and 1990s (see also section 7.1). One promising example is the operational rainfall nowcasting system presented by Kunitsugu et al. (2001). It uses data from 20 radar sites and 1300 rain-gauges with 10-minute data provision. The system is a combination of a NWP model and a conventional extrapolation method and issues hydrometeorological forecasts with 6-hour lead time.

At the moment, integrated mesoscale meteorological modeling developments mainly consists of linking existing short-range and NWP models. However, the two model approaches are fundamentally different and evolved independently; straightforward connections are usually difficult to establish. In the future, a new generation of truly 'integrated' models, consistent over a range of both temporal and spatial scales, could provide an appropriate representation of rainfall processes and improve forecasting results. This, however, requires a scaling framework for a unified model theory in both meteorology and hydrology, which has yet to be developed. One approach, the 'Dominant Process Concept' (DPC) was suggested by Blöschl (2001). The principal idea is that, instead of trying to capture all processes when upscaling, methods should be developed to identify dominant processes that control any system response, be it catchment runoff or rainfall formation in the atmosphere, in different environments and at different scales, and then develop models to focus on these dominant processes.

The second look into the far future, addressing new observation techniques, goes into space. Seeking ways to avoid the problems associated with weather radar observations from the ground, namely Anaprop and topographic effects, space-borne radar systems have been developed in recent years. The advantage of such systems is that measurements from space are very clean. They are free from the problems of ground radars mentioned above and are generally very well maintained and calibrated. In fact, in the TRMM (Tropical Rainfall Measurement Mission) project it was found that many discrepancies between ground and space-borne radar rainfall estimates were on the ground radar side. Recently, in the framework of the Global Precipitation Mission (GPM), a new space-borne precipitation radar, ATMOS-A1, is under development and scheduled for 2007 (Kenji, 2001). Consisting of a core satellite and many microwave radiometer satellites, it will be able to provide 3-hourly rainfall distributions over the entire globe. Clearly, space-borne weather radar could provide invaluable data for the validation of large-scale rainfall models, and, in the long run, even reduce ground-based measurements to the role of validation.

10 References

ABOTT, M., BATHURST, J., CUNGE, J., O'CONNELL, P., RASMUSSEN, J. (1986a): An introduction to the European Hydrologic System – Systeme Hydrologique Europeen, "SHE" 1: hisory and philosophy of a physically based distributed modeling system. *Journal of Hydrology, Vol. 87, pp. 45 – 59, 1986.*

ABOTT, M., BATHURST, J., CUNGE, J., O'CONNELL, P., RASMUSSEN, J. (1986b): An introduction to the European Hydrologic System – Systeme Hydrologique Europeen, "SHE" 1: structure of a physically based distributed modeling system. *Journal of Hydrology, Vol. 87, pp. 61 – 77, 1986.*

AG BODEN (1994): Bodenkundliche Kartieranleitung. *Bundesanstalt für Geowissenschaften und Rohstoffe, 4. Auflage, Hannover, 1994.*

AMITAI, E., MORIN, E., MARCOVINA, M. (2001): Sensitivity of the Distribution of Radar Derived Rain Rates to Different Gauge Adjustment Techniques. *Proceedings of 5th International Symposium on Hydrological Applications of Weather Radar, Heian-Kaian, Kyoto, Japan, November 19-22.*

AUSTIN, G., SMITH, K. (2001): The Predictability of Areal Rainfall for Hydrological Modeling and Flood Forecasts. *Proceedings of 5th International Symposium on Hydrological Applications of Weather Radar, Heian-Kaian, Kyoto, Japan, November 19-22.*

BÁRDOSSY, A., PLATE, E. (1992): Space-Time Model for Daily Rainfall using Atmospheric Circulation Patterns. *Water Resources Research, 28(5), pp. 1247 - 1259, 1992.*

BÁRDOSSY, A. (1995): Untersuchung zur Stationarität der Extremabflüsse an ausgewählten Pegeln in Baden-Württemberg. *Technischer Bericht 95/18, Landesanstalt für Umweltschutz, Karlsruhe.*

BÁRDOSSY, A., DUCKSTEIN, L. (1995): Fuzzy-rule based Modeling with Applications to Geophysical, Biological and Engineering Systems. *CRC Press, New York, 1995*

BÁRDOSSY, A., (1998): Generating precipitation time series using simulated annealing. *Water Resources Research, 34(7), pp. 1737 - 1744, 1998.*

BÁRDOSSY, A. (2000): Fuzzy rule based flood forecasting. *Proceedings European Conference on Advances in Flood Research, Potsdam Institute for Climate Impact Research, 2000, pp. 494 – 503.*

BECKER, A. (1986): Neue Anforderungen und Lösungen bei der großflächigen hydrologischen Modellierung. *Wasserwirtschaft – Wassertechnik, H. 7, pp. 150 – 152, 1986.*

BELL, T. (1987): A space-time stochastic model of rainfall for satellite remote-sensing studies. *Journal of Geophysical Research, Vol. 92, No. D8, pp. 9631 – 9643, 1987.*

BELLON, A., ZAWADSKI, I. (1994): Forecasting of hourly accumulations of precipitation by optimal extrapolation of radar maps. *Journal of Hydrology, 157, pp. 211 – 233, 1994.*

BERGSTRÖM, S., FORSMAN, A.(1973): Development of a conceptual deterministic rainfall-runoff model. *Nordic Hydrology 4, pp. 174-170.*

BEVEN, K., HORNBERGER, G. (1982): Assessing the effect of spatial pattern of precipitation in modeling streamflow hydrographs. *Water Resources Bulletin, Vol. 18, No. 5, pp. 823 – 829.*

BEVEN, K. LAMB, R., QUINN, P., ROMANOWICZ, R., FREERE, J. (1995): TOPMODEL, In: Vijay P. Singh (Publisher): Computer Models of Watershed Hydrology. *Water Resources Publications, Colorado, USA, pp. 627 – 668.*

BEVEN, K. (1996): A Discussion of Distributed Hydrological Modeling. *M.B. Abbot and J.C. Refsgaard (Editors), Distributed Hydrological Modeling, Water Science and Technology Library, Kluwer Academic Publishers, Doordrecht, pp. 255 – 278.*

BEVEN, K. (2001): Rainfall-Runoff Modeling: *The Primer. John Wiley and Sons, Chichester, 2001.*

BLOOMFIELD, P. (1976): Fourier Analysis of Time Series: An Introduction. *John Wiley & Sons, New York.*

BLÖSCHL, G. (2001): Scaling in Hydrology. *Hydrological Processes 15, pp. 709 – 711, John Wiley & Sons, New York.*

BORGA M., ANAGNOSTOU, E., FRANK, E. (1997): On the use of real-time radar rainfall estimates for flood prediction in mountainous basins. *Proceedings Second International River Basin modeling, management and flood mitigation (RIBAMOD), Montselice, Italy, published 1999.*

BORGA, M., CREUTIN, J. (2000): Recent advances in Radar-based flash flood monitoring and forecasting. *Proceedings European Conference on Advances in Flood Research, Potsdam Institute for Climate Impact Research, 2000, pp. 356 – 367.*

BRAS, R., RODRÍGUEZ-ITURBE, I. (1993): Random Functions and Hydrology. *Dover Publications, Inc., NewYork.*

BRATH, A. (1997): On the role of numerical weather prediction models in real-time flood forecasting. *Proceedings Second International River Basin modeling, management and flood mitigation (RIBAMOD), Montselice, Italy, published 1999.*

BREMAUD, P., POINTIN, Y. (1993): Forecasting heavy rainfall from rain cell motion using radar data. *Journal of Hydrology, 142, pp. 373-389, 1993.*

BREMICKER, M. (2000): Das Wasserhaushaltsmodell LARSIM – Modellgrundlagen und Anwendungsbeispiele. *Freiburger Schriften zur Hydrologie, Band 11, Institut für Hydrologie der Universität Freiburg.*

BROWN, R., NEWCOMB, P., CHEUNG-LEE, J., RYALL, G. (1994): Development and evaluation of the forecast step of the FRONTIERS short-term precipitation forecasting system. *Journal of Hydrology, 158, 1994, pp. 79 – 105.*

BRUEN, M. (1997): Space and time scales of meteorological and hydrological models. *Proceedings Second International River Basin modeling, management and flood mitigaion (RIBAMOD), Montselice, Italy, published 1999.*

CASPARY, H., BÁRDOSSY, A. (1995): Markieren die Winterhochwasser 1990 und 1993 das Ende der Stationarität in der Hochwasserhydrologie infolge von Klimaänderungen? *Wasser & Boden, 47. Jg., 3/1195, pp. 18-24.*

CASPARY, H. (2000): Increased risk of river flooding in Southwest Germany caused by changes of the atmospheric circulation across Europe. *Proceedings European Conference on Advances in Flood Research, Potsdam Institute for Climate Impact Research, 2000, pp. 212 - 223.*

CASPARY, H. (2001): Zusammenhang zwischen der Verschärfung des Hochwasserrisikos in Südwestdeutschland seit Mitte der siebziger Jahre und einem veränderten Winterklima. *GAIA – Ecological Perspectives in Science, Humanities, and Economics 10, No. 4, pp. 286 – 293.*

CHEN, Z., KAVVAS, M. (1992): An automated method for representing, tracking and forecasting rain fields of severe storms by Doppler weather radars. *Journal of Hydrology, 132, pp. 179 – 200, 1992.*

CHEN, J., UYEDA, H., KINOSITA, T. (2001): Establishment of Z-R Relationship for the Baiu Precipitation Using the Window Probability Matching Method: *Proceedings of 5th International Symposium on Hydrological Applications of Weather Radar, Heian-Kaian, Kyoto, Japan, November 19-22.*

CIACH, G., KRAJEWSKI, W. (1999): On the estimation of radar rainfall error variance. *Advances in Water Resources, Vol. 22, No. 6, pp. 585 – 595, 1999.*

CIACH, G., HABIB, E., KRAJEWSKI, W. (2001): Validation of the Zero-Covariance Assumption in the Error Variance Separation Method of Radar-Rain-gauge Comparisons. *Proceedings of 5th International Symposium on Hydrological Applications of Weather Radar, Heian-Kaian, Kyoto, Japan, November 19-22.*

CLARKE, R. (1973): Mathematical Models in Hydrology. *Food and Agriculture Organisation ,Irrigation and Drainage Paper 19, Rome, Italy.*

CLOTHIER, A., PEGRAM, G. (2001): Space-Time Modeling of Rainfall using the String of Beads model: Integration of Radar and Rain-gauge data. *Report to the Water Research Commission, personal handover by the authors.*

COLLIER, C. (1986): Accuracy of Rainfall Estimates by Radar, Part I: Calibration by Telemetering Rain-gauges. *Journal of Hydrology, 83, pp. 207 – 223, 1986.*

COLLIER, C. (1989): Applications of Weather Radar Systems. *Ellis Horwood Limited, Chichester, 1989.*

CRANE, R. (1986): Horizontal small-scale structure of precipitation. *Proceedings 23d Conference on Radar Meteorology by the American Meteorological Society, Snowmass, Colorado, Vol. 1, pp. 181 – 184.*

CROZIER, C. (1986): Kint Weather Radar Operations Manual and Users Guide. *Research Report No. 1, Toronto Weather Radar Research Station, king City, Ontario, 1986.*

DAWSON, C., WILBY, R. (1998): An artificial neural network approach to rainfall-runoff modeling. *hydrological Sciences Journal, 43 (1), 1998.*

DELAMARRE, D., VIROT, B. (1998): Simulated Annealing Algorithm: Technical Improvements. *Operations Research, Vol. 32, No. 1, 1998, pp. 43-73.*

DIXON, M., WIENER, G. (1993): TITAN: Thunderstorm Identification, Tracking, Analysis and Nowcasting – A radar-based methodology. *Journal of Atmospheric and Oceanic Technology, Vol. 10, No. 6, pp. 785 – 797, 1993.*

DOELLING, I., JOSS, J., RIEDL, J. (1996): Systematic variations of raindrop size distributions measured in northern Germany during 7 years. *12th International Conference on Clouds and Precipitation, Zürich, Switzerland, pp. 1310-1331, 1996.*

DONEAUD, A., NISCOV, S., PRIEGNITZ, D., SMITH, P. (1994): The area-time integral as an indicator for convective rain volumes. *Journal of Climatology and Applied Meteorology, 23, pp. 555 – 561, 1994.*

DUBOIS, D., PRADE, H. (1980): Fuzzy Sets and Systems: Theory and Applications. *Academic Press, New York, 1980.*

DWD (1990): Die Verdunstung in der Bundesrepublik Deutschland Zeitraum 1951 – 1980, Teil I. *Selbstverlag Deutscher Wetterdienst, Offenbach am Main, 1990.*

DWD (1998): RADOLAN – Routineverfahren zur Online-Aneichung der Radarniederschlagsdaten mit Hilfe von automatischen Bodenniederschlagsstationen (Ombrometer). *Zweiter Zwischenbericht, Deutscher Wetterdienst, Geschäftsfeld Hydrometerologie, 12/98.*

DWD (2000): RADOLAN – Routineverfahren zur Online-Aneichung der Radarniederschlagsdaten mit Hilfe von automatischen Bodenniederschlagsstationen (Ombrometer). *Vierter Zwischenbericht, Deutscher Wetterdienst, Geschäftsfeld Hydrometerologie, 01/00.*

DWD (2001): RADOLAN – Routineverfahren zur Online-Aneichung der Radarniederschlagsdaten mit Hilfe von automatischen Bodenniederschlagsstationen (Ombrometer). *Fünfter Zwischenbericht, Deutscher Wetterdienst, Geschäftsfeld Hydrometerologie, 04/01.*

EILTS, M., JOHNSON, J., MITCHELL, E., SANGER, S., STUMPF, G., WITT, A., THOMAS, K., HONDL, K., RHUE, D., JAIN, M. (1996): Severe weather warning decision support system. *Preprints AMS 18th Conference on severe local storms, San Francisco, USA, pp. 536 – 540, 1996.*

EINFALT, T., DENOEUX, T., JACQUET, G. (1990): A radar rainfall forecasting technique designed for hydrological purposes. *Journal of Hydrology, 114, 1990, pp. 229 – 244.*

EINSELE, G. (1986): Das landschaftsökologische Forschungsprojekt Naturpark Schönbuch. *VCH Verlagsgesellschaft mbH, Weinheim, 1986.*

FERGUSON, R. (1999): Snowmelt Runoff Models. *Progress in Physical Geography 23, pp. 205 – 227.*

FOUFOULA-GEORGIOU, E.; KRAJEWSKI, W. (1995): Recent advances in rainfall modeling, estimation, and forecasting. *U.S. National Report to International Union of Geodesy and Geophysics, Reviews of Geophysics, Supplement, pp. 1125 - 1137, 1995.*

FOX, N., SLEIGH, M., BALLY, J., SILLS, D., JOE, P., MITCHELL, E., DUNDA, P. (2001): Using Radar Based Nowcasting Techniques to Improve Severe Weather Warning Lead Time. *Proceedings of 5th International Symposium on Hydrological Applications of Weather Radar, Heian-Kaian, Kyoto, Japan, November 19-22.*

FRENCH, M.; KRAJEWSKI, W. (1994): A model for real-time quantitative rainfall forecasting using remote sensing. *Water Resources Research,30(4), pp. 1075-1082, 1994.*

FUJIYOSHI, Y. (2001): How to interpret and use radar information. *Proceedings of 5th International Symposium on Hydrological Applications of Weather Radar, Heian-Kaian, Kyoto, Japan, November 19-22.*

GABELLA, M., NOTARPIETRO, R., PERONA, G. (2001): The weighted multiple regression method for improving radar estimates of precipitation fields in a complex orography environment. *Proceedings of 5th International Symposium on Hydrological Applications of Weather Radar, Heian-Kaian, Kyoto, Japan, November 19-22.*

GEORKAKAKOS, K., BRAS, R. (1984): A hydrologically useful station precipitation model. *Water Resources Research, 20(11), pp. 1585-1596, 1994.*

GEORKAKAKOS, K., KRAJEWSKI, W. (1991): Short-term rainfall forecasting using radar data and hydrometeorological models. *Hydrological Applications of Weather Radar, I. Cluckie and C. Collier [Ed.], Chapter 34. pp. 368 – 378, Ellis Horward, New York, 1991.*

GOOVAERTS, P. (1999): Performance comparison of geostatistical algorithms for incorporating elevation into the mapping of precipitation. *Prcoceedings IV International Conference on GeoComputation, Fredericksburg, VA, USA, 25.-28. July, 1999.*

GORGUCCI, E., SCHARCHILLI, G., CHANDRASEKAR, V. (1994): A robust pointwise estimator of rainfall rate using differential reflectivity, *Journal of Atmospheric and Oceanic Technology, 11(2), pp. 586 – 592, 1994.*

GRAHAM, P. (2000): Large-scale hydrologic modeling in the Baltic Basin. *Doctoral Thesis at the Royal Institute of Technology, Division of Hydraulic Engineering, Stockholm, 2000.*

GREGORY, J., WIGLEY, T., JONES, P. (1993): Determining and interpreting the order of a two-state Markov chain: Application to models of daily precipitation. *Water Resources Research, 28(5), pp. 1443 – 1446, 1992.*

GUPTA, V., WAYMIRE, E. (1993): A statistical analysis of mesoscale rainfall as a random cascade. *Journal of Applied Meteorology, 32(2), pp. 251 – 267, 1993.*

GYSI, H. (1995): Niederschlagsmessung mit Radar in orographisch geliedertem Gelände. *University of Karlsruhe, Faculty of Physics, Dissertation.*

HABERLANDT, U. (1998): Stochastic processes using regionalized model parameters. *Journal of Hydrologic Engineering, 3, (3), pp. 160 – 168..*

HOMAGK, P., LUDWIG, K. (1998): Operationeller Einsatz von Flußgebietsmodellen bei der Hochwasser-Vorhersage-Zentrale Baden-Württemberg *Wasserwirtschaft 88, pp. 160 - 167.*

HOSSAIN, F., ANAGNOSTOU, E., BORGA, M., DINKU, T. (2001): A probabilistic assessment of the impact of radar rainfall systematic error on TOPMODEL runoff simulation uncertainty for a mountainous watershed. *Proceedings of 5th International Symposium on Hydrological Applications of Weather Radar, Heian-Kaian, Kyoto, Japan, November 19-22.*

HUPFER, P., KUTTLER, W. (1998): Witterung und Klima. B.G. Teubner, Stuttgart.

HURVICH, C., TSAI, C. (1989): Regression and Time Series Model Selection in Small Samples. *Biometrika, Vol. 76, No. 2, pp. 297 - 307.*

HYDROLOGIC ENGINEERING CENTER (1981): HEC-1, Flood Hydrograph Package – Users Manual. U.S. Army Corps of Engineers, Davis, California, 1981.

ICHIKAWA, Y., TACHIKAWA, Y., SHIIBA, M. (2001): Investigation of Rainfall Spatial Variation Scale to be Considered in Runoff .Simulation Using Distributed Model and Radar Data. *Proceedings of 5th International Symposium on Hydrological Applications of Weather Radar, Heian-Kaian, Kyoto, Japan, November 19-22.*

IMK (1999): Das C-Band Doppler-Wetterradar des Forschungszentrums Karlsruhe. *Information brochure of the Forschungszentrums Karlsruhe, Institut für Meteorologie und Klimaforschung, 1999.*

ISLAM, S., BRAS, R., EMANUEL, K. (1993): Predictability of mesoscale rainfall in the tropics. *Journal of Aplied Meteorology, 30(11), pp. 297 – 310, 1993.*

JÄHNE, B. (1997): Digitale Bildverarbeitung. *Springer Verlag Berlin, Heidelberg, 1997*.

JOE, P. (2001): Summary of the Radar Calibration Workshop. *Proceedings of 5th International Symposium on Hydrological Applications of Weather Radar, Heian-Kaian, Kyoto, Japan, November 19-22.*

JOHNSON, D., ZAPOTOCNY, F., REAMES, F., WOLF, B., PIERCE, R. (1993): A comparison of simulated precipitation by hybrid isentropic-sigma and sigma models. *Monthly Weather Review, 121(7), pp. 2088 – 2114, 1993.*

JORDAN, P., SEED, A., WEINMANN, E. (2001): Radar measurement errors in rainfall at catchment scale. *Proceedings of 5th International Symposium on Hydrological Applications of Weather Radar, Heian-Kaian, Kyoto, Japan, November 19-22.*

JOSS, J., THAMS, J., WALDVOGEL, A. (1968): The Accuracy of Daily Rainfall Measurements by Radar. *Proceedings of the 13th Radar Meteorology Conference, McGill University, Montreal, Canada, 1968.*

JOSS, J., WALDVOGEL, A. (1970): A Method to Improve the Accuracy of Radar Measured Amounts of Precipitation. *Proceedings of the 14th Radar Meteorology Conference, Tucson, Arizona, USA, 1970.*

KATAOKA, K., DAITOU, H., KAMISAKA, K., IKEBUCHI, S., NAKAKITA, E., OISHI, S., FUJITA, A., TAKADA, N. (2001): Study on orographic rainfall characteristics and short term prediction using radar data in mountainous region. *Proceedings of 5th International Symposium on Hydrological Applications of Weather Radar, Heian-Kaian, Kyoto, Japan, November 19-22.*

KATZ, R. (1985): Probabilistic models. *Probability, Statistics, and Decision Making in the Atmospheric Sciences. A. H. Murphy and R. W. Katz, eds., Westview, Boulder, CO, pp. 261 – 288, 1985.*

KEENAN, T. (1999): Hydrometeor classification with a C-Band polarimetric radar. *Preprints AMS 29th International Conference on Radar Meteorology, Montreal , Canada, pp. 184 – 187, 1999.*

KENJI, N. (2001): Future satellite observation of precipitation. *Proceedings of 5th International Symposium on Hydrological Applications of Weather Radar, Heian-Kaian, Kyoto, Japan, November 19-22.*

KIRKPATRICK, S., GELATT, C., VECCHI, M. (1983): Optimization by Simulated Annealing. *Science, 220 (4598), 1983, pp. 671-680.*

KITANIDIS, P. K. (1997): Introduction to Geostatistics. Cambridge Unversity Press, Cambridge.

KITANO, M., ITOH, M., NAKAKITA, E., YAMAJI, A., FUJI, T. (2001): A study on an application of Doppler radar data to a short term rainfall prediction method. *Proceedings of 5th International Symposium on Hydrological Applications of Weather Radar, Heian-Kaian, Kyoto, Japan, November 19-22.*

KLATT, P., SCHULTZ, G. (1983): Flood forecasting on the basis of radar rainfall measurement and rainfall forecasting. *Hydrological Applications of Remote Sensing and Remote Data Transmission. IAHS Publ. 145, 1983.*

KOZYNIAK, K., CLUCKIE, I., HAN, D. (2001): Integrated Mesoscale-Hydrometeorological Modeling for Rainfall and Flood Forecasting. *Proceedings of 5th International Symposium on Hydrological Applications of Weather Radar, Heian-Kaian, Kyoto, Japan, November 19-22.*

KRAJEWSKI, W. (1987): Cokriging Radar-Rainfall and Rain Gage Data. *Journal of Geophysical Research, Vol. 92, No. D8, pp. 9571-9580, 1987.*

KRZYSZTOFOWICZ, R. (1993): A Theory of Flood Warning Systems. *Water Resources Research, Vol. 29, No. 12, pp. 3981 – 3994.*

KUMAR, P., FOUFOULA-GEORGIOU, E. (1993): A new look at rainfall fluctuations and scaling properties of spatial rainfall. *Journal of Applied Meteorology, 32(2), pp. 209 – 222, 1993.*

KUN, Z., WENZHONG, G., GUOQING, L. (2001): The improved Kalman filter combined with Variational Analysis – A new way to calibrate radar rainfall. *Proceedings of 5th International Symposium on Hydrological Applications of Weather Radar, Heian-Kaian, Kyoto, Japan, November 19-22.*

KUNITSUGU, M., MAKIHARA, Y., SHINPO, A. (2001): Nowcasting system in the JMA. *Proceedings of 5th International Symposium on Hydrological Applications of Weather Radar, Heian-Kaian, Kyoto, Japan, November 19-22.*

LEOPOLD, L., MADDOCK, T. (1953): The hydraulic geometry of stream channels and some physiographic implications. *Geological Survey Professional Paper 252, U. S. Government Printing Office, Washington.*

LFU (1985): Das Hochwasser am 21.6.1984 im Main-Tauber-Kreis. *Handbuch Hydrologie Baden-Württemberg Teil 6.2, 1985, Bearbeiter: Landesanstalt für Umweltschutz.*

LINDSTRÖM, G., JOHANSSON, B., PERSSON, M., GARDELIN, M., BERGSTRÖM, S. (1997): Development and test of the distributed HBV-96 hydrological model. *Journal of Hydrology, Vol. 201, pp. 272 – 288, 1997.*

LÖFFLER-MANG, M., JOSS, J. (2000): An Optical Disdrometer for Measuring Size and Velocity of Hydrometeors. *Journal of Atmospheric and Oceanic Technology, Vol. 17, No. 2, pp. 130-139, 2000.*

LORENZ, E. (1993): The essence of chaos. UCL Press, London, 1993.

LOVEJOY, S., MANDELBROT, B. (1985): Fractal properties of rain, and a fractal model. *Tellus, 37 A, pp. 209 – 232, 1985.*

LUDWIG, K. (1978): Das Programmsystem FGMOD zur Berechnung von Hochwasser-Abflußvorgängen in Flußgebieten. *Wasserwirtschaft 69, Heft 7/8, pp. 226 - 228.*

LUDWIG, K. (1989): Hochwasservorhersgae für große, semiaride Einzugsgebiete am Beispiel des Gelben Flusses. *Mitteilungen des Instituts für Wasserwirtschaft, Hydrologie und landwirtschaftlichen Wasserbau der Universität Hannover, Heft 70.*

LUDWIG, K. (2000): Flussgebietsmodell für den Goldersbach als Baustein für die Hochwasservorhersage. *Erläuterungsbericht.*

LUDWIG, K. (2001): Einsatz verschiedener Verfahren zur Optimierung der Eichung des Flußgebietsmodells für den Goldersbach. *Erläuterungsbericht.*

MANIAK, U. (1997): Hydrologie und Wasserwirtschaft. *Springer Verlag Berlin, Heidelberg, New York, 1997.*

MARSHALL, J., PALMER, W. (1948): The distribution of raindrops with size. *Journal of Meteorology, 5, pp. 165 – 166, 1948.*

MATHERON, G. (1971): The Theory of Regionalized Variables and its Applications. *Ecole des Mines, Fontainebleau, France, 1971.*

MATSOUKAS, C., ISLAM, S. (1999): Fusion of radar and rain gage measurements for an accurate estimation of rainfall. *Journal of Geophysical Research, Vol. 104, No. D24, 1999*.

MENABDE, M., SEED, A., HARRIS, D., AUSTIN, G. (1997): Self-similar random fields and rainfall simulation. *Journal of Geophysical Research, Vol. 102, No. D12, pp. 13509 – 13515, 1997.*

MICHAUD, J., SOROOSHIAN, S. (1994): Effect of rainfall sampling errors on simulations of desert flash floods. *Water Resources Research, 30, 10, pp. 2765-2775, 1994.*

MOORE, R., AUSTIN, R., CARRINGTION, D. (1993): Evaluation of FRONTIERS and Local Radar Rainfall Forecasts for use in Flood Forecasting Models. R*&D Note 225, Research Contractor. Institute of Hydrology, National Rivers Authority, 1993.*

MOORE, R., JONES, D., BLACK, K., AUSTIN, R., CARRINGTION, D. (1994a): RFFS and HYRAD: Integrated systems for rainfall and river flow forecasting in real time and their application in Yorkshire. '*Analytical techniques for the development and operations planning of water resource and supply systems'. BHS National meeting, University of Newcastle, 16.11.1994, BHS Occasional Paper No. 4.*

MOORE, R.; MAY, B.; JONES, D.; BLACK, K. (1994b): Local Calibration of Weather Radar Over London. *Advances in Radar Hydrology, European Commission, 1994.*

MOORE, R., BEL, V., ROBERTS, G., MORRIS, D. (1994c): Development of distributed flood forecasting models using weather radar and digital terrain data. *R&D Note 252, Research Contractor: Institute of Hydrology, National Rivers Authority.*

MOORE, R. (1995): Rainfall and Flow forecasting using weather radar. *Proceedings British Hydrological Society National Meeting on Hydrological Uses of Weather Radar, Institution of Civil Engineers, London, 1995.*

MOORE, R. (1996): Aspects of uncertainty, reliability and risk in flood forecasting systems incorporating weather radar. *Risk, Reliability and Robustness of Water Resources Systems, 3rd IHP/IAHS George Kovacs Coloquium, UNESCO, Paris, 19-21 September 1996.*

MOSZKOWICZ, S. (2001): Anisotropy of spatial correlation function of rainfall at different scales basing on a digital gauge network and on MRL-5 Legionowo Radar. *Proceedings of 5th International Symposium on Hydrological Applications of Weather Radar, Heian-Kaian, Kyoto, Japan, November 19-22.*

MÜNCHENER RÜCK (2000): CD-ROM 'Welt der Naturgefahren', Münchener Rückversicherungs-Gesellschaft, München.

NAGATA, K., SMITH, T., NICOL, J., AUSTIN, G. (2001): The effects of spatial variability on rainfall estimation. *Proceedings of 5th International Symposium on Hydrological Applications of Weather Radar, Heian-Kaian, Kyoto, Japan, November 19-22.*

NAGAYA, K., HARA, K. (2001): Development and evaluation observation of a micro radar rain gauge. *Proceedings of 5th International Symposium on Hydrological Applications of Weather Radar, Heian-Kaian, Kyoto, Japan, November 19-22.*

NAKAKITA, E., IKEBUCHI, S, NAKAMURA, T., KANMURI, M., OKUDA, M., YAMAJI, A., TAKASAO, T. (1996): Short-term rainfall prediction method using a volume scanning radar and grid point value data from numerical weather prediction. *Journal of Geophysical Research, 101, pp. 26181 – 26197, 1996.*

NAKAKITA, E., TAKUYA YAGAMI & SHUICHI (2001): Analysis of characteristics of generation and propagation of localized heavy rainfall utilizing dynamic indices for short-term rainfall prediction: *Proceedings of 5th International Symposium on Hydrological Applications of Weather Radar, Heian-Kaian, Kyoto, Japan, November 19-22.*

NEXRAD (1986): Next Generation Weather Radar. *Product Description Document R400-PD202, NEXRAD Joint Systems Program Office, US Department of Commerce.*

OBLED, C., WENDLING, J., BEVEN, K. (1994): The role of spatially variable rainfalls in modeling catchment response: an evaluation using observed data. *Journal of Hydrology, 159, pp. 305 – 333, 1994.*

OBLED C., DATIN, R. (1997): Rainfall information requirements for mediterranean flood operational forecasts. *Proceedings Second International River Basin modeling, management and flood mitigation (RIBAMOD), Montselice, Italy, published 1999.*

ONOF, C., NORTHROP, P., WHEATER, H., ISHAM, V. (1996): Spatiotemporal storm structure and scaling property analysis for modeling. *Journal of Geophysical Research, Vol. 101, No. D21, pp. 26415 – 26425, 1996.*

ONOF, C., WHEATER, H. (1996): Modeling of time-series of spatial coverages of British rainfall fields. *Journal of Hydrology, 176, pp. 115 – 131, 1996.*

PARKER, S. (1997): Dictionary of Earth Science. *McGraw-Hill, New York, 1997.*

PAVLOPOULUS, H., KEDEM, B. (1992): Stochastic modeling of rain rate processes: A diffusion model. *Commun. Statis.-Stochastic Models, 8(3), pp. 397 – 420, 1992.*

PEGRAM, G., CLOTHIER, A. (2001): High-resolution Space-Time Modeling of Rainfall: The "String of Beads" model. *J. Hydrology. Vol. 241, pp. 26-41.*

QUIRMBACH, M., SCHULTZ, G., FREHMANN, T. (1999): Use of weather radar for combined control of an urban drainage system and a sewage treatment plant. *Proceedings of IUGG 99 Symposium HS5, Birmingham, IAHS Publication No. 259, 1999.*

REDDY, K., KOZU, T., VISWANATHAN, G., RAO, R., NAKMURA, K. (2001): Application of ground based wind profilers and disdrometer for understanding precipitation cloud systems observed during monsoon. *Proceedings of 5th International Symposium on Hydrological Applications of Weather Radar, Heian-Kaian, Kyoto, Japan, November 19-22.*

REFSGAARD, J. (1996): Distributed Physically-Based Modeling of the Entire Land Phase of the Hydrological Cycle. *M.B. Abbot and J.C. Refsgaard (Editors), Distributed Hydrological Modeling, Water Science and Technology Library, Kluwer Academic Publishers, Doordrecht, pp. 55 –67.*

ROSENFELD, D., WOLFF, D., ATLAS, D. (1993): General probability relations between radar reflectivity and rain rate. *Journal of Applied Meteorology, 32(1), pp. 50 – 72, 1993.*

RYDER, P., COLLIER, C. (1987): Future development of the UK weather radar network. *Weather Radar and Flood Forecasting, V. Collinge and C. Kirby [Ed.], John Wiley, Chichester, pp. 271-285, 1987.*

SALAS, J., PEGRAM, G. (1977): A Seasonal Multivariate Multilag Autoregressive Model in Hydrology. *Modeling Hydrologic Processes, Water Resources Publications1, pp. 125 – 145.*

SANCHEZ-DIEZMA, R., SEMPERE-TORRES, D., ZAWADZKI, I., CREUTIN, J. (2001): Hydrological Assessment of Factors Affecting the Accuracy of Weather Radar Measurements of Rain: *Proceedings of 5th International Symposium on Hydrological Applications of Weather Radar, Heian-Kaian, Kyoto, Japan, November 19-22.*

SCHERTZER, D., LOVEJOY, S. (1987): Physical and Modeling and Analysis of Rain and Clouds by Anisotropic Scaling Multiplicative Processes. *Journal of Geophysical Research, Vol. 92, No. D8, pp. 9693 – 9714, 1987.*

SEED, A. (2001): A dynamic and spatial scaling approach to advection forecasting. *Proceedings of 5th International Symposium on Hydrological Applications of Weather Radar, Heian-Kaian, Kyoto, Japan, November 19-22.*

SEED, A., KEENAN, T. (2001): A dynamic and scaling approach to advection forecasting. *Preprints AMS 30th International Conference on Radar Meteorology, Munich, Germany, pp. 492 – 494, 2001.*

SEO, D., KRAJEWSKI, W., BOWLES, D. (1990a): Stochastic interpolation of rainfall data from rain-gauges and radar using kogriging. 1. Design of experiments. *Water Resources Research, 26(3), 469 – 477, 1990.*

SEO, D., KRAJEWSKI, W., BOWLES, D. (1990b): Stochastic interpolation of rainfall data from rain-gauges and radar using kogriging. 2. Results. *Water Resources Research, 26(5), 915 – 924, 1990.*

SEO, D., SMITH, J. (1992): Radar-based short term rainfall prediction. *Journal of Hydrology, 131, pp. 341 – 367, 1992.*

SEO, D. (1997): Rainfall Estimation in the Nexrad Era-Operational Experience, Issues, and Ongoing Efforts in the U.S. National Weather Service. *Proceedings Second International River Basin modeling, management and flood mitigaion (RIBAMOD), Montselice, Italy, published 1999.*

SEO, D., BREIDENBACH, J. (2001): Real-Time Correction of Spatially Nonuniform Bias in Radar Rainfall Data Using Rain Gauge Measurements. *Proceedings of 5th International Symposium on Hydrological Applications of Weather Radar, Heian-Kaian, Kyoto, Japan, November 19-22.*

SHARIF, H., OGDEN, F., KRAJEWSKI, W., XUE, M. (2001): Using Radar-Rainfall Estimates at Ground Level: Beam, Storm, and Watershed Geometric Interaction. Proceedings of 5th International Symposium on Hydrological Applications of Weather Radar, Heian-Kaian, Kyoto, Japan, November 19-22.

SINGH, V. (1995): Computer Models of Watershed Hydrology. *Water Resources Publications, Colorado, USA, 1995.*

SMITH, J., SEO, D., BAECK, M., HUDLOW, M. (1996): An intercomparison study of NEXRAD precipitation estimates. *Water Resources Research, 32(7), pp. 2035 – 2045, 1996.*

STÜBER, M., GEMMAR, P., GREVING, M. (2000): Machine supported development of Fuzzy-flood forecast systems. *Proceedings European Conference on Advances in Flood Research, Potsdam Institute for Climate Impact Research, 2000, pp. 504 - 515.*

SUGIMOTO, S., HIRAKUCHI, H., TOYODA, Y., SHIMOGAKI, H. (2001a): Considerations in Dealiasing of Doppler Velocities and Single-Doppler Retrieval of Horizontal Wind Field. *Proceedings of 5th International Symposium on Hydrological Applications of Weather Radar, Heian-Kaian, Kyoto, Japan, November 19-22.*

SUGIMOTO, S., NAKAKITA, E.; IKEBUCHI, S. (2001b): A stochastic approach to short-term rainfall prediction using a physically based conceptual rainfall model. *Journal of Hydrology,242, pp. 137 – 155, 2001.*

SUMNER, G. (1988): Precipitation: Process and Analysis. John Wiley & Sons Ltd, UK, 1988.

TAKADA, N., MASUDA, A., TSUJIMOTO, H., OKUDA, M., YOSHIHARU, T. (2001): A short term rainfall forecast using a numerical model assimilated by the radar data. *Proceedings of 5th International Symposium on Hydrological Applications of Weather Radar, Heian-Kaian, Kyoto, Japan, November 19-22.*

TANAKA, K. (1997): An Introduction to Fuzzy Logic for Practical Applications. *Springer, New York, Berlin, Tokyo.*

TAYLOR, G. (1935): The spectrum of turbulence. P*roceedings Royal Society Series, London, A 151, pp. 421-478, 1935.*

TSONIS, A., AUSTIN, G. (1981): An evaluation of extrapolation techniques for the short-term prediction of rain amounts. *Atmosphere-Ocean, 19, pp. 54 – 65, 1981.*

VIEUX, B., ESHLEMAN, J., MOREDA, F. (2001): Assessing Radar To Gage Calibration In A Distributed Modeling Context. *Proceedings of 5th International Symposium on Hydrological Applications of Weather Radar, Heian-Kaian, Kyoto, Japan, November 19-22.*

WALDVOGEL, A. (1975): Tropfenspektren, Niederschlagstyp und Z-R-Beziehungen. *Meteorologische Rundschau, 28, pp. 33-36, 1975.*

WAYMIRE, E., GUPTA, V., RODRIGUEZ-ITURBE, I. (1984): A Spectral theory of rainfall intensity at the Meso-ß Scale. *Water Resources Research, Vol. 20, No. 10, pp. 1453-1465, 1984.*

WILKS, D. S. (1995): Statistical Methods in the Atmospheric Sciences. Academic Press, New York.

WILLIAMS, J. (1969): Flood routing with variable travel time or variable storage coefficients. *Transactions of the ASAE, pp. 100 ff.*

WILSON, C., VALDES, J., RODRIGUEZ-ITURBE, I. (1979): On the Influence of the Spatial Distribution of Rainfall on Storm Runoff. *Water Resources Research, 15, pp. 321 – 328, 1979.*

WILSON, J., BRANDES, E. (1979): Radar measurement of rainfall – A summary. *Bulletin of the American Meteorological Society, Vol. 60, No. 9, pp. 1048 – 1055, 1979.*

WMO (1986): Intercomparison of Models of Snowmelt Runoff. *WMO – No. 646, Secretariat of the World Meteorological Organisation, Geneva, 36 & annexes.*

WWA REUTLINGEN (1987): Dokumentation über das Goldersbach-Hochwasser in Tübingen-Lustnau und Tübingen-Bebenhausen am 8. Juli 1987. *Wasserwirtschaftsamt Reutlingen, Dezember 1987.*

WWV (1983): 17. Lehrgang des Ministeriums Ernährung, Landwirtschaft, Umwelt und Forsten Baden-Württemberg, *Oktober 1983.*

ZADEH, L. (1965): Fuzzy Sets. Information and Control, 8, pp. 338-353.

ZADEH, L. (1973): Outline of a new approach to the analysis of complex systems and decision process. *IEEE Transactions SMC-3, 1, pp. 1585 – 1588.*

ZAWADSKI, I. (1975): On radar-rain gage comparison. *Journal of Applied Meteorology, 14, pp. 1430 – 1436, 1975.*

ZAWADSKI, I. (1984): Factors affecting the precision of radar measurements of rain. *Proceedings International Conference on Radar Meteorology, pp. 251-256, Zürich, 1984.*

ZAWADZKI, I., LAROCHE, S., PROTAT, A., MONTMERLE, T., CAYA, A. (2001): First Attempts at Precipitation Nowcasting by Radar Data Assimilation into a Cloud-resolving Numerical Model. *Proceedings of 5th International Symposium on Hydrological Applications of Weather Radar, Heian-Kaian, Kyoto, Japan, November 19-22.*

ZHANG, Z., KOREN, V., SMITH, M., REED, S. (2001): Application of a distributed modeling system using gridded NEXRAD data. *Proceedings of 5th International Symposium on Hydrological Applications of Weather Radar, Heian-Kaian, Kyoto, Japan, November 19-22.*

11 Appendix

A1 Simulated Annealing

The Simulated Annealing algorithm was introduced as an optimization method, by Kirkpatrick et al. (1983). From a mathematical point of view, this stochastic algorithm allows the minimization of a numeric function (cost function, objective function or energy) $x \rightarrow E(x)$, where the variable x represents the current state of the system. In usual combinatorial applications, the space ε of all the possible states is very large and the function E has numerous local minima. The Simulated Annealing algorithm produces a sequence of approximate solutions, and unlike gradient methods it can generate moves which increase the cost E(x). These are accepted according to a law of probability suitably chosen, controlled by a parameter called temperature, which permits the escape from local minima. To obtain solutions close to the optimum, one classically decreases the temperature according to an appropriate law termed temperature schedule. In the following, the mathematical model of the Simulated Annealing algorithm in the Markovian description as presented in Delamarre and Virot (1998) is shown:

E is defined as the energy function to be minimized. It is defined on the set X of the states of a system. A family of partial mappings of X to itself called moves, or elementary transformations, is defined. A state $x_2 \in X$ is a neighbor of a state x_1 if there exists an elementary transformation from x_1 to x_2. A transition matrix $\mathbf{P} = (p_{x1x2})$ on $X \times X$ is defined such that

$$p_{x_1x_2} > 0 \text{ if } x_2 \text{ is neighbour of } x_1 \text{ and } x_2 \neq x_1 \tag{11.1}$$

The Simulated Annealing algorithm can be modelled as the evolution of a Markov chain (x_n) controlled by a sequence (t_n) of parameters, called temperatures. Suppose x_0, ..., x_n are built. Then at random an elementary transformation of the state x_n to x_{n+1} is chosen according to the law

$$\mathbf{P}(X_{n+1} = x_{n+1} \mid x_0, \ldots, x_n) = p_{x_n x_{n+1}} \tag{11.2}$$

then, x_{n+1} among X_{n+1} and x_n is chosen at random, according to the law

$$\mathbf{P}(X_{n+1} = x_{n+1} \mid x_0, \ldots, x_n, x_{n+1}) = \min\left(1, \exp\left(\frac{-\Delta E}{t_n}\right)\right) \tag{11.3}$$

where ΔE represents the variation of energy corresponding to the elementary transformation of x_n into x_{n+1}. The sequence (t_n) is called temperature schedule. If $X_{n+1} = x_{n+1}$, one says the chosen move is accepted, otherwise the move is rejected. Note that the subscript n represents the time, namely the number of trials effectuated so far. A chain is a finite sequence of states such that, for every i, x_{i+1} is a neighbor of x, i.e. the chain joins x_n to x_{n+1}. It is supposed that the transition matrix

P is symmetrical and irreducible: for any pair of states x_1, $x_2 \in X$, $p_{x1x2} = p_{x2x1}$ and, moreover, there always exists a chain which joins x_1 to x_2.

A2 Kriging

Kriging has been extensively used in mining engineering and hydrology as a method to estimate linear functions of random fields or point values. The objective of Kriging is to find the best linear unbiased estimate of a linear function of a random field. The qualifiers of the estimate can be defined as

Linearity: The estimator X^* is formed as a linear combination of the observed values

$$X(\mathbf{u})^* = \sum_{i=1}^{n} \lambda_i X(\mathbf{u}_i) \tag{11.4}$$

where:

u	location in a random field
$X^*(\mathbf{u})$	estimator of X at location (**u**)
λ_i	weights for observations
n	number of observations
$X(\mathbf{u}_i)$	observation at location (u_i)

Unbiasedness: This requires that the expected value of the estimator $X^*(\mathbf{u})$ be equal to the expected value of the field.

$$E\left[X^*(\mathbf{u})\right] = E\left[X(\mathbf{u})\right] \tag{11.5}$$

Best criterion: The estimator will be considered 'best' if it gives the smallest estimation variance. the estimation variance or mean square error is defined as

$$VAR = E\left[\left(X(\mathbf{u}) - X^*(\mathbf{u})\right)^2\right] \tag{11.6}$$

where:

VAR estimation variance

Kriging estimates the values in the random fields under the assumption of second-order stationarity or the intrinsic hypothesis. A random fields is said to be second-order stationary if it satisfies the following conditions in its mean, variance and covariance:

$$E\left[X(\mathbf{u})\right] = \bar{X} \quad \text{with } \bar{X} \text{ independent of } \mathbf{u} \tag{11.7}$$

$$VAR\left[X(\mathbf{u})\right] = \sigma^2 \quad \text{with } \sigma^2 \text{ independent of } \mathbf{u} \tag{11.8}$$

$$COV\left[\mathbf{u}_1, \mathbf{u}_2\right] = COV\left[\mathbf{u}_1 - \mathbf{u}_2\right] = COV\left[h\right] \tag{11.9}$$

where:

$\bar{X}$	random field mean
σ^2	random field variance
COV	estimation covariance
h	distance of $\mathbf{u}_1$ and $\mathbf{u}_2$

which means that the covariance between the field at points $\mathbf{u}_1$ and $\mathbf{u}_2$ is independent from the individual location but only dependent on their difference h. The covariance is defined as

$$COV\left[\mathbf{u}_1, \mathbf{u}_2\right] = E\left[\left(X(\mathbf{u}_1) - \bar{X}(\mathbf{u}_1)\right)\left(X(\mathbf{u}_2) - \bar{X}(\mathbf{u}_2)\right)\right] \tag{11.10}$$

The random process $X(\mathbf{u})$ is said to satisfy the intrinsic hypothesis if its first-order differences $X(\mathbf{u}_1) - X(\mathbf{u}_2)$ are stationary in the mean and variance

$$E\left[X(\mathbf{u}_1) - X(\mathbf{u}_2)\right] = m(h) \tag{11.11}$$

$$VAR\left[X(\mathbf{u}_1) - X(\mathbf{u}_2)\right] = 2\gamma(h) \tag{11.12}$$

The mean and the variance of the first-order difference $X(\mathbf{u}_1) - X(\mathbf{u}_2)$ are independent of the actual location of $\mathbf{u}_1$ and $\mathbf{u}_2$ and dependent only on their vector difference h. The semi-variogram, usually simply termed variogram $\gamma(h)$ is defined as

$$\gamma(h) = \frac{1}{2} E\left[\left(X(\mathbf{u}_1) - X(\mathbf{u}_2)\right)^2\right] - \frac{1}{2}\left[\left(m(\mathbf{u}_1) - m(\mathbf{u}_2)\right)^2\right] \tag{11.13}$$

where:

γ	semi-variogram

The variogram and the covariance function are related through the relation

$$\gamma(h) = COV(0) - COV(h) \tag{11.14}$$

Second-order stationarity automatically implies intrinsic properties, but not vice versa.

Assuming the covariance function of the field is known, the estimation variance $\sigma^2(\mathbf{u}) = \mathrm{VAR}[X(\mathbf{u})\text{-}X^*(\mathbf{u})]$ can be calculated using the second-order stationarity hypothesis. According to the 'best' criterion in (11.6), the estimation variance can then be minimized with the help of the covariance function COV(h) and a Lagrange multiplier. This leads to a linear equation system of the form

$$\begin{aligned}&\sum_{j=1}^{n} \lambda_j \mathrm{COV}(\mathbf{u}_i - \mathbf{u}_j) - \mu = \mathrm{COV}(\mathbf{u}_i - \mathbf{u}) \qquad i=1,...,n\\ &\sum_{j=1}^{n} \lambda_j = 1\end{aligned} \tag{11.15}$$

where:

n	number of points with known values
μ	Lagrange multiplier

Solving this system yields the set of weights λ_i needed in (11.4).

Using the variogram and the intrinsic property leads again to a linear equations system that minimizes the estimation error and gives the weights λ_i to calculate the field estimate at the desired point **u** in the field.

$$\begin{aligned}&\sum_{j=1}^{n} \lambda_j \gamma(\mathbf{u}_i - \mathbf{u}_j) - \mu = \gamma(\mathbf{u}_i - \mathbf{u}) \qquad i=1,...,n\\ &\sum_{j=1}^{n} \lambda_j = 1\end{aligned} \tag{11.16}$$

Kriging as an interpolator has a number of properties, of which some will be discussed here briefly.

- Kriging is an exact interpolator. For each observation point, the corresponding estimation variance is zero.
- Kriging weights are calculated with the help of the variogram and the location of the measurement points as well as the unknown point. Not only distances between measurement points and the point to be estimated are considered, but also the relative position of the measurement points.
- Kriging weights sum up to 1, but the individual weights can be negative. Therefore estimations $X^*(\mathbf{u})$ can be either smaller than $\min[X(\mathbf{u})]$ or larger than $\max[X(\mathbf{u})]$.
- Kriging weights are influenced by the measurement values only indirectly through the variogram estimated from the measurement values.

Often, in the distribution of a quantity in space, the previously stated properties of the intrinsic hypothesis are not fulfilled, but $X(\mathbf{u})$ may exhibit systematic change in the expected value. If external knowledge based on the observation of a secondary quantity $Y(\mathbf{u})$ is known and linearly related to $X(\mathbf{u})$, External-Drift Kriging can be used for estimation, replacing the assumption of the constant expected value by

$$E\left[X(\mathbf{u}) \mid Y(\mathbf{u})\right] = a + bY(\mathbf{u}) \tag{11.17}$$

where:

$Y(\mathbf{u})$	secondary observation at both the observation and estimation points
a	linear relation bisector
b	linear relation slope

With the desired best linear unbiased estimation

$$X(\mathbf{u}) = \sum_{i=1}^{n} \lambda_i X(\mathbf{u}_i) \tag{11.18}$$

the linear equation system

$$\begin{gathered} \sum_{j=1}^{n} \lambda_j \gamma(\mathbf{u}_i - \mathbf{u}_j) - \mu_1 + \mu_2 Y(\mathbf{u}_i) = \gamma(\mathbf{u}_i - \mathbf{u}) \qquad i=1,...,n \\ \sum_{j=1}^{n} \lambda_j = 1 \\ \sum_{j=1}^{n} \lambda_j Y(\mathbf{u}_j) = Y(\mathbf{u}) \end{gathered} \tag{11.19}$$

has to be solved with μ_1 and $\mu_{1,}$ being Lagrange multipliers.

A3 Fourier Analysis

A3.1 Fundamentals

A given discrete data series consisting of V points can be represented exactly, meaning that a harmonic function can be found that passes through each of the points by adding a series of V/2 harmonic functions.

$$x_v = \sum_{k=0}^{V/2} C_k \cos\left[\omega_k v - \phi_k\right] \tag{11.20}$$

with

$$\omega_k = \omega_1 k = \frac{2\pi k}{V} \tag{11.21}$$

where:

x_v	value of a discrete series in normal space at point v
C_k	amplitude of harmonic k
ϕ_k	phase angle of harmonic k
ω_1	fundamental frequency
ω_k	harmonic of order k
k	harmonic
V	number of values in discrete series v

For k = 0, the mean of the series is calculated. The fundamental frequency ω_1 passes one full cycle over the length V of the data series. The highest or Nyqist frequency goes through one cycle over the distance of two intervals v of the series. C_k and ϕ_k can be estimated with least-squares regression from the time-series using

$$A_k = \frac{2}{V}\sum_{v=1}^{V} x_v \cos\left[\omega_k v\right] \quad \text{and} \quad B_k = \frac{2}{V}\sum_{v=1}^{V} x_v \sin\left[\omega_k v\right] \tag{11.22}$$

and

$$C_k = \left[A_k{}^2 + B_k{}^2\right]^{1/2} \quad \text{and} \quad \phi_k = \tan^{-1}\left[\frac{B_k}{A_k}\right] \tag{11.23}$$

where:

A_k	amplitude of harmonic k
B_k	amplitude of harmonic k

However, although straightforward in notation, this may be a cumbersome task when working with large amounts of data. It is however possible to avoid many redundancies in computing the spectrum using the Fast Fourier Transform (FFT) to achieve the same goal. In the simplest case, the number of data in the original series is a power of 2. Using the Cooley-Tukey algorithm then requires ($\log_2$V)/V less operations to calculate the spectrum compared to the standard method. Those computations are usually indicated in complex notation, therefore, using the Euler complex relation

$$e^{i\omega v} = \cos(\omega v) + i \sin(\omega v) \tag{11.24}$$

where:

i unit imaginary number satisfying i^2=-1

one can rewrite (11.20) as

$$x_v = \sum_{k=0}^{V/2} H_k e^{i\omega_k v} \tag{11.25}$$

with

$$H_k = C_k e^{i\phi_k} \tag{11.26}$$

where:

H_k complex Fourier coefficient

It is a remarkable property of the harmonic functions that they are uncorrelated as a consequence of the orthogonality property of sine and cosine functions. Consequently, the quantity $|H_k|^2$, plotted against the frequency ω_k, called the Fourier or power spectrum conveys the proportion of variation in the original data series accounted for by oscillations at the harmonic frequencies, but does not supply information about when in time these oscillations are expressed. Those properties of a series in Fourier space, in the one-dimensional as well as the multi-dimensional case enable the fast computation of several important quantities, namely the cross-covariance between 2-dimensional fields and the generation of random fields which reproduce the power spectrum of a given series.

The Fourier transform of a 2-dimensional (U × V) field can be expressed in complex notation as

$$\mathbf{M}_{u,v} = \sum_{j=0}^{U/2} \sum_{k=0}^{V/2} H_{j,k} e^{i[\omega_j u + \omega_k v]} \tag{11.27}$$

where:

U size of a spatial field in first (u-) dimension
V size of a spatial field in second (v-) dimension

A3.2 Lag cross-covariance of spatial fields

The cross-covariance between two 2-dimensional spatial fields with a lag or shift in the image coordinates of the second field as integer multiple of the field dimension u and v can be calculated as

$$\mathrm{COV}(\mathbf{M},\mathbf{N},\tau_u,\tau_v)=\sum_{j=0}^{U/2}\sum_{k=0}^{V/2}\mathrm{H}_{\mathbf{M},j,k}\hat{\mathrm{H}}_{\mathbf{N},j,k}e^{i\left[\omega_j u\tau_u+\omega_k v\tau_v\right]} \tag{11.28}$$

where:

M, **N**	Spatial fields
τ_u, τ_v	Incremental shift of image coordinates in u and v direction
$\hat{\mathrm{H}}_{\mathbf{N},j,k}$	Complex conjugate of complex Fourier coefficient $\mathrm{H}_{\mathbf{N},j,k}$

With **M** and **N** being identical, application of (11.28) obtains the (lag-u, lag-v) auto-covariance.

A 3.3 Generation of random fields

Using the principle of phase-randomization, it is possible to generate random fields that contain the auto-covariance function expressed by the set of complex Fourier coefficients $H_{j,k}$ of any observed field. Due to the orthogonality property of the sine and cosine function, random variations of the phase angle of each harmonic in the range $[0,2\pi]$ in a Fourier transform while keeping the amplitude will produce fields with a given auto-covariance, but random locations of the original field values.

$$\mathbf{M}^*_{u,v}=\sum_{j=0}^{U/2}\sum_{k=0}^{V/2}\mathrm{H}_{j,k}e^{i\left[\omega_j u\eta_j+\omega_k v\eta_k\right]} \tag{11.29}$$

where:

$\mathbf{M}^*_{u,v}$	random field value generated from a known spectrum
η_j, η_k	uniformly distributed, [0,1]random numbers

A3.4 Imprinting spatial structure on existing fields

Similar to the generation of random fields with a desired spatial structure as described above, existing fields can also be adjusted, or rather filtered to follow a desired spatial structure. In principle, the Fourier spectrum $|H_{j,k}|^2_{obs}$ of an existing field is adjusted to follow a desired spectrum $|H_{j,k}|^2_{new}$ by individually multiplying each complex Fourier coefficient $(H_{j,k})_{obs}$ with the ratio of the observed and desired spectra.

$$(\tilde{\mathrm{H}}_{j,k})_{obs}=(\mathrm{H}_{j,k})_{obs}\cdot\sqrt{\frac{\left|\mathrm{H}_{j,k}\right|^2_{new}}{\left|\mathrm{H}_{j,k}\right|^2_{obs}}} \tag{11.30}$$

where:

$(\tilde{\mathrm{H}}_{j,k})_{obs}$	adjusted complex Fourier coefficient of the existing field
$(\mathrm{H}_{j,k})_{obs}$	complex Fourier coefficient of the existing field
$\left|\mathrm{H}_{j,k}\right|^2_{new}$, $\left|\mathrm{H}_{j,k}\right|^2_{obs}$	desired Fourier spectrum, Fourier spectrum of the existing field

A4 Fuzzy Set Theory

Fuzzy logic was born in 1965. In that year, Lotfi Zadeh of the University of California, Berkeley published a paper titled 'Fuzzy sets' (Zadeh, 1965), seeing the limitations of 'crisp' mathematics in many fields, namely control. He referred to this idea as the 'principle of incompatibility' in his 1973 paper (Zadeh, 1973). The principle of incompatibility claims that as the complexity of a system exceeds a certain limit, precise and meaningful description of the system's behavior becomes impossible and its description must incorporate imprecision. This is where fuzzy logic comes into play. It is a broad theory including fuzzy set theory, fuzzy measure, fuzzy control and others. Fuzziness, as handled in fuzzy logic, is an extension of conventional (binary) logic to handle vagueness mathematically. In the following, a brief introduction to the basic ideas of fuzzy sets, fuzzy rules and fuzzy rule systems will be given, following mainly the description given by Bárdossy (2000).

A4.1 Fuzzy sets

A fuzzy set is a set of objects without clear boundaries; in contrast with ordinary sets where for each object it can be decided whether it belongs to the set or not, a partial membership in a fuzzy set is possible. Formally a fuzzy set is defined as follows:

Definition*:* Let X be a set (universe). A is called a fuzzy sub-set of X if A is a set of ordered pairs:

$$A = \{(x, \mu_A(x)); x \in X \quad \mu_A(x) \in [0,1]\} \tag{11.31}$$

where $\mu_A(x)$ is the grade of membership of x in A. The function $\mu_A(x)$ is called the membership function of A. The closer $\mu_A(x)$ is to 1 the more x belongs to A – the closer it is to 0 the less it belongs to A. If [0,1] is replaced by the two-element set {0,1}, then A can be regarded as an ordinary sub-set of X. In this text for simplicity the notion fuzzy set instead of fuzzy sub-set is used.

Definition: A fuzzy sub-set A of the set of real numbers is called a fuzzy number if there is at least one x such that $\mu_A(x) = 1$ (normality assumption) and such that for every real numbers a, b, c with $a < c < b$

$$\mu_A(c) \geq \min(\mu_A(a), \mu_A(b)) \tag{11.32}$$

This second property is the so-called quasi convexity assumption, meaning that the membership function of a fuzzy number usually consists of an increasing and a decreasing part. Any real number can be regarded as a fuzzy number with a single point support, and is called a 'crisp number' in fuzzy mathematics. The simplest fuzzy numbers are the so-called triangular fuzzy numbers.

Definition: The fuzzy number $A = (a_1,a_2,a_3)_T$ with $a_1 \le a_2 \le a_3$ is a triangular fuzzy number if its membership fuzzy number can be written in the form:

$$\mu_A(x) = \begin{cases} 0 & \text{if } x \le a_1 \\ \dfrac{x-a_1}{a_2-a_1} & \text{if } a_1 < x \le a_2 \\ \dfrac{a_3-x}{a_3-a_2} & \text{if } a_2 < x \le a_3 \\ 0 & \text{if } a_3 < x \end{cases} \tag{11.33}$$

The application of logical operations on sets can be extended to fuzzy set theory, where the application of a fuzzy set operation on two fuzzy sets maps all members of the input sets into a resulting fuzzy set. In fuzzy set operations, the crisp logical functions are replaced by equivalent fuzzy operators. Different operators exist for each logical functions. For the logical operation 'AND', the fuzzy equivalent can be:

$$\begin{aligned} &\mu_{A\ AND\ B}(x) = \min\{\mu_A(x);\mu_B(x)\} && \text{Minimum-operator} \\ &\mu_{A\ AND\ B}(x) = \mu_A(x)\cdot\mu_B(x) && \text{Product-operator} \end{aligned} \tag{11.34}$$

while for 'OR', possible representations are:

$$\begin{aligned} &\mu_{A\ OR\ B}(x) = \max\{\mu_A(x);\mu_B(x)\} && \text{Maximum-operator} \\ &\mu_{A\ OR\ B}(x) = \mu_A(x)+\mu_B(x)-(\mu_A(x)\cdot\mu_B(x)) && \text{Sum-operator} \end{aligned} \tag{11.35}$$

At the end of this incomplete list, the operator 'NOT' can be represented in fuzzy set theory as

$$\mu_{NOT\ A}(x) = 1-\mu_A(x) \tag{11.36}$$

A4.2 Fuzzy rules and rule systems

Fuzzy rules have been used very successfully for process control. They follow the usual logical scheme IF(criteria) THEN (consequence). A fuzzy rule can be regarded as the experience of a certain aspect or state of the process considered that is more or less applicable to the current situation. A fuzzy rule consists of a set of premises $A_{i,j}$ in the form of fuzzy sets with membership functions $\mu_{A_{i,j}}$ and a consequence B_i also in the form of a fuzzy set.

$$\text{If } A_{i,1} \text{ AND } A_{i,2} \text{ AND ... AND } A_{i,J} \text{ THEN } B_i \tag{11.37}$$

A fuzzy rule system consists of I such rules. The applicability of a fuzzy rule for a certain case depends on the 'truth grade' of the certain rule and it depends also on the arguments $(a_1,\ldots,a_J)$ to which the rule is to be applied. The truth value is not a qualitative statement on the accuracy of a rule, but it is a degree to which the rule can be applied to the particular case. The truth value corresponding to the fulfillment of the conditions of a rule is called the degree of fulfillment (DOF)

ν of that rule. There are several different possibilities to calculate the DOF, with the most common being the product inference:

$$\nu\left(A_{i,1} \text{ AND } A_{i,2} \text{ AND ... AND } A_{i,J}\right) = \prod_{j=1}^{J} \mu_{A_{i,j}}\left(a_j\right) \tag{11.38}$$

Fuzzy rules are usually formulated such that several rules can be applied to the same situation expressed as a vector of premises. These rules not only have different consequences but depending on the conditions they also have different DOF's for the given input ($a_1,\ldots,a_J$). Therefore, the overall response which can be derived from the rule system has to be a combination of the individual rule responses, while taking into consideration the individual DOF's. For this procedure, termed inference, several possibilities exist, e.g. clipping of each rules answer at the height of its DOF, multiplication of each rule answer set with the rule DOF, and division with the answer set area. This methods has the advantage of favoring precise answers and is known as the normed weighted sum combination of responses (B_i,ν_i) for $i=1,\ldots,I$ being the fuzzy set B with the membership function:

$$\mu_B\left(x\right) = \frac{\sum_{i=1}^{I} \nu_i \beta_i \mu_{B_i}(x)}{\max \sum_{i=1}^{I} \nu_i \beta_i \mu_{B_i}(x)} \tag{11.39}$$

where:

$$\beta_i = \frac{1}{\int_{-\infty}^{+\infty} \mu_{B_i}(x)dx} \tag{11.40}$$

This combination method delivers for each vector of arguments a fuzzy set as response. However, in order to calculate exact values as required in models this fuzzy response has to be replaced by a well defined or 'crisp' number. The procedure of replacing the fuzzy response with a single value is called defuzzification. Here too, several possibilities exist: The mean of maximum, where the crisp number is the center of the line of maximum DOF or the center of gravity of the rule system answer fuzzy set. The latter is also known as the fuzzy mean m(A) of a fuzzy set A defined on the real line where

$$\int_{-\infty}^{m(A)} \left(m(A) - t\right)\mu_A(t)dt = \int_{M(A)}^{+\infty} \left(t - m(A)\right)\mu_A(t)dt \tag{11.41}$$

Combining the normed weighted sum inference with the fuzzy mean defuzzification has the advantage of extremely fast and simple response calculation. It was shown in Bárdossy and Duckstein (1995) that the fuzzy mean of the combined response m(B) is:

$$m(B) = \frac{\sum_{i=1}^{I} \nu_i m(B_i)}{\sum_{i=1}^{I} \nu_i} \tag{11.42}$$

A5 Curriculum Vitae

Uwe Ehret

22.04.1971	Born in Stuttgart as second child of Christel and Gerhard Lorch
09/77 – 07/81	Goethe elementary school in Asperg
09/81 – 05/90	Friedrich-List Gymnasium (advanced level secondary school) in Asperg
05/90	Abitur (advanced level high school diploma)
11/90 – 01/92	Community Service Work in Ludwigsburg
03/92 – 08/96	Civil Engineering studies at the University for applied science Stuttgart (Fachhochschule für Technik Stuttgart)
02/94 - 07/94	Internship in Seattle, USA
08/96	Graduation as Diplom-Ingenieur (FH), Josef-von-Egle Award
10/96 – 05/98	Civil Engineering studies at the University of Stuttgart
09/97 –04/98	International study exchange at the University of Waterloo, Canada
05/98	Graduation as Diplom-Ingenieur
since 06/98	Research assistant at the Institute for Hydraulic Engineering, University of Stuttgart (Institut für Wasserbau)
06/98 – 06/99	ACCORD project (Atmospheric circulation classification and regional downscaling
07/99 – 07/02	Rainfall and runoff forecasting in the Goldersbach catchment

Institut für Wasserbau
Universität Stuttgart

Pfaffenwaldring 61
70569 Stuttgart (Vaihingen)
Telefon (0711) 685 - 64717/64749/64752/64679
Telefax (0711) 685 - 67020 o. 64746 o. 64681
E-Mail: iws@iws.uni-stuttgart.de
http://www.iws.uni-stuttgart.de

Verzeichnis der Mitteilungshefte

1 Röhnisch, Arthur: *Die Bemühungen um eine Wasserbauliche Versuchsanstalt an der Technischen Hochschule Stuttgart*,
und
Fattah Abouleid, Abdel: *Beitrag zur Berechnung einer in lockeren Sand gerammten, zweifach verankerten Spundwand*, 1963

2 Marotz, Günter: *Beitrag zur Frage der Standfestigkeit von dichten Asphaltbelägen im Großwasserbau*, 1964

3 Gurr, Siegfried: *Beitrag zur Berechnung zusammengesetzter ebener Flächentragwerke unter besonderer Berücksichtigung ebener Stauwände, mit Hilfe von Randwert- und Lastwertmatrizen*, 1965

4 Plica, Peter: *Ein Beitrag zur Anwendung von Schalenkonstruktionen im Stahlwasserbau*, und Petrikat, Kurt: *Möglichkeiten und Grenzen des wasserbaulichen Versuchswesens*, 1966

5 Plate, Erich: *Beitrag zur Bestimmung der Windgeschwindigkeitsverteilung in der durch eine Wand gestörten bodennahen Luftschicht*,
und
Röhnisch, Arthur; Marotz, Günter: *Neue Baustoffe und Bauausführungen für den Schutz der Böschungen und der Sohle von Kanälen, Flüssen und Häfen; Gestehungskosten und jeweilige Vorteile*, sowie Unny, T.E.: *Schwingungsuntersuchungen am Kegelstrahlschieber*, 1967

6 Seiler, Erich: *Die Ermittlung des Anlagenwertes der bundeseigenen Binnenschiffahrtsstraßen und Talsperren und des Anteils der Binnenschiffahrt an diesem Wert*, 1967

7 *Sonderheft anläßlich des 65. Geburtstages von Prof. Arthur Röhnisch mit Beiträgen von* Benk, Dieter; Breitling, J.; Gurr, Siegfried; Haberhauer, Robert; Honekamp, Hermann; Kuz, Klaus Dieter; Marotz, Günter; Mayer-Vorfelder, Hans-Jörg; Miller, Rudolf; Plate, Erich J.; Radomski, Helge; Schwarz, Helmut; Vollmer, Ernst; Wildenhahn, Eberhard; 1967

8 Jumikis, Alfred: *Beitrag zur experimentellen Untersuchung des Wassernachschubs in einem gefrierenden Boden und die Beurteilung der Ergebnisse*, 1968

9 Marotz, Günter: *Technische Grundlagen einer Wasserspeicherung im natürlichen Untergrund*, 1968

10 Radomski, Helge: *Untersuchungen über den Einfluß der Querschnittsform wellenförmiger Spundwände auf die statischen und rammtechnischen Eigenschaften*, 1968

11 Schwarz, Helmut: *Die Grenztragfähigkeit des Baugrundes bei Einwirkung vertikal gezogener Ankerplatten als zweidimensionales Bruchproblem*, 1969

12 Erbel, Klaus: *Ein Beitrag zur Untersuchung der Metamorphose von Mittelgebirgsschneedecken unter besonderer Berücksichtigung eines Verfahrens zur Bestimmung der thermischen Schneequalität*, 1969

13 Westhaus, Karl-Heinz: *Der Strukturwandel in der Binnenschiffahrt und sein Einfluß auf den Ausbau der Binnenschiffskanäle*, 1969

14 Mayer-Vorfelder, Hans-Jörg: *Ein Beitrag zur Berechnung des Erdwiderstandes unter Ansatz der logarithmischen Spirale als Gleitflächenfunktion*, 1970

15 Schulz, Manfred: *Berechnung des räumlichen Erddruckes auf die Wandung kreiszylindrischer Körper*, 1970

16 Mobasseri, Manoutschehr: *Die Rippenstützmauer. Konstruktion und Grenzen ihrer Standsicherheit*, 1970

17 Benk, Dieter: *Ein Beitrag zum Betrieb und zur Bemessung von Hochwasserrückhaltebecken*, 1970

18 Gàl, Attila: *Bestimmung der mitschwingenden Wassermasse bei überströmten Fischbauchklappen mit kreiszylindrischem Staublech*, 1971, vergriffen

19 Kuz, Klaus Dieter: *Ein Beitrag zur Frage des Einsetzens von Kavitationserscheinungen in einer Düsenströmung bei Berücksichtigung der im Wasser gelösten Gase*, 1971, vergriffen

20 Schaak, Hartmut: *Verteilleitungen von Wasserkraftanlagen*, 1971

21 *Sonderheft zur Eröffnung der neuen Versuchsanstalt des Instituts für Wasserbau der Universität Stuttgart mit Beiträgen von* Brombach, Hansjörg; Dirksen, Wolfram; Gàl, Attila; Gerlach, Reinhard; Giesecke, Jürgen; Holthoff, Franz-Josef; Kuz, Klaus Dieter; Marotz, Günter; Minor, Hans-Erwin; Petrikat, Kurt; Röhnisch, Arthur; Rueff, Helge; Schwarz, Helmut; Vollmer, Ernst; Wildenhahn, Eberhard; 1972

22 Wang, Chung-su: *Ein Beitrag zur Berechnung der Schwingungen an Kegelstrahlschiebern*, 1972

23 Mayer-Vorfelder, Hans-Jörg: *Erdwiderstandsbeiwerte nach dem Ohde-Variationsverfahren*, 1972

24 Minor, Hans-Erwin: *Beitrag zur Bestimmung der Schwingungsanfachungsfunktionen überströmter Stauklappen*, 1972, vergriffen

25 Brombach, Hansjörg: *Untersuchung strömungsmechanischer Elemente (Fluidik) und die Möglichkeit der Anwendung von Wirbelkammerelementen im Wasserbau*, 1972, vergriffen

26 Wildenhahn, Eberhard: *Beitrag zur Berechnung von Horizontalfilterbrunnen*, 1972

27 Steinlein, Helmut: *Die Eliminierung der Schwebstoffe aus Flußwasser zum Zweck der unterirdischen Wasserspeicherung, gezeigt am Beispiel der Iller*, 1972

28 Holthoff, Franz Josef: *Die Überwindung großer Hubhöhen in der Binnenschiffahrt durch Schwimmerhebewerke*, 1973

29 Röder, Karl: *Einwirkungen aus Baugrundbewegungen auf trog- und kastenförmige Konstruktionen des Wasser- und Tunnelbaues*, 1973

30 Kretschmer, Heinz: *Die Bemessung von Bogenstaumauern in Abhängigkeit von der Talform*, 1973

31 Honekamp, Hermann: *Beitrag zur Berechnung der Montage von Unterwasserpipelines*, 1973

32 Giesecke, Jürgen: *Die Wirbelkammertriode als neuartiges Steuerorgan im Wasserbau*, und Brombach, Hansjörg: *Entwicklung, Bauformen, Wirkungsweise und Steuereigenschaften von Wirbelkammerverstärkern*, 1974

33 Rueff, Helge: *Untersuchung der schwingungserregenden Kräfte an zwei hintereinander angeordneten Tiefschützen unter besonderer Berücksichtigung von Kavitation*, 1974

34 Röhnisch, Arthur: *Einpreßversuche mit Zementmörtel für Spannbeton - Vergleich der Ergebnisse von Modellversuchen mit Ausführungen in Hüllwellrohren*, 1975

35 *Sonderheft anläßlich des 65. Geburtstages von Prof. Dr.-Ing. Kurt Petrikat mit Beiträgen von*: Brombach, Hansjörg; Erbel, Klaus; Flinspach, Dieter; Fischer jr., Richard; Gàl, Attila; Gerlach, Reinhard; Giesecke, Jürgen; Haberhauer, Robert; Hafner Edzard; Hausenblas, Bernhard; Horlacher, Hans-Burkhard; Hutarew, Andreas; Knoll, Manfred; Krummet, Ralph; Marotz, Günter; Merkle, Theodor; Miller, Christoph; Minor, Hans-Erwin; Neumayer, Hans; Rao, Syamala; Rath, Paul; Rueff, Helge; Ruppert, Jürgen; Schwarz, Wolfgang; Topal-Gökceli, Mehmet; Vollmer, Ernst; Wang, Chung-su; Weber, Hans-Georg; 1975

36 Berger, Jochum: *Beitrag zur Berechnung des Spannungszustandes in rotationssymmetrisch belasteten Kugelschalen veränderlicher Wandstärke unter Gas- und Flüssigkeitsdruck durch Integration schwach singulärer Differentialgleichungen*, 1975

37 Dirksen, Wolfram: *Berechnung instationärer Abflußvorgänge in gestauten Gerinnen mittels Differenzenverfahren und die Anwendung auf Hochwasserrückhaltebecken*, 1976

38 Horlacher, Hans-Burkhard: *Berechnung instationärer Temperatur- und Wärmespannungsfelder in langen mehrschichtigen Hohlzylindern*, 1976

39 Hafner, Edzard: *Untersuchung der hydrodynamischen Kräfte auf Baukörper im Tiefwasserbereich des Meeres*, 1977, ISBN 3-921694-39-6

40 Ruppert, Jürgen: *Über den Axialwirbelkammerverstärker für den Einsatz im Wasserbau*, 1977, ISBN 3-921694-40-X

41 Hutarew, Andreas: *Beitrag zur Beeinflußbarkeit des Sauerstoffgehalts in Fließgewässern an Abstürzen und Wehren*, 1977, ISBN 3-921694-41-8, vergriffen

42 Miller, Christoph: *Ein Beitrag zur Bestimmung der schwingungserregenden Kräfte an unterströmten Wehren*, 1977, ISBN 3-921694-42-6

43 Schwarz, Wolfgang: *Druckstoßberechnung unter Berücksichtigung der Radial- und Längsverschiebungen der Rohrwandung*, 1978, ISBN 3-921694-43-4

44 Kinzelbach, Wolfgang: *Numerische Untersuchungen über den optimalen Einsatz variabler Kühlsysteme einer Kraftwerkskette am Beispiel Oberrhein*, 1978, ISBN 3-921694-44-2

45 Barczewski, Baldur: *Neue Meßmethoden für Wasser-Luftgemische und deren Anwendung auf zweiphasige Auftriebsstrahlen*, 1979, ISBN 3-921694-45-0

46 Neumayer, Hans: *Untersuchung der Strömungsvorgänge in radialen Wirbelkammerverstärkern*, 1979, ISBN 3-921694-46-9

47 Elalfy, Youssef-Elhassan: *Untersuchung der Strömungsvorgänge in Wirbelkammerdioden und -drosseln*, 1979, ISBN 3-921694-47-7

48 Brombach, Hansjörg: *Automatisierung der Bewirtschaftung von Wasserspeichern*, 1981, ISBN 3-921694-48-5

49 Geldner, Peter: *Deterministische und stochastische Methoden zur Bestimmung der Selbstdichtung von Gewässern*, 1981, ISBN 3-921694-49-3, vergriffen

50 Mehlhorn, Hans: *Temperaturveränderungen im Grundwasser durch Brauchwassereinleitungen*, 1982, ISBN 3-921694-50-7, vergriffen

51 Hafner, Edzard: *Rohrleitungen und Behälter im Meer*, 1983, ISBN 3-921694-51-5

52 Rinnert, Bernd: *Hydrodynamische Dispersion in porösen Medien: Einfluß von Dichteunterschieden auf die Vertikalvermischung in horizontaler Strömung*, 1983, ISBN 3-921694-52-3, vergriffen

53 Lindner, Wulf: *Steuerung von Grundwasserentnahmen unter Einhaltung ökologischer Kriterien*, 1983, ISBN 3-921694-53-1, vergriffen

54 Herr, Michael; Herzer, Jörg; Kinzelbach, Wolfgang; Kobus, Helmut; Rinnert, Bernd: *Methoden zur rechnerischen Erfassung und hydraulischen Sanierung von Grundwasserkontaminationen*, 1983, ISBN 3-921694-54-X

55 Schmitt, Paul: *Wege zur Automatisierung der Niederschlagsermittlung*, 1984, ISBN 3-921694-55-8, vergriffen

56 Müller, Peter: *Transport und selektive Sedimentation von Schwebstoffen bei gestautem Abfluß*, 1985, ISBN 3-921694-56-6

57 El-Qawasmeh, Fuad: *Möglichkeiten und Grenzen der Tropfbewässerung unter besonderer Berücksichtigung der Verstopfungsanfälligkeit der Tropfelemente*, 1985, ISBN 3-921694-57-4, vergriffen

58 Kirchenbaur, Klaus: *Mikroprozessorgesteuerte Erfassung instationärer Druckfelder am Beispiel seegangsbelasteter Baukörper*, 1985, ISBN 3-921694-58-2

59 Kobus, Helmut (Hrsg.): *Modellierung des großräumigen Wärme- und Schadstofftransports im Grundwasser*, Tätigkeitsbericht 1984/85 (DFG-Forschergruppe an den Universitäten Hohenheim, Karlsruhe und Stuttgart), 1985, ISBN 3-921694-59-0, vergriffen

60 Spitz, Karlheinz: *Dispersion in porösen Medien: Einfluß von Inhomogenitäten und Dichteunterschieden*, 1985, ISBN 3-921694-60-4, vergriffen

61 Kobus, Helmut: *An Introduction to Air-Water Flows in Hydraulics*, 1985, ISBN 3-921694-61-2

62 Kaleris, Vassilios: *Erfassung des Austausches von Oberflächen- und Grundwasser in horizontalebenen Grundwassermodellen*, 1986, ISBN 3-921694-62-0

63 Herr, Michael: *Grundlagen der hydraulischen Sanierung verunreinigter Porengrundwasserleiter*, 1987, ISBN 3-921694-63-9

64 Marx, Walter: *Berechnung von Temperatur und Spannung in Massenbeton infolge Hydratation*, 1987, ISBN 3-921694-64-7

65 Koschitzky, Hans-Peter: *Dimensionierungskonzept für Sohlbelüfter in Schußrinnen zur Vermeidung von Kavitationsschäden*, 1987, ISBN 3-921694-65-5

66 Kobus, Helmut (Hrsg.): *Modellierung des großräumigen Wärme- und Schadstofftransports im Grundwasser*, Tätigkeitsbericht 1986/87 (DFG-Forschergruppe an den Universitäten Hohenheim, Karlsruhe und Stuttgart) 1987, ISBN 3-921694-66-3

67 Söll, Thomas: *Berechnungsverfahren zur Abschätzung anthropogener Temperaturanomalien im Grundwasser*, 1988, ISBN 3-921694-67-1

68 Dittrich, Andreas; Westrich, Bernd: *Bodenseeufererosion, Bestandsaufnahme und Bewertung*, 1988, ISBN 3-921694-68-X, vergriffen

69 Huwe, Bernd; van der Ploeg, Rienk R.: *Modelle zur Simulation des Stickstoffhaushaltes von Standorten mit unterschiedlicher landwirtschaftlicher Nutzung*, 1988, ISBN 3-921694-69-8, vergriffen

70 Stephan, Karl: *Integration elliptischer Funktionen*, 1988, ISBN 3-921694-70-1

71 Kobus, Helmut; Zilliox, Lothaire (Hrsg.): *Nitratbelastung des Grundwassers, Auswirkungen der Landwirtschaft auf die Grundwasser- und Rohwasserbeschaffenheit und Maßnahmen zum Schutz des Grundwassers*. Vorträge des deutsch-französischen Kolloquiums am 6. Oktober 1988, Universitäten Stuttgart und Louis Pasteur Strasbourg (Vorträge in deutsch oder französisch, Kurzfassungen zweisprachig), 1988, ISBN 3-921694-71-X

72 Soyeaux, Renald: *Unterströmung von Stauanlagen auf klüftigem Untergrund unter Berücksichtigung laminarer und turbulenter Fließzustände*,1991, ISBN 3-921694-72-8

73 Kohane, Roberto: *Berechnungsmethoden für Hochwasserabfluß in Fließgewässern mit überströmten Vorländern*, 1991, ISBN 3-921694-73-6

74 Hassinger, Reinhard: *Beitrag zur Hydraulik und Bemessung von Blocksteinrampen in flexibler Bauweise*, 1991, ISBN 3-921694-74-4, vergriffen

75 Schäfer, Gerhard: *Einfluß von Schichtenstrukturen und lokalen Einlagerungen auf die Längsdispersion in Porengrundwasserleitern*, 1991, ISBN 3-921694-75-2

76 Giesecke, Jürgen: *Vorträge, Wasserwirtschaft in stark besiedelten Regionen; Umweltforschung mit Schwerpunkt Wasserwirtschaft*, 1991, ISBN 3-921694-76-0

77 Huwe, Bernd: *Deterministische und stochastische Ansätze zur Modellierung des Stickstoffhaushalts landwirtschaftlich genutzter Flächen auf unterschiedlichem Skalenniveau*, 1992, ISBN 3-921694-77-9, vergriffen

78 Rommel, Michael: *Verwendung von Kluftdaten zur realitätsnahen Generierung von Kluftnetzen mit anschließender laminar-turbulenter Strömungsberechnung*, 1993, ISBN 3-92 1694-78-7

79 Marschall, Paul: *Die Ermittlung lokaler Stofffrachten im Grundwasser mit Hilfe von Einbohrloch-Meßverfahren*, 1993, ISBN 3-921694-79-5, vergriffen

80 Ptak, Thomas: *Stofftransport in heterogenen Porenaquiferen: Felduntersuchungen und stochastische Modellierung*, 1993, ISBN 3-921694-80-9, vergriffen

81 Haakh, Frieder: *Transientes Strömungsverhalten in Wirbelkammern,* 1993, ISBN 3-921694-81-7

82 Kobus, Helmut; Cirpka, Olaf; Barczewski, Baldur; Koschitzky, Hans-Peter: *Versucheinrichtung zur Grundwasser und Altlastensanierung VEGAS, Konzeption und Programmrahmen*, 1993, ISBN 3-921694-82-5

83 Zang, Weidong: *Optimaler Echtzeit-Betrieb eines Speichers mit aktueller Abflußregenerierung*, 1994, ISBN 3-921694-83-3, vergriffen

84 Franke, Hans-Jörg: *Stochastische Modellierung eines flächenhaften Stoffeintrages und Transports in Grundwasser am Beispiel der Pflanzenschutzmittelproblematik*, 1995, ISBN 3-921694-84-1

85 Lang, Ulrich: *Simulation regionaler Strömungs- und Transportvorgänge in Karstaquiferen mit Hilfe des Doppelkontinuum-Ansatzes: Methodenentwicklung und Parameteridentifikation*, 1995, ISBN 3-921694-85-X, vergriffen

86 Helmig, Rainer: *Einführung in die Numerischen Methoden der Hydromechanik*, 1996, ISBN 3-921694-86-8, vergriffen

87 Cirpka, Olaf: *CONTRACT: A Numerical Tool for Contaminant Transport and Chemical Transformations - Theory and Program Documentation* -, 1996, ISBN 3-921694-87-6

88 Haberlandt, Uwe: *Stochastische Synthese und Regionalisierung des Niederschlages für Schmutzfrachtberechnungen*, 1996, ISBN 3-921694-88-4

89 Croisé, Jean: *Extraktion von flüchtigen Chemikalien aus natürlichen Lockergesteinen mittels erzwungener Luftströmung*, 1996, ISBN 3-921694-89-2, vergriffen

90 Jorde, Klaus: *Ökologisch begründete, dynamische Mindestwasserregelungen bei Ausleitungskraftwerken*, 1997, ISBN 3-921694-90-6, vergriffen

91 Helmig, Rainer: *Gekoppelte Strömungs- und Transportprozesse im Untergrund - Ein Beitrag zur Hydrosystemmodellierung-*, 1998, ISBN 3-921694-91-4

92 Emmert, Martin: *Numerische Modellierung nichtisothermer Gas-Wasser Systeme in porösen Medien,* 1997, ISBN 3-921694-92-2

93 Kern, Ulrich: *Transport von Schweb- und Schadstoffen in staugeregelten Fließgewässern am Beispiel des Neckars*, 1997, ISBN 3-921694-93-0, vergriffen

94 Förster, Georg: *Druckstoßdämpfung durch große Luftblasen in Hochpunkten von Rohrleitungen 1997*, ISBN 3-921694-94-9

95 Cirpka, Olaf: *Numerische Methoden zur Simulation des reaktiven Mehrkomponententransports im Grundwasser*, 1997, ISBN 3-921694-95-7, vergriffen

96 Färber, Arne: *Wärmetransport in der ungesättigten Bodenzone: Entwicklung einer thermischen In-situ-Sanierungstechnologie*, 1997, ISBN 3-921694-96-5

97 Betz, Christoph: *Wasserdampfdestillation von Schadstoffen im porösen Medium: Entwicklung einer thermischen In-situ-Sanierungstechnologie*, 1998, ISBN 3-921694-97-3

98 Xu, Yichun: *Numerical Modeling of Suspended Sediment Transport in Rivers*, 1998, ISBN 3-921694-98-1, vergriffen

99 Wüst, Wolfgang: *Geochemische Untersuchungen zur Sanierung CKW-kontaminierter Aquifere mit Fe(0)-Reaktionswänden,* 2000, ISBN 3-933761-02-2

100 Sheta, Hussam: *Simulation von Mehrphasenvorgängen in porösen Medien unter Einbeziehung von Hysterese-Effekten*, 2000, ISBN 3-933761-03-4

101 Ayros, Edwin: *Regionalisierung extremer Abflüsse auf der Grundlage statistischer Verfahren*, 2000, ISBN 3-933761-04-2, vergriffen

102 Huber, Ralf: *Compositional Multiphase Flow and Transport in Heterogeneous Porous Media*, 2000, ISBN 3-933761-05-0

103 Braun, Christopherus: *Ein Upscaling-Verfahren für Mehrphasenströmungen in porösen Medien*, 2000, ISBN 3-933761-06-9

104 Hofmann, Bernd: *Entwicklung eines rechnergestützten Managementsystems zur Beurteilung von Grundwasserschadensfällen*, 2000, ISBN 3-933761-07-7

105 Class, Holger: *Theorie und numerische Modellierung nichtisothermer Mehrphasenprozesse in NAPL-kontaminierten porösen Medien,* 2001, ISBN 3-933761-08-5

106 Schmidt, Reinhard: *Wasserdampf- und Heißluftinjektion zur thermischen Sanierung kontaminierter Standorte*, 2001, ISBN 3-933761-09-3

107 Josef, Reinhold:, *Schadstoffextraktion mit hydraulischen Sanierungsverfahren unter Anwendung von grenzflächenaktiven Stoffen*, 2001, ISBN 3-933761-10-7

108 Schneider, Matthias: *Habitat- und Abflussmodellierung für Fließgewässer mit unscharfen Berechnungsansätzen*, 2001, ISBN 3-933761-11-5

109 Rathgeb, Andreas: *Hydrodynamische Bemessungsgrundlagen für Lockerdeckwerke an überströmbaren Erddämmen*, 2001, ISBN 3-933761-12-3

110 Lang, Stefan: *Parallele numerische Simulation instätionärer Probleme mit adaptiven Methoden auf unstrukturierten Gittern*, 2001, ISBN 3-933761-13-1

111 Appt, Jochen; Stumpp Simone: *Die Bodensee-Messkampagne 2001, IWS/CWR Lake Constance Measurement Program 2001*, 2002, ISBN 3-933761-14-X

112 Heimerl, Stephan: *Systematische Beurteilung von Wasserkraftprojekten,* 2002, ISBN 3-933761-15-8

113 Iqbal, Amin: *On the Management and Salinity Control of Drip Irrigation,* 2002, ISBN 3-933761-16-6

114 Silberhorn-Hemminger, Annette: *Modellierung von Kluftaquifersystemen: Geostatistische Analyse und deterministisch-stochastische Kluftgenerierung,* 2002, ISBN 3-933761-17-4

115 Winkler, Angela: *Prozesse des Wärme- und Stofftransports bei der In-situ-Sanierung mit festen Wärmequellen,* 2003, ISBN 3-933761-18-2

116 Marx, Walter: *Wasserkraft, Bewässerung, Umwelt - Planungs- und Bewertungsschwerpunkte der Wasserbewirtschaftung,* 2003, ISBN 3-933761-19-0

117 Hinkelmann, Reinhard: *Efficient Numerical Methods and Information-Processing Techniques in Environment Water,* 2003, ISBN 3-933761-20-4

118 Samaniego-Eguiguren, Luis Eduardo: *Hydrological Consequences of Land Use / Land Cover and Climatic Changes in Mesoscale Catchments*, 2003, ISBN 3-933761-21-2

119 Neunhäuserer, Lina: *Diskretisierungsansätze zur Modellierung von Strömungs- und Transportprozessen in geklüftet-porösen Medien*, 2003, ISBN 3-933761-22-0

120 Paul, Maren: *Simulation of Two-Phase Flow in Heterogeneous Poros Media with Adaptive Methods*, 2003, ISBN 3-933761-23-9

121 Ehret, Uwe: *Rainfall and Flood Nowcasting in Small Catchments using Weather Radar*, 2003, ISBN 3-933761-24-7

122 Haag, Ingo: *Der Sauerstoffhaushalt staugeregelter Flüsse am Beispiel des Neckars - Analysen, Experimente, Simulationen -,* 2003, ISBN 3-933761-25-5

123 Appt, Jochen: *Analysis of Basin-Scale Internal Waves in Upper Lake Constance,* 2003, ISBN 3-933761-26-3

124 Hrsg.: Schrenk, Volker; Batereau, Katrin; Barczewski, Baldur; Weber, Karolin und Koschitzky, Hans-Peter: *Symposium Ressource Fläche und VEGAS - Statuskolloquium 2003, 30. September und 1. Oktober 2003,* 2003, ISBN 3-933761-27-1

125 Omar Khalil Ouda: *Optimisation of Agricultural Water Use: A Decision Support System for the Gaza Strip,* 2003, ISBN 3-933761-28-0

126 Batereau, Katrin: *Sensorbasierte Bodenluftmessung zur Vor-Ort-Erkundung von Schadensherden im Untergrund*, 2004, ISBN 3-933761-29-8

127 Witt, Oliver: *Erosionsstabilität von Gewässersedimenten mit Auswirkung auf den Stofftransport bei Hochwasser am Beispiel ausgewählter Stauhaltungen des Oberrheins*, 2004, ISBN 3-933761-30-1

128 Jakobs, Hartmut: *Simulation nicht-isothermer Gas-Wasser-Prozesse in komplexen Kluft-Matrix-Systemen*, 2004, ISBN 3-933761-31-X

129 Li, Chen-Chien: *Deterministisch-stochastisches Berechnungskonzept zur Beurteilung der Auswirkungen erosiver Hochwasserereignisse in Flussstauhaltungen,* 2004, ISBN 3-933761-32-8

130 Reichenberger, Volker; Helmig, Rainer; Jakobs, Hartmut; Bastian, Peter; Niessner, Jennifer: *Complex Gas-Water Processes in Discrete Fracture-Matrix Systems: Upscaling, Mass-Conservative Discretization and Efficient Multilevel Solution,* 2004, ISBN 3-933761-33-6

131 Hrsg.: Barczewski, Baldur; Koschitzky, Hans-Peter; Weber, Karolin; Wege, Ralf: *VEGAS - Statuskolloquium 2004,* Tagungsband zur Veranstaltung am 05. Oktober 2004 an der Universität Stuttgart, Campus Stuttgart-Vaihingen, 2004, ISBN 3-933761-34-4

132 Asie, Kemal Jabir: *Finite Volume Models for Multiphase Multicomponent Flow through Porous Media*. 2005, ISBN 3-933761-35-2

133 Jacoub, George: *Development of a 2-D Numerical Module for Particulate Contaminant Transport in Flood Retention Reservoirs and Impounded Rivers,* 2004, ISBN 3-933761-36-0

134 Nowak, Wolfgang: *Geostatistical Methods for the Identification of Flow and Transport Parameters in the Subsurface,* 2005, ISBN 3-933761-37-9

135 Süß, Mia: *Analysis of the influence of structures and boundaries on flow and transport processes in fractured porous media*, 2005, ISBN 3-933761-38-7

136 Jose, Surabhin Chackiath: *Experimental Investigations on Longitudinal Dispersive Mixing in Heterogeneous Aquifers,* 2005, ISBN: 3-933761-39-5

137 Filiz, Fulya: *Linking Large-Scale Meteorological Conditions to Floods in Mesoscale Catchments,* 2005, ISBN 3-933761-40-9

138 Qin, Minghao: *Wirklichkeitsnahe und recheneffiziente Ermittlung von Temperatur und Spannungen bei großen RCC-Staumauern*, 2005, ISBN 3-933761-41-7

139 Kobayashi, Kenichiro: *Optimization Methods for Multiphase Systems in the Subsurface - Application to Methane Migration in Coal Mining Areas*, 2005, ISBN 3-933761-42-5

140 Rahman, Md. Arifur: *Experimental Investigations on Transverse Dispersive Mixing in Heterogeneous Porous Media,* 2005, ISBN 3-933761-43-3

141 Schrenk, Volker: *Ökobilanzen zur Bewertung von Altlastensanierungsmaßnahmen,* 2005, ISBN 3-933761-44-1

142 Hundecha, Hirpa Yeshewatesfa: *Regionalization of Parameters of a Conceptual Rainfall-Runoff Model*, 2005, ISBN: 3-933761-45-X

143 Wege, Ralf: *Untersuchungs- und Überwachungsmethoden für die Beurteilung natürlicher Selbstreinigungsprozesse im Grundwasser,* 2005, ISBN 3-933761-46-8

144 Breiting, Thomas: *Techniken und Methoden der Hydroinformatik - Modellierung von komplexen Hydrosystemen im Untergrund*, 2006, 3-933761-47-6

145 Hrsg.: Braun, Jürgen; Koschitzky, Hans-Peter; Müller, Martin: *Ressource Untergrund: 10 Jahre VEGAS: Forschung und Technologieentwicklung zum Schutz von Grundwasser und Boden,* Tagungsband zur Veranstaltung am 28. und 29. September 2005 an der Universität Stuttgart, Campus Stuttgart-Vaihingen, 2005, ISBN 3-933761-48-4

146 Rojanschi, Vlad: *Abflusskonzentration in mesoskaligen Einzugsgebieten unter Berücksichtigung des Sickerraumes,* 2006, ISBN 3-933761-49-2

147 Winkler, Nina Simone: *Optimierung der Steuerung von Hochwasserrückhaltebecken-systemen,* 2006, ISBN 3-933761-50-6

148 Wolf, Jens: *Räumlich differenzierte Modellierung der Grundwasserströmung alluvialer Aquifere für mesoskalige Einzugsgebiete*, 2006, ISBN: 3-933761-51-4

149 Kohler, Beate: *Externe Effekte der Laufwasserkraftnutzung*, 2006, ISBN 3-933761-52-2

150 Hrsg.: Braun, Jürgen; Koschitzky, Hans-Peter; Stuhrmann, Matthias: *VEGAS-Statuskolloquium 2006,* Tagungsband zur Veranstaltung am 28. September 2006 an der Universität Stuttgart, Campus Stuttgart-Vaihingen, 2006, ISBN 3-933761-53-0

151 Niessner, Jennifer: *Multi-Scale Modeling of Multi-Phase - Multi-Component Processes in Heterogeneous Porous Media*, 2006, ISBN 3-933761-54-9

152 Fischer, Markus: *Beanspruchung eingeerdeter Rohrleitungen infolge Austrocknung bindiger Böden,* 2006, ISBN 3-933761-55-7

153 Schneck, Alexander: *Optimierung der Grundwasserbewirtschaftung unter Berücksichtigung der Belange der Wasserversorgung, der Landwirtschaft und des Naturschutzes*, 2006, ISBN 3-933761-56-5

154 Das, Tapash: *The Impact of Spatial Variability of Precipitation on the Predictive Uncertainty of Hydrological Models,* 2006, ISBN 3-933761-57-3

155 Bielinski, Andreas: *Numerical Simulation of CO_2 sequestration in geological formations*, 2007, ISBN 3-933761-58-1

156 Mödinger, Jens: *Entwicklung eines Bewertungs- und Entscheidungsunterstützungssystems für eine nachhaltige regionale Grundwasserbewirtschaftung*, 2006, ISBN 3-933761-60-3

157 Manthey, Sabine: *Two-phase flow processes with dynamic effects in porous media - parameter estimation and simulation,* 2007, ISBN 3-933761-61-1

158 Pozos Estrada, Oscar: *Investigation on the Effects of Entrained Air in Pipelines,* 2007, ISBN 3-933761-62-X

159 Ochs, Steffen Oliver: *Steam injection into saturated porous media – process analysis including experimental and numerical investigations*, 2007, ISBN 3-933761-63-8

160 Marx, Andreas: *Einsatz gekoppelter Modelle und Wetterradar zur Abschätzung von Niederschlagsintensitäten und zur Abflussvorhersage, 2007,* ISBN 3-933761-64-6

161 Hartmann, Gabriele Maria: *Investigation of Evapotranspiration Concepts in Hydrological Modelling for Climate Change Impact Assessment*, 2007, ISBN 3-933761-65-4

162 Kebede Gurmessa, Tesfaye: *Numerical Investigation on Flow and Transport Characteristics to Improve Long-Term Simulation of Reservoir Sedimentation*, 2007, ISBN 3-933761-66-2

163 Trifković, Aleksandar: *Multi-objective and Risk-based Modelling Methodology for Planning, Design and Operation of Water Supply Systems*, 2007, ISBN 3-933761-67-0

164 Götzinger, Jens: *Distributed Conceptual Hydrological Modelling - Simulation of Climate, Land Use Change Impact and Uncertainty Analysis*, 2007, ISBN 3-933761-68-9

165 Hrsg.: Braun, Jürgen; Koschitzky, Hans-Peter; Stuhrmann, Matthias: *VEGAS – Kolloquium 2007,* Tagungsband zur Veranstaltung am 26. September 2007 an der Universität Stuttgart, Campus Stuttgart-Vaihingen, 2007, ISBN 3-933761-69-7

166 Freeman, Beau: *Modernization Criteria Assessment for Water Resources Planning; Klamath Irrigation Project, U.S.*, 2008, ISBN 3-933761-70-0

167 Dreher, Thomas: *Selektive Sedimentation von Feinstschwebstoffen in Wechselwirkung mit wandnahen turbulenten Strömungsbedingungen*, 2008, ISBN 3-933761-71-9

168 Yang, Wei: *Discrete-Continuous Downscaling Model for Generating Daily Precipitation Time Series*, 2008, ISBN 3-933761-72-7

169 Kopecki, Ianina: *Calculational Approach to FST-Hemispheres for Multiparametrical Benthos Habitat Modelling,* 2008*,* ISBN 3-933761-73-5

170 Brommundt, Jürgen: *Stochastische Generierung räumlich zusammenhängender Niederschlagszeitreihen*, 2008, ISBN 3-933761-74-3

171 Papafotiou, *Alexandros: Numerical Investigations of the Role of Hysteresis in Heterogeneous Two-Phase Flow Systems*, 2008, ISBN 3-933761-75-1

172 He, Yi: *Application of a Non-Parametric Classification Scheme to Catchment Hydrology*, 2008, ISBN 978-3-933761-76-7

173 Wagner, Sven: *Water Balance in a Poorly Gauged Basin in West Africa Using Atmospheric Modelling and Remote Sensing Information*, 2008, ISBN 978-3-933761-77-4

174 Hrsg.: Braun, Jürgen; Koschitzky, Hans-Peter; Stuhrmann, Matthias; Schrenk, Volker: *VEGAS-Kolloquium 2008 Ressource Fläche III*, Tagungsband zur Veranstaltung am 01. Oktober 2008 an der Universität Stuttgart, Campus Stuttgart-Vaihingen, 2008, ISBN 978-3-933761-78-1

175 Patil, Sachin: *Regionalization of an Event Based Nash Cascade Model for Flood Predictions in Ungauged Basins*, 2008, ISBN 978-3-933761-79-8

176 Assteerawatt, Anongnart: *Flow and Transport Modelling of Fractured Aquifers based on a Geostatistical Approach,* 2008, ISBN 978-3-933761-80-4

Die Mitteilungshefte ab der Nr. 134 (Jg. 2005) stehen als pdf-Datei über die Homepage des Instituts: www.iws.uni-stuttgart.de zur Verfügung.